

Nikolaou, Charalambos (2026) *Development of a low order model for preliminary design and analysis of scramjet intake/isolator configurations.* PhD thesis.

https://theses.gla.ac.uk/86346/

Copyright and moral rights for this work are retained by the author

A copy can be downloaded for personal non-commercial research or study, without prior permission or charge

This work cannot be reproduced or quoted extensively from without first obtaining permission from the author

The content must not be changed in any way or sold commercially in any format or medium without the formal permission of the author

When referring to this work, full bibliographic details including the author, title, awarding institution and date of the thesis must be given

Enlighten: Theses
https://theses.gla.ac.uk
research-enlighten@glasgow.ac.uk



Development of a Low Order Model for Preliminary Design and Analysis of Scramjet Intake/Isolator Configurations

Charalambos Nikolaou

A thesis submitted in fulfilment of the requirements for the degree of

Doctor of Philosophy

AUTONOMOUS SYSTEMS AND CONNECTIVITY RESEARCH DIVISION

JAMES WATT SCHOOL OF ENGINEERING

COLLEGE OF SCIENCE AND ENGINEERING

UNIVERSITY OF GLASGOW

December 2025

Abstract

Scramjets are an airbreathing propulsion system that holds the potential to revolutionise both intra- and extra-atmospheric flight. In the flight envelope between Mach 5 and Mach 10, incoming flow momentum causes ramjet compression to become prohibitively inefficient. Elimination of the normal shock characterising ramjets leads to the flow entering the combustor supersonically, resulting in the supersonic combustion ramjet, or scramjet. Supersonic combustion allows the engine to expand its operating envelope to around Mach 10, past which atmospheric conditions become too rarified to efficiently compress using airbreathing engines, at which point a rocket engine would take over in combined cycle engines. Despite the recent advancements in modelling, low order methods do not consider the evolution of the viscous elements along the scramjet.

This thesis is dedicated to integrating these components into a low-order unified design framework. Its purpose is the design of dual-mode and pure scramjets with inclusion of viscous elements, which can accelerate preliminary design processes. Optimisation is achieved through a metaheuristic algorithm.

Firstly, a low-order model for the characterisation of a compressible turbulent boundary layer is developed based on a physics-based incompressible universal turbulent velocity profile. For application to compressible high-speed flows, the compressibility transformation of Van Driest is used. Comparison of the velocity profile method with experimental studies show superior performance to the Van Driest correlation in predicting skin friction and integral quantities and has the capability of predicting the boundary layer thickness at each point. Subsequently, low order methodology is presented to address the Shock-Boundary Layer Interactions (SBLI) that are critical to the operation of scramjets. At the intake exit, an isolator-combustor-nozzle model is used to separate the two operating modes, size the isolating duct and obtain performance metrics. Combustion is modelled as a heat release due to fuel addition. An adiabatic nozzle is used for expansion of the combustion products to ambient pressure, as to not contribute to the thrust. For dual-mode scramjets, the isolator is sized based on an analytical relation, to match a prescribed pressure rise.

Verification of the model is performed using Computational Fluid Dynamics (CFD), comparing the performance of the resulting configuration to what is predicted by the model. The results show the very good performance of the model in the external region of the engine, with the internal part being in line with the model, provided the added heat is reduced from the predicted

value. A parametric study is performed on the designer-selected parameters, investigating their influence on the design of scramjets.

This thesis, which has performed a rigorous development and validation of various viscous sub-models pertaining to scramjets, has been demonstrated through high-fidelity simulations to be suitable for use in the early development process of scramjets. This research has provided a solid foundation for development of low-order models, through robust investigation of the primary designer-determined parameters.

Acknowledgements

“As you set out for Ithaka hope your road is a long one, full of adventure, full of discovery.” writes Konstantinos Kavafis in his famous poem, “Ithaka”. After having finally reached my doctorate “Ithaka”, I can safely say the road has indeed been full of adventures, successes, failures and many discoveries.

At the sunset of this long adventure, I would like to give my heartfelt gratitude to my supervisor, Dr. Ian Taylor, whose knowledge, support and guidance helped immensely in reaching this point.

As importantly, I would like to thank and extend my boundless love to my parents, Maria and Stelios, as well as my brothers, Theodoulos, Kyprianos and Christos, who have always been by my side, supporting me all the way to my final port of call in this doctorate. Many thanks to every other member of my family for your endless support.

A special thanks goes out to my best friends Monica and Loizos, as well as Mohsen, Jin, and Dr. Ramona Blanes who have been indispensable parts of my journey. Thanks for being part of my ship as I finally moor at the shore of Ph.D. Ithaka.

Table of Contents

Abstract i
Acknowledgements iii
List of Tables vi
List of Figures viii
Author's Declaration xiii
Nomenclature xiv
Chapter 1 - Introduction 1
1.1. Background and Motivation 1
1.2. Thesis Structure 4
Chapter 2 - State of the Art / Literature Review 6
2.1. Scramjet development history 7
2.2. Research on hypersonic intakes 8
2.2.1. Shock-Boundary layer interactions in scramjets 11
2.2.2. Experimental and numerical studies on intakes 16
2.2.3. Mixed compression intake design modelling 26
2.3. Research on hypersonic isolators 42
2.3.1. Experimental studies on isolators 43
2.3.2. Modelling of Isolators and Pseudo-shock systems 45
2.4. Chapter Summary 55
Chapter 3 - Modelling Strategy (PSO and CFD) 57
3.1. Modelling strategy and Optimisation 57
3.2. Computational Fluid Dynamics (CFD) 68
3.2.1. Numerical methods 71
3.2.2. Solver Validation & Grid dependence study 72
3.3. Chapter Summary 81
Chapter 4 - Hypersonic Flat Plate Modelling 82
4.1. Zero Pressure Gradient (ZPG) Compressible boundary layers – Model formulation 82
4.1.1. Universal incompressible boundary layer profiles 82
4.1.2. Temperature-Velocity relations 85
4.1.3. Compressibility Transformation 87
4.1.4. Final model 88

4.1.5. Flat Plate Skin Friction Coefficient correlations....92
4.2. Validation of zero pressure gradient model....95
4.2.1. Model structure and evaluation....96
4.2.2. Skin friction coefficient prediction....100
4.2.3. Influence of wake factor....101
4.3. Chapter summary....103
Chapter 5 - Shock-Turbulent Boundary Layer Interactions....107
5.1. STBLI Model Formulation....108
5.1.1. Separation state prediction....108
5.1.2. Pressure distribution prediction....110
5.2. Validation of STBLI Model....115
5.3. Chapter Summary....120
Chapter 6 - Isolator Modelling....123
6.1. Determination of operation mode....124
6.1.1. Combustion chemistry....126
6.2. Dual mode design....135
6.2.1. Shock train region....135
6.3. Chapter Summary....143
Chapter 7 - Results and Discussion of Combined Modelling....145
7.1. Verification of optimised solutions through CFD....147
7.1.1. Optimum configuration results....151
7.2. Influence of design parameters on objective functions....165
7.2.1. Variation of Mach number....165
7.2.2. Variation of mass flow rate....169
7.2.3. Variation of wall temperature....178
7.2.4. Variation of number of ramps....185
7.3. Chapter Summary....192
Chapter 8 - Conclusions / Future Work....195
8.1. Conclusions....195
8.2. Future perspectives....197
Chapter 9 - References....199

List of Tables

Table 2-1: Updated proposed high-quality studies by Roy and Blottner[13]. The quantities measured in the experiments are Stanton Number (St), local skin friction coefficient (c_f) and pressure ratio (P/P_∞).....14
Table 2-2 Variables used in parametric study of Busemann intake-based scramjet by Ispir et al.....36
Table 3-1: Decision variables with their bounds used in the optimisation process 63
Table 3-2: Experimental conditions by Schulein[18], [19].....72
Table 3-3: Boundary Conditions – Non-turbulence quantities. FV – fixedValue, ZG – zeroGradient, WT – waveTransmissive , SP – slip.....74
Table 3-4: Boundary Conditions - Turbulence quantities. FV – FixedValue, ZG – zeroGradient, WT – waveTransmissive, SP – slip.....75
Table 3-5: Discretisation schemes set in *fvSchemes* 76
Table 3-6: Grid dependence geometric and initialisation data.....78
Table 3-7: Comparison of experimental and URANS data at stations along the plate.....78
Table 4-1: Experiments used for validation of individual sub-models.....95
Table 4-2: Effect of wake parameter Π on the model prediction of δ+ and θ.....102
Table 5-1: Properties of validation studies.....116
Table 6-1: Frozen chemistry specie. Number of moles, **n**, molecular mass, $\mathbf{M_i}$, and mass fraction, $\mathbf{Y_i}$, of each substance present in complete combustion of H_2 with air, based on equivalence ratio, φ.....127
Table 6-2: Equilibrium model dependent specie and calculation of moles present in each computation step 130
Table 6-3: Experimental properties for experiments of Burrows & Kurkov and Paull, Frost & Alesi 131
Table 6-4: Variables and their range used in parametric study of frozen vs equilibrium chemistry models 132
Table 6-5: Comparison of isolator entry boundary layer properties as calculated using the UTVP developed in this work vs experimental data by Geerts & Yu.....138
Table 7-1: Range of input parameters to CMOPSO 147
Table 7-2 Resulting geometry from optimisation used as verification 148
Table 7-3: Range and increment of designer-selected inputs used in parametric study 165
Table 7-4 Angles and width/height ratio representing the optimum configurations at the Mach numbers considered 167
Table 7-5: Angles and width/height ratio representing the optimum configuration at the mass flow rates considered for dual-mode scramjet.....173
Table 7-6: Angles and width/height ratio representing the optimum configuration at the mass flow rates considered for pure scramjet.....176
Table 7-7: Angles and width/height ratio representing the optimum configuration at the wall temperatures considered for dual mode scramjet.....180

Table 7-8: Angles and width/height ratio representing the optimum configuration at the wall temperatures considered for pure scramjet 184
Table 7-9: Angles and width/height ratio representing the optimum configuration at the number of external ramps considered for dual mode scramjet 187
Table 7-10: Angles and width/height ratio representing the optimum configuration at the number of external ramps considered for pure scramjet 192

List of Figures

Figure 1-1: Engine type specific impulse with increasing Mach number. Reproduced from [3] 2
Figure 2-1: Vehicle with a mixed compression intake operating at dual-mode, due to the separated region observed in the isolator 9
Figure 2-2: Vehicle with mixed compression intake operating as a pure scramjet. In the configuration shown, the isolator becomes redundant, as the external compression system produces sufficient compression without the need for an internal shock train 10
Figure 2-3: Generic 3-ramp mixed compression intake-isolator configuration 11
Figure 2-4: Incipient separation angle (a_I) with increasing Reynolds number based on boundary layer thickness. The lines represent the prediction of the modelling approach used by the authors, with the symbols representing experimental observations from other researchers. Reproduced from original work [15]. 15
Figure 2-5: Subsonic spillage unstart. The boundary layer is fully ejected with a bow shock, resulting the loss of mass flow at subsonic speeds. 17
Figure 2-6: Supersonic spillage unstart. The boundary layer is fully ejected with an oblique shock, with mass flow loss occurring at supersonic speeds. 18
Figure 2-7: Intake starting limits. Note that y-axis is 1/ICR. 19
Figure 2-8: Comparison of base configuration to final iteration with a 2 deg cowl angle (Config VIII) and a retraction from the original location of 0.5*h, where h is the isolator duct height. Authors consider this the optimum configuration due to high startability angle and high compression. Reproduced from [37] 21
Figure 2-9: Pressure increase across the double compression angle. DC3 configuration shows superior performance, with minimum inflection noted. Reproduced from [46] 24
Figure 2-10: Evolution of integral quantities in the streamwise direction. Evolution of DC3 (2nd longest distance between ramps) shows the best stability, with low amplitude and quickest recovery. Reproduced from [46] 25
Figure 2-11: Mixed compression intake geometry optimised by Araujo et al[48]. Reproduced from [48] 27
Figure 2-12: Parameters of optimised intakes from low-order method of Araujo et al.[48]. Reproduced from original work [48] 28
Figure 2-13: Workflow schematic for the isolator-combustor modelling of Verma et al.[51]. Reproduced from original work [51] 32

Figure 2-14: MSU workflow. Reproduced from original work [54] 34
Figure 2-15: Generic schematic of configuration considered by Ispir et al. Reproduced from original work. [55] 36
Figure 2-16: Constant-Divergent area combustor examined by Lee and Lee. Reproduced from original work[56] 37
Figure 2-17: Scramjet configuration considered by Kline et al.[60], with the methodologies used for solution and sizing of individual components 42
Figure 2-18: Influence of wall temperature on shock train length. Reproduced from [67].....45
Figure 2-19: Shockless model by Crocco. Reproduced from [68] 47
Figure 2-20: Original diffusion model by Ikui. Reproduced from [68].....47
Figure 2-21: Prediction of shock train by Ikui diffusion model (line) against experimental (dot) data at different upstream Mach numbers. Reproduced from [69]. 48
Figure 2-22: Modified diffusion model by Ikui. Reproduced from [68] 49
Figure 2-23: Modelling approach for flux-conserved models. Stream thrust averaging uses McLafferty's method. 50
Figure 2-24: Schematic of dual combustion scramjet experimentally tested by Byun et al. Reproduced from [79].....54
Figure 3-1: General schematic of the overall modelling approach, with the individual sub-models shown and the way they interact with each other.....58
Figure 3-2: Illustration of geometric constraints 1-4. This configuration represents the ideal case for a mixed compression intake, with shocks from ramps impinging on the cowl tip and cowl shocks impinging (after boundary layer effects) on the ramp shoulder.....61
Figure 3-3: Convergence of optimisation algorithm for test case of Kita et al.[94] Top: 0 and 70 generations, Bottom: 140 and 210 generations. 66
Figure 3-4: Convergence of optimisation algorithm for test case by Binh and Korn[95]. Top: 0 and 70 generations, Bottom: 140 and 210 generations 67
Figure 3-5: Computational domain for experiment by Schulein 73
Figure 3-6: Selected mesh after grid dependence study 79
Figure 3-7: Mesh dependency results and solver validation.....79
Figure 4-1: Comparison between viscosity laws. Most significant difference at low temperatures (50K – 100K). 87
Figure 4-2: Generic flat plate showing the locations of transition start, end and virtual origin 90

Figure 4-3: Comparison of actual and predicted transition end Reynolds number. ★- Deem & Murphy model,■ - Kanda model, ✕ - Simeonides model 96
Figure 4-4: Predicted and experimental non-dimensional velocity profiles. Experiments: Schulein[18], Elfstrom[126], Kussoy & Hortsman[17] 98
Figure 4-5: Comparison of predicted velocity profile vs experimental data of Sahoo et al.[130] 99
Figure 4-6: Predicted and experimental skin friction coefficient. Experiments: Schulein[18], Wallace[129] 101
Figure 4-7: Influence of the wake factor Π on the predicted velocity profile 102
Figure 4-8: Influence of the wake factor Π on the skin friction coefficient 103
Figure 5-1: Generic shock-turbulent boundary layer interaction (left) and associated streamwise pressure rise (right). Reproduced from Delery [133] 107
Figure 5-2: Comparison of partial (cyan - up to $\delta u = 0.99+$) and full (magenta – up to $\delta u = 1+$) velocity profiles considered at ramp foot. Considering the velocity profile up to boundary layer thickness underpredicts the shock interaction. 112
Figure 5-3: Stratification of predicted velocity profile, shock shape and Mach waves for the DNS of Priebe and Martin[125] 114
Figure 5-4: STBLI schematic for geometric points used in post-shock boundary layer thickness determination 115
Figure 5-5: Comparison of pressure rise predicted by proposed model and experiment/numerical studies a-c) Elfstrom [15], [126] (EXP), d) Priebe and Martin [125] (DNS), e) Zuo [134] (RANS) 118
Figure 5-6: Numerical Schlieren of Priebe & Martin, recreated from[125]. Red lines indicate the location of boundary layer estimation for comparison to model prediction. 119
Figure 6-1: Influence of pressure and temperature on ignition (left) and reaction (right) times in a supersonic combustor. Symbols represent evaluations performed by Smart on different temperatures and pressures to investigate effect of the parameters on combustor reaction and ignition delay times. Lines represent correlations by Pergament [135] at different pressures. Reproduced from Smart [11] 124
Figure 6-2: Parametric study results. Variation of combustor entry (a) static temperature (K), (b) static pressure (Pa), (c) Mach number and (d) equivalence ratio 134

Figure 6-3: Schematic of geometric properties used to determine the isolator height based on geometric constraints. The reference frame is such that the x-axis is parallel to the final compression ramp 136
Figure 6-4: Prediction of shock train length with increasing pressure ratio (Data from experiment of Geerts and Yu[65] with the error bars being +-10%) 139
Figure 6-5: Assumed isolator flow field of a supersonic core surrounded by regions of separated flow to combustor entry 140
Figure 7-1: Resulting Pareto front for the parameters selected in the verification study. Red point indicates the minimum Euclidean distance point 149
Figure 7-2: Schematic of resulting geometry used for verification. Red dots indicate points determined by model p to combustor entry 149
Figure 7-3: Comparison of boundary layer growth as predicted by model and CFD..... 152
Figure 7-4: Comparison of velocity profiles before each SBTLI predicted by model and CFD. 153
Figure 7-5: Comparison of wall pressure rise along the external compression ramps predicted by model and CFD 153
Figure 7-6: Comparison of skin friction coefficient evolution along the external compression ramps predicted by model and CFD. 155
Figure 7-7: Numerical Schlieren near the cowl tip showing the location of shock convergence as a red dot. The shocks converge slightly further away from cowl tip, resulting in a loss of mass flow rate. Blue line denotes the surface of the cowl 156
Figure 7-8: Evolution of flowfield for case of high heat addition 158
Figure 7-9: Numerical schlieren for started configuration using lower heat value of 2.15 GW/m^3 158
Figure 7-10: Velocity + schlieren fields along with evolution of boundary layer from CFD. 159
Figure 7-11: Velocity profile at location where cowl tip shock impinges on bodyside boundary layer (end of red dotted line on Figure 7-10). 159
Figure 7-12: Velocity + schlieren fields at body shoulder near isolator entrance 160
Figure 7-13: Velocity + schlieren in isolator/combustor region 161
Figure 7-14: Pressure and temperature rise in supersonic core in isolator/combustor 161
Figure 7-15: Mach number in supersonic core in isolator/combustor 162
Figure 7-16: Influence of Mach number on objective functions 166

Figure 7-17: Pareto front variation with Mach number. a) Mach 6, b) Mach 7, c) Mach 8, d) Mach 9 169
Figure 7-18: Pareto front variation of dual-mode scramjet with mass flow rate, MFR. a) MFR = 10 kg/s, b) MFR = 30 kg/s, c) MFR = 50 kg/s, d) MFR = 70 kg/s 171
Figure 7-19: Pareto front variation of pure scramjet with mass flow rate, MFR. a) MFR = 10 kg/s, b) MFR = 30 kg/s, c) MFR = 50 kg/s, d) MFR = 70 kg/s 176
Figure 7-20: Influence of MFR on objective functions for dual-mode (red) and pure scramjet (blue) configurations 177
Figure 7-21: Pareto front variation of dual-mode scramjet with wall temperature. a) 300K, b) 600K, c) 900K, d) 1200K 180
Figure 7-22: Influence of wall temperature of external ramps on objective functions for dual-mode (red) and pure scramjet (blue) configurations 181
Figure 7-23: Pareto front variation of pure scramjet with wall temperature. a) 300K, b) 600K, c) 900K, d) 1200K 183
Figure 7-24: Pareto front variation of dual-mode scramjet with number of external ramps. a) 2, b) 3, c) 4, d) 5 187
Figure 7-25: Influence of number of external ramps on objective functions for dual-mode (red) and pure scramjet (blue) configurations 188
Figure 7-26: Pareto front variation of pure scramjet with number of external ramps. a) 2, b) 3, c) 4, d) 5 191

Author's Declaration

I, Charalambos Nikolaou, declare that, except where explicit reference is made to the contribution of others, this thesis is the result of my own work and has not been submitted for any other degree at the University of Glasgow or any other institution.

Nomenclature

A = Area, m^2

a_T = temperature-velocity relation coefficient, $\sqrt{\left(\frac{T_\infty - T_{aw}}{T_w} + (1-\theta_{DM})\frac{(T_{aw}-T_w)}{T_w}\right)}$

b_T = temperature-velocity relation coefficient, $\theta_{DM}\frac{(T_{aw}-T_w)}{T_w}$

c_f = local skin friction coefficient

c_p = specific heat capacity at constant pressure, $J \cdot kg^{-1}K^{-1}$

E = destruction term

$f_{stoichio}$ = hydrogen/air stoichiometric combustion ratio, 0.0254

$F_{specific}$ = specific thrust, $N \cdot kg \cdot s^{-1}$

H = isolator height, m

H_{fuel} = hydrogen lower heating value, 120 $MJ \cdot kg^{-1}$

ICR = internal contraction ratio

I_{sp} = specific impulse, s^{-1}

k = turbulent kinetic energy, $m^2 \cdot s^{-2}$

L_{ST} = shock train length, m

$\dot{m}$ = mass flow rate, kg/s

Ma = Mach number

p = pressure, Pa

P = production term

Pr = laminar Prandtl number, 0.72

Pr_t = turbulent Prandtl number, 0.86

$\dot{q}$ = heat addition, $W \cdot m^{-3}$

q_T = compressibility correction coefficient, $\sqrt{4a_T^2 + b_T^2}$

r = turbulent recovery factor, $\sqrt[3]{Pr}$

R_{gas} = specific gas constant, $J \cdot kg^{-1}K^{-1}$

Re_{unit} = unit Reynolds number, m^{-1}

Re_θ = momentum thickness Reynolds number

T = temperature, K

T_{aw} = wall recovery temperature, $T\left(1 + r\left(\frac{\gamma-1}{2}\right)Ma^2\right)$, K

u = flow velocity, $m \cdot s^{-1}$

u_τ = friction velocity, $m \cdot s^{-1}$

u^+ = non-dimensional velocity, u/u_τ

W = width, m

x = streamwise distance, m

y = vertical distance in local frame of reference, m

y^+ = non-dimensional distance from wall, $y \cdot u_\tau / \nu_w$

Greek symbols

β = shock angle, degrees

γ = ratio of specific heats

γ_{int} = intermittency

δ = boundary layer thickness, m

δ^* = displacement thickness, m

δ^+ = non-dimensional boundary layer thickness, $\delta \cdot u_\tau / \nu_w$

η = efficiency

θ_{DM} = Duan-Martin thermal coefficients term, 0.8259

θ = momentum thickness, m

κ = von Kármán constant, 0.385

μ = dynamic viscosity, $Ns \cdot m^{-2}$

μ_n = Mach angle, degrees

ν = kinematic viscosity, $m^2 \cdot s^{-1}$

Π = wake intensity

Π_t = total pressure ratio (TPR)

ρ = density, $kg \cdot m^{-3}$

τ_w = wall shear stress, N/m^2

τ_{ID} = ignition delay time, μs

τ_R = reaction time, μs

φ = flow deflection, degrees

φ_{fuel} = fuel/air equivalence ratio

ω = specific dissipation rate, s^{-1}

Subscripts

ad = adiabatic quantity

avg = average quantity

aw = adiabatic wall quantity

closure = quantity at cowl closure location

comb = combustor quantity

inc = incompressible quantity

isen = isentropic quantity

max = maximum quantity

post = post-shock quantity

pre = pre-shock quantity

t = turbulent quantity

to = total quantity

virt = quantity at virtual origin

w = wall quantity

∞ = local freestream quantity

* = quantity at reference temperature

Superscripts

- = local quantity

= = ratio of local quantity to freestream quantity

Abbreviations

CFD = Computational Fluid Dynamics

DNS	=	Direct Numerical Simulations
PSO	=	Particle Swarm Optimisation
MOPSO	=	Multi-Objective Particle Swarm Optimisation
CMOPSO	=	Constrained Multi-Objective Particle Swarm Optimisation
R&D	=	Research & Development
STLS	=	Shock Train Leading Shock
SST	=	Shear Stress Transport
SSTLM	=	Shear Stress Transport Langtry-Menter
URANS	=	Unsteady Reynolds-Averaged Navier-Stokes
SBLI	=	Shock-Boundary Layer Interaction
STBLI	=	Shock-Turbulent Boundary Layer Interaction
AoA	=	Angle of Attack

Chapter 1 - Introduction

1.1. Background and Motivation

As technology marches forward at an ever-increasing rate, the demand for high speed, clean and safe point-to-point transport across the globe as well as efficient access to space have come to the forefront of aerospace research. Current technologies rely primarily on turbofan-powered aircraft for atmospheric point-to-point flight, and liquid or solid fuelled rockets for access to space. While these powerplants have shown reliability, long atmospheric flight times in the case of turbofans and high operating costs in the case of liquid fuelled rockets as well as detrimental environmental impact due to the use of hydrocarbon fuel, have prompted researchers to search for alternative powerplants for future aircraft.

A class of engines that can offer both atmospheric flight and access to space are the combined cycle engines (CCE). They are broadly categorised into two main classes, rocket-based (RBCC) and turbine-based (TBCC). CCEs operate by sequentially transitioning between different engine types or modes at different flight regimes through the flight envelope of the engine. RBCCs integrate rocket, ramjet, and scramjet engines in one flow path, exploiting the high thrust to weight ratio of rockets with the high specific impulse of ramjets and scramjets [1], as seen from Figure 1-1 below. TBCCs utilise a turbofan to accelerate the vehicle from standstill to low supersonic speeds [2].

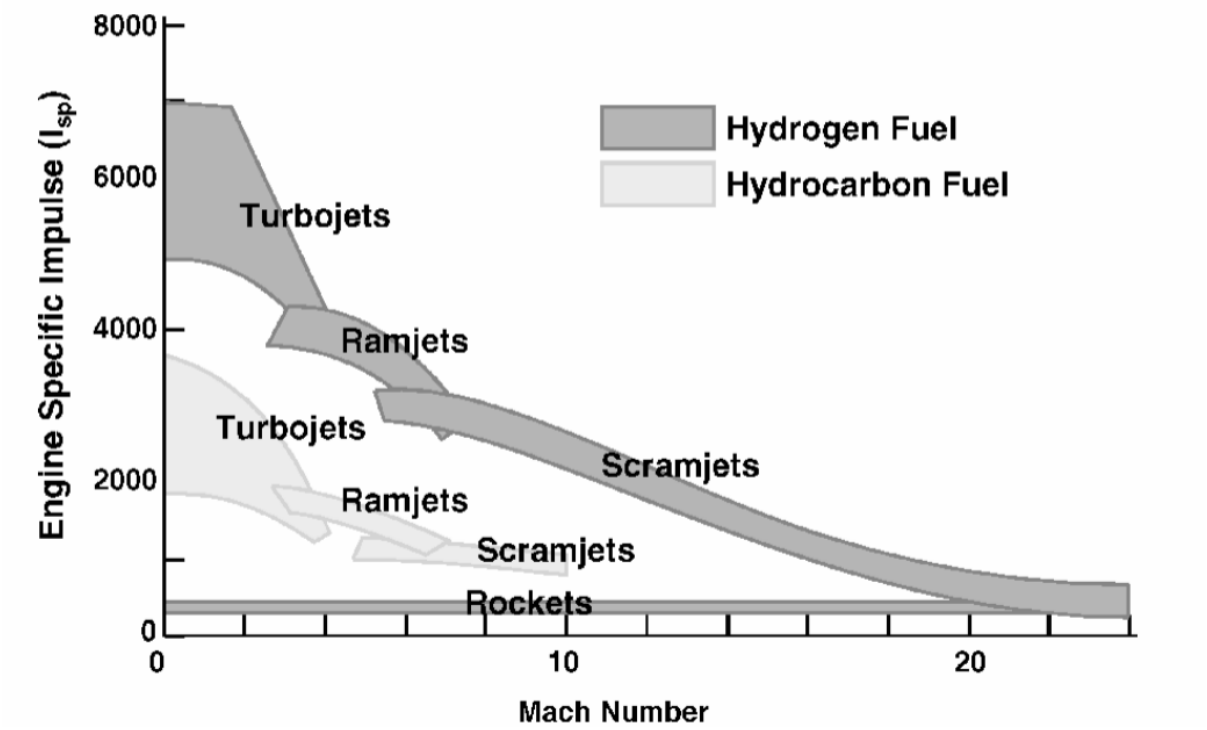


Figure 1-1: Engine type specific impulse with increasing Mach number. Reproduced from [3]

However, these types of engines would require enormous amounts of research and development, evident by a recent study by Fusaro et al. [4], in which the authors considered a conceptual CCE and estimated a cost for 9.5 billion USD for the Scimitar CCE for research and development alone. Thus, an analysis or design tool capable of accelerating the design process of the components of CCEs would greatly reduce the costs associated with R&D.

A common engine type found in both types is the scramjet. Scramjets operate without moving parts, achieving compression using the ram effect and shock waves, combusting the fuel within a still supersonic airflow. While the concept of scramjets dates to the 1950s, viable commercial scramjet engines have yet to emerge. This is primarily attributed to the limited experimental data available for high-enthalpy boundary layers and the incomplete understanding of the physical mechanisms governing hypersonic turbulent boundary layers and their shock interactions. This is evident in the design of intakes and isolators for scramjets, where shock-boundary layer interactions dominate the design constraints of these components. As such, design of hypersonic engines is not trivial due to multiple flow interactions and relies heavily on the use of Computational Fluid Dynamics (CFD).

Hence, coupling of the intake-isolator components is vital to ensure meaningful configurations are obtained. The boundary layer has a direct influence on the mass flow capture of the intake and the capability of the of the engine to resist the heat release in the combustor, which itself

influences the upstream flowfield through the shock train in a dual-mode scramjet. Determining the mode of operation is also vital, as a pure scramjet alleviates the need for an isolator, making the overall length shorter and increasing compression efficiency. Treating these components independently neglects these interactions and can lead to non-robust designs with limited operability.

Based on the above observations, the overall aim of this work is to develop a low order, computationally cheap and effective framework for the design of scramjet engines during the preliminary design process. This framework will capture the influence of the boundary layers on scramjet engine development, primarily through shock-boundary layer interactions and the influence of the non-equilibrium boundary layers on the isolator length. Further, a parametric study is conducted on the designer-selected variables to evaluate their influence on the design characteristic of scramjets.

Thus, the research question this thesis sets out to answer is:

"*Can a reduced-order modelling approach that sequentially couples intake, isolator, and combustor models capture the dominant physics governing hypersonic intake–isolator interactions with sufficient fidelity to support preliminary scramjet design and optimisation?"*

The modelling approach achieves the intake-isolator coupling by sequentially solving the external shock system, with the mode of operation (dual mode or pure scramjet) being determined through coupling of the resulting flow to a reduced-order combustor-nozzle model. The resulting flow incorporates the effects of the ramp and cowl boundary layers, and in the case of a dual mode scramjet, uses pressure matching at the isolator exit to ensure robust combustion and ensuring backpressure effects are accounted for. The entire coupled system is then used within an optimisation routine to obtain optimum scramjet geometries based on the maximisation/minimisation of key performance metrics.

Finally, the novelty of this work lies in the integration of low-order turbulent boundary layer and SBLI models into an intake–isolator–combustor framework suitable for optimisation. Unlike existing preliminary design approaches that rely on decoupled analyses or costly CFD, the proposed method enables rapid exploration of design trade-offs while retaining the dominant flow physics governing scramjet operability.

1.2. Thesis Structure

Following this introduction, the rest of the thesis is structured in the following manner:

Chapter 2 presents a literature survey of hypersonic modelling approaches and experimental studies for intakes and isolators, along with a brief history of the evolution of the hypersonic propulsion system. More pertinently to this research, the current modelling approaches for both components are discussed along with their advantages and drawbacks.

Chapter 3 introduces the general modelling approach and the optimising algorithm used in this thesis. A flowchart of the sub-model coupling is presented. The optimisation algorithm and constraint criteria are introduced. The Constrained Multi-Objective Particle Swarm Optimisation (CMOPSO) is shown to be a suitable optimisation method, providing a good balance between computational efficiency and accuracy in obtaining the Pareto front of the objective functions.

Chapter 4 describes the theory, implementation and validation of the compressible flat plate model. The model uses an incompressible universal velocity profile for a turbulent boundary layer transformed through the Van Driest compressibility transformation. To capture turbulence, a wake profile is included in the velocity profile. Correlations are used in the determination of the boundary layer thickness, wake parameter and transition region. The model is then subsequently validated through comparison with experimental and numerical studies of hypersonic boundary layers.

Chapter 5 presents the derivation and validation of the shock-turbulent boundary layer model. A separation model is firstly introduced based on the work of Souverein but extended to account for wall cooling and additional data points. Prediction of the pressure rise distance and boundary layer properties across the shock is only performed for attached boundary layers. Inviscid shock relations are applied above the viscous sublayer to predict shock trajectory within the boundary layer. Post-shock properties are solved in the reverse manner of the upstream boundary layer, at the streamwise location where the pressure rise stops. The model is validated against experimental and DNS studies, examining the accuracy of prediction of both pressure rise and post-shock boundary layer properties where possible.

Chapter 6 describes the final component of the global model: the isolator–combustor–nozzle model. Prediction of the isolator length is done through an analytical equation, coupling it to the intake through the incoming momentum thickness, required pressure increase and

geometric parameters. Combustion is modelled as a heat release due to fuelling, while the nozzle is modelled as an imperfect adiabatic expansion process.

Chapter 7 presents the verification of a dual-mode scramjet configuration obtained from the proposed modelling approach. The data obtained through CFD are compared to what is predicted by the model and against which the accuracy of the model is evaluated. Subsequently, the results of a parametric study on the designer-selected parameters are presented, with their influence on both dual-mode and pure scramjet configurations discussed.

Chapter 8 summarises the key contributions of the thesis and provides suggestions for future work in this field.

Chapter 2 - State of the Art / Literature Review

As elucidated in Chapter 1.1, scramjet engines hold the potential to faster point-to-point travel and can provide efficient transition in the hypersonic flight envelope for combined cycle engines. As will be explored later in this chapter, the concept of scramjet engines has been investigated for 80 years. Despite the long history, only recently has it received appreciable attention, and as such many challenges and difficulties remain, including the design process of the scramjet itself. The high-speed flow encountered by the vehicle introduces significant boundary layer, shock-boundary layer interactions and other viscous phenomena that must be considered during the design process. This, coupled with the difficulty in testing such vehicles in wind tunnels due to the high enthalpies required to emulate real flight conditions, lead to a slower overall process in scramjet design. The primary goal of this thesis is to streamline the preliminary design process, by developing a viscous low order model, which although computationally inexpensive, provides accurate dual-mode and pure scramjet configurations for use in the design phase of a vehicle.

This chapter presents a history of the evolution and the operating principles of scramjets with a comprehensive literature survey of analytical and numerical methods developed by researchers for the design of intakes and isolators as well as experimental and numerical studies conducted on intakes and isolators.

2.1. Scramjet development history

Scramjet development followed rapidly after the initial development of ramjets in the 1950s. The first scramjet to be produced and tested was designed by Ferri in 1960, with the whole engine being tested in 1963, demonstrating the capabilities of scramjets as viable engines for propulsion of high-speed vehicles [5]. Over the next four decades, up to the turn of the millennium, numerous projects have been proposed, of which only a handful progressed to flight tests. The most prominent flight tests are further elaborated here, with a more comprehensive review of the progress of the development of scramjets over the latter half of the 20th century and beginning of the 21st century compiled by Fry [3].

The first of the large-scale experiments conducted on scramjets was the Kholod project, initially developed by Russia and subsequently developed in collaboration with France and later with the United States [6]. The engine tested was a hydrogen-fuelled, axisymmetric three-shock external compression scramjet attached to the tip of an SA-5 surface-to-air missile. Various successful tests were performed, each increasing the complexity of the system carried onboard, with the latest flights incorporating a real combustor as well as hydrogen fuel being fed to the chamber. Investigation of the engine after recovery indicated that the combustor was operational during the 78s flight. The experiment was successful in demonstrating dual-mode scramjet combustors in realistic flight conditions giving data for comparison against ground-test facilities.

Another milestone in hypersonic propulsion came with the successful launch of the X-43A platform by the United States. The vehicle was the culmination of research aimed to test a variety of tools used to design hypersonic aircraft, and after a ground testing of the engine, it was fitted to the vehicle. The airframe-integrated scramjet consisted of a wedge external compression system, feeding to a hydrogen-fuelled combustor. Three flights were undertaken, with the first one failing 20s in flight due to structural failure caused by inadequate control by the autopilot. The second flight was successful, with the scramjet operating at Mach 7 for 10s, after which the vehicle glided into the Pacific Ocean[7]. The third and final flight of the X-43 program was performed in November 2004 at Mach 10. This vehicle X-43 demonstrated the capability of various analytical and numerical tools that were used to design the vehicle and engine, providing experimental data for validation in the process. The X-43 program was subsequently terminated and replaced with the X-51 program. The X-51 shared many features with its predecessor, such as the external compression system, however the fuel used was

changed from hydrogen to hydrocarbons (JP7). The new vehicle flew its first successful flight in 2013, after three failed attempts, flying for 240 seconds at a speed of Mach 6[8]. The X-51 marked the end of the US' declassified scramjet program.

Australia made substantial contributions to hypersonic propulsion with their HyShot program. The collaborative program was spearheaded by Australia but had international collaboration and consisted of a scramjet which achieved net positive thrust at a Mach number of 7.6 for 6 seconds after being accelerated into a parabolic trajectory by a rocket motor. The contributions of the HyShot program cannot be understated, as the entire program was developed based on knowledge and understanding obtained from shock tunnel experiments. Besides the experimental supersonic combustion data obtained, the program showed that shock tunnels can be used effectively for design of hypersonic engines[9].

The national experiments outlined above have shown the capabilities of scramjets as engines and have provided valuable information on failure points. To address the failure points, research has been ongoing on all elements of the powerplant. A critical point of any high speed powerplant is the intake. Intake research has increased in the recent years, with experimental and mainly numerical studies investigating various elements of intakes, from geometry to shock-boundary layer interactions.

2.2. Research on hypersonic intakes

Due to the nature of the local atmospheric conditions that a scramjet is expected to operate in, ram compression is of vital importance to any hypersonic intake. As scramjets operate at Ma $\geq$ 5, the deceleration of air to subsonic speeds for combustion becomes non-viable. The pressure loss resulting from the presence of the normal shock results in prohibitively large losses in total pressure.

Hypersonic intakes are not only expected to decelerate and compress the oncoming flow, but they must also do so while meeting a myriad of additional requirements. Firstly, the operation of the intake must be done in such a manner that the intake remains in its started configuration. Secondly, operation must be done at high thermodynamic efficiency, with minimum losses in total pressure. Thirdly, flow into the combustion chamber must enter at favourable combustion conditions, ideally at a temperature and pressure that allow for autoignition of the fuel. Fourthly, the engine should operate efficiently at a wide flight envelope and do so predictably and reliably[10].

One of the promising candidate engine configurations is that of a mixed compression intake. Scramjet engines with this type of intake have two primary modes of operation, dual-mode (Figure 2-1) and pure scramjet (Figure 2-2). In both modes, the fuel is combusted supersonically. The difference arises from the effects of combustion on the upstream flow. In pure scramjet, the energy released during combustion has minimal influence on the flow field's structure, allowing the flow to exit the combustor supersonically. In dual mode, the ignition of fuel results in thermal choking of the exit flow, meaning the exit flow reaches Mach 1. The flow is unable to support further reduction in flow speed, resulting in a backpressure applied to the incoming flow. The adverse pressure gradient introduced to the boundary layer causes it to separate, with the pressure disturbance propagating upstream through the subsonic portion of the boundary layer. This backpropagation causes the boundary layer to further separate upstream, resulting in the creation of a virtual throat, bounded by the top and bottom separation bubbles. Due to the presence of the separation bubble, a detachment shock is generated at the separation point, initiating a shock train, which causes the flow to gradually compress to the level of the backpressure imposed.

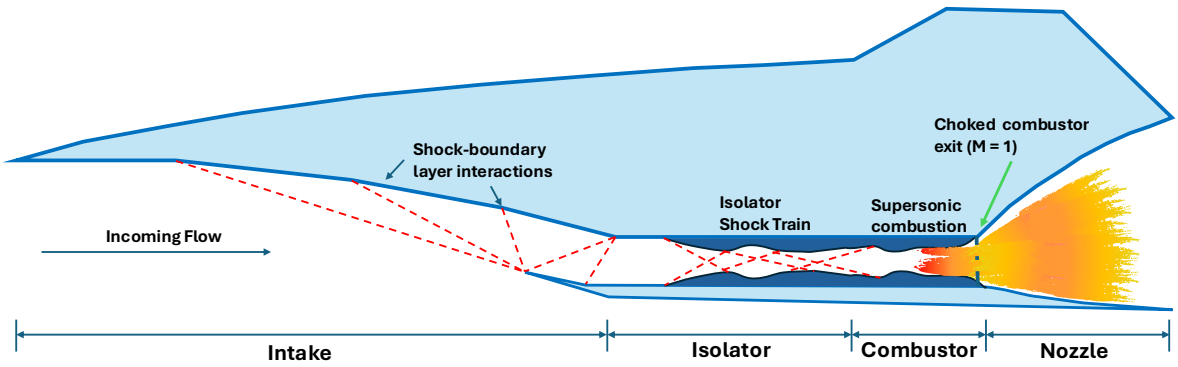


Figure 2-1: Vehicle with a mixed compression intake operating at dual-mode, due to the separated region observed in the isolator

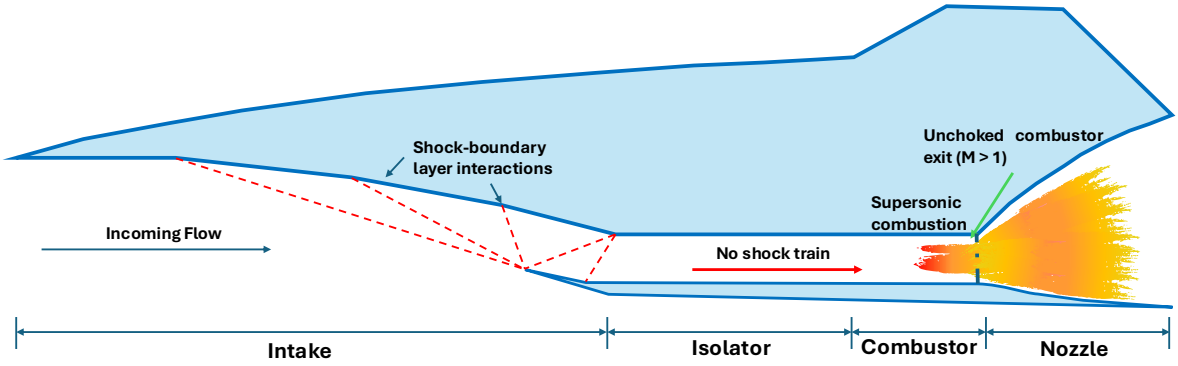


Figure 2-2: Vehicle with mixed compression intake operating as a pure scramjet. In the configuration shown, the isolator becomes redundant, as the external compression system produces sufficient compression without the need for an internal shock train

In both modes, the combustion occurs supersonically, meaning very little time is available for fuel ignition and combustion. As such, the combustion would be performed more readily if the incoming flow is at sufficiently high pressure and temperature for the auto-ignition of hydrogen. Additionally, to reduce both ignition and burning time, higher pressure and temperatures past the ignition point reduce both times, allowing for more robust and complete combustion [11].

A typical 3-ramp mixed compression intake is presented in Figure 2-3. A mixed compression intake operates using external ramps to generate oblique shocks which compress, decelerate and turn the flow towards the isolating duct. The isolator acts to isolate the intake flow field from the backpressure effects of combustion. In the case of a dual mode scramjet, it contributes to the compression of the flow through the pseudo-shock train that develops due to the insufficient flow momentum and hence boundary layer separation. Pure scramjets resist the backpressure and hence no separation occurs, but internal compression might occur if the pressure generated purely by the external portion of the intake is insufficient. A more detailed explanation on the flow field within the isolator is presented in Chapter 6.

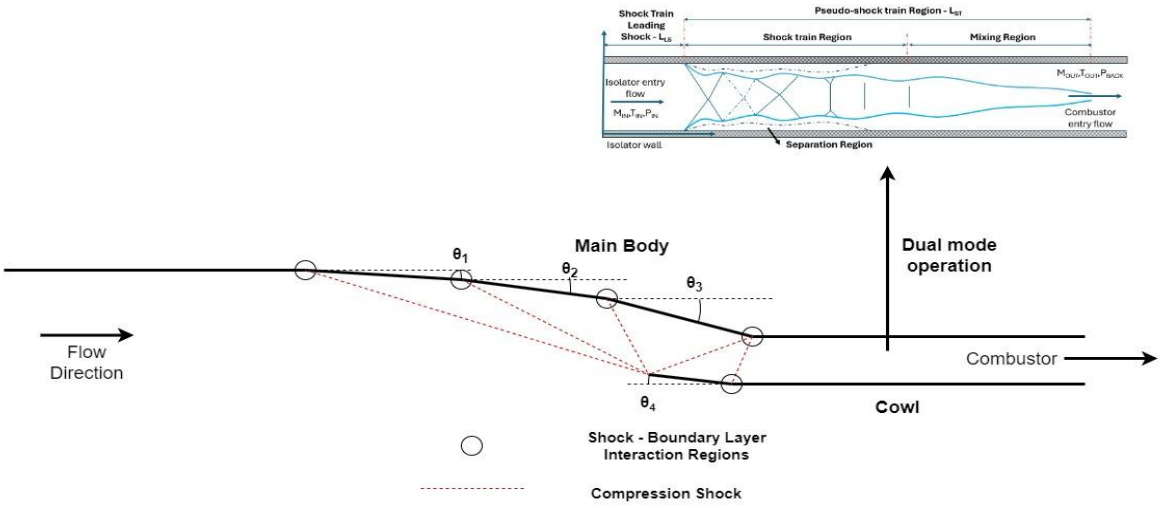


Figure 2-3: Generic 3-ramp mixed compression intake-isolator configuration

Research on mixed compression intakes has been increasing over the last decade, with research on design modelling and unstart detection, prevention and mitigation presented in detail in the next section, along with experimental studies conducted over the last several decades. The phenomenon of unstart is strongly coupled with the intake design, hence both must be considered in parallel for a successful intake design.

2.2.1. Shock-Boundary layer interactions in scramjets

When a fluid moving above sonic speeds encounters an abrupt change in flow direction, a series of weak compression waves are generated, which coalesce to form a shock wave to mediate the transition. On surfaces, near-wall behaviour is dominated by viscous effects, generating a boundary layer with which a shock wave interacts to produce a family of shock-boundary layer interactions (SBLI). The nature of the interaction depends on the state of the boundary layer and the intensity and orientation of the shock. As the schematic of a mixed compression intake shows in Figure 2-3, understanding and implementation of SBLI for a mixed compression intake is vital.

In the case of a mixed compression intake, the boundary layer encounters a series of shocks during the external compression process, which should remain attached to alleviate losses and prevent unstart from starting externally. Additionally, the boundary layer is highly susceptible to separation from the shocks generated by the cowl. A common design requirement necessitates that the shocks generated by the cowl plate impinge on the ramp-isolator corner, alleviating the need for an expansion fan to turn the flow into the isolator (an example is shown in Figure 2-1, where the dual mode scramjet has shocks impinging on the body corner). The

cowl shocks impinge on the body-side boundary layer, which might cause the boundary layer to separate, causing the flow to choke and unstart the engine. Internally, the flow proceeds into the isolator, which under the influence of combustor backpressure generated by the combustion process and insufficient combustor area, causing the boundary layer to separate, generating an internal shock system which further reflects downstream, interacting with the boundary layer throughout.

The phenomenon of SBLIs has been extensively studied in the last three decades. The vast majority of the experimental studies are from wind tunnels, as it allows for a controlled environment where more data can be collected. Despite the number of experiments, the number of useable experimental data that can be used for validation of numerical and analytical methods is a tiny fraction of the overall experimental dataset. Of particular importance are measurements characterising both the incoming and outgoing boundary layers, including boundary layer thickness, displacement and momentum thicknesses and velocity profiles where available. These data are required to assess whether the models correctly capture the evolution of the boundary layer through the SBLI and subsequent recovery. The experimental geometry and operating conditions must also be sufficiently well defined to permit the experimental configuration to be reproduced within the model. Experiments providing only freestream conditions or limited wall-pressure measurements therefore offer limited value for validating the modelling approach developed in this work.

This is evident from the databases of Settles and Dodson[12] and an updated version produced by Roy and Blottner[13]. For a 2D compression ramp only the experiments of Coleman,Stollery[14] and Elfstrom[15] and the experiments of Holden[16] are recommended as experiments for CFD to be validated against. For shock impingement, the experiments of Kussoy and Hortsman[17] and Schulein[18][19] are suggested.

The experiments were shortlisted from a list of 107 experiments in the original compilation by Settles. Some of the "must meet" criteria used by both data compilations are listed below in a shortened form:

1. *Baseline applicability*: Must be a supersonic/hypersonic shock-turbulent interaction.
2. *Specific applicability*: Must have useful data as part of their reporting, which can be used by other researchers for validation.
3. *Well-defined experimental boundary conditions*: Adequate information about the flow conditions must be provided as to eliminate the need for assumptions. For instance,

transition data or velocity profiles need to be provided to have adequate knowledge of the incoming boundary layer.

4. *Error margins*: Must provide error margins for their measurements, which can be used by other researchers to reproduce their data or identify sources of discrepancy.
5. *Data consistency*: The dataset examined must not produce contradictory results with itself.

The same thoughts are echoed by both authors, those being that additional high quality experimental studies are necessary to supplement the very limited existing database. An investigation of a recent compilation of experiments from 1970 to 2021 by Knight [20], no newer experiments could be determined to fulfil the criteria used by the previous databases.

As such, only the experiments and numerical studies that are deemed as high quality are presented. The experiments that have been proposed as high quality and form the benchmark studies against which CFD cases are being commonly tested are presented in Table 2-1. SBLIs are observed in the external compression system between the turbulent boundary layer formed on both the body and cowl and the shocks generated but also observed in the isolating duct, where cowl shocks impinge on the corner of the body, to fulfil the so-called "shock-on-shoulder" condition, as well as during the formation of the internal shock train. These conditions are required to be satisfied for different reasons, all relating to the performance of the engine. The shock-on-lip condition should be satisfied in order to capture the maximum mass flow rate that the engine is designed for. Deviation from this condition results in subcritical operation (shocks converge upstream of cowl, thus spillage occurs) or supercritical (shocks converge inboard of the engine, impinging on the cowl boundary layer, potentially causing separation as well as reflection downstream). The other condition, shock-on-shoulder, should be satisfied in order to eliminate the expansion fan that would otherwise occur on the body shoulder, and prevent shock reflections from entering the isolator/combustor, potentially destabilising the boundary layers and causing separation.

Therefore, the relevant experiments from the above databases presented are those for a 2D compression ramp and shock impingement from a shock generator.

Table 2-1: Updated proposed high-quality studies by Roy and Blottner[13]. The quantities measured in the experiments are Stanton Number (St), local skin friction coefficient (c_f) and pressure ratio (P/P_∞)

Experiment	Reference	Year	Flow geometry	Mach	Measured quantities
Coleman, Stollery & Elfstrom	[14], [15]	1972	Compression Ramp	8.96 / 9.22	St, P/P_∞
Holden	[16]	1977	Compression Ramp	6.5 - 13	St, c_f, P/P_∞
Kussoy & Horstman	[17]	1991	Shock impingement	-	-
Schulein	[18], [19]	1996	Shock impingement	5	St, c_f, P/P_∞

Coleman, Stollery and Elfstrom [14], [15] performed hypersonic experiments on a naturally transitioned turbulent boundary layer and a variety of compression angles. The experiments were performed at the Imperial College hypersonic gun tunnel, with the working gas being Nitrogen. The aim of the research was to investigate the incipient separation limits and extend the then limited literature on experimental studies of hypersonic boundary layers. Their results provide insight in the mechanism of incipient separation and its associated separation length, with an increase in Reynolds number based on boundary layer thickness showing a reversal in the maximum angle that can be supported by the boundary layer before separation, as seen from Figure 2-4.

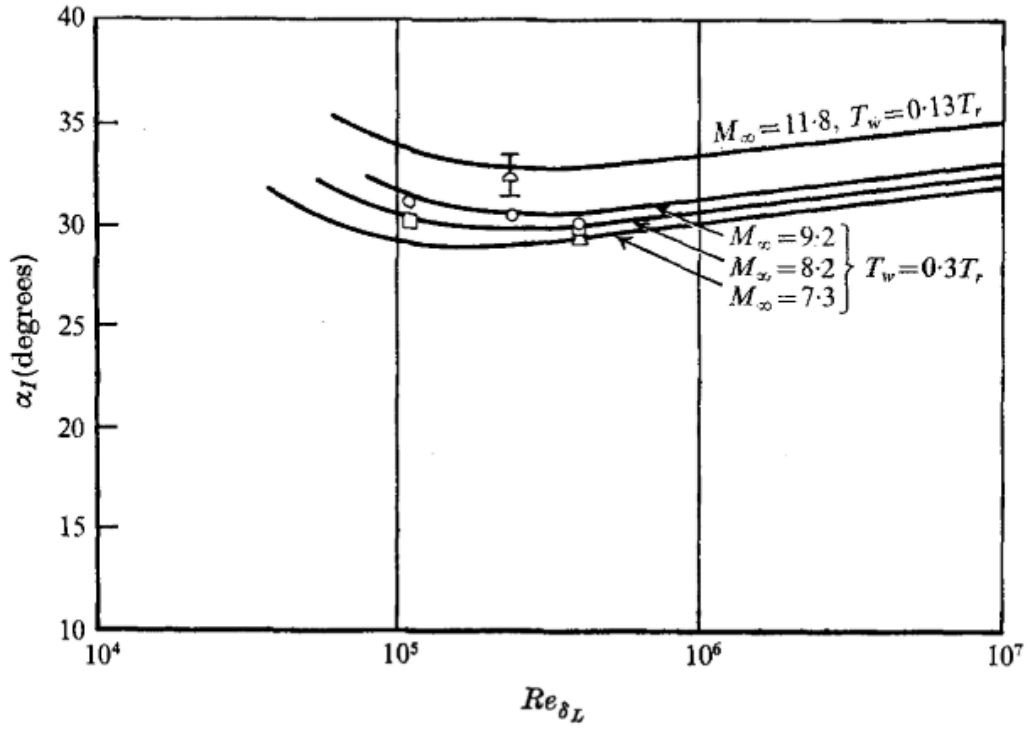


Figure 2-4: Incipient separation angle (a_I) with increasing Reynolds number based on boundary layer thickness. The lines represent the prediction of the modelling approach used by the authors, with the symbols representing experimental observations from other researchers. Reproduced from original work [15].

The authors propose that this effect is due to the development of the wake, with the wake parameter, Π, being the major influence. Additionally, the effect of wall temperature appears to be rather significant. An increase in wall temperature for a given pair of Mach and Reynolds numbers results in the destabilisation of the boundary layer, leading to earlier separation. Therefore, wall cooling plays an even more important role on hypersonic vehicles beyond material thermal properties. This conclusion is further supported by the findings of Holden [16], who performed experiments for a variety of Mach numbers, Reynolds numbers and wall temperature ratios. The working fluid is air, and the aims of the research were similar to those of Coleman, Stollery and Elfstrom. Their results show that an increase in wall temperature ratio as well as Reynolds number would lead to a larger separation region being created. Furthermore, the turbulent viscous interaction region was found to be highly unsteady, with amplitudes being sufficient to cause damage to the equipment used in the experiment. This only serves to support the point that separation in the external compression system must be avoided to maintain the mechanical and structural integrity of scramjets. A point worth mentioning is the inverse response of the heat transfer and skin friction coefficient. While in the laminar shock-boundary layer interaction, the expected drop in skin friction coefficient is accompanied

by a drop in the heat transfer coefficient, turbulent interactions show an increase in the heat transfer coefficient. The reasons for this can be perhaps attributed to the amplification of turbulence in conjunction with the higher flow properties which occur as a result of the presence of the separation shock along with the incident shock. This effect further deposits thermal energy to the surface and would be detrimental to the thermomechanical properties of the surface.

On shock impingement, Schulein's [18], [19] experiment was performed on a cooled plate (T_w = 300K) which was subsequently impinged by an incoming shock generated by a shock generator mounted over the plate. Various shock generator angles were tested, with the results providing further insight into the turbulence mechanisms of separated STBLIs. Similar to the compression ramp experiment of Holden, the heat transfer and skin friction show inverse trends at the point of flow separation, which shows that the two cases share similar mechanisms. The shock system disrupts the turbulent boundary layer significantly, causing the boundary layer to significantly delay its return to the equilibrium state. This delay causes extended regions downstream of the interaction to experience elevated skin and heat coefficients, which would be detrimental to the performance of any hypersonic propulsion system.

The experimental dataset, while small, provides valuable information on the evolution of the boundary layer pre- and post- shock as well as flow properties during separation. Mechanisms for ramp-induced or impingement-induced separation appear to have common trends but any engine design must eliminate any significant separation events at high Mach numbers, due to the tremendous unsteadiness experienced by the boundary layer and the prominent spikes in heat transfer. As importantly though, they provide validation data for numerical methods which can be used to increase their accuracy and use them in lieu of experimental studies.

2.2.2. Experimental and numerical studies on intakes

The intake has seen a lot of attention and research effort diverted to it in both supersonic and hypersonic propulsion due to its vital role in the powerplants. As previously mentioned, national programs from the US, ex-Soviet Union and Australia have performed flights on hypersonic vehicles, which provided invaluable data for researchers. Despite these successes, many experiments ended in failure. One such example is the first Hyshot launch, which resulted in failure. This was attributed to unstart, which caused a premature engine shutdown.

Unstart is commonly described as a state where the internal flow field affects the mass flow capturing capability of the intake[21]. Unstart is characterised by severe degradation of

performance and possible engine flameout occur, meaning it must be avoided at all costs. Unstart has been found to occur due to different reasons [22], with the primary ones summarised by Im and Do [23] in their comprehensive review as being freestream conditions, geometric/design parameters, and downstream conditions during operation. The subsonic and supersonic spillage unstart states for a generic mixed compression are shown in Figure 2-5 and Figure 2-6 respectively. Ramjets tend to experience the former, while scramjets suffer from the latter. A further classification of unstart was done by Van Wie et al [24], who classified unstart into "soft" and "hard" unstarts. Hard unstart occurs due to flow choking, while soft unstart is a result of a separation bubble near the throat of the intake.

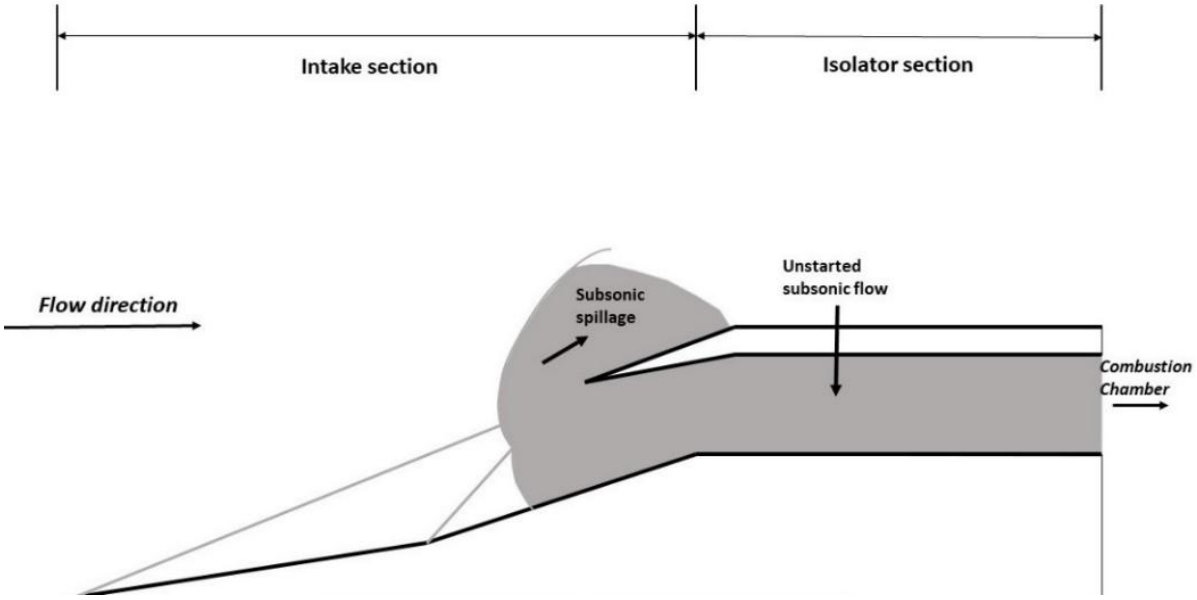


Figure 2-5: Subsonic spillage unstart. The boundary layer is fully ejected with a bow shock, resulting the loss of mass flow at subsonic speeds.

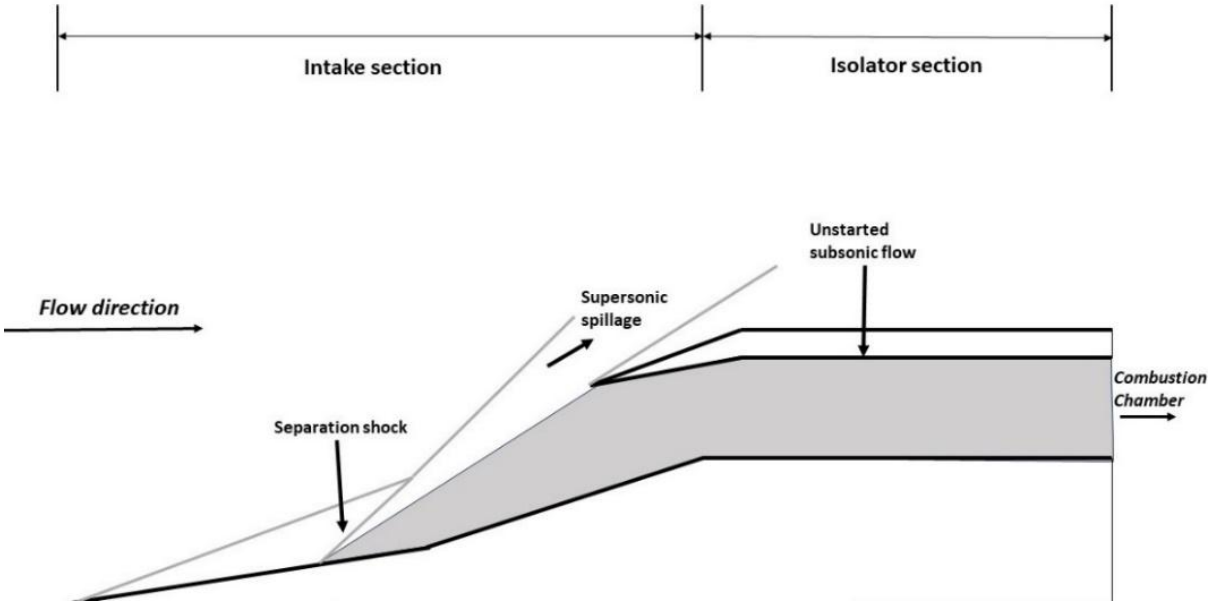


Figure 2-6: Supersonic spillage unstart. The boundary layer is fully ejected with an oblique shock, with mass flow loss occurring at supersonic speeds.

Unstart is related to another phenomenon, referred to as “buzzing”. This phenomenon is linked to motion of the shock system, which, depending on the mode, might have significant effects on the operation of the intake and result in unstart, due to viscous interactions with the shock system. Buzzing was first reported by Oswatitch [25], and it’s a pressure oscillation phenomenon. Two main types of buzzing occur, “little” and “big” buzz. The former was first described by Ferri [26] and it is characterised by high frequency, low amplitude oscillations. It primarily occurs due to shear layers being ingested near the cowl side of an intake, which cause the cowl-side boundary layer to destabilise. The latter, “big” buzz, identified by Dailey [27], is a lower frequency but high amplitude phenomenon that occurs due to shock-boundary layer interactions between the cowl shock and compression side boundary layer. Buzzing in supersonic intakes leads to performance loss due to the mass flow and pressure fluctuations that occur [28] , as shown by numerical simulations by Abedi et al. [29], who conducted URANS simulations with the SST k-ω turbulence closure model on a ramjet model operating at Mach 2. Their findings indicate that the performance of an intake experiencing buzzing remains in an underperforming condition due to the hysteresis associated with buzzing. Most notably, the captured mass flow rate is significantly reduced, which further feeds into the buzzing cycle. The resulting reduction in flux entering the intake leads to lower resistance to backpressure, leading to a feedback loop. The loss in performance manifests in the lower total pressure recovery compared to the ideal cycle case observed.

In hypersonic intakes, buzzing may occur in a different manner to supersonic intakes [30]. Research by Chang et al. [31] revealed additional buzzing modes, one that is a mix of big and little buzz and another that has the oblique shock system exhibit very small oscillations at its most upstream position. The presence of both buzz modes was observed through LES simulations by de Vanna et al. [32] by varying the blockage (and by extension the backpressure) applied to a Mach 5 mixed compression intake. During nominal operation, the intake demonstrated low buzzing, but the addition of partial blockage downstream showed big buzz, which causes the cowl shock to vibrate between attached and detached. When a hypersonic intake experiences buzzing, it is possible that unstart may subsequently occur due to the movement of the shock system. This movement causes shock impingement on different parts of the boundary layer, which may have greater susceptibility to separation, and depending on their location, may cause unstart.

A prominent reason for the occurrence of unstart is intake geometry. An important property that is of influence is the internal contraction ratio (ICR). The internal contraction ratio refers to the ratio between the area at the cowl closure plane and the throat area of the intake and given by equation 2.1:

$$ICR = \frac{A_{cowl,closure}}{A_{throat}} \qquad 2.1$$

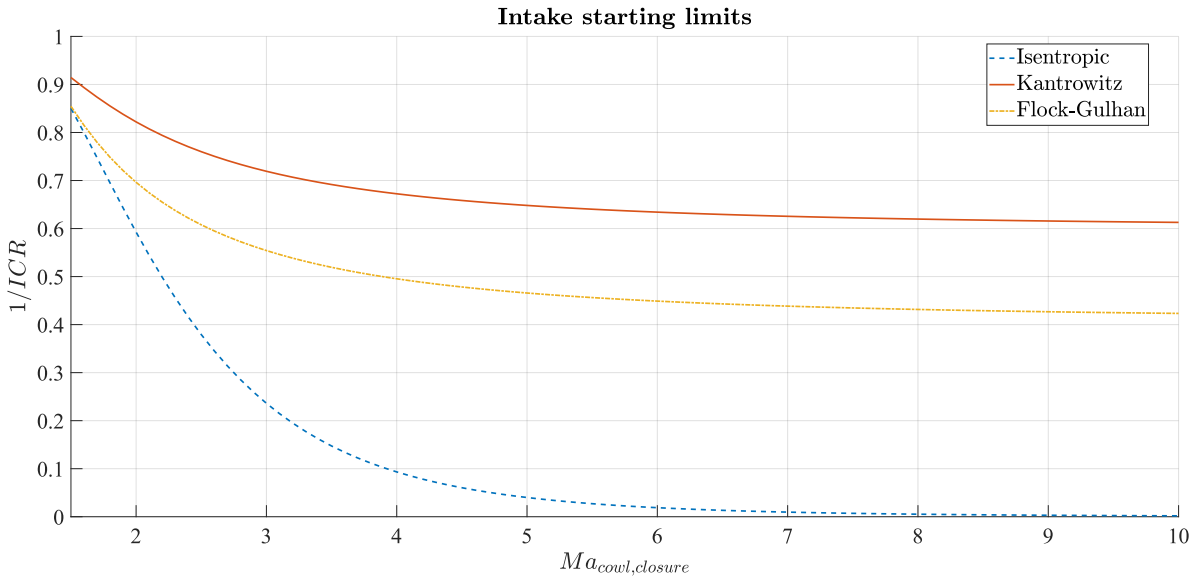


Figure 2-7: Intake starting limits. Note that y-axis is 1/ICR

Determination of whether an intake is self-starting can be done by determining whether its ICR at a given closure Mach number remains in the self-starting region, shown in Figure 2-7. An

intake will self-start above the Kantrowitz-Donaldson [33] limit (equation 2.2), meaning the intake will remain started independent of the flow's condition. An intake will not operate if its ICR is below the isentropic limit, which represents isentropic compression to Mach 1 and is determined with equation 2.3. The bounded region between the two is the dual solution region, in which an intake will remain started, but it is heavily dependent on the flow conditions of the engine. Thus, in the dual solution region, intakes may or may not be self-starting. A third line is present in Figure 2-7, which denotes a modified isentropic limit by Flock and Gulhan [34]. This is a semi-empirical limit proposed by the authors based on findings from various experiments and allows for the increase of the self-starting envelope for internal contraction ratios, as the Kantrowitz limit was found to be rather conservative in its estimation[24]. The modified limit is described by equation 2.4. The value of Π_t represents the total pressure recovery obtained at the point of maximum flow deflection. This is the deflection which occurs before shock detachment.

$$ICR_{Kan} = \left[\frac{(\gamma + 1)Ma_{closure}^2}{(\gamma - 1)Ma_{closure}^2 + 2}\right]^{0.5} \left[\frac{(\gamma + 1)Ma_{closure}^2}{2\gamma Ma_{closure}^2 - (\gamma - 1)}\right]^{\frac{1}{\gamma-1}} \quad 2.2$$

$$ICR_{isen} = \frac{1}{Ma_{closure}}\left[\frac{2}{\gamma + 1}\left(1 + \frac{\gamma - 1}{2}Ma_{closure}^2\right)\right]^{\frac{\gamma+1}{2(\gamma-1)}} \quad 2.3$$

$$ICR_{F\&G} = ICR_{isen} * \Pi_t(\beta_{max}) \quad 2.4$$

An example of the conservative prediction of the Kantrowitz limit can be seen from the experimental and numerical results of Devaraj et al. [35] who used a scramjet intake at Mach 6 to investigate unstart. The dual-ramped mixed compression intake remained started at an ICR significantly higher than the Kantrowitz limit. Additional findings by the authors display subsonic spillage (Figure 2-5), which is an unusual condition for a hypersonic intake. Experiments by Hohn and Gülhan[36] and Joseph et al. [37] further show the importance of ICR as an important metric for intake performance. The work of Hohn and Gülhan focused on a compact mixed compression intake at Mach 7 with a movable cowl, allowing for the ICR to be modified. It was found that ICR played an important role not only on the startability of the intake, but also its performance once started. The value of ICR required for intake self-starting matches well with the predictions of semi-empirical relations and especially with the one of Flock and Gülhan. Despite the intake starting, low ICRs provide poor performance during operation, seen by the low total pressure recovery. Higher performance and stability were

achieved when the intake operated at higher ICR. Joseph et al. investigated the startability of a proposed hypersonic intake for use by the Indian Space Research Organisation (ISRO). The specifications required the intake to operate up to a maximum AoA of 6 degrees. However, baseline model failed to start at an AoA of 2 degrees, as the cowl shock impinging on the intake would result in flow separation at the inlet throat. Interestingly, the model was designed to meet the Kantrowitz criterion, and the intake operates at 0 angle of attack. Despite this, when the intake attempts to compress the flow at a higher AoA, the strength and impingement of the cowl shock causes a separation bubble on the ramp, causing unstart. The final iteration of the design proposed by the authors modify the cowl by adding a small closure angle and moving it further downstream to mitigate the strength of the incoming shock and make the shock impinge further downstream, allowing the intake to operate at higher AoA, presented below in Figure 2-8.

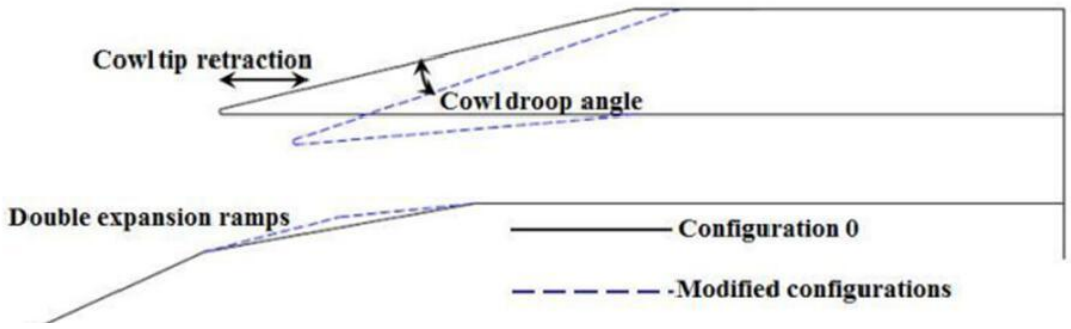


Figure 2-8: Comparison of base configuration to final iteration with a 2 deg cowl angle (Config VIII) and a retraction from the original location of 0.5*h, where h is the isolator duct height. Authors consider this the optimum configuration due to high startability angle and high compression. Reproduced from [37]

The location of the cowl evidently plays an important role in the startability and overall flow stability. In their extensive testing of 250 dual-mode scramjet configurations at Mach 4, Emami et al. [38] showed that cowl impingement on the corner of the ramp, known as the "shock-on-shoulder" condition, produces the most uniform flow into the isolator. This condition was achieved by varying the length of the cowl. Contrary to the previous studies though, in the results of Emami et al. [38], ICR didn't appear to have a significant effect on unstart which is surprising, considering that an increase in cowl length would result in an increase in contraction ratio. The authors concluded that the most significant mechanism for unstart regarding inlet geometry was the shock-boundary layer interactions. This is supported by the fact that at two different boundary layer states, significant changes in the supported turning angle were seen. Thinner boundary layers were seen to have a higher resistance to separation and thus could

support a higher turning angle. This can perhaps be explained though the findings of experimental study of Lanson and Stollery [39], who noticed that lower Reynolds numbers would lead to thicker boundary layers, which were more susceptible to separation. Their study demonstrated that the Mach 8.2 mixed compression intake would perform better at higher Reynolds numbers, when the boundary layer would be thinner. Additional findings were that increasing the isolator height (moving the cowl away from the ramp) had a positive effect on the stability of the intake, due to the reduction of the shock strength and change in impingement location.

The studies of Lanson and Stollery and Emami et al. demonstrate the importance of the cowl location and by extension the convergence of the cowl shock. In the case of Emami et al., the shock on shoulder condition led to superior performance but meeting this condition also simplifies the design of the intake. The inviscid modification to the intake of Idris et al. [40] by Sandeep and Gupta [41] demonstrates this. The attempt to impose a shock-on-shoulder condition on the original intake provided superior performance in the absence of viscous effects. However, introduction of viscous elements shows that the convergence of the cowl shocks on the corner causes unstart due to the boundary layer separating on the corner. As the design is fixed, most of the parametric studies would constitute off-design operation. The most significant change is observed with an increase in flight Mach number. As the flight Mach number is increased, shock inclination (or shock angle, β, on all ramps is decreased. This causes the shocks to intersect at different locations from the design goal of shock-on-lip. At lower speeds, the shocks meet upstream of the cowl tip, causing mass flow spillage and drag increase. At higher speeds, the shocks would impinge inboard of the cowl, and potentially the ramp shocks would interact with each other. This causes a sharp drop in the TPR, but an increase in static pressure ratio. More crucially though, the separation bubble in the corner increases in size, from roughly 50% of the isolator height at Mach 4, to over 70% at Mach 8. This would probably result in unstart in all cases, either due to flame-out of the combustor due to insufficient air or unstart due to backpressure of combustion due to the lack of flow momentum.

Further studies by the Krishnan et al. [42] and Khobragade et al. [43]. have echoed this. The former performed LES simulations on a mixed compression intake used by the LAPCAT program at Mach 6. Twin shock impingement on the shoulder results in flow separation and unstart of the engine. Moving the impingement locations apart by means of a splitter plate contained and reduced the separation bubble, allowing for intake start. Similar results were observed by Khobragade et al. in their experimental and numerical campaign. The splitter plate

produced similar patterns to the ones observed by Krishnan et al. and the addition of a notched splitter plate further stabilised the separation bubble. It can be concluded that passive measures for controlling the separation bubble are beneficial and do not have the adverse effects of bleeds.

The external ramp system is critical to mixed-compression intakes due to the presence of SBLIs. Although SBLI-induced separation must be avoided, an additional challenge arises in multi-ramp configurations.

To reduce total pressure losses and reduce the ramp angle encountered by the flow, multi-ramped systems split the overall external compression through two or three ramps. This produces higher total pressure recoveries, as weaker shocks are used to compress the flow successively, instead of a strong singular shock. This leads to questions as to what the spacing of successive ramps should be to avoid interference between them and allow the boundary layer to recover to close to its equilibrium state before the next SBLI. This was experimentally tested by Gaisbauer et al. [44], who tested a double ramp configuration ($\theta_1 = 9$ and $\theta_2 = 11$) at Mach numbers 2.5 and 3 as well as varying Reynolds numbers. Although the freestream Mach numbers do not match hypersonic flow conditions, valuable information about the trends of multi-ramped systems can be obtained. Results show that for a sufficiently long distance between the two ramps, the two interactions decouple and can be treated separately. Secondly, the boundary layer becomes more resistant to the adverse pressure gradient imposed by the second shock as a result of the amplification of turbulence. Therefore, it can be concluded that for a successful design of a mixed compression intake, a sufficiently long distance between ramps is required to suppress flow separation, but the length of which might decrease for successive interactions, as the increase in energy within the boundary layer results in higher resistance to flow separation for a given set of ramp angles.

Complimentary numerical studies on ramp distancing have been conducted by Goldfeld et al. [45] and more recently by Tong et al. [46] using RANS and DNS respectively, which provide supporting evidence towards the conclusions drawn by the experiments of Gaisbauer. Goldfeld's numerical results support the argument that an increase in turbulence is observed behind the first interaction, but only as an effect of a localised flow separation on the first ramp. With attached flow, no such effect is observed, with the separation region at ramp 2 being unaffected. The DNS study of Tong et al. [46] displays the decoupling of the two separation bubbles as the length between the ramps is increased. As the length between the two ramps is

increased while keeping all other variables constant, the separation bubble first reduces and then fully separates into two different ones, with the second bubble being eventually diminished to negligible levels. An interesting point to note is that the boundary layer appears to stabilise faster in the second longest separation between the ramps, seen by smoother pressure rise between the kinks (Figure 2-9) and the subsequent reaching of an equilibrium state past shock 2, which itself is marked by the non-fluctuating integral parameters, demonstrated in Figure 2-10. This can perhaps be attributed to the presence of a larger separation bubble on ramp 1, which as discussed increases turbulence in the boundary layer.

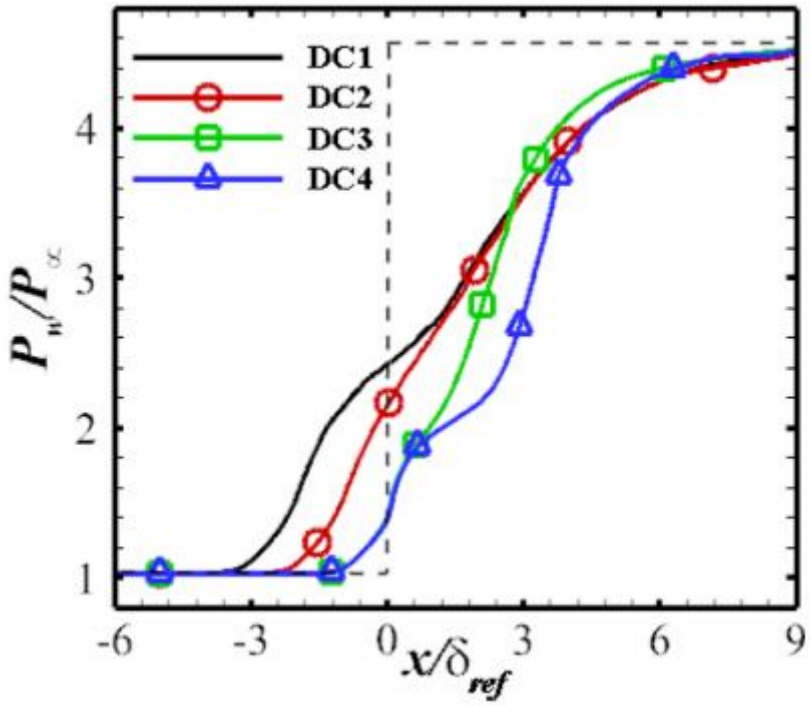


Figure 2-9: Pressure increase across the double compression angle. DC3 configuration shows superior performance, with minimum inflection noted. Reproduced from [46]

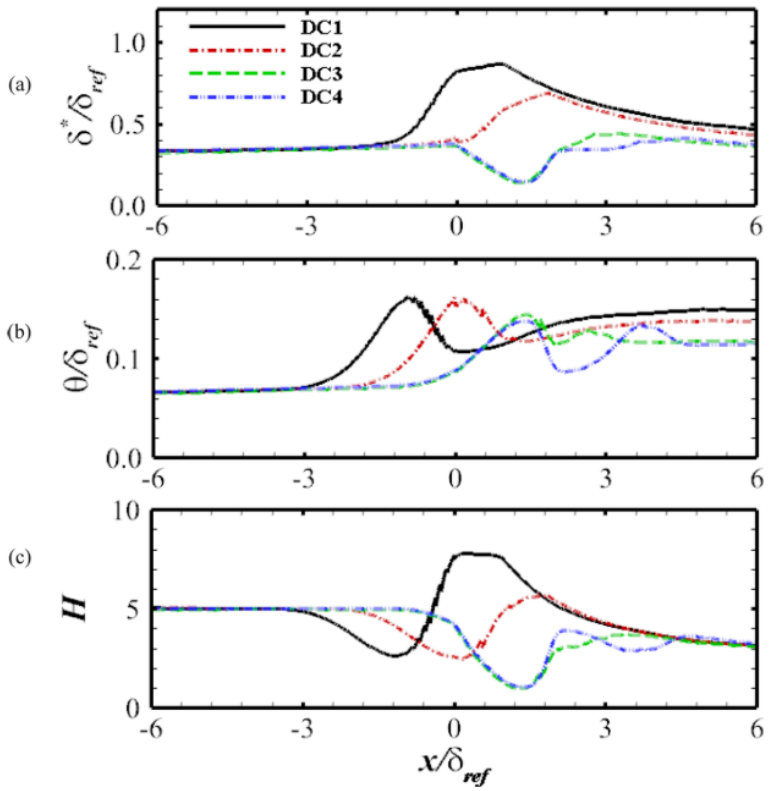


Figure 2-10: Evolution of integral quantities in the streamwise direction. Evolution of DC3 (2nd longest distance between ramps) shows the best stability, with low amplitude and quickest recovery. Reproduced from [46]

Further applications of CFD to mixed compression intake performance include the studies of Siquiera, Rosa and Ribeiro [15] and Kang, Kwon and Park [21]. Siquiera, Rosa and Ribeiro [15] employed the γ-Re_θ transition model in steady 3D RANS simulations of a fixed geometry, three-ramp, mixed compression intake to investigate the effects of Mach number, altitude and angle of attack. Increasing Mach number strengthened the shocks and associated SBLI, resulting in increased heat transfer and more pronounced isolator separation. Higher Mach number and altitude also increased sidewall separation, while the lower static pressure at altitude reduced aerodynamic loading. Angle of attack altered the shock impingement locations and pre-compression of the flow, with positive angles producing greater compression and increased loads, as well as higher heating on the upper isolator wall due to separation.

Kang, Kwon and Park [21] similarly used 3D RANS simulations, employing the SST k-ω model with compressibility and curvature corrections, to investigate the effects of leading-edge bluntness, engine width and sidewall angle on a single-ramp mixed compression intake. The CFD results were combined with one-factor-at-a-time and Latin hypercube sampling to develop a surrogate model, which was subsequently incorporated into a multi-objective

optimisation framework (NSGA-3). The optimisation metrics are TPR maximisation, maximum mass flow rate captured and minimum drag. Engine width and sidewall angle were identified as the primary geometric drivers, while leading-edge bluntness had comparatively little influence. The surrogate-based method shows promise but would require multiple high-fidelity simulations for accurate results and to widen the design envelope. The authors noted, however, that transition of the boundary layer on the leading plate can significantly affect intake performance and was not included due to limitations in available universal RANS transition models.

The hypersonic intake literature shows the sensitivity of the intake's performance on a variety of factors, ranging from freestream conditions to geometric considerations. Of vital importance is the internal contraction ratio (ICR) and shock convergence, as those tend to lead to unstart if not properly managed. Controlling the geometry of the cowl and ramps allows for simultaneous mitigation of both, but proper optimisation is needed to reduce losses and deliver sufficiently conditioned flow to the combustor through the isolator.

2.2.3. Mixed compression intake design modelling

In the last decade, a great many researchers have investigated supersonic and hypersonic intakes, as they are not only crucial to scramjets, but they are also vital to the operation of a combined cycle engine. Intakes are crucial to the operation of both engine types, as they are solely responsible for the compression and deceleration of the incoming flow. It is worth re-iterating that these duties must be performed with the lowest aerodynamic losses possible. This implies that the intake should perform compression and deceleration with minimum total pressure and entropy losses, good airflow conditioning for combustion, avoidance of the unstart condition, low drag, and high backpressure resistance [47].

Existing modelling methodologies can be broadly categorized into three distinct fidelity tiers: (1) low-order analytical/ODE-based models, (2) high-fidelity 3D RANS/CFD simulations, and (3) hybrid or multi-fidelity surrogate frameworks.

To satisfy the above requirements, efficient designs of intakes are required for a wide range of operations. To produce satisfactory designs, researchers take different approaches in the design of these components. Two broad categories can be defined for these approaches, low fidelity and high fidelity modelling of intakes or full scramjet cycles. The two approaches attempt to model or optimise components or full scramjets but differ in the physical fidelity employed and the physical phenomena they capture. This in turn influences the computation time and

accuracy of prediction of the various phenomena. The aforementioned phenomena include the capturing of viscous elements such as boundary layer evolution, combustion reactions and backpressure and shock-boundary layer interactions. Both approaches have seen many publications over the last few years, with researchers taking various approaches in modelling, even within the same fidelity category.

In the low fidelity category, Araujo et al.[48] developed an inviscid intake model coupled with an optimiser to optimise for the ramp angles of a hypersonic mixed compression intake. Their approach uses the 0^{th} and 1^{st} laws of thermodynamics to calculate the temperature rise required at combustor entry to transfer sufficient energy to the hydrogen fuel to auto-ignite it. Combustion is modelled using the 1D Rayleigh heat addition process. There are additional requirements for capturing the maximum mass flow rate (shock-on-tip condition) and eliminate the internal shock reflections from the cowl (shock-on-shoulder condition) applied to the model. In the absence of boundary layers, the authors use the Korkegi criterion[49], which is purely a function of the incoming Mach number, to predict separation at the compression ramp intersection. The inviscid mixed compression intake optimised for in this study is presented in Figure 2-11 below.

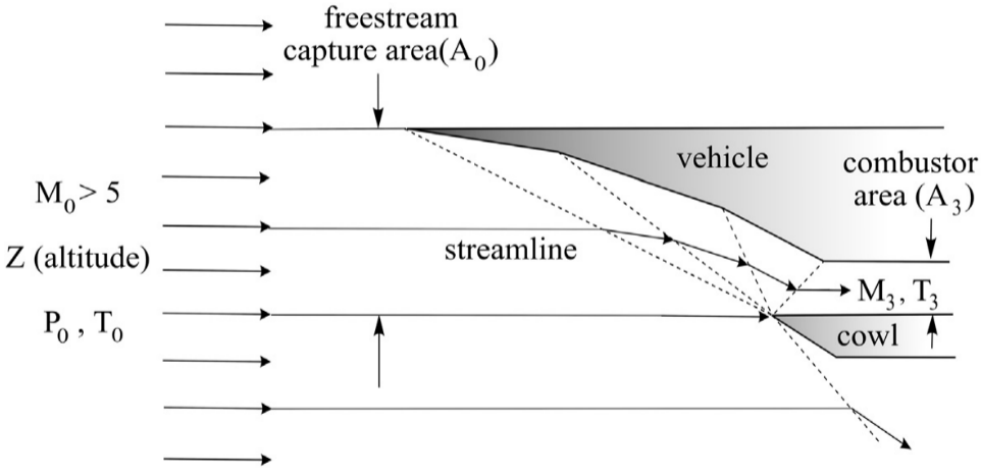


Figure 2-11: Mixed compression intake geometry optimised by Araujo et al[48]. Reproduced from [48]

External compression section (incident shock waves)					
	1 ramp	2 ramps	3 ramps	4 ramps	5 ramps
θ_1 (deg)	19.006	9.100	6.008	4.477	3.564
β_1 (deg)	26.116	15.510	12.673	11.398	10.679
M_{1C}	3.802	5.390	5.931	6.198	6.357
θ_2 (deg)		11.795	7.077	5.048	3.919
β_2 (deg)		20.315	15.012	12.898	11.774
M_{2C}		4.059	4.988	5.468	5.761
θ_3 (deg)			8.387	5.708	4.316
β_3 (deg)			17.938	14.657	13.012
M_{3C}			4.150	4.801	5.207
θ_4 (deg)				6.478	4.762
β_4 (deg)				16.747	14.424
M_{4C}				4.189	4.692
θ_5 (deg)					5.269
β_5 (deg)					16.051
M_{5C}					4.209
$M_{in} \sin \beta$	3.083	1.872	1.536	1.383	1.299
p_{out}/p_{in}	10.910	3.919	2.587	2.066	1.796
T_{out}/T_{in}	2.777	1.586	1.345	1.244	1.189
π	0.306	0.781	0.918	0.962	0.980
Internal compression section (reflected shock waves)					
	1 ramp	2 ramps	3 ramps	4 ramps	5 ramps
θ_{ref} (deg)	19.006	20.896	21.473	21.711	21.830
β_{ref} (deg)	32.100	33.285	33.660	33.807	33.884
M_3	2.533	2.533	2.533	2.533	2.533
T_3 (K)	1071.477	1071.497	1071.473	1071.487	1071.508
p_3 (kPa)	60.012	103.360	124.351	134.621	140.148
π	0.711	0.616	0.583	0.570	0.563
p_{t_3}/p_{t_0}	0.218	0.375	0.451	0.488	0.508

Figure 2-12: Parameters of optimised intakes from low-order method of Araujo et al.[48]. Reproduced from original work [48]

Figure 2-12 above shows the optimised angles and performance for ramp numbers between 1 and 5 for a scramjet flying at Mach 7 at 30 km. It is clear from the results that an increase in ramp number results in superior performance in total pressure recovery. However, an increase in ramp number will inevitably result in an increase in length and weight of the aircraft, which is undesirable for aircraft design.

While this approach is simple and computationally cheap, as it uses well-known analytic solutions for the solution of the inviscid system, it has significant drawbacks. The algorithm does not differentiate between the modes of operation (dual-mode or pure scramjet) and hence an isolator is not considered at all, or its effects on the flowfield and unstart. The engine is maintained at pure scramjet mode for the entirety of this study. Additionally, the pressure rise across the combustion chamber is maintained at or near the Korkegi limit[49] to prevent separation. While this might be a valid method, no proof has been shown, experimental or CFD, that would demonstrate the efficacy of this method. Another drawback at combustion is that non-equilibrium effects are not considered in any capacity. The heat release in scramjet combustors causes the incoming air to dissociate and exhibit significant variations in

thermodynamic properties. Not considering these will result in erroneous heat addition requirements and hence might violate separation criteria.

Korkegi limit (exceeding this assumes that flow is separated):

$$\frac{p_{out}}{p_{in}} = \begin{cases} 1 + 0.3Ma_{in}^2 & M_{in} \leq 4.5 \\ 0.17Ma_{in}^{2.5} & M_{in} > 4.5 \end{cases} \quad 2.5$$

In a subsequent work, Araujo et al.[50] expand this model to include a limited number of viscous elements and expand the optimisation criteria by calculation of viscous drag as one of the objective functions. The boundary layer is not explicitly considered, but correlations are used to model the skin friction coefficient and estimate viscous drag. Additionally, to account for STBLI, a correction is applied to the freestream Mach number to allow for shocks to coalesce on the cowl tip. The viscous correction to the freestream Mach number is expressed as:

$$Ma_{\infty,corr} = \frac{Ma_{\infty,orig} + 0.799}{1.22} \quad 2.6$$

Additionally, the 1D Rayleigh heat model does not consider fuelling. In this work, CFD validations of the model are included, solving the compressible 2D URANS equations using the transition k-ω turbulence closure model. The value of turbulent intensity is selected to be 5% and the turbulent viscosity ratio is 10, both of which indicate a medium turbulence level. The transition location depends directly on the intensity selected and the value set by the authors would result in a very early transition due to the nature of the transition modelling. No validation of the CFD is presented explicitly in the paper, thus the transition model's performance on the boundary layer growth is not known.

The results show good agreement between the analytical method and CFD as the flight Mach number is increased. While the boundary layer is not considered, it is evident that its importance is great inside the isolator, as the combined blockage between the top and bottom boundary layers is about 40% of the channel height. This would influence the flow passing through the isolator both in startability and compression. The CFD has no heat addition effects and is therefore unable to consider whether the isolator or the combustor can sufficiently contain the incoming flow. As with the previous work, no dual-mode solutions are obtained, as the maximum combustor exit Mach number is capped at supersonic flows, not allowing for combustor effects to back-propagate into the isolator. Despite the lack of back-pressure, an isolator appears to exist in the engine, perhaps used as a first stage combustion, a constant area

combustor, before opting for a second stage combustion with a more conventional diverging combustor. The validations were performed at roughly Mach 6 and different altitudes. In this flight regime, the engine would more likely than not favour dual-mode combustion, as the external compression would normally not suffice for robust combustion. Thus, the isolator would also serve to rise the pressure internally. Despite this, the optimisation constrains do not allow for dual-modes, which is a significant drawback for this lower hypersonic flow speeds. The work provides a better insight into the optimisation routines used, considering a variety of methods, from metaheuristics to genetic algorithms. It does not provide analysis on the best approach; however, it shows that many methods are viable for use in hypersonic optimisation problems.

A more advanced low-order model was developed by Verma et al.[51], who, while still not considering effects of the boundary layer on the external compression system, have a higher fidelity isolator-combustor model, which uses a system of ODEs for mass, momentum and the equation of state in its differential form, along with supporting functions to determine the evolution of the flow within the combustor. The workflow of the model is shown in Figure 2-13.

These ODEs take the form:

Variation of streamwise combustor total temperature:

$$\frac{dT_t}{dx} = \frac{2c_f(T_w - T_{aw})}{D_h} + f_{stoichio}\varphi LHV\eta_c \frac{d\eta_{mix}}{dx} \tag{2.7}$$

Where T_t, D_h are the total temperature and hydraulic diameter respectively. The other symbols take the meanings as denoted in the nomenclature. The last term, $\frac{d\eta_{mix}}{dx}$, describes the mixing efficiency variation along the combustor. This occurs due to the turbulent nature of the incoming flow. To model this, the authors use correlations, based on the work of Fotia et al.[52] and use the convective Mach number, along with other empirical relations.

Variation of streamwise combustor Mach number:

$$\frac{dMa^2}{dx} = \frac{Ma^2\left(1 + \frac{\gamma - 1}{2}\right)Ma^2}{1 - Ma^2}\left[(1 + \gamma Ma^2)\left(\frac{1}{T_t}\frac{dT_t}{dx}\right) + \frac{4c_f\gamma Ma^2}{D_h} - \frac{2}{A}\frac{dA}{dx}\right] \tag{2.8}$$

Variation of streamwise combustor total pressure:

$$\frac{dp_t}{dx} = -p_t\left(\frac{\gamma Ma^2}{2}\right)\left(\frac{1}{T_t}\frac{dT_t}{dx} + \frac{4c_f}{D_h}\right) \quad 2.9$$

The authors call this the no-shock solution, as it does not consider the isolator shock train. In contrast to the previous works by Araujo et al., the work of Verma et al. also includes a prediction for the isolator length, which significantly improves the usability of the model, allowing for a more complete and robust model. The shock train is one of the outputs of the model, and only happens if the minimum Mach number calculated by the no shock model is lower than:

$$Ma_{min,ODE} \leq 0.762 Ma_{iso,entry} \quad 2.10$$

In the case where this is satisfied, it is assumed that a shock train is developed, and the maximum pressure at this location is used as the input to the empirical relations for estimation of the shock train length,L_s:

$$L_s = \frac{\sqrt{D\theta}}{\left(Ma_{iso,entry}^2 - 1\right)Re_\theta^{0.25}}\left[50\left(\frac{p_{sd}}{p_{iso,entry}}\right) + 170\left(\frac{p_{sd}}{p_{iso,entry}}\right)^2\right] \quad 2.11$$

With p_{sd} being calculated using Billig et al.'s[53] empirical relation. The isolator is assumed to be adiabatic in this work.

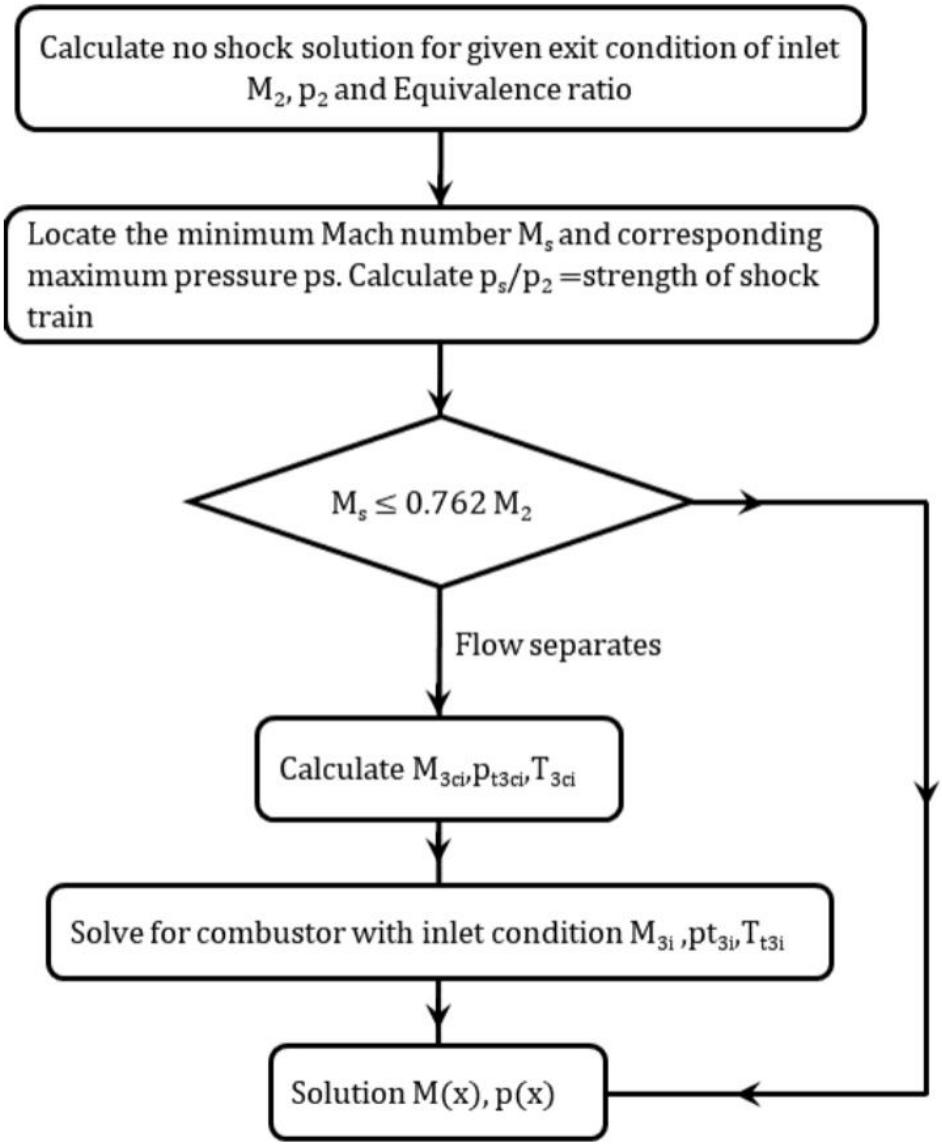


Figure 2-13: Workflow schematic for the isolator-combustor modelling of Verma et al.[51]. Reproduced from original work [51]

Verification is once again performed using the solution of the 2D URANS equations; however, this work uses the conventional k-ω SST turbulence closure model. The engine surfaces are assumed to be adiabatic. The turbulence intensity selected is not known.

Despite the improvements made, the lack of explicitly accounting for the boundary layer growth along both body and cowl surfaces appears to have an effect on the efficacy of the developed model, From the CFD results, the shocks do not converge on the prescribed locations that would meet the shock-on-tip and shock-on-shoulder conditions. Instead, spurious shock reflections are seen internally, which would severely influence the internal flowfield. Compounding this, no heat release was included in the simulations, which similar to the Araujo

case, does not allow for validation of the isolator-combustor model. Although there are shortcomings, their results provide insight into the design compromises that must be made to ensure all the contradicting requirements of a scramjet design are met. Increasing the compression of the external flow results in significant elongation of the entire engine, which would make the entire aircraft's weight increase. Further, if the capture area is maintained at a constant value, an increase in Mach number results in longer intakes, due to the shallower shocks.

Chakir et al.[54] present a currently developed code, *MSU*, which contains many of the elements found in Verma et al.'s model but presents a coupled isolator-combustor system. The inlet is modelled assuming isentropic compression with oblique shocks, while the isolator is treated as a Fanno flow region, separated into two distinct sub-models. Where the flow remains attached, it is treated as a normal Fanno flow (Equation 2.12), but in the region where a shock train would develop, a modified Fanno flow set of equations is utilised (Equations [2.13–2.14]).

Attached Fanno in differential form:

$$\frac{dMa^2}{Ma^2} = \frac{1+\frac{\gamma-1}{2}Ma^2}{1-Ma^2}\frac{4\gamma c_f Ma^2}{D_h}dx \tag{2.12}$$

Detached Fanno in differential form:

$$\frac{dMa^2}{Ma^2} = -\left(1+\frac{\gamma-1}{2}Ma^2\right)\left(\frac{{}^{dP}/_{P}}{\frac{\gamma Ma^2}{2}\frac{A_C}{A}}+\frac{4c_f\frac{dx}{D_h}}{\frac{A_C}{A}}+\frac{dT_t}{T_t}\right) \tag{2.13}$$

$$\frac{{}^{dA_C}/_{A}}{{}^{A_C}/_{A}} = \left(\frac{1-Ma^2\left(1-\gamma\left(1-\frac{A_C}{A}\right)\right)}{\gamma Ma^2\frac{A_C}{A}}\right)\frac{dP}{P}+4c_f\left(\frac{1+(\gamma-1)Ma^2}{2\frac{A_C}{A}}\right)\frac{dx}{D_h} + \left(1+\frac{\gamma-1}{2}Ma^2\right)\frac{dT_t}{T_t} \tag{2.14}$$

The streamwise pressure gradient is modelled by an empirical correlation as:

$$\frac{dP}{dx} = P\frac{89\gamma c_f Ma^2}{2D_h} \tag{2.15}$$

In a similar manner to Verma et al. work, the combustor flowfield is modelled through the solution of a set of coupled ODEs, which subsequently returns the pressure applied as

backpressure on the isolator. Unlike Verma et al. who solved the conservation equations, Chakir et al. use the Heiser and Pratt relation for the evolution of the streamwise Mach number and coupled it with different equations for change in area and total temperature to obtain:

$$\frac{d(\ln A)}{dx} = \frac{\ln\left(\frac{D + 2\tan(\alpha)}{D}\right)}{dx} \tag{2.16}$$

$$\frac{d(\ln(T_t))}{dx} = \frac{d(\ln T)}{dx} + \frac{(\gamma - 1)Ma}{1 + \frac{\gamma - 1}{2}Ma^2} + \frac{dMa}{dx} \tag{2.17}$$

$$\left(1 - Ma\left(\frac{(\gamma - 1)Ma}{1 - Ma^2}\right)\frac{(1 + \gamma Ma^2)}{2}\right)\frac{dMa}{dx} = \frac{Ma\left(1 + \frac{\gamma - 1}{2}Ma^2\right)}{1 - Ma^2}\left[\frac{(1 + \gamma Ma^2)}{2}\left(\frac{d(\ln T)}{dx}\right) - \frac{d(\ln A)}{dx}\right] \tag{2.18}$$

They also include a mixing model, which is different to the one applied by Verma et al. but serve the same purpose. The entire model is solved iteratively and in a similar way to Verma et al. the Mach number ratio is used to determine separation. In the case of flow separation, the modified Fanno flow is executed. The entire model is presented in Figure 2-14. This work enables dynamic coupling between combustor pressure rise and upstream isolator behaviour.

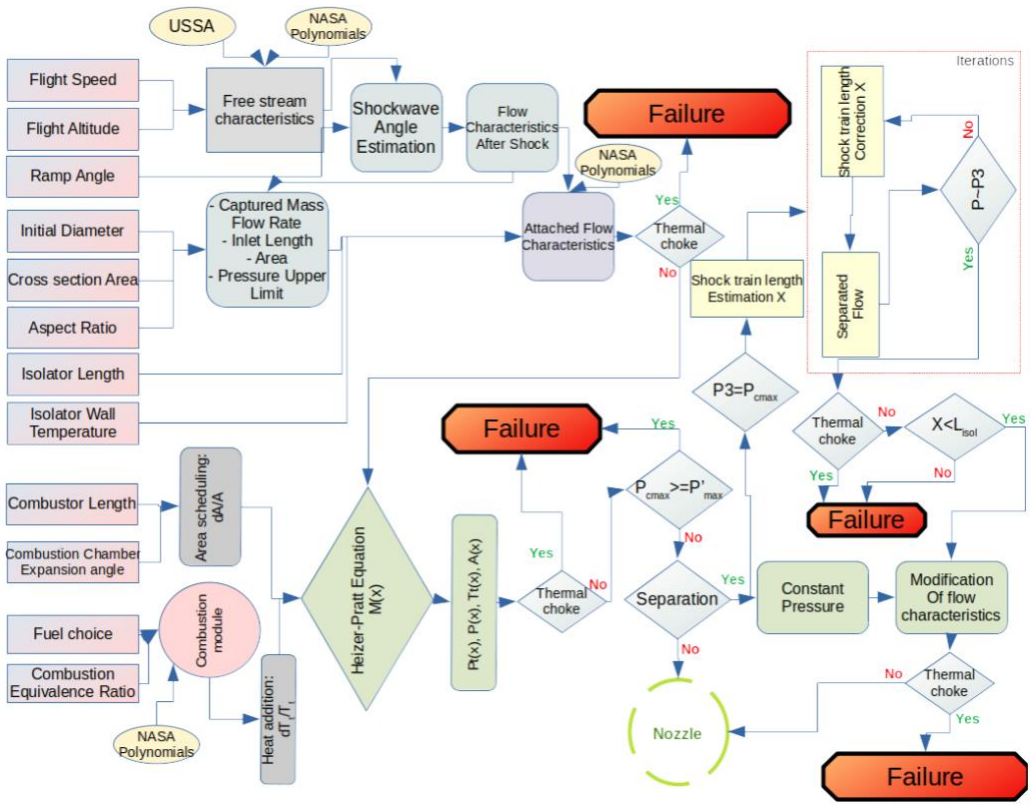


Figure 2-14: MSU workflow. Reproduced from original work [54]

This method allows estimation of diabatic isolator shock trains and is strongly coupled to the combustor's behaviour and heat release. The authors have not provided execution time requirements, and their verification of the individual sub-models show promise but have not been shown to work together to design an engine at the presented state, the model is only used for examining the performance of prescribed isolator/combustor configurations, as seen by the TEST-I and TEST-II cases. However, valuable lessons can be obtained. Altering the wall cooling on the isolator influences the development of the boundary layer in the isolator, with an increase in temperature resulting in a shorter shock train. Additionally, a decrease in Mach number results in an engine that enters unstart more readily, due to thermal choke occurring in the combustor. Through parametric studies, the authors demonstrate that increasing fuel equivalence ratio leads to higher combustor pressure rise, which can induce flow separation and extend the shock train beyond the isolator length, ultimately resulting in engine unstart. Conversely, higher flight Mach numbers enhance flow momentum and reduce susceptibility to separation, improving operability. The model also captures the competing effects of wall temperature and friction, showing that increased wall temperature can reduce shock-train length by increasing the effective friction coefficient, thereby stabilizing the flow.

Despite the seemingly good performance, it still lacks the ability to process an incoming boundary layer from the outside and hence take into account the effects of the boundary layer. In this model, similar to the work of Verma, the skin friction coefficient (c_f) is used to account for the boundary layer. This treatment inherently removes the capability to predict other vital viscous phenomena such as shock-turbulent boundary layer interactions. Furthermore, while the combustor model is robust, similar to previous approaches, it misses non-equilibrium effects which will inevitably appear in scramjet combustors. Lastly, as with Verma et al.'s work, while each individual sub-model is verified against separate experiments, there is no combined solution of the two models that is validated or verified through experimental or CFD work.

Further progress in the modelling of the combustor and nozzle was made by Ispir et al.[55], who developed a scramjet combustor-nozzle module based on Busemann intake considerations for the incoming flow to the combustor. The general schematic of the engine considered by the authors is shown in Figure 2-15, reproduced from the original work.

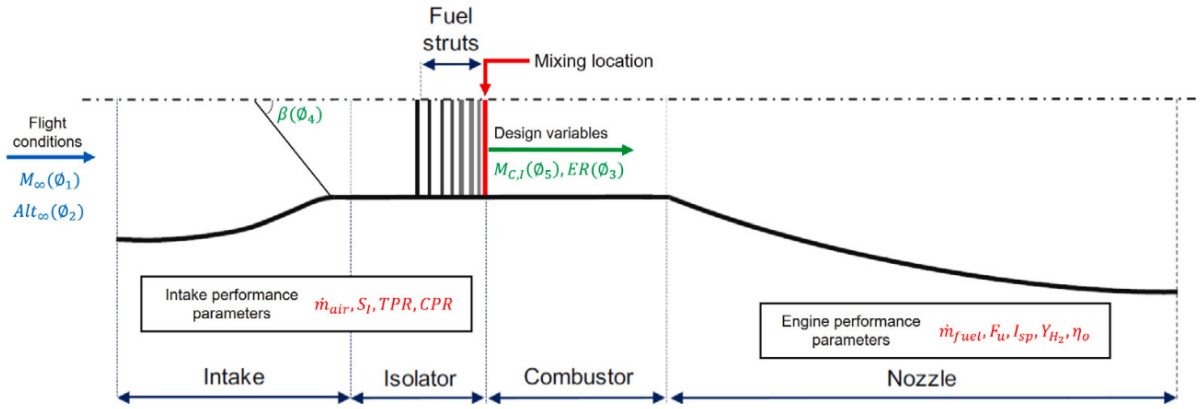


Figure 2-15: Generic schematic of configuration considered by Ispir et al. Reproduced from original work. [55]

As with previous cases, a set of coupled ODEs for mass, momentum and energy is solved in the streamwise direction in the combustor. A significant change done by the authors in this work is the introduction of an additional ODE, that of the transport of species. This allows for finite rate chemistry effects to be included during the solution. While this work considers finite reaction rates, it does not consider mixing dynamics, since the fuel and air are assumed to be mixed at combustor entry. Additionally, it does not consider heat losses to the combustor walls. Fuel is heated to stream temperature in model, thus no heat exchange between two streams. Combustor pressure (constant area combustor) does not agree well with experiments, but divergent section does. Using the SHAP framework, the authors performed parametric studies on the parameters shown in Table 2-2 below to investigate their effect on performance metrics.

Table 2-2 Variables used in parametric study of Busemann intake-based scramjet by Ispir et al.

Design Variables	**Investigation Range**
Cruise Mach	6,7,8
Cruise Altitude (km)	25,30,35
Equivalence Ratio	0.1 – 0.7
Truncation Angle (deg)	0 - 8
Combustor Entry Mach	1.1 - 3

From this investigation, it was found that the flight Mach number and altitude are the most influential operating parameters for scramjet performance, with the intake exit Mach number also having a significant influence through its effects on captured mass flow rate and the pre-combustion flow conditions. In general, increasing flight Mach number increases captured mass flow rate and uninstalled thrust, while increasing altitude reduces thrust as a result of the

lower atmospheric density and consequently reduced mass flow rate. However, the higher flight Mach numbers also modify the operating limits of the combustor. For Mach 6 and 7, thermal choking can occur when the intake exit Mach number is sufficiently low and/or the equivalence ratio is sufficiently high, with the thermal-choking region becoming smaller as altitude increases. In contrast, no thermal choking was observed for the Mach 8 cases within the investigated range of intake exit Mach number and equivalence ratio. At the other limit, non-ignition was observed across all investigated Mach numbers and altitudes when the intake exit Mach number was too high, as insufficient compression resulted in unfavourable pre-combustion conditions for auto-ignition. Consequently, the intake exit Mach number must be selected within an appropriate range to balance sufficient compression for ignition against excessive deceleration and thermal choking. The results, therefore, demonstrate that scramjet operation is governed by the coupled effects of flight Mach number, altitude, intake exit Mach number and equivalence ratio, which collectively define the operational envelope between non-ignition, viable propulsion and thermal choking.

Further work on combustion was done by Lee and Lee[56], who investigated the ideal combustion case for both ramjet and scramjet flowpaths, with a particular focus on the dual-mode scramjet. The analysis is performed on a two-stage combustor comprised of a constant area first stage and a diverging second stage, as shown in Figure 2-16.

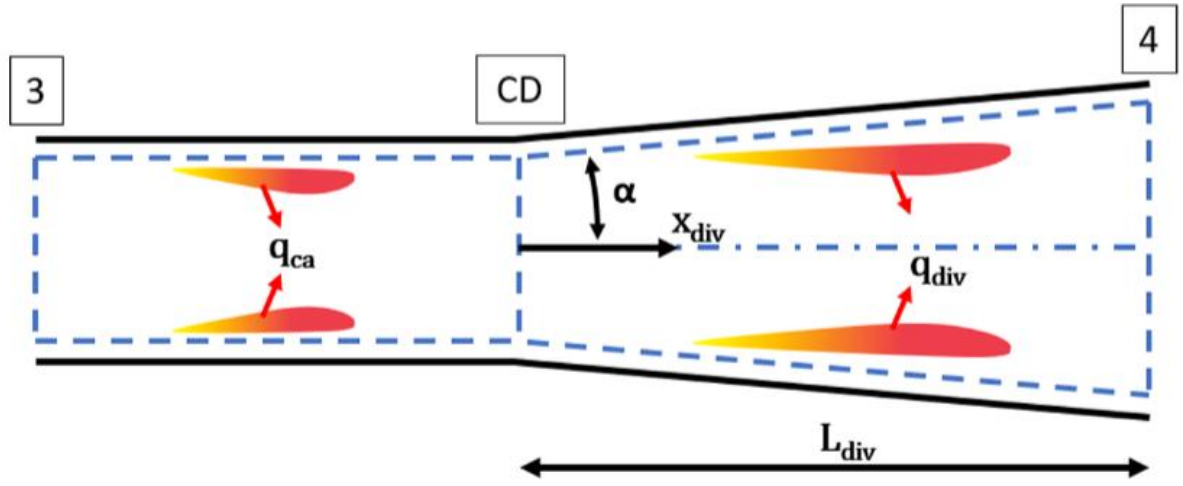


Figure 2-16: Constant-Divergent area combustor examined by Lee and Lee. Reproduced from original work[56]

The modelling of the two components is thus significantly different. The constant area section of the combustor is modelled as a Rayleigh heat addition process at stoichiometric conditions. The diverging section is modelled through a similar method as Verma et al. methods, but with

more assumptions, of which the most prominent is the assumption that combustion in the divergent section is done at almost sonic conditions. With all the assumptions applied, an analytical solution is obtained for the ratio of areas between the end and start of the divergent combustor. For a rectangular combustor, this analytic solution is a function of the total temperature at the exit of the divergent combustor $\left(T_{t,4}\right)$ and the heat added (q_{div}):

$$\frac{A_4}{A_3} = \left(\frac{c_p T_{t,4}}{c_p T_{t,4} - \frac{1+\gamma}{2} q_{div}} \right)^2 \tag{2.19}$$

Their findings show that for realistic flight conditions, a scramjet will operate at optimum conditions when the constant area combustor brings the flow to sonic conditions. The reason is that the diverging area combustor will maintain the flow at roughly the same magnitude under the assumptions of this work and hence will result in a longer residence time in the diverging area, conducive to better mixing and combustion. Additional findings indicate that while ideal flowpaths indicate that ram mode would be preferable in all flight conditions, a scram cycle would be superior in realistic conditions. Despite this, lower specific impulse is seen as the Mach number is increased, attributed by the authors to the lower difference between exit and entry velocities. It is worth noting that the cycles of scramjets in this work deviate from the Brayton cycle. They also quantitatively show the effect of unstart on thrust production, which is severely hampered primarily due to the reduction of the incoming mass flow rate. Interestingly, this effect remains consistent at all Mach numbers. Once unstart is triggered, then the effects are effectively identical, with loss of thrust being observed, which would rapidly accelerate due to the positive feedback between a reduction in Mach number and lower heating required to achieve unstart at lower Mach numbers. This study gives a great insight into these mechanisms as well as the ideal scramjet cycles for both ram and scram operation.

Despite these contributions, the model is subject to several important limitations. The analysis is restricted to one-dimensional and quasi-one-dimensional flow assumptions, neglecting multidimensional effects such as shock–boundary layer interactions, flow separation, and complex mixing processes that are known to play a critical role in real scramjet operation. Furthermore, combustion is treated in a highly idealised manner, assuming instantaneous mixing, complete reaction, and a prescribed heat release profile, thereby excluding finite-rate chemistry, turbulence–chemistry interactions, and ignition dynamics. The assumption of inviscid flow within the combustor and a calorically perfect gas further limits the applicability of the model at high enthalpy conditions where real gas effects become significant. Like some

of the previous works in this section, no higher fidelity validation is performed, thus the overall modelling approach cannot be verified.

The above studies have shown that low-order approaches can predict the macroscopic flow structures that occur on hypersonic engines. This has inspired researchers to combine higher-fidelity CFD methods with optimisation routines to arrive at optimum scramjet configurations.

One such research is that of Brahmachary, Fujio and Ogawa [58], who aimed to optimise a 3-ramp axisymmetric hypersonic intake, starting from a baseline configuration, for minimum drag and maximum compression for operation at two flight conditions, using an evolutionary algorithm and the solution of RANS using the SST k-ω turbulence closure model. The selected optimisation technique was the Non-Sorting Genetic Algorithm II (NSGA-II). The optimised configurations show a trade-off between compression efficiency and drag. This was determined to be an effect of the increase in static pressure ratio required at the combustor entry. It was also determined that from a design perspective, the most important parameters were found to be the combustor radius and the first ramp angle. Also, the optimum configurations appear to be clustered into two geometrically different clusters. The first is characterised by a longer intake, but a lower combustor radius (or isolator exit), while the second exhibits the opposite trend, having shorter intake length, but higher combustor radius.

Using a similar process, De Vanna et al. [59] optimised a mixed compression intake at Mach 5, starting from a baseline configuration comprising of a two-ramp external compression system and a fully open cowl. The intake was optimised through modification of the external compression system, which is characterised by a series of Bezier splines. The optmisation metrics used were drag, total pressure recovery and static pressure ratio. NSGA-II is similarly used as the optimisation routine. Their optimum configurations show a distinct bump on the first ramp, modified through Bezier splines. For optimum drag / TPR, the leading shock converges on the cowl, whereas for optimum SPR, the shock impinges downstream of the cowl tip. It can be concluded that for optimum efficiency, the shocks must impinge on the cowl, which ensures both maximum mass flow rate capture, but also higher boundary layer stability. Another interesting output from their analysis shows an interesting result regarding the selection of optimisation variables. Their selected optimisation functions were the total pressure ratio (TPR), static pressure ratio (SPR) and skin friction coefficient. From their analysis, it appears that optimising for TPR is functionally identical to optimising for the skin friction coefficient. Therefore, while viscous elements are crucial, due to flow separation and

shock train development in dual-mode engines, optimising for the total pressure recovery captures viscous losses adequately, and thus a need for drag calculation becomes redundant.

The design of hypersonic inlets is particularly sensitive to both operating conditions and geometric parameters. In this context, the DiGregorio et al.[57] present a framework that integrates multifidelity modelling, uncertainty quantification, and global optimisation to enable robust inlet design for scramjet applications. The study formulates the inlet design problem within both deterministic and stochastic settings, explicitly accounting for uncertainties in freestream conditions such as Mach number, angle of attack, and dynamic pressure.

The modelling approach employs a multifidelity structure, where low-fidelity analysis is based on inviscid analytical compressible flow relations (notably oblique shock theory), while high-fidelity analysis is performed using CFD. The compressible RANS equations are solved for a thermally perfect air, with the Menter-BSL closure model with wall functions. This implies that the results would be somewhat poorer than wall resolved turbulence but at a reduced computational load. This works well with the authors' work, as many CFD simulations are needed to obtain the correction to their low-fidelity model. This does not, however, prevent some scepticism regarding the influence of the numerical resolution on the viscous effects, since this is the primary goal of their work. These two levels are coupled through polynomial chaos expansion (PCE)-based uncertainty quantification, allowing the propagation of uncertainties with significantly reduced computational cost compared to purely high-fidelity approaches.

A key feature of the methodology is the use of non-intrusive PCE with multifidelity correction, in which the low-fidelity model captures the dominant physics with a correction term correcting for discrepancies with high-fidelity results. This enables accurate estimation of statistical quantities such as mean and variance of performance metrics, including total pressure recovery and throat Mach number. To address the high computational cost of robust optimisation, the study employs the Efficient Global Optimization (EGO) algorithm, a surrogate-based, derivative-free method that balances exploration and exploitation through an expected improvement criterion. This approach avoids the prohibitive cost associated with gradient-based robust optimisation, where uncertainty propagation must be performed repeatedly for gradient evaluations.

The results demonstrate that robust optimisation yields inlet designs that exhibit reduced sensitivity to uncertain inputs, albeit sometimes at the cost of reduced peak deterministic

performance. In particular, the study identifies that increasing total flow turning (i.e., larger deflection angles) can reduce sensitivity in post-shock Mach number, thereby improving robustness. Furthermore, it is shown that viscous effects captured by high-fidelity CFD can lead to deviations from classical inviscid design trends, such as those predicted by Oswatitsch, highlighting the importance of incorporating higher-fidelity physics in the design process. Importantly, the multifidelity uncertainty quantification approach is shown to closely reproduce the results of full high-fidelity uncertainty propagation at a fraction of the computational cost.

Despite its strengths, the framework retains several limitations. The low-fidelity model relies on inviscid compressible flow assumptions and simplified shock representations, which cannot capture complex phenomena such as shock–boundary layer interactions or flow separation. While high-fidelity CFD is incorporated, its use is limited by computational cost, and the overall methodology still depends on surrogate approximations and assumed uncertainty distributions. Additionally, the optimisation is performed for fixed-geometry inlets under specified conditions, with further work required to extend the approach to variable-geometry systems and full vehicle-level integration.

Attempts to reduce the computational cost of optimisation while maintaining the accuracy of CFD has been recently conducted by Kline et al. [60].The authors reduced the computational cost of CFD by extending the adjoint method to work with CFD solvers. This allows for the solver to reduce the number of calculations required for convergence and extend the objective functions for any outflow-based functions. Their optimisation starts from a basic single ramp mixed compression intake, with variation of the ramp surface being done through Bezier splines. A schematic of the configuration examined, and the methods employed for each component are presented in Figure 2-17 below. Limiting the use of CFD in the intake and isolator reduces the computational load, but it would still be significant for hypersonic velocities.

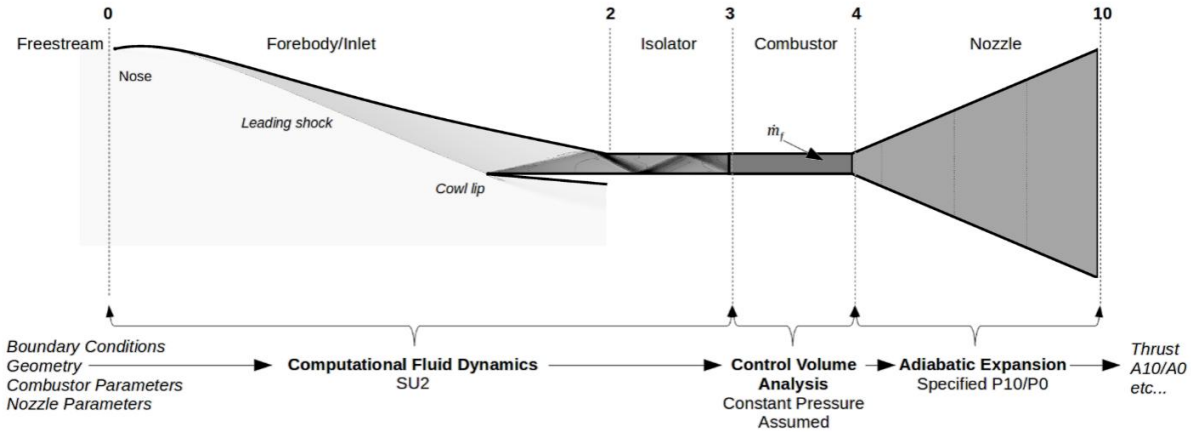


Figure 2-17: Scramjet configuration considered by Kline et al.[60], with the methodologies used for solution and sizing of individual components

Using this framework, they carried out multi-objective optimisation studies at Mach 7, where Pareto fronts revealed clear physical trade-offs between efficiency, thrust, and nozzle compactness. They showed that achieving higher efficiency or thrust inevitably required larger nozzle exit areas, while compact designs suffered performance penalties, with a notable compromise point appearing at roughly 0.35 efficiency with a nozzle exit area about four times the capture area.

The capabilities of low order modelling have been steadily increasing over the last decade, as seen by the relevant studies presented including more accurate equations to capture more flow parameters. Current state-of-the-art analytical methods still predominantly rely on inviscid assumptions. As demonstrated by the CFD literature reviewed, neglecting viscous phenomena provides heavily erroneous intake designs, rendering high-fidelity simulations mandatory to accurately resolve the flow field. Therefore, it is evident that the influence of the boundary layers both externally and internally play a vital role in the operation of scramjets and must thus be considered even during the preliminary process. The external and internal boundary layer development, particularly viscous displacement and shock interactions, dictate the true operating limits of scramjets and must be accounted for during early design phases. As such, a low-order routine that includes viscous effects would greatly benefit designers, as it would reduce reliance on CFD for the preliminary design process, accelerating the overall timeframes.

2.3. Research on hypersonic isolators

An isolator is a duct between the intake and the combustor. As mentioned previously, the role of the isolator is to prevent the disturbances generated by the combustion process from influencing the intake flow field. During combustion, a backpressure is applied to the flow

field entering the combustor due to the release of energy. As the area of the combustor is usually insufficient to fully accommodate the heat release of combustion, thermal chocking occurs, which results in an adverse pressure gradient (APG) being applied to the incoming boundary layer. This causes the boundary layer to separate and propagate upstream. This leads to the development of a shock train region, which is the product of multiple shock-boundary layer interactions occurring due to the presence of the adverse pressure gradient. This phenomenon was first described by Crocco[61], noting that for supersonic to subsonic deceleration within an isolator, the shock system does not comprise of a single normal shock expected of the limiting inviscid case, but by a series of shocks, resulting in a gradual deceleration of the flow instead of an instantaneous one.

Additional observations by Crocco were that the separation zone and thickening of the boundary layer caused by the successive shock-boundary layer interactions on the top and bottom surfaces could effectively be treated as a throat. With increasing inflow Mach number, the size of the throat decreases as the separation regions and boundary layer thickening increase in magnitude. This leads to higher blockage of the flow as well as extension of the pseudo-shock train length. The multiplicity of reflected shocks also contributes to lower pressure recoveries overall. The resulting centreline pressure distribution shows a rapid increase in pressure at the initial shock, followed by a rippling pattern in the pressure increase. The rippling pattern is caused by rapid compression and expansion of the flow near regions of shock impingement on the boundary layer.

The shock train properties are influenced by both upstream and downstream properties. Upstream, the shock system is influenced heavily by the incoming boundary layer and channel height, while the downstream influence arises from the difference in pressure between the incoming flow and pressure caused by combustion.

2.3.1. Experimental studies on isolators

The complexity of the flow field within an isolator with and without the effects of backpressure has been extensively investigated in the literature. Sugiyama et al. [62] investigated the features of a pseudo-shock train developed within a rectangular duct at Mach numbers 2 and 4. The flow exhibits extremely different behaviour patterns, with Mach 2 flows showing the creation of a bifurcated “λ” shock pattern at the leading shock of the shock train (STLS), reduced separation intensity and symmetric separation bubbles and faster pressure rise. In contrast, an increase in Mach number leads to the creation of an “X” shaped STLS, increased separation

zone and asymmetric separation as well as reduced pressure increase rate. The shape of the STLS was found to vary with Mach number in a number of other studies. The study conducted by Fan et al. [63] and Xiong et al.[64] on a Mach 3 rectangular intake with a constant backpressure show the same "X" shape for the STLS. Their study also exhibited asymmetric separation, would switch from top to bottom wall, which would induce massive pressure gradients as the separation bubbles grew and shrank. This switch of the separation mode is attributed to inherent instabilities within the separated flow field by the authors. Another study by Geerts and Yu [65] was conducted on two rectangular isolators with different aspect ratios at Mach 2.5. The shock structure of the STLS is a hybrid structure between the "λ" and "X" types. The objective of the study was to see the effects of aspect ratio on rectangular isolators, and interestingly, the high aspect ratio isolator showed a more 2D flow structure. These studies show that the Mach number and boundary layer profile of the incoming flow have a direct effect on the STLS. The effect of the Mach number was studied previously, with the change between "λ" and "X" types being reported by Matsuo et al. [66] to occur between 1.8 and 2.2. The experiment of Fotia and Driscoll [52], which used a direct connect facility to investigate the effects of total temperature and equivalence ratio on the shock system, provides an insight on the effect of the boundary layer effect on the STLS. According to their findings, thicker boundary layers (high flow containment) tend to lead to "X" shaped STLS while thinner ones (low flow containment) will lead to "λ" ones. The effect of the boundary layer seems to only be relevant near the range of change between the two patterns, with higher Mach numbers resulting in "X" shapes.

The flow in the isolator shows sensitivity to a variety of parameters. The experiment of Fotia and Driscoll [52] showed that an increase in total temperature for a fixed equivalence ratio results in shorter pseudo-shock trains. Increasing the total pressure results in longer pseudo-shock trains, and so does an increase in equivalence ratio. The length of the pseudo-shock train was also observed to be influenced by the wall temperature by Fischer and Olivier [67]. Increasing the temperature of the wall lead to shortening of the shock train, as demonstrated by Figure 2-18, which presents the increase in pressure coefficient along the duct. As the temperature increases, the location of pressure increase shifts further downstream but the point of pressure increase termination remains the same. This directly indicates that the length of the shock train decreases with increasing wall temperature at a constant backpressure.

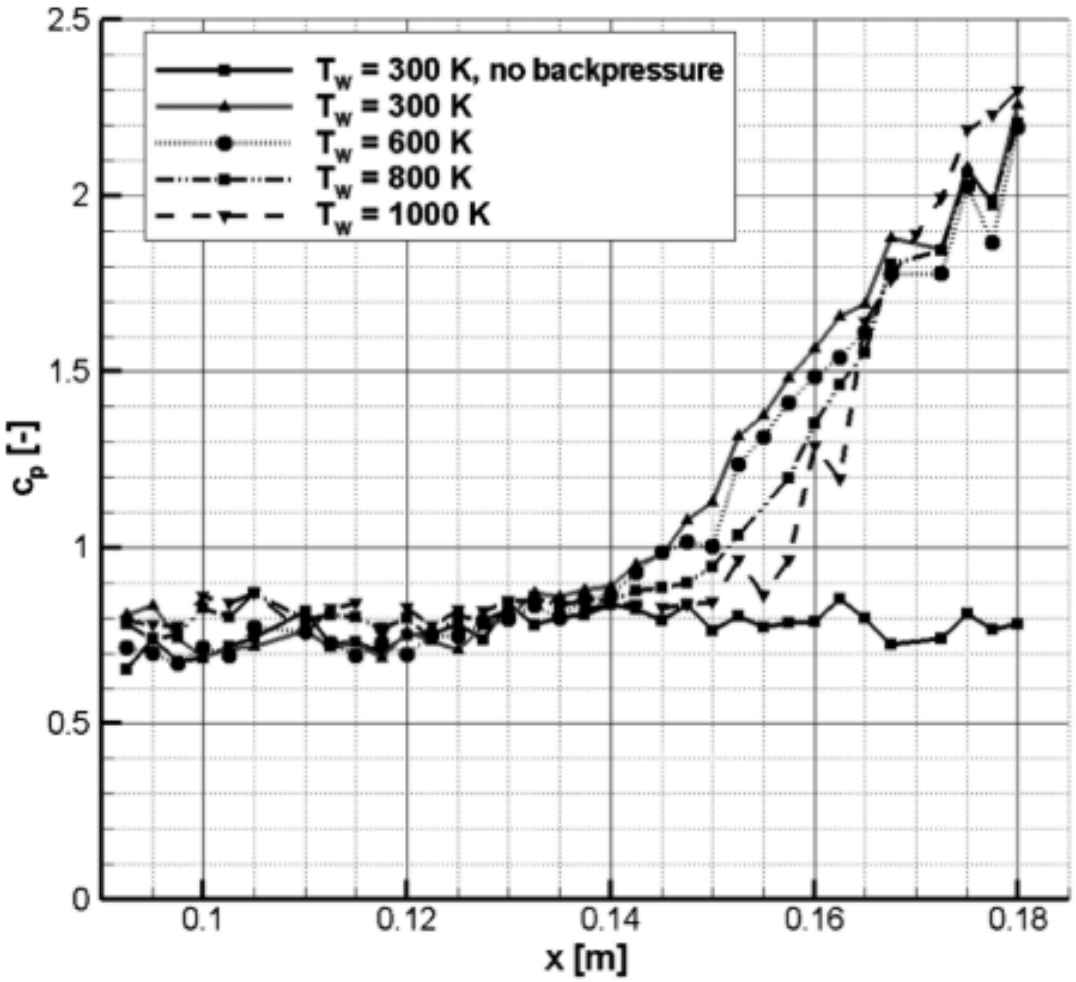


Figure 2-18: Influence of wall temperature on shock train length. Reproduced from [67]

The experimental literature shows the sensitivity of the isolator flow to both upstream and downstream influences. It is thus imperative that modelling of the important parameters of the isolator are modelled, to reduce the requirement of experimental studies.

2.3.2. Modelling of Isolators and Pseudo-shock systems

Evidently, the pseudo-shock train region is a highly complicated system of viscous-inviscid interactions; simplification of such a system requires a number of assumptions to be made about the dimensionality of the flow as well as the geometry it is applicable to. Thus, the majority of models derived assume the system to be one dimensional or quasi-1D and the duct to be of constant area. Matsuo et al [66] provided a review of the analytical models developed as well as experimental studies performed to validate the various models. Gnani et al.[68] present an updated review of shock train modelling approaches.

The models make no attempt to fully define the pseudo-shock train flow field, as the number of variables that would contribute to such an endeavour makes it extremely challenging. Thus, the modelling of such systems is centred around the prediction of the length required to achieve a desired pressure increase within the isolator.

One of the first models proposed for estimating the length of the isolator was the "shockless model" by Crocco[61]. He postulated that the total entropy change within a system of oblique shocks would be much less than that across a normal shock. The basis of this postulation was that the main dissipative mechanism of the pseudo-shock train was not the shock themselves, but the turbulence generated near the walls, called the dissipative region. With these assumptions, he further proposed that at the limiting case, the shocks can be fully disregarded and be substituted by an isentropic uniform supersonic core region surrounded by a uniform subsonic dissipative region near the wall. These regions were initialised at section 1 in Figure 2-19 with appropriate averaged values, and the length of the pseudo-shock is taken to be the point where the core fully merges with the dissipative region and the outflow is subsonic. Neglecting the wall friction, which results in constant total enthalpy and temperature, the resulting pressure increase at a given downstream region is:

$$\frac{p}{p_1} = \left(\frac{1 - w'^2}{1 - w_1^2}\right)^{\frac{\gamma}{\gamma-1}} \tag{2.20}$$

The quantity "w" represents the Crocco number which is given by:

$$w = \frac{u}{\sqrt{2C_pT_0}} \tag{2.21}$$

with the single prime quantity being found in the supersonic core. Figure 2-19 presents a schematic of the flow, with quantities "p" and "m" representing the pressure and mass flow rate at the current region. Equation 2.20 above is solved along with conservation equations to obtain a value of the downstream length where the two cores mix. The double prime quantities represent properties in the subsonic dissipative region.

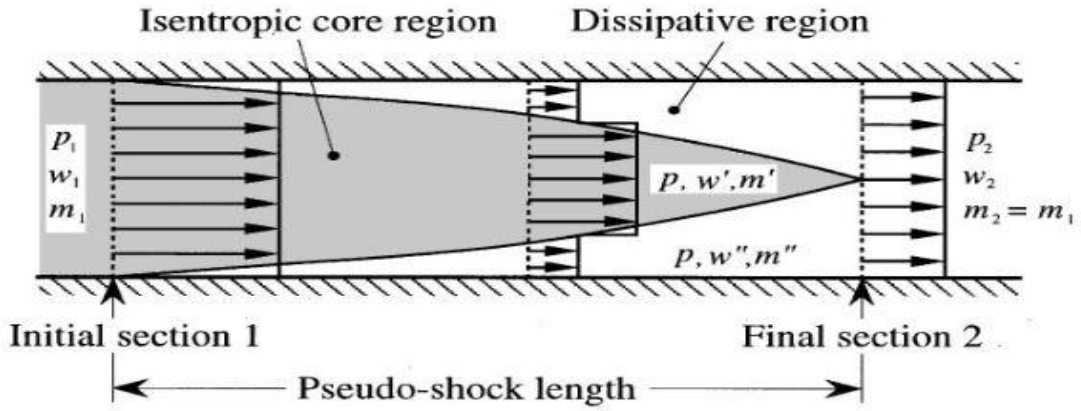


Figure 2-19: Shockless model by Crocco. Reproduced from [68]

A model which builds upon the model of Crocco was proposed by Ikui et al.[69]. This new model, named "diffusion model", removes the assumption of isentropic flow made by the "shockless" model as well as the assumption made that the core flow mass flow rate vanishes at the end point. A representation of the diffusion model is shown in Figure 2-20.

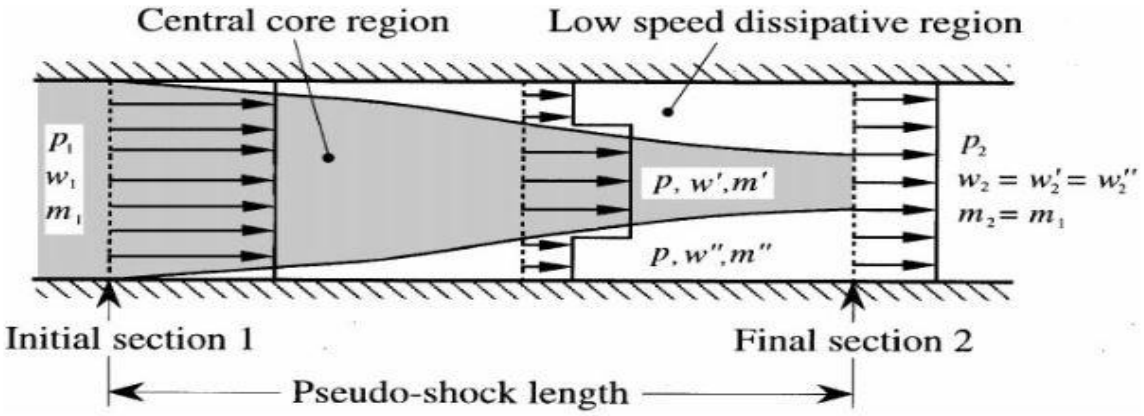


Figure 2-20: Original diffusion model by Ikui. Reproduced from [68]

As the latter was used to terminate the calculation, Ikui et al. [69] estimated the length of the pseudo-shock by determining the point where w' equals w'', or where the Crocco parameter of the core equals that of the diffusive core. Similar to the Crocco model, the upstream mass flow rate m_1 is purely supersonic.

The flow enters at state 1 and eventually diffuses to a uniform subsonic flow at state 2. The analytical expression for the pressure rise along the streamwise direction is described by:

$$\frac{p - p_1}{p_2 - p_1} = \frac{\left[w_1^2(w_1^2 - 2w^{*2}) + w_1^2 w^{*2} e^{-c\frac{x}{D}}\right]\left(1 - e^{-c\frac{x}{D}}\right)}{(w_1^2 - w^{*2})^2 - w_1^2(w_1^2 - w^{*2})e^{-c\frac{x}{D}}\left(1 - e^{-c\frac{x}{D}}\right)} \quad 2.22$$

The quantity "w*" is the Crocco number at sonic speed, D is the duct diameter, and x is the distance along the isolator, while the constant "c" was experimentally determined to have a value of 0.114 and it is determined by the deceleration of the core flow in the streamwise direction:

$$\frac{dw'}{dx} = -cw' \quad 2.23$$

The Ikui diffusion model correlates well with high upstream Mach number experimental data, however less satisfactory agreement is seen with lower upstream Mach numbers, as demonstrated against experimental results in Figure 2-21. The reason is attributed to the less diffusive nature of lower Mach numbers, which deviates from the basic assumptions of uniform upstream and downstream flows.

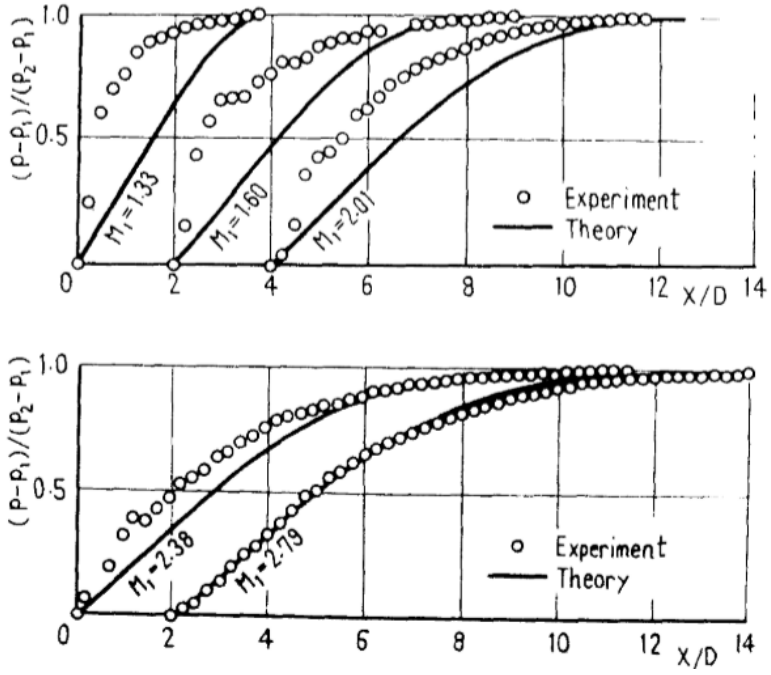


Figure 2-21: Prediction of shock train by Ikui diffusion model (line) against experimental (dot) data at different upstream Mach numbers. Reproduced from [69].

Ikui et al.[70] subsequently updated their original model to include the upstream boundary layer as an influence on the pseudo-shock behaviour. Their original model as well as the model of Crocco ignore the influence of the incoming boundary layer. Their updated model is schematically represented by Figure 2-22 below.

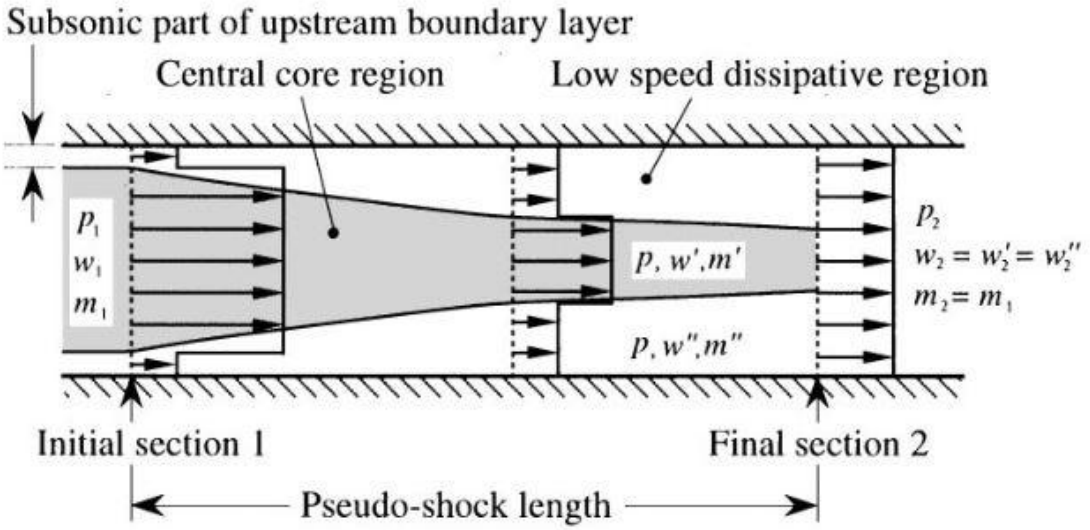


Figure 2-22: Modified diffusion model by Ikui. Reproduced from [68]

The variables in Figure 2-22 have the same meaning as the previous models. One of the significant changes made to the updated model by Ikui et al., unlike the Crocco and their original model, the incoming mass flow rate m_1 is not purely supersonic but contains a subsonic element.

A more advanced methodology in solving isolator flowfields is the 1D flux conservation model, first proposed by Smart[71] and then modified by Fievet[72] and more recently, by Edelman[73], [74]. They are a derivative of Crocco's shockless model but use a system of ODEs to describe the evolution of the supersonic core.

The two methods differ in various ways. Crocco's model uses a two-stream formulation (supersonic core and subsonic dissipative region), whereas Smart's model replaces this by a stream thrust averaged, single flow. The two methods utilise the same physical method for compression, diffusion, but apply it differently in the evolution of the flow. Since Crocco's model uses the true properties of the flow, it models the loss of flow momentum of the core to the boundary layer through mass entrainment. Smart's model uses flux conserved properties and hence models the pressure rise using the empirical relation of Ortwerth, which links the pressure gradient to the skin friction coefficient.

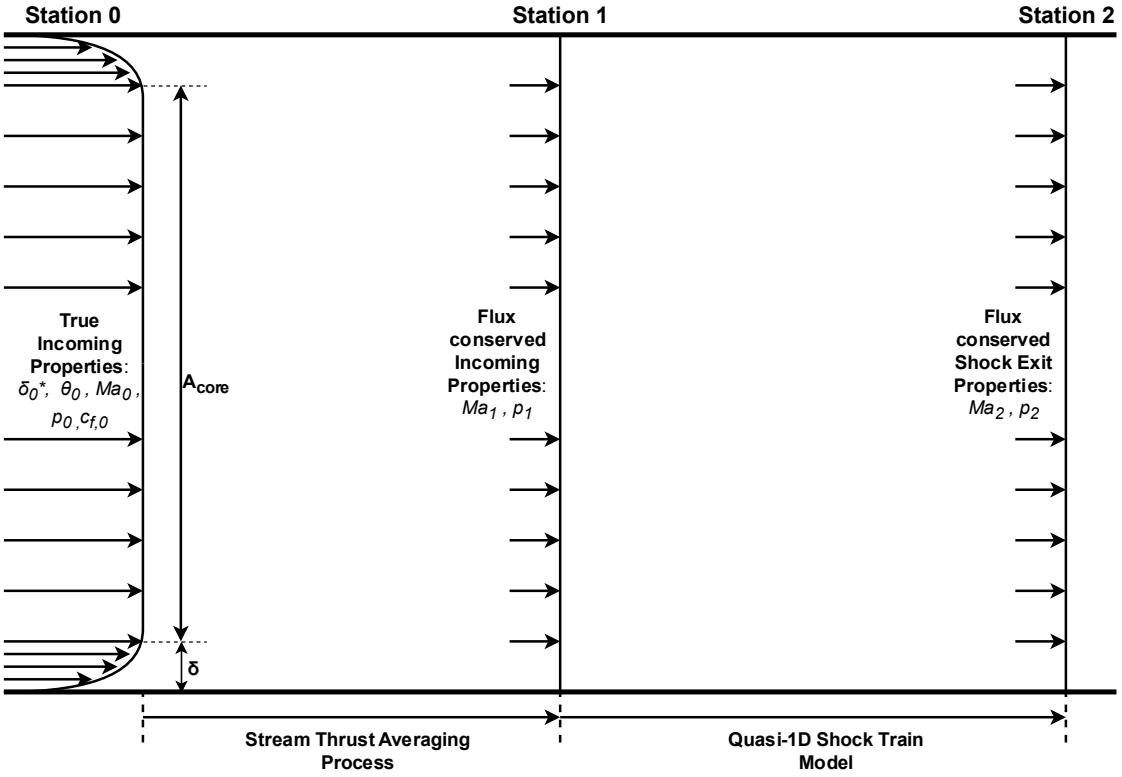


Figure 2-23: Modelling approach for flux-conserved models. Stream thrust averaging uses McLafferty's method.

The core principle behind this model is that the pseudo-shock train is replaced by a supersonic core surrounded by a region of separated flow. Thus, all mass flow is concentrated in the supersonic core, which has an area A_c. The models solve three coupled ODEs for the conservation of mass, momentum and energy in the core, predicting the change in the core area, Mach number and total temperature (if non-adiabatic). In the case of adiabatic flow, the total temperature derivative is set to zero.

$$\frac{d\left({}^{A_c}/_{A}\right)}{{}^{A_c}/_{A}} = \frac{1 - Ma^2\left(1 - \gamma\left(1 - {}^{A_c}/_{A}\right)\right)}{\gamma Ma^2\, {}^{A_c}/_{A}}\frac{dP}{P} + \frac{1 + (\gamma - 1)Ma^2}{2\, {}^{A_c}/_{A}} 4C_f \frac{dx}{D_h} + \left(1 + \frac{\gamma - 1}{2} Ma^2\right)\frac{dT_{tot}}{T_{tot}} \tag{2.24}$$

$$\frac{dMa^2}{Ma^2} = -\left(1 + \frac{\gamma - 1}{2} Ma^2\right)\left(\frac{2}{\gamma Ma^2}\frac{A}{A_c}\frac{dP}{P} + \frac{A}{A_c}\frac{4C_f dx}{D_h} + \frac{dT_{tot}}{T_{tot}}\right) \tag{2.25}$$

$$\frac{dT_{tot}}{T_{tot}} = \frac{dQ + dH_r}{c_p T} \tag{2.26}$$

Closure to the system of equations is required for the pressure gradient in the shock train, *dp/dx*. As previously mentioned, the physical mechanism behind the pressure rise is the diffusion of energy from the supersonic core to the boundary layer. In the absence of the physical boundary layer (due to flux conservation), the conversion of kinetic energy to pressure require an empirical closure as opposed to the modelling of the physical mechanism.

All models adopt Ortwerth's diffusion model[75], which connects the pressure rise in the shock system to the conversion of kinetic energy to pressure through coefficient, *k*. The diffusion model's assumption is that the compression of the flow in the shock train is transferred to the wall through diffusion, which also limits the compression that can be sustained. The version of the model used by Smart is the default model, while Fievet and Edelman have modified the model with additional coefficient obtained through data-driven optimisation:

Original/Smart:

$$\frac{dP}{dx} = \frac{qk_{ref}}{D_h} c_{f,0} \tag{2.27}$$

Fievet/Edelman:

$$\frac{dP}{dx} = \frac{qk_{Fievet}}{D_h} {c_{f,0}}^{\alpha} \sigma^{\beta} \tag{2.28}$$

$$k_{Fievet} = \frac{k_{ref}\left(a_1 + \frac{q(x)}{q_0}\right)^{\kappa}}{\int_0^1 (a_1 + y)^{\kappa} dy} \tag{2.29}$$

$$\kappa = b_1\left(1 - \tanh\left(c_1\left[Ma_{ref} - Ma_1\right]\right)\right) \tag{2.30}$$

$$C_f = dC_{f,0} + e \tag{2.31}$$

Where σ is the static pressure recovery ratio between the shock train and a normal shock with the same incoming properties. Fievet uses a fixed value of 0.796, while Edelman solves the original equations by McLafferty to change the coefficient based on the incoming flow. The constants α, β, a_1, b_1, d and e are found using data analysis of experiments and take different values between Fievet and Edelman.

The solution of these solvers is universally done through flux conserved properties. The change from true to flux conserved flowfields is done using the method proposed by McLafferty[76]. The incoming true core Mach number and pressure are converted into their flux conserved counterparts using the set of equations below. The terms $\bar{A}_{\delta^*}$ and $\bar{A}_{\theta}$ are the blockage areas due

to the total displacement and momentum thicknesses respectively, defined as $\bar{A}_{\delta^*} = \frac{W\delta^*_{tot}}{A}$ and $\bar{A}_{\theta} = \frac{W\theta_{tot}}{A}$. A schematic of the process is provided in Figure 2-23.

$$F = P_0 A\left(1 + \gamma Ma_0^2(1 - \bar{A}_{\delta^*} - \bar{A}_{\theta})\right) \quad 2.32$$

$$\dot{m}_{core} = P_0 A Ma_0 \sqrt{\frac{\gamma}{RT}}(1 - \bar{A}_{\delta^*}) \quad 2.33$$

$$U_1 = \frac{\gamma}{\gamma+1}\frac{F}{\dot{m}_{core}} + \sqrt{\left(\frac{\gamma}{\gamma+1}\frac{F}{\dot{m}_{core}}\right)^2 - \frac{2\gamma R T_{tot}}{\gamma+1}} \quad 2.34$$

$$Ma_1 = \frac{U_1}{\sqrt{\gamma R\left(T_{tot} - \frac{U_1^2}{2R}\left(1 - \frac{1}{\gamma}\right)\right)}} \quad 2.35$$

$$P_1 = \frac{F}{A} - \frac{\dot{m}_{core} U_1}{A} \quad 2.36$$

The solvers are solved using forward Euler marching and termination of the model occurs when the area ratio reaches unity, ${}^{A_c}/_{A} = 1$.

All models have the drawback of being unable to explicitly provide the length of isolator required. To that extend, Waltrup et al.[77] developed a relation between various upstream parameters that relate the length of isolator required for a given pressure rise in circular ducts. The relation is:

$$\frac{L_S(Ma_1^2 - 1)Re_\theta^{\frac{1}{4}}}{D^{\frac{1}{2}}\theta^{\frac{1}{2}}} = 50\left(\frac{P}{P_1} - 1\right) + 170\left(\frac{P}{P_1} - 1\right)^2 \quad 2.37$$

With L_s being the length required for the pressure rise P/P_1, D the hydraulic diameter of the circular duct, θ is the momentum thickness and Re_θ is the Reynolds number based on momentum thickness. Billig[78] modified the above equation for use in rectangular ducts by replacing the hydraulic diameter, D, with the duct height, H and changing the momentum thickness Reynolds number index to 1/5.

It is evident from the geometry of most intakes that the flow compressed along the compression ramps will enter the isolator with boundary layer properties very different to the ones from the boundary layer developed along the cowl side. This introduces flow asymmetry to the isolator. Further modification to the Waltrup correlation was done by Wang et al., who introduced an additional term meant to compensate for the asymmetry of the flow entering the isolator. The

modified Wang et al. equation introduces "D_θ", which is calculated using the upper and lower wall momentum boundary layer thicknesses using:

$$D_\theta = \frac{\theta_{max} - \theta_{min}}{\theta_{max}} * 100 \quad 2.38$$

And then used in the modified equation:

$$\frac{L_S(Ma_1^2 - 1)Re_\theta^{\frac{1}{4}}}{(1 + D_\theta)^\beta H^{\frac{1}{2}}\theta^{\frac{1}{2}}} = 50\left(\frac{P}{P_1} - 1\right) + 170\left(\frac{P}{P_1} - 1\right)^2 \quad 2.39$$

where β is experiment specific. While the value will inevitably change from experiment to experiment, or even flight to flight, it provides an indication that the asymmetry of the flow within the isolator influences the overall shock train length.

Other correlations have used the Waltrup correlation as their starting point to include more effects that the original does not capture. The correlation developed by Fischer and Olivier[67] modified the original to include the effects of temperature on the development of the shock train. Their modification is done on the momentum thickness term of the equation. Two correlations (equations 2.40 and 2.41) are presented for low enthalpy with high Mach numbers, the normalised shock train length, s_T is:

$$\frac{s_T}{L} = A\left(\frac{P_2}{P_1} - 1\right) \quad 2.40$$

And for high enthalpy as well as low Mach numbers with low enthalpy:

$$\frac{s_T}{L} = A\left(50\left(\frac{P_2}{P_1} - 1\right) + 170\left(\frac{P_2}{P_1} - 1\right)^2\right) \quad 2.41$$

Where L is the length of the isolator duct and A is a coefficient found by solving equation 2.42 for a constant duct height, Mach number and Reynolds number:

$$\frac{A}{\left[\left(\frac{q_w A_w}{\dot{m} c_p T_t}\right)^{0.8} + b\left(\frac{2\theta_2}{h}\right)^{1.07}\right]^{0.23}} = \frac{A}{C} = const \quad 2.42$$

Where q_w, A_w, $\dot{m}$, T_t, θ_2 and h represent the heat flux, wetted isolator area, mass flow rate through the isolator, total temperature and momentum thickness at the exit plane of the isolator and isolator height respectively. The momentum thickness is found using the reference temperature method.

However, the authors specify that this correlation has only been validated for the range described in their study, which is rather limited. Additional difficulties arise from the need to calculate the momentum thickness at the isolator exit instead of the inlet as used by the original equation.

A set of different correlations was developed by Byun et al.[79] for a dual combustion scramjet. Their correlations considered the effects of equivalence ratio on both the total length of the shock train and the length of the shock train extending into the main combustor, diagrammatically shown in Figure 2-24.

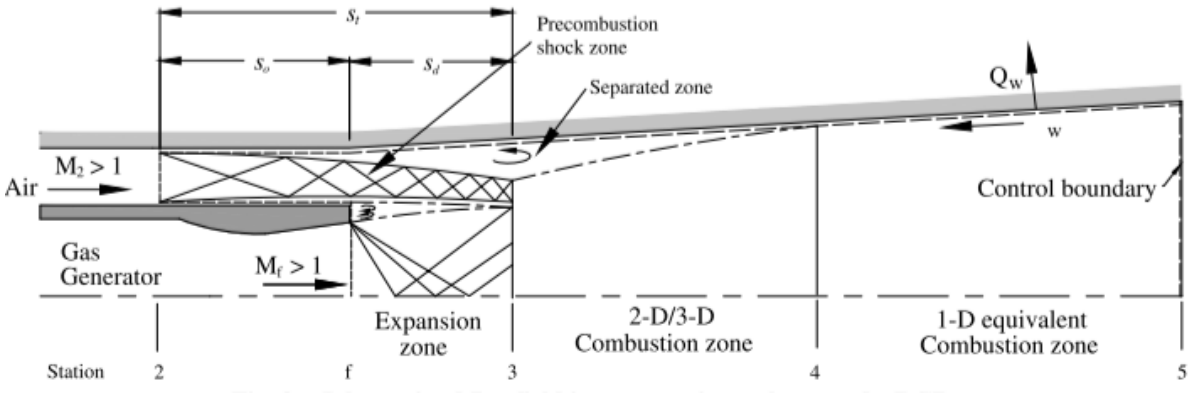


Figure 2-24: Schematic of dual combustion scramjet experimentally tested by Byun et al. Reproduced from [79]

Their correlations were obtained through data fitting of the results obtained in an annular combustor with two fuel equivalence ratios, φ_t and φ_{gg}, which represent the fuel equivalence ratio for combustor and gas generator respective and only for limited isolator entry Mach numbers, and they have not seen use in the literature for designing of isolators. Their correlations for total shock length, s_t and combustor shock length, s_{comb} are given by:

$$\varphi_t^{0.52}\left(\frac{D_h}{s_t}\right)\left(\frac{M_1^2-1}{M_1^2}\right)Re_\theta^{0.25}\left(\frac{D_h}{\theta}\right)^{0.5} = 1.35\left(\frac{P}{P_1}-1\right)+1.45\left(\frac{P}{P_1}-1\right)^2 \qquad 2.43$$

$$\varphi_t^{0.52}\left(\frac{D_h}{s_{comb}}\right)\left(\frac{Ma_1^2-1}{Ma_1^2}\right)Re_\theta^{0.25}\left(\frac{D_h}{\theta}\right)^{0.5} = \left(\frac{P}{P_1}-1\right)^{3.3} \qquad 2.44$$

with s_t, s_{comb}, D_h and φ_t being the total precombustion shock train length, shock train length extending in the combustor, hydraulic diameter and combustor equivalence ratio.

Ortwerth [80], [81], similar to Waltrup and Billig, developed an analytical function for the isolator length based on the pressure ratio across it (Equation 2.45). This semi-empirical

relation does not explicitly consider the incoming boundary layer like the Waltrup and Billig function. The influence of the boundary layer is included within the skin friction coefficient at the isolator entry only.

$$L_S = \frac{D_h g_2^2}{4K\gamma f_2}\left[\frac{{}^{P_3}/_{P_2} - 1}{\left(f_2 - {}^{P_3}/_{P_2}\right)(f_2 - 1)} + \frac{1}{f_1}\ln\frac{{}^{P_3}/_{P_2}(f_2 - 1)}{\left(f_2 - {}^{P_3}/_{P_2}\right)}\right] + \frac{\gamma - 1}{2\gamma}\ln\frac{P_3}{P_2} \qquad 2.45$$

Where 4K = 44.5c_f, $f_2 = \frac{p_2A_2 + \rho_2 u_2 A_2}{p_2 A_2}$, $g_2 = \frac{\dot{m}\sqrt{(\gamma-1)H_t}}{p_2 A_2}$ and H_t is the stagnation enthalpy. Subscripts 2 and 3 represent isolator entry and exit respectively.

The Mach number after a shock train would be difficult to estimate across the shock train for scramjets, as the flow does not decelerate to subsonic speeds. Lin et al.[82] correlated the centreline exit Mach number to the pressure ratio across the shock train using experimental data. For rectangular ducts, the correlation is:

$$\frac{M_{CL}}{M_0} = -1.17M_0^{-2.40}\left(\frac{P_3}{P_2}\right) + 1.78M_0^{-0.64} \qquad 2.46$$

And for circular ducts:

$$\frac{M_{CL}}{M_0} = -0.94M_0^{-2.20}\left(\frac{P_3}{P_2}\right) + 1.60M_0^{-0.48} \qquad 2.47$$

The current literature on isolators treats it as a standalone component. The most prominent correlation, that of Waltrup, assumes uniform flow entering the isolator, which is not representative of operating conditions of a scramjet. Attempts to extend it have been partially successful, and viscous elements are only accounted by the presence of the momentum thickness. Linking the intake and isolator and coupling the performance should prove beneficial to designers.

2.4. Chapter Summary

Currently, state of the art models tend to treat the intake and isolator as two independent components, usually optimising or predicting the flow of one without considering the other. This leads to optimisations that use inviscid analytical/low fidelity methods, or optimisation through CFD. The former ignores viscous dynamics, which as seen in the literature have significant effects on the overall flow field. The latter, captures the viscous effects that arise on both intake and isolator and thus provide optimised configurations with these effects already accounted for. However, this comes with a high computational cost, especially with hypersonic

flows, as each new iteration must be solved numerically to extract the required data. Based on the above observations, a blending of the two techniques would be highly beneficial to modelling of intake-isolator configurations.

Based on the above observations, this research aims to achieve the following:

1. *Construct a low-order intake-isolator model that includes viscous elements, to address the shortcomings of current low order models that assume inviscid conditions.*
2. *Provide optimised configurations for rectangular hypersonic intakes based on a variety of criteria for performance and safety to aid in the preliminary design process.*
3. *Investigate the effects of design parameters to the performance of intake and the variance of geometry.*

To that end, a reduced-order model is developed to incorporate hypersonic boundary-layer development, shock–turbulent boundary-layer interactions, and isolator effects. The resulting framework combines analytical formulations with low-order numerical methods to provide rapid evaluation of configurations, suitable for optimisation. Global optimisation techniques can be implemented to such a model with relative ease. The results of optimisation can then be further investigated using high fidelity methods.

Global optimisation, constraints and high-fidelity numerical methods are presented in the next chapter.

Chapter 3 - Modelling Strategy (PSO and CFD)

The current work aims to produce a combined intake-isolator model that is used to compliment high-fidelity numerical methods and can be utilised for preliminary design purposes. As important as the models themselves, is the strategy used during modelling and the method of optimisation used. To validate/verify the proposed model, higher fidelity methods are employed.

3.1. Modelling strategy and Optimisation

The intake and isolator are coupled as explored in the previous chapter. While many modelling approaches were suggested and developed by researchers, none have developed a low-order, rapid execution method that includes viscous elements. This research aims to address the above requirements through development of a low order model by coupling various sub models together along the flow direction up to the combustor entry. A more rudimentary combustor/nozzle model is introduced to complete the engine cycle.

A generic schematic of the overall algorithm is shown in Figure 3-1.The current approach does not require a starting geometry to work, contrary to the methods developed by de Vanna et al.[59], Brahmachary, Fujio and Ogawa [58], DiGregorio et al. [57] and Kline et al. [60], as all geometric parameters are determined by the algorithm. This removes the need for an initial guess on any geometric parameters, which would limit the configuration. As this is a fully low order method, removing the need for CFD significantly accelerates the determination of optimum configurations, and thus can be run for multiple flight conditions and ramp systems.

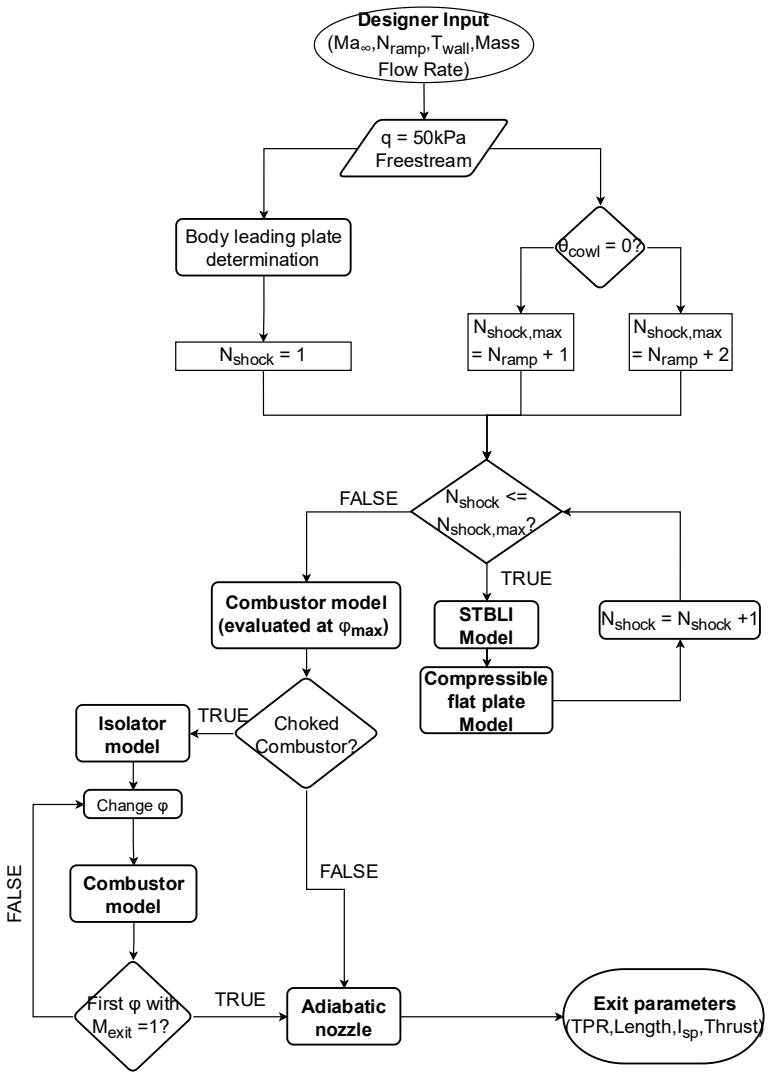


Figure 3-1: General schematic of the overall modelling approach, with the individual sub-models shown and the way they interact with each other

The global model implemented in this work is presented schematically in Figure 3-1, and is composed of three sub-models, executed streamwise along the engine. The process begins with the designer-defined inputs, namely the freestream Mach number, ramp configuration, wall temperature, and required 3D mass flow rate to be captured by the engine. Together with the fixed dynamic pressure of 50 kPa, the body leading plate and initial flow conditions are established and the maximum number of external shocks, $N_{\text{shock,max}}$, is determined based on the number of external ramps and cowl angle. The dynamic pressure is selected based on structural and operational limits[83]. A trajectory with dynamic pressure below 24 kPa results in insufficient pressure for compression and lift, whereas one with a dynamic pressure above 72

kPa imposes severe structural loads. Therefore, a trajectory an intermediate dynamic pressure of 50 kPa is selected.

For each ramp surface, the compressible turbulent boundary layer flat plate model described in Chapter 4 is applied to determine local boundary-layer properties. This model employs a compressibility correction to a universal turbulent velocity profile, supplemented by semi-empirical relations, to predict boundary-layer thickness, skin friction, and related quantities along the external compression surfaces. Where shocks are generated by ramps or the cowl, this solution is coupled with the Shock–Turbulent Boundary-Layer Interaction (STBLI) model introduced in Chapter 5, as shown in Figure 3-1. The incoming boundary-layer profile at the shock foot is discretised into multiple strata and inviscid shock relations are applied to each stratum to predict the shock trajectory within the boundary layer and downstream boundary-layer state. In addition, the model determines the skin-friction coefficient and boundary-layer properties at the location of zero pressure gradient following the interaction. This approach encapsulates the complex physics of the interaction within a reduced-order formulation, treating them as a 'black box', significantly speeding up and simplifying the interaction, enabling efficient iteration over successive shocks, as reflected by the loop on the shock index N_{shock}in Figure 3-1.

Once the maximum number of external shocks ($N_{\text{shock, max}}$) has been reached, based on the ramp configuration and cowl geometry, the methodology transitions to the internal flowpath model and the isolator-combustor-nozzle model put forth in Chapter 6. Based on the condition at the combustor exit, the internal modelling approach is altered, seen from the branching in Figure 3-1. In the case of a choked combustor, reflecting dual-mode scramjet operation, an isolator is required, and is modelled through the Waltrup-Billig relation[77][78]. The momentum thickness is evaluated at isolator entry. For both conditions, combustion is modelled as an adiabatic heat release process resulting from fuel addition at a prescribed equivalence ratio, φ. The nozzle is modelled as an imperfect adiabatic expansion process. The final output of the methodology consists of the engine exit flow conditions and integral performance metrics, including total pressure ratio, engine length, specific impulse, and specific thrust.

The combination of these models allows for an improvement on the inviscid models on the external compression system, such as the ones used by Verma et al. [51] and Cakir et al. [54]. Taken together, this structured framework extends classical inviscid external compression

methodologies. It explicitly incorporates turbulent boundary layer development and shock–boundary layer interaction effects, while retaining the computational efficiency implied by the reduced-order structure of the model.

The inputs to the optimisation routine are minimal, only requiring the flight Mach number, external wall temperature, number of ramps for the external compression system and the required mass flow rate to be captured. These are variables are basic design parameters that a designer would have access to during the preliminary process without requiring more specialised calculations.

The objective functions selected to be optimised for are the Total Pressure Recovery/Ratio (TPR), overall length of intake/isolator combination (L_{config}) and the engine specific thrust, $F_{specific}$. The total pressure ratio was selected to represent the losses incurred due to the presence of the ramps. Also, as per de Vanna [59], using TPR represents the drag force of the engine as well. This parameter must be maximised, which represents minimum losses, both viscous and mechanical. The length of the intake/isolator pairing is minimised, which shortens and thus lightens the overall engine configuration. The engine specific thrust, $F_{specific}$, is to be maximised, which shows the thrust capable of being produced, and can be considered as an efficiency metric, independent of the mass flow rate required of the engine. Also, it is obtained by also considering various thermodynamic losses, wrapped in U_{10}, thus gives a metric of the thermodynamic efficiency of the engine.

The optimisation functions for TPR, engine specific thrust and length are given by:

1. $\max\left(TPR = \prod_{i=1}^{N}\left[\frac{(\gamma+1)Ma_{i-1}^2\sin^2(\beta_i)}{(\gamma-1)Ma_{i-1}^2\sin^2(\beta_i)+2}\right]^{\frac{\gamma}{\gamma-1}}\left[\frac{(\gamma+1)}{2\gamma Ma_{i-1}^2\sin^2(\beta_i)-(\gamma-1)}\right]^{\frac{1}{\gamma-1}}\right)$
2. $\max(F_{specific} = (1 + \varphi_{fuel}f_{stoichio})U_{10} - U_0)$
3. $\min(L_{config})$

where N is the number of shocks present before the isolator entry, Ma is the Mach number before the i^{th} shock, β is the shock angle of the i^{th} shock, φ_{fuel} is the fuel/air equivalence ratio, $f_{stoichio}$ is the stoichiometric fuel/air combustion ratio and U is the flow velocity.

As part of the optimisation routine, the valid configurations must satisfy a series of constraints. The constraints include geometric considerations, unstart prevention and performance constraints. They are dynamically evaluated during the global model execution to terminate the configuration early if it is found to be undesirable, further speeding up optimisation.

The first category concerns geometric considerations. The first constraint requires all compression angles being successively larger, producing a compressive shock. Secondly, the cowl closure angle (angle from the horizontal) is less than the sum of all compression angles, resulting in a cowl tip shock being generated. Thirdly, cowl tip and cowl spike shocks converge on the boundary layer before the ramp shoulder. This satisfies the shock-on-shoulder condition, which eliminates the reflected shocks and expansion fan from the corner, but also allows for the shock to penetrate into the boundary layer without the creation of an expansion fan. This creates an additional constraint, which is that the boundary layer impingement location of the cowl tip shock must be upstream of the impingement location of the cowl spike shock. The constraints are illustrated in Figure 3-2 below. As evaluated during execution (constraint functions), they are represented in the following manner:

1. $\theta_1 < \theta_2 < \cdots < \theta_n$
2. $\theta_{cowl} < \theta_n$
3. $x_{cowl-impinge} < x_{spike-impinge}$
4. $x_{spike-impinge} < x_{shoulder}$

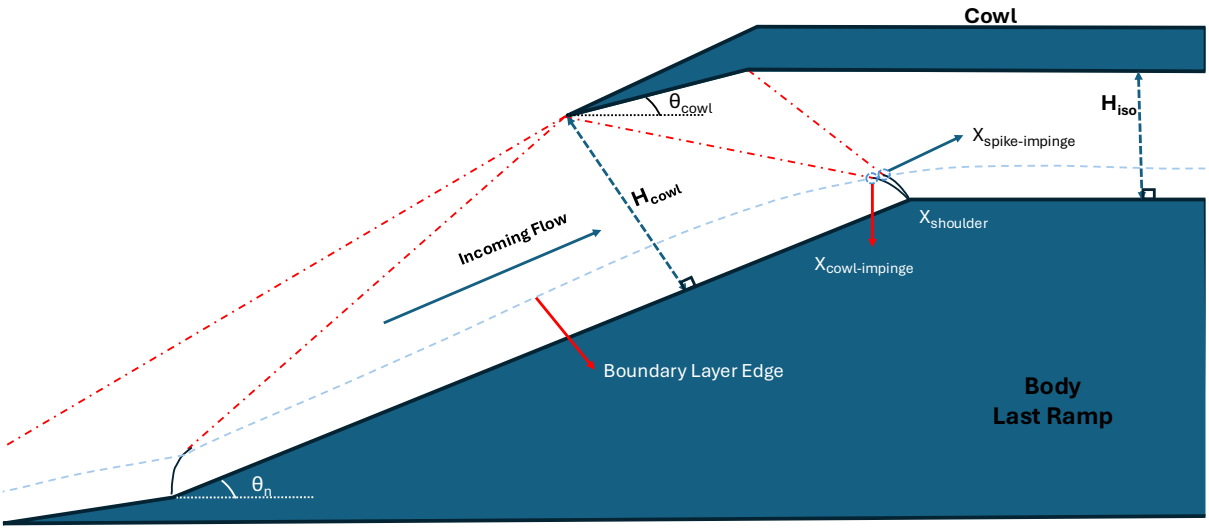


Figure 3-2: Illustration of geometric constraints 1-4. This configuration represents the ideal case for a mixed compression intake, with shocks from ramps impinging on the cowl tip and cowl shocks impinging (after boundary layer effects) on the ramp shoulder

The second category concerns the safe operation of the engine. To achieve safe operation, the engine must stay in its started configuration. From the previous discussion in Chapter 2, the internal contraction ratio plays a vital role in unstart prevention and must be maintained above a certain limit. In this work, the criterion chosen is that of Flock and Gulhan [34]. This ensures

that the intake always operates in the self-starting region. From Figure 3-2 above, the internal contraction ratio would be the ratio H_{iso}/H_{cowl}.

Additional constraints are added to each shock-boundary layer interaction, to ensure severe flow separation is avoided. As it was seen from various researchers[10], [24], severe flow separation on the ramps, but especially in the ramp shoulder can cause sufficient flow blockage that the intake enters unstart. To quantify the separation state and ensure flow attachment or minimal separation, a modified version [84], [85] of the criterion, L^* introduced by Souverein [86] is used. Solutions are only accepted if all shock-boundary layer interactions satisfy the criterion and do not separate or exhibit minimum separation. Non-separated solutions have a value of $L^* < 2$. These are included as additional constraints during optimisation that must be satisfied before a configuration is accepted as viable.

In criterion form:

5. $\frac{H_{iso}}{H_{cowl}} < ICR_{F\&G}(Ma_{closure})$
6. $L^*_{SBLI} < 2$

The last category constraints performance parameters to ensure robust performance of the engine. The first performance related constraint limits the combustor entry (isolator exit if present) temperature of the fuel/air mixture above 900K. This is done to ensure that the hydrogen fuel self-ignites, aiding in more robust combustion. The mixture temperature is obtained as a function of the equivalence ratio, φ[87]:

$$T_{comb,mix} = T_{air} - \frac{0.327\varphi}{1 + 0.327\varphi}\left(T_{air} - T_{fuel}\right) \quad 3.1$$

The fuel temperature is set at 300K.

The second criterion is applied to both dual-mode and pure scramjets but is more relevant to the dual-mode due to the lower flow momentum. This criterion restricts the combustor entry Mach number to be above 1.1. This is done to allow supersonic combustion initially and allow the combustor model to function. In the case where a combustor exit Mach number of 1 is obtained, the solution is rejected, as the engine would be operating in ramjet mode. Expressed in criterion form, these constraints take the form:

7. $T_{comb,mix} \geq 900K$
8. $Ma_{comb,entry} \geq 1.1$

The decision variables that are used within the optimisation routine are the compression angles for the number of compression ramps required, as well as the width-to-cowl ratio, n_{depth}. The design space upper and lower bounds for the variables are shown in Table 3-1 below.

Table 3-1: Decision variables with their bounds used in the optimisation process

Decision variable	**Lower Bound**	**Upper Bound**
$\theta_1, \theta_2, \ldots, \theta_n$	1	15
n_{depth}	0.1	1

To obtain multiple configurations that satisfy the various criteria imposed on the design, a suitable algorithm is required, which has the capability to optimise for multiple objectives, while being computationally efficient and simple to use. For that purpose, the Multi-Objective Particle Swarm Optimisation (MOPSO) algorithm was selected. Besides their simplicity, PSO-based algorithms have been demonstrated to have superior performance in high-speed optimisation applications compared to other optimisation methods. Examples of this are the works of Lee and Kim [88] and Su et al. [89]. The former compares PSO-based methods to Genetic Algorithm-based (GA) methods for thermal radiation analysis, while the latter performs similar comparisons for the optimisation of the glide trajectory of a hypersonic glide vehicle. Both studies have concluded that PSO-based methods show superior performance to GA algorithms, as they require fewer evaluations to converge. While not benchmarking PSO-based algorithms against other optimisation methods, the works of Araujo et al. [50] and Ma et al.[90] show the widespread use of the algorithm in hypersonic engine optimisation problems.

The algorithm is an extension of Particle Swarm Optimisation (PSO), which is a metaheuristic algorithm, inspired by the social behaviour of birds, developed by Kennedy and Eberhart[91]. The original algorithm is only capable of optimising for a single objective. The method used to extend the capability of PSO into its multi-objective form was done by Coello-Coello et al [92], who used the roulette method to select for the global best and mutation for a more even spread of the Pareto front across the possible range of values.

The code used in this research was coded directly in MATLAB version 2024b[93], instead of relying on the software's pre-packaged optimisation application suite. This was done to enable greater flexibility in integration of the optimisation tool with the function to be optimised.

To extend the capability of the MOPSO algorithm to allow for constraints to be taken into account, the value of each particle is only stored as a viable candidate if it satisfies all constraints. Additionally, to reduce computational load, the mutation to allow for values closer to the fringe of the Pareto front to be found has been disabled. This was determined not to have a significant effect, as only the extreme configurations might be affected, which would not be considered by designers due to the extreme variation in the optimisation functions.

The constrained MOPSO (CMOPSO) has been validated against a series of benchmark test cases [94], [95]. The test problems are selected on the basis of being multi-objective (two or more objective functions) and being subject to any number of constraints, to demonstrate the capability of the algorithm in successfully obtaining the Pareto front of such optimisation problems.

The pseudocode for the CMOSPO algorithm is presented below along with the results of the benchmark cases for constrained optimisation. The algorithm was executed with 100 particles over 210 generations, with results presented every 70 generations. The empty black circles represent the Pareto front at the current generation, while the full circles represent the solution obtained from the original sources.

ALGORITHM 1: CMOPSO ALGORITHM

Input: *Objective Functions (OF), constraints (C)*

Output: *Repository of optimum points with OF fitness*

Initialisation phase:
While i ≤ Number of Particles **Do:**
    If particle satisfies constraints, **Then**:
        Evaluate and store fitness of particle for all OF
        Initialise velocity of particle as zero
        Assign particle to *BestPosition* array
        Assign fitness to *BestFitness* array
    End if
End while
Evaluate particle dominance, save non-dominated particles
Search phase:
While gen ≤ Maximum generations **Do:**
    Select global leader particle and fitness

```
14      For j = 1 to Number of Particles Do:
15          While Particle does not satisfy constraints Do:
16              Update particle velocity
17              Update particle position
18              If particle satisfies constraints, Then:
19                  Evaluate and store fitness of particle for all OF
20                  Update particle in corresponding Position array index
21                  Update fitness in corresponding Fitness array index
22                  Update velocity in corresponding Velocity array index
23              End if
24          End While
25      Update Repository
26      Update particle best position and fitness
27      Evaluate particle dominance, save non-dominated particles
28  End While
29  Return Repository()
```

Test problem 1: Kita et al [94]

Optimisation functions:

$$\begin{aligned} &\max(f_1(x,y) = -x^2 + y) \\ &\max\left(f_2(x,y) = \frac{1}{2}x^2 + y + 1\right) \end{aligned} \tag{3.2}$$

Subject to the constraints:

$$\begin{aligned} \frac{1}{6}x + y - \frac{13}{2} &\leq 0 \\ \frac{1}{2}x + y - \frac{15}{2} &\leq 0 \\ 5x + y - 30 &\leq 0 \\ x \geq 0\,,\ \ y &\geq 0 \end{aligned} \tag{3.3}$$

The search space is defined as $0 \leq [x, y] \leq 7$.

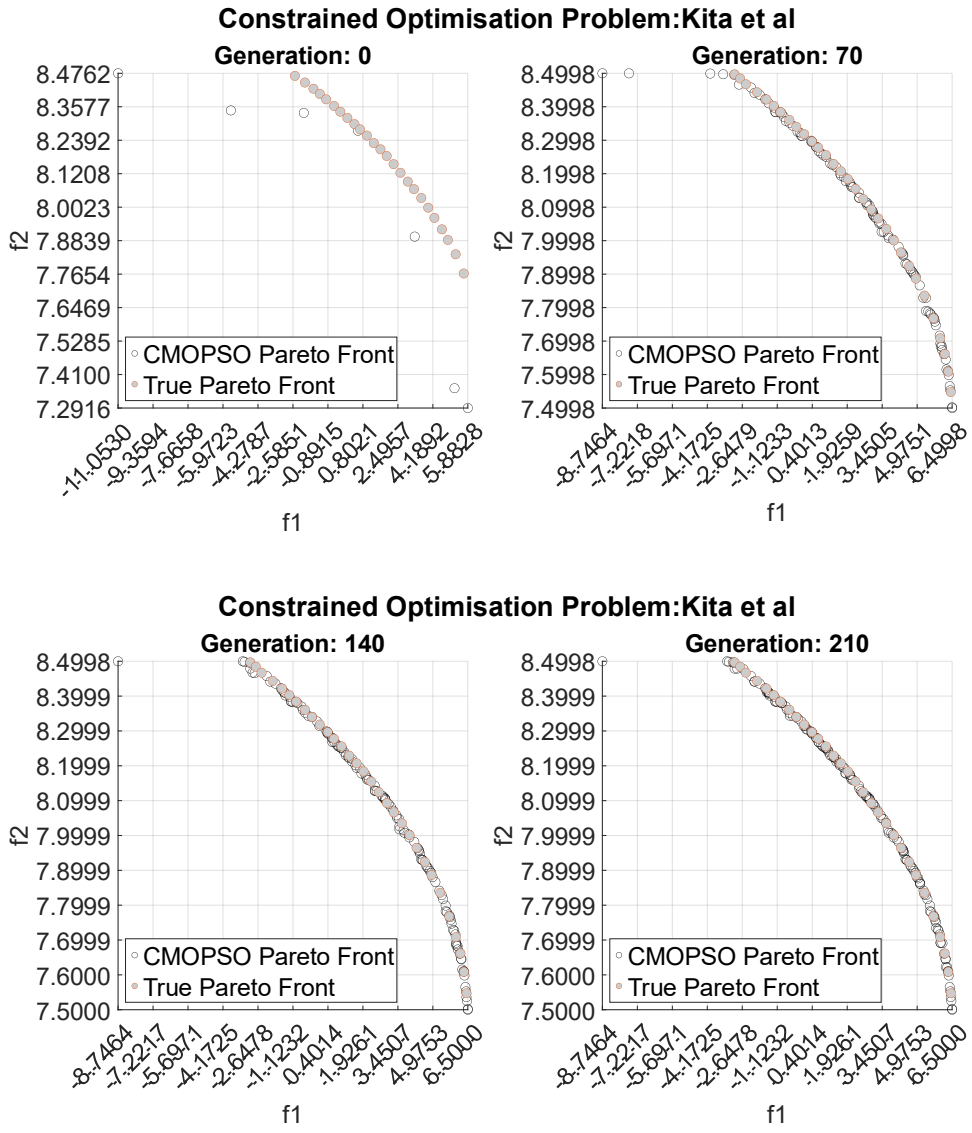


Figure 3-3: Convergence of optimisation algorithm for test case of Kita et al.[94] Top: 0 and 70 generations, Bottom: 140 and 210 generations.

The execution in MATLAB 2024b. requires approximately 10 seconds.

Test problem 2: **Binh and Korn** [95]

Optimisation functions:

$$\begin{aligned} \min(f_1(x,y) = \ 4x^2 + 4y^2) \\ \min(f_2(x,y) = (x-5)^2 + \ (y-5)^2) \end{aligned} \tag{3.4}$$

Subject to the constraints:

$$\begin{aligned} (x-5)^2 + \ y^2 - 25 \ \leq 0 \\ -(x-8)^2 - \ (y+3)^2 + 7.7 \ \leq 0 \end{aligned} \tag{3.5}$$

The search space is defined as -15 ≤ [x, y] ≤ 30.

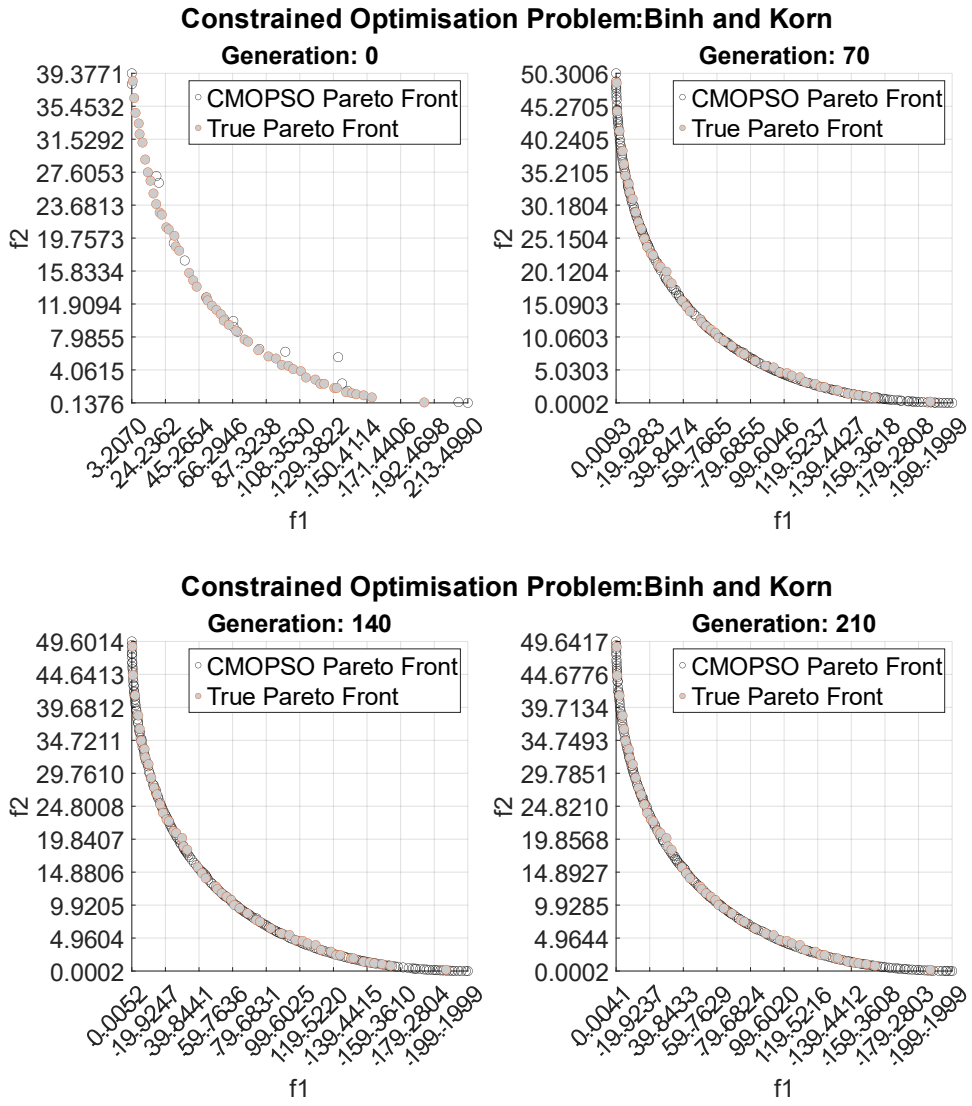


Figure 3-4: Convergence of optimisation algorithm for test case by Binh and Korn[95]. Top: 0 and 70 generations, Bottom: 140 and 210 generations

Execution requires approximately 12 seconds.

To select a representative point from the Pareto front which would provide a balance between the objective functions, the point which has the minimum Euclidean distance after objective function normalisation is selected. For an optimisation based on *n* objective functions, F_1, F_2, …., F_n, the optimum point is selected as follows:

-Objective function normalisation

$$F_{x,norm} = \frac{F_x - min(F_x)}{max(F_x) - min(F_x)} \qquad 3.6$$

-Minimum n-D Euclidean Distance

$$F_{select} = min\left(\sqrt{\sum_{x=1}^{n} F_{x,norm}^2}\right) \quad 3.7$$

It can be seen from both test cases that the global optimisation algorithm selected is able to determine the Pareto front of the given set of functions constrained by a set of equations rapidly and accurately. Therefore, it is deemed suitable for use in the current optimisation problem, which is comprised of a series of objective functions and multiple constrains.

3.2. Computational Fluid Dynamics (CFD)

For verification of the model and the resulting configurations produced through optimisation, the computational fluid dynamics (CFD) open-source package, OpenFOAM [96], is utilised. Several studies have shown the applicability of its density-based solver shockFluid (formerly rhoCentralFoam) for hypersonic flow fields. shockFluid is a segregated solver based on the work of Greenshields et al. [97], and it has been validated over a wide range of high-speed flows [98], [99], [100].

To capture effects such as potential shock instability or unsteady shock movements, the compressible Unsteady Reynolds-Averaged Navier-Stokes (URANS) equations are solved with the four-equation Langtry-Menter k-ω shear stress transport (SSTLM) turbulence closure model [101]. This model is based on the two-equation k-ω shear stress transport (SST) turbulence closure model of Menter [102], but solves an additional two transport equations for transition onset momentum thickness Reynolds number, $Re_{\theta,t}$ and intermittency, γ_{int}. The transition component is less reported in literature, but from the limited investigations by researchers, the SSTLM model provides better prediction of transition, given that the turbulent intensity is properly adjusted [103], [104].

The conservation of mass, momentum and energy are as follows:

Mass conservation:

$$\frac{\partial \bar{\rho}}{\partial t} + \frac{\partial\left(\bar{\rho}\widetilde{U_j}\right)}{\partial x_j} = 0 \quad 3.8$$

Momentum conservation:

$$\frac{\partial\left(\bar{\rho}\widetilde{U_j}\right)}{\partial t} + \frac{\partial\left(\bar{\rho}\widetilde{U_i}\widetilde{U_j}\right)}{\partial x_j} = -\frac{\partial \bar{p}}{\partial x_i} + \frac{\partial}{\partial x_j}\left(2\bar{\mu}\left(S_{ij} - \frac{1}{3}\frac{\partial \widetilde{U_k}}{\partial x_k}\delta_{ij}\right) - \widetilde{\bar{\rho}u_i u_j}\right) \quad 3.9$$

Energy conservation:

$$\frac{\partial(\bar{\rho}\hat{E})}{\partial t} + \frac{\partial(\bar{\rho}\hat{H}\widetilde{U}_j)}{\partial x_j} = \frac{\partial}{\partial x_j}\left[\left(2\bar{\mu}\left(S_{ij} - \frac{1}{3}\frac{\partial \widetilde{U}_k}{\partial x_k}\delta_{ij}\right) - \bar{\rho}\widetilde{u_i''u_j''}\right)\widetilde{U}_i\right] + \frac{\partial}{\partial x_j}\left(\frac{c_p\bar{\mu}}{Pr}\frac{\partial \tilde{T}}{\partial x_j} + \bar{\rho}\frac{c_p\nu_t}{Pr_t}\frac{\partial \tilde{T}}{\partial x_i}\right) \quad 3.10$$

Where:

$$\hat{H} = \tilde{h} + \frac{1}{2}\tilde{u}_k\tilde{u}_k \qquad \hat{E} = \tilde{e} + \frac{1}{2}\tilde{u}_k\tilde{u}_k \qquad k = \frac{1}{2}\widetilde{u_k''u_k''}$$

And ρ, μ, ν_τ, Pr, Pr_τ, p, S_{ij} and c_p being the density, molecular dynamic viscosity, Prandtl number, turbulent Prandtl number, pressure, Reynolds stress tensor and specific heat capacity respectively. The overbar and the tilde denote Reynolds averaging ($\varphi = \bar{\varphi} + \varphi'$) and density-weighted (Favre) averages ($\varphi = \frac{\overline{\rho\varphi}}{\bar{\rho}} + \varphi''$), respectively.

Modelling of the turbulent terms is required, with this work making use of the SSTLM transition model, which is based on the k-ω SST turbulence closure model. The model is based on the Boussinesq hypothesis, which relates the Reynolds shear stresses to the velocity gradient using a fictious quantity, turbulent viscosity μ_T:

$$-\bar{\rho}\widetilde{u_i''u_j''} = \mu_T\frac{\partial U}{\partial y} \quad 3.11$$

Further derivations lead to the expression of the Reynolds stresses as:

$$\tau_{ij} = -\bar{\rho}\widetilde{u_i''u_j''} = \mu_T\left(\frac{\partial \widetilde{U}_i}{\partial x_j} + \frac{\partial \widetilde{U}_j}{\partial x_i} - \frac{2}{3}\frac{\partial \widetilde{U}_k}{\partial x_k}\delta_{ij}\right) - \frac{2}{3}\bar{\rho}k\delta_{ij} \quad 3.12$$

The Kronecker Delta, δ_{ij} , takes a value of 1 for the normal stress component and a 0 for the shear stress component.

The SST model solves two additional transport equations for k and ω, turbulent kinetic energy and specific dissipation rate respectively. The first transport equation is that of turbulent kinetic energy, k:

$$\frac{\partial(\bar{\rho}k)}{\partial t} + \frac{\partial(\bar{\rho}U_i k)}{\partial x_i} = \frac{\partial}{\partial x_j}\left[\left(\mu + \frac{\mu_t}{\sigma_k}\right)\frac{\partial k}{\partial x_j}\right] + P_k - \bar{\rho}\epsilon \quad 3.13$$

Where P_k is the turbulent kinetic energy production term, σ_k is the turbulent Prandtl number and ϵ is the turbulent dissipation rate.

The turbulent dissipation rate is related to the specific dissipation rate through:

$$\epsilon = C_\mu k\omega \tag{3.14}$$

Where C_μ is a constant with a value of 0.09.

The second transport equation is that of specific dissipation rate, ω. For the SST variant of the k-ω family of models, there exists a blending function, F_1 that switches from k-ω close to the wall, to the k-ε model. The transport equation with the blending function is:

$$\frac{\partial(\bar{\rho}\epsilon)}{\partial t} + \frac{\partial(\bar{\rho}U_i\epsilon)}{\partial x_i} = \frac{\partial}{\partial x_j}\left[\left(\mu + \frac{\mu_t}{\sigma_\epsilon}\right)\frac{\partial \epsilon}{\partial x_j}\right] + \frac{\gamma}{\nu_t}P_k - \beta\bar{\rho}\omega^2 + \frac{2\bar{\rho}\sigma_\omega^2}{\omega}\frac{\partial k}{\partial x_j}\frac{\partial \omega}{\partial x_j}(1 - F_1) \tag{3.15}$$

The value of F_1 takes a value between 0 and 1 and smoothly goes from 0 (pure k-ε) to 1 (pure k-ω).

The turbulent viscosity is calculated with the following equation for the baseline k- ω model:

$$\mu_t = \frac{\bar{\rho}k}{\omega} \tag{3.16}$$

For the SST model, the turbulent viscosity is calculated with another blending function, F_2:

$$\mu_t = \frac{a_1\bar{\rho}k}{max(a_1\omega, SF_2)} \tag{3.17}$$

With S being the shear strain magnitude and a_1 being another constant with value 0.31. The denominator of the SST viscosity does not depend purely on the specific dissipation rate but includes a limiter function instead. S and F_2 act to limit the viscosity, as if they take over the denominator function, the value of turbulent viscosity is lower than the baseline model.

Transition is predicted through the transport of the two scalar quantities, transition onset momentum thickness Reynolds number and intermittency. These are defined as:

Transition onset momentum thickness Reynolds number:

$$\frac{\partial\left(\bar{\rho}\widehat{Re}_{\theta,t}\right)}{\partial t} + \frac{\partial\left(\bar{\rho}U_i\widehat{Re}_{\theta,t}\right)}{\partial x_i} = \frac{\partial}{\partial x_i}\left[\sigma_{\theta,t}(\mu + \mu_\tau)\frac{\partial \widehat{Re}_{\theta,t}}{\partial x_i}\right] + P_{\theta,t} \tag{3.18}$$

Intermittency:

$$\frac{\partial(\bar{\rho}\gamma_{int})}{\partial t} + \frac{\partial(\bar{\rho}U_i\gamma_{int})}{\partial x_i} = \frac{\partial}{\partial x_j}\left[\left(\mu + \frac{\mu_t}{\sigma_f}\right)\frac{\partial \gamma_{int}}{\partial x_j}\right] + P_{\gamma_{int}} - E_{\gamma_{int}} \tag{3.19}$$

Where the hatted quantity represents the transported $Re_{\theta,t}$ and $P_{\theta,t}$ and $P_{\gamma_{int}}$ are the respective source terms and $E_{\gamma_{int}}$ is the destruction term for intermittency.

3.2.1. Numerical methods

The model is discretised through the use of the OpenFOAM "*blockmesh*" utility, which results in a hexahedral structured mesh. Spatial and temporal discretisation is done using second order schemes. To address the presence of strong discontinuities such as shocks, the use of Total Variation Diminishing (TVD) schemes is made. In particular, the Van Albada [105] TVD scheme is used to limit the gradient changes. The default TVD scheme used by OpenFOAM is van Leer with studies supporting its use over other TVDs[97]. However, a different study by Marcantoni et al.[98], and more recently by Stoldt et al.[99], suggest that the van Albada TVD scheme produces higher quality shocks and provides higher accuracy.

Time integration uses the Crank-Nicholson implicit method. Despite this being an implicit method, the implementation of shockFluid is fully explicit, therefore the scheme is not used in its original form, as a second order implicit scheme, but functions as a second order explicit scheme. Despite this, the scheme maintains its second order accuracy, despite the penalty to the overall stability.

Initialisation of the flow field is performed through the definition of the initial conditions in the *0/* directory. For the turbulence quantities, the resolved boundary layer models are being used. Therefore, for the turbulent quantities, equations 3.20 and 3.21 are used to initialise turbulent kinetic energy and specific dissipation rate respectively:

Turbulent kinetic energy, $\boldsymbol{k}$:

$$\begin{gathered} k = \frac{3}{2}(UI)^2 - \ [Freestream] \\ k = 0 \ (or\ small\ number) - \ [Wall] \end{gathered} \tag{3.20}$$

Specific dissipation rate, $\boldsymbol{\omega}$:

$$\begin{gathered} \omega = \frac{\sqrt{k}}{C_\mu^{0.25} L} - \ [Freestream] \\ \omega = \frac{60\nu}{\beta_1 y_1^2} - \ [Wall] \end{gathered} \tag{3.21}$$

Transition onset momentum thickness Re, $\boldsymbol{Re_{\theta,t}}$ *:*

$$Re_{\theta,t} = \begin{cases} 1173.51 - 589.428(100 * I) + \dfrac{0.2169}{(100 * I)^2} & I \leq 1.3 \\ \dfrac{331.5}{\left((100 * I) - 0.5658\right)^{0.671}} & I > 1.3 \end{cases} - \ [Inlet] \tag{3.22}$$

$$Re_{\theta,t} = 0 \; and \; \frac{\partial Re_{\theta,t}}{\partial \boldsymbol{n}} = 0 - [Wall]$$

Intermittency, $\boldsymbol{\gamma}$:

$$\gamma_{int} = 1 - [Inlet]$$
$$\gamma_{int} = 0 \; and \; \frac{\partial \gamma_{int}}{\partial \boldsymbol{n}} = 0 - [Wall] \qquad 3.23$$

For the initialisation of the turbulent quantities, turbulent intensity, *I*, must be specified. The turbulent intensity is defined as the ratio between the fluctuating component of the streamwise velocity to the freestream value. Thus, a higher value of turbulent intensity indicates stronger turbulence in the system. For hypersonic flows, the amount of turbulence is reduced to compressibility, which acts to dampen the transport of energy. Hence, for this work, a value of 0.01% is selected for *I*. The selection is based on the fact that externally, in freestream conditions, the turbulence would be rather low even in low-speed applications, in the order of 0.01%. As such, to account for the effect of compressibility, the freestream turbulence is selected to be much lower than incompressible freestream flows. Additionally, the freestream turbulence is low to avoid forced transition, which would occur if turbulent energy were high. The value of the characteristic length scale, L, required for the initialisation of ω, is selected to be on the scale of the boundary layer.

3.2.2. Solver Validation & Grid dependence study

To validate the capability of the solver to predict hypersonic boundary layer properties on a cooled plate and accurately resolve shock waves, the experimental study of Schulein[18] was used, as data at various stations are provided, along with the effects of shock impingement. The experimental data were collected at the DLR shock tube tunnel, on a sharp plate of length 500mm and width 400mm. The impinging shocks were generated using a shock generator placed on a location such that the inviscid shock impinges on the flat plate below at a distance of 350mm from the leading edge. The experimental conditions are summarised in Table 3-2 below.

Table 3-2: Experimental conditions by Schulein[18], [19]

Quantity	Value
Mach number	5
Total Pressure (MPa)	2.12
Total Temperature (K)	410

Unit Reynolds Number (1/m)	$37x10^6$
Wall Temperature (K)	300 ± 5

A flow domain schematic is presented in Figure 3-5 below. The location of the shock generator is placed in such a manner that the inviscid shock would impinge at a streamwise location of x = 0.350 m from the leading edge of the plate, replicating the conditions of the experiment.

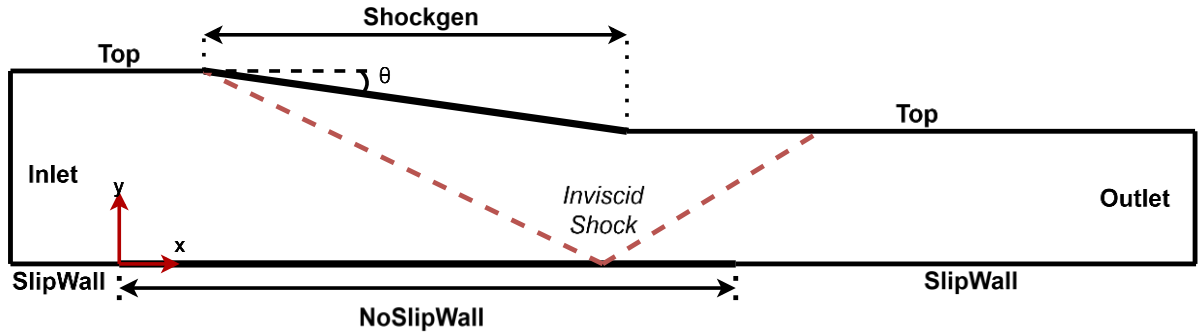


Figure 3-5: Computational domain for experiment by Schulein

The boundaries shown in Figure 3-5 above must be individually initialised and assigned a boundary type. The boundaries along with their initialisation for each quantity are presented in Table 3-3 and

Table 3-4. The boundaries imposed at the plate and shock generator for the turbulent properties reflect wall-resolved turbulence, which improves the accuracy of the results.

Table 3-3: Boundary Conditions – Non-turbulence quantities. FV – fixedValue, ZG – zeroGradient, WT – waveTransmissive , SP – slip

	Quantity				
Boundary	T (K)	U (m/s)	P (Pa)	γ	$Re_{\theta,t}$
Inlet	FV – 68.33	FV – 828.5	FV – 4000	FV – 1	FV – 3363.6
Outlet	ZG	ZG	WT	ZG	ZG
SlipWall	SP	SP	SP	SP	SP
noSlipWall	FV - 300	noSlip	ZG	ZG	ZG
Top	ZG	ZG	WT	ZG	ZG
ShockGen	ZG	noSlip	ZG	ZG	ZG

Table 3-4: Boundary Conditions - Turbulence quantities. FV – FixedValue, ZG – zeroGradient, WT – waveTransmissive, SP – slip

Boundary	Quantity			
	k (m2/s2)	ω (1/s)	ν_t (m2/s)	α_t (kg/ms)
Inlet	FV – 1.03e-2	FV -1852.6	Calculated - 0	Calculated - 0
Outlet	ZG	ZG	Calculated - 0	Calculated - 0
SlipWall	SP	SP	SP	SP
NoSlipWall	FV – 1e-10	omegaWallFunction – 3.175e11	nutLowReWallFunction – 1e-10	Compressible:: alphatWallFunction
Top	ZG	FV – 185.26	Calculated - 0	Calculated - 0
ShockGen	FV – 1e-10	omegaWallFunction – 3.175e11	nutLowReWallFunction – 1e-10	Compressible:: alphatWallFunction

The thermodynamical properties are set assuming an ideal gas, with specific heat capacity at constant pressure, c_p calculated using the JANAF thermodynamic relations. Viscosity is estimated using Sutherland's Law.

The selection of schemes is vital to the accuracy of the solver. As previously discussed, time discretisation is done using the Crank-Nicholson time scheme. Beyond that, the gradient, divergence and interpolation schemes are defined as per Table 3-5 below. The schemes selected are all of second order, selected to maximise accuracy. The gradient scheme for velocity has its limiter slightly lowered to allow the SSTLM turbulence model to operate, while the gradient schemes of pressure and internal energy have their limiters relaxed as to not add artificial numerical diffusion to the results.

Table 3-5: Discretisation schemes set in *fvSchemes*

Discretisation Category	Parameter	Discretisation scheme/limiter
Temporal		Crank-Nicholson 0.9
Gradient		
	default	Gauss linear 1
	U	Gauss linear 0.9
	p, e	Gauss linear 0.3
Divergence		
	default	None
	ρU, ρe	Gauss vanAlbada(V)
	τ	Gauss linear
	k, ω, ε, γ_{int}, $Re_{\theta,t}$	Gauss limitedLinear 1
	$\nabla\cdot[\nu_{eff}(\nabla U+(\nabla U)T)]$	Gauss linear
	$\nabla\cdot[\mu_{eff}(\nabla U+(\nabla U)T-2/3(\nabla\cdot U)I)]$	Gauss linear
Interpolation		

default	Linear
U, T, ρ	vanAlbada(V)
Laplacian / Surface-Normal	limited 1

To ensure sufficient mesh resolution to capture shock boundary layer interactions and other spatially sensitive features without inefficient use of computational resources, three meshes are tested. The meshes are composed of tetrahedral cells of total cell numbers 46k, 76k and 175k for the coarse, fine and very fine meshes, respectively. First cell height is set to 2e-6 meters for coarse and fine meshes, and 1e-6 meters for the very fine mesh. The low cell height ensures that the first cell y^+ is below 1, ensuring turbulence is fully resolved without the use of wall functions. The number of cells clustered in the near-wall region is also increased between mesh qualities to ensure enough cells are within the boundary layer region. Mesh grading is performed in critical regions both horizontally and vertically. Mesh grading follows a geometric relation in OpenFOAM. The number of cells as well as the initial freestream quantities are displayed in Table 3-6.

Table 3-6: Grid dependence geometric and initialisation data

	Geometry					*Freestream*			*Turbulence*		
Mesh Quality	$\boldsymbol{N_{cell}}$	$\boldsymbol{N_{cell,x}}$	$\boldsymbol{N_{cell,y}}$	$\boldsymbol{y_1}$, m	$\boldsymbol{M_\infty}$	$\boldsymbol{Re_{unit}}$, m^{-1},10^6	$\boldsymbol{P_\infty}$, Pa	$\boldsymbol{T_\infty}$, K	k, m^2s^{-2}	ω, s^{-1}	$Re_{\theta,t}$
Coarse	46000	304	150	2e-6	5	37	4007	68.3	0.0103	1852.6	3363.6
Fine	76000	362	210	2e-6	5	37	4007	68.3	0.0103	1852.6	3363.6
Very Fine	178000	658	270	1e-6	5	37	4007	68.3	0.0103	1852.6	3363.6

Table 3-7: Comparison of experimental and URANS data at stations along the plate

Location, mm	Experiment					k-ω SSTLM				
	δ, mm	δ^*, mm	θ, mm	δ^*_{inc}, mm	θ_{inc}, mm	δ, mm	δ^*, mm	θ, mm	δ^*_{inc}, mm	θ_{inc}, mm
266	3.814	1.574	0.157	0.540	0.414	3.552	1.534	0.148	0.481	0.329
296	4.175	1.788	0.177	0.626	0.473	3.923	1.691	0.164	0.524	0.363
316	4.410	1.792	0.177	0.636	0.477	4.153	1.792	0.174	0.550	0.384
376	2.651	0.9	0.175	0.407	0.312	2.573	0.895	0.159	0.369	0.269
396	3.364	0.953	0.192	0.407	0.331	2.883	0.931	0.172	0.363	0.275
426	4.466	1.263	0.267	0.560	0.446	3.319	1.015	0.189	0.382	0.294
449	4.837	1.289	0.264	0.550	0.443	3.794	1.071	0.211	0.411	0.319
$x_{trans,end}$			125					120		

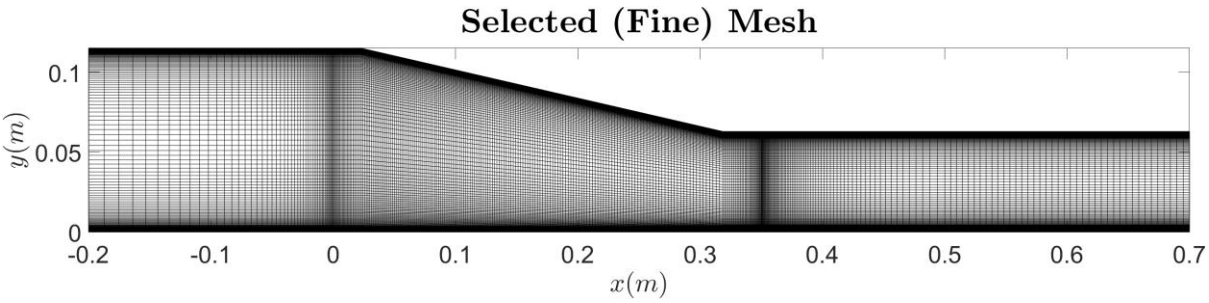


Figure 3-6: Selected mesh after grid dependence study

The fine mesh is selected, displayed in Figure 3-6 above, as the pressure and skin friction distributions convergence to the same values as the very fine mesh, seen in Figure 3-7. The experimental results are also overlayed, showing the capability of the SSTLM model to predict both the magnitude and distribution of the normalised wall pressure with good accuracy.

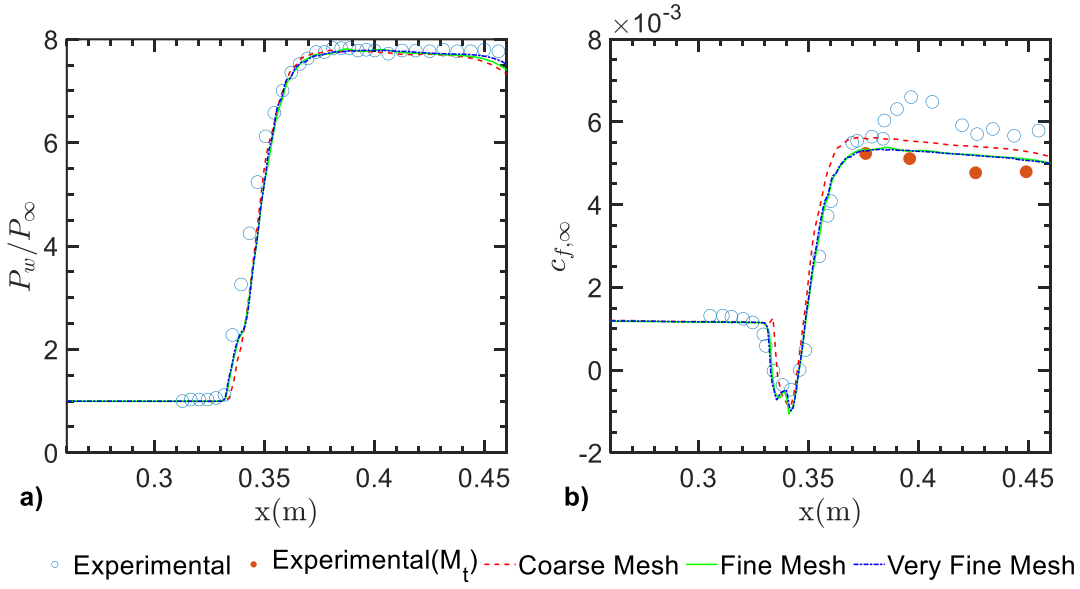


Figure 3-7: Mesh dependency results and solver validation

There is good agreement with experimental data on pressure prediction, seen in Figure 3-7a) as well as the location and span of the separation bubble, determined by the location of zero skin friction coefficient in Figure 3-7b). A comparison of the boundary layer and integral thicknesses obtained through the SSTLM turbulence model is compared to the experimental results in

Table 3-7 above. There is very good prediction by the model upstream of the shock, but a much poorer prediction downstream of the interaction. Discrepancies also arise from the prediction

of the skin friction coefficient past the shock impingement. The separation and reattachment locations are predicted accurately, supporting the conclusion that the solver can capture the macroscopic flow structures. However, the magnitude of the skin friction coefficient shows significant mismatch. The experimental data obtained using the global interferometry skin-friction (GISF) method show a peak in the skin friction that is not observed in the CFD simulations.

Presented in Figure 3-7b) are also data obtained from the friction Mach number, Ma_τ. Using the friction number and the definition of sonic speed at the isothermal wall temperature of 300K, provides the wall friction velocity, U_t. The wall shear stress, τ_w, is obtained using:

$$\tau_w = \rho_w Ma_\tau^2 \gamma R_{gas} T_w \qquad 3.24$$

The skin friction coefficient obtained through this method shows a much closer agreement to the predicted values through CFD. However, as the source of the friction velocity used to calculate the friction Mach number is not clear by the authors, these data are not as reliable as the ones obtained from the GISF method.

This underprediction can be attributed to multiple factors. Firstly, the data were collected at differing ambient conditions and/or different experimental runs. The values of ambient pressure, temperature and velocity result in differing flow fields. Due to the sensitivity of the flow to ambient conditions, small variations in the freestream conditions result in significant downstream alterations in boundary layer thickness and integral quantities. Naturally, the distribution of the skin friction and separation scale will vary, as they depend on the local state of the boundary layer. Additionally, this could also be potentially attributed to three-dimensional effects which are not considered in the 2D case [106]. Crossflow in the 3D case would influence the boundary layer state which would once again affect the distribution of the skin friction coefficient. The effects of crossflow can be seen from the experimental results, in positions 4 and 4a-c). The boundary layer shows significant growth away from the centreline, which is an indication of the non-homogeneity of the flow in the 3rd dimension. It is thus reasonable to conclude that crossflow effects influence the boundary layer to some extent.

Further limitation to the accuracy of any URANS simulation would be the amplification of turbulence during an STBLI, along with the breakdown of traditional Reynolds stresses assumptions that go into RANS simulations. Inherent to any RANS-based simulation is the time averaging that occurs and the Boussinesq approximation inherent to most turbulence closure models, such as the k-ω model used in this work. During STBLI there is a significant

increase in turbulence fluctuations due to the recirculation zone, both upstream and downstream of the interaction. This was demonstrated by the DNS study of Fang et al.[107], which demonstrated the mechanisms of turbulence amplification as being deceleration-based upstream and free shear layer-based downstream of the interaction. As the downstream region of the interaction is driven by shear layer phenomena, the discrepancy of the results arises because of the failure of proper prediction of the anisotropy in turbulence arising within the shear layer [108]. More specifically, it appears that RANS-based models incorrectly transport turbulent kinetic energy within the shear layer. This distortion of turbulent quantities is at least partially responsible for the errors in estimation of boundary layer properties aft of the STBLI.

Despite the above drawbacks of RANS-based simulations inherent in their formulation, the solver is capable of properly capturing the mean flow effects of the interaction, the extent of the separation region as well as the pressure rise distances. It is thus used forward to verify the optimised configurations that are returned through the overall optimisation process described in this chapter.

3.3. Chapter Summary

To optimise an optimum dual-mode or pure scramjet intake/isolator configuration with multiple objectives and numerous constraints, a suitable optimising algorithm is required. For this purpose, the Constrained-Multi-Objective Particle Swarm Optimisation (CMOPSO) algorithm is selected. Its capability has been tested against benchmark cases with multiple objectives and constraints and will be used for the remainder of this work.

Validation of the optimised configurations is done through the use of CFD. The open-source code OpenFOAM is selected. Verification of the solver is done for a shock impingement on a viscous flat plate. The solver shows good quantitative and qualitative agreement with experimental finding, and it is thus used henceforth.

Chapter 4 - Hypersonic Flat Plate Modelling

Typical scramjet operation occurs in the stratosphere, where the ambient dynamic pressure can be maintained within a range of 30-70 kPa. The flow speed along with the ambient temperature result in very high stagnation temperatures, which would cause any material to melt. As such, the surface of the vehicle must be cooled, which in turn influences the boundary layer development. Accurate prediction of the boundary layer development and its associated quantities is vital to prediction of Shock-Boundary Layer Interactions and isolator boundary layer development.

Accordingly, this chapter presents the modelling strategy employed for the prediction of hypersonic flat plate boundary layers along with their validation against experimental and numerical studies from literature.

4.1. Zero Pressure Gradient (ZPG) Compressible boundary layers – Model formulation

In low-speed boundary layers, the flow is of constant density and therefore compressibility effects are negligible. Flows past the transonic regime experience appreciable compressibility effects which become more severe with increasing Mach number, with the boundary layer experiencing significant variations in temperature along its height. As such, the velocity profile deviates from the laws that can be used to describe incompressible boundary layers.

Accuracy in predicting the boundary layer thickness and integral quantities is paramount on mixed compression intakes, as the behaviour of the external shock system directly depends on the boundary layer thickness and integral quantities, as will be explored in Chapter 5. To ensure that the results obtained through the proposed modelling approach reflect actual conditions, a physics-based approach is adopted in this work, using a universal turbulent velocity profile to determine the friction velocity and integral quantities for a turbulent boundary layer.

4.1.1. Universal incompressible boundary layer profiles

The velocity profile of a boundary layer is one of its most important properties, as it can be used to determine valuable information about the boundary layer. For instance, the integral properties, displacement and momentum thickness, as well as the friction velocity can all be determined from the velocity profile. The integral quantities for compressible boundary layers are evaluated using the following equations:

$$\delta^* = \int_0^{\delta} \left(1 - \frac{\bar{\rho}}{\rho_\infty}\frac{\bar{u}}{U_\infty}\right) dy \tag{4.1}$$

$$\theta = \int_0^{\delta} \frac{\bar{\rho}}{\rho_\infty}\frac{\bar{u}}{U_\infty}\left(1 - \frac{\bar{u}}{U_\infty}\right) dy \tag{4.2}$$

Where ρ and U represent the density and velocity respectively. Quantities with the overbar symbol represent local values in the boundary layer, with the ∞ representing freestream quantities.

In both quantities, the variation in density within the boundary layer can be accounted for by assuming no pressure variation normal to the flow direction within the boundary layer, which directly relates the density variation to the temperature variation. Assuming, as in this study, that air behaves as a perfect gas, the density variation is related to the temperature variation by:

$$\frac{\bar{\rho}}{\rho_\infty} = \frac{T_\infty}{\bar{T}} \tag{4.3}$$

However, the velocity profile is still required for the temperature relations and the integral quantities overall.

Thus, a method is required to predict the velocity profile without experimental or numerical data. An idea that has progressively been refined over the years is that of a universal velocity profile. Various incompressible turbulent universal profiles have been proposed, which take into account the laminar sublayer and log-region. The one selected in this study is the profile developed by Monkewitz[109]. The Monkewitz profile was selected due to the profile being constructed through asymptotic matching of the inner and outer layers.

$$U^+_{inner} = U^+_{inner,23} + U^+_{inner,25} \tag{4.4}$$

With $U^+_{inner,23}$ being:

$$\begin{aligned} U^+_{inner,23} = {} & 0.68285472 \ln\left(y^{+2} + 4.7673096y^+ + 9545.9963\right) \\ & + 1.2408249 \tan^{-1}\left(0.010238083y^{+2} + 0.024404056\right) \\ & + 1.2384572 \ln\left(y^+ + 95.232690\right) - 11.930683 \end{aligned} \tag{4.5}$$

And $U^+_{inner,25}$:

$$
\begin{aligned}
U^{+}_{inner,25} = &-0.50435126\ln\left(y^{+2} - 7.8796955y^{+} + 78.389178\right) \\
&+ 4.7413546\tan^{-1}(0.12612158y^{+} - 0.49689982) \\
&- 2.7768771\ln\left(y^{+2} - 16.209175y^{+} + 933.16587\right) \\
&+ 0.37625729\tan^{-1}(0.033952353y^{+} + 0.27516982) \\
&+ 6.5624567\ln(y^{+} + 13.670520) + 13.670520
\end{aligned}
\tag{4.6}
$$

With U^{+} and y^{+} referring to velocity and vertical distance from the wall in wall units, non-dimensionalised using friction velocity, u_τ and wall kinematic viscosity, ν_w. They are calculated using $u^{+} = {\bar{u}}/{u_\tau}$ and $y^{+} = {yu_\tau}/{\nu_w}$,

To capture the wake of the turbulent boundary layer, correlations have also been developed. The correlations make use of the wake parameter Π, which is a measure of the intensity of turbulence in the boundary layer. It is commonly determined from boundary layer data; however, correlations have been developed based on experimental boundary layers to predict a value for Π. A correlation based on the value of the incompressible momentum thickness Reynolds number, $Re_{\theta,inc}$, has been used to obtain a value for the wake parameter[110]:

$$
\Pi = 0.69\left(1 - exp\left(-0.243\sqrt{\frac{Re_{\theta,inc}}{425} - 1} - 0.15\left(Re_{\theta,inc} - 1\right)\right)\right) \tag{4.7}
$$

To obtain an estimation of the local incompressible momentum thickness Reynolds number, the correlation of Karman and Schoenherr[13] is used, which links the incompressible momentum thickness Reynolds number to the incompressible skin friction coefficient:

$$
c_{f,inc} = \frac{1}{\log_{10}\left(2Re_{\theta,inc}\right)\left(17.075\log_{10}\left(2Re_{\theta,inc}\right) + 14.832\right)} \tag{4.8}
$$

An additional term is included to account for turbulence in the defect layer. The wake function proposed by Finley and later implemented by Krogstad et al.[111] is used due to its simplicity and comparable results to other wake functions:

$$
u^{+}_{wake} = \frac{1}{\kappa}\left((1 + 6\Pi)\left(\frac{y^{+}}{\delta^{+}}\right)^{2} - (1 + 4\Pi)\left(\frac{y^{+}}{\delta^{+}}\right)^{3}\right) \tag{4.9}
$$

Equations 4.4, 4.5 and 4.9 are combined into a single velocity profile that describes the entire boundary layer. This produces a single incompressible velocity profile, which allows for the turbulent boundary layer to be collapsed onto a single profile. The combined form of the incompressible universal profile takes the final form:

$$U^+_{incomp} = U^+_{inner} + u^+_{wake} \tag{4.10}$$

However, the compressibility effects observed in hypersonic boundary layers must be accounted for. To do so, corrections must be applied to the velocity profile. As such, transformations that cast a compressible boundary layer into an equivalent incompressible one have been developed. Similarly, solving the transformations backwards, casts an incompressible universal profile into a compressible one.

4.1.2. Temperature-Velocity relations

To fully capture the properties of a compressible boundary layer, the effects of temperature variance within the boundary layer must be considered.

Crocco and Busemann[112] independently proposed the first correlation between temperature within the boundary layer and the velocity profile, given by:

$$\frac{\bar{T}}{T_w} = 1 + \frac{(T_{aw} - T_w)}{T_w}\frac{u}{U_\infty} - \frac{ru^2}{2c_pT_wU_\infty^2}$$
$$T_{aw} = T_e\left(1 + r\left(\frac{\gamma - 1}{2}\right)M_e^2\right) \tag{4.11}$$

The above relation assumes a zero-pressure gradient and a laminar Prandtl number of unity, which subsequently means that adiabatic wall temperature is the same as the total temperature. The above relation was then updated by Walz, who modified the relation by considering a non-unity Prandtl number and thus a non-unity adiabatic recovery coefficient, r. The Walz[113] relation reads as follows:

$$\frac{\bar{T}}{T_w} = 1 + \frac{(T_{aw} - T_w)}{T_w}\frac{u}{U_\infty} + \frac{T_\infty - T_{aw}}{T_w}\left(\frac{u}{U_\infty}\right)^2 \tag{4.12}$$

Further improvements were made to the Walz relation by Duan and Martin[114], which correlated DNS data for compressible high-speed data on turbulent boundary layers, resulting in an updated version of the Walz relation:

$$\frac{\bar{T}}{T_w} = 1 + \theta_{DM}\frac{(T_{aw} - T_w)}{T_w}\frac{u}{U_\infty} + \left(\frac{T_\infty - T_{aw}}{T_w} + (1 - \theta_{DM})\frac{(T_{aw} - T_w)}{T_w}\right)\left(\frac{u}{U_\infty}\right)^2 \tag{4.13}$$

The value of θ_{DM} takes a value of 0.8259. Another relation was proposed by Zhang et al[115], which uses the Generalised Reynolds Analogy (GRA) to modify the Walz relation:

$$\frac{\bar{T}}{T_w} = 1 + \frac{(T_{rg} - T_w)}{T_w}\frac{u}{U_\infty} + \left(\frac{T_\infty - T_{rg}}{T_w}\right)\left(\frac{u}{U_\infty}\right)^2$$

$$T_{rg} = T_\infty + \frac{r_g U_\infty^2}{2c_p} \qquad 4.14$$

$$r_g = 2c_p\left(\frac{T_w - T_\infty}{U_\infty^2}\right) - \frac{2Pr}{U_\infty}\frac{q_w}{\tau_w}$$

Ultimately, the relation of Duan and Martin is selected for use in this work, since the relations of both Duan and Martin and that of Zhang provide similar results, but the relation of Duan and Martin is significantly simpler, as it does not require estimation of the heat transfer, q_w.

Alongside the temperature variation, there is a significant dynamic viscosity variation. Thus, an additional equation is required to determine the dynamic viscosity of air within the boundary layer. The dynamic viscosity varies significantly with temperature. The relation used in this work to estimate air viscosity is that of Keyes. Compared to the more commonly used Sutherland's law (Equation 4.16), Keyes' law (Equation 4.15) provides a closer agreement to actual air viscosity at lower temperatures, hence it can be used to verify the models with experimental data which are typically run at very low ambient conditions. A comparison of the two laws for a temperature range of 50K to 2000K is presented in Figure 4-1.

$$\mu = 1.488 * 10^{-6}\left(\frac{\sqrt{T}}{1 + \frac{122.1}{T} * 10^{-\frac{5}{T}}}\right) \qquad 4.15$$

$$\mu = \mu_{ref}\left(\frac{T}{T_{ref}}\right)^{1.5}\frac{T_{ref} + S}{T + S} \qquad 4.16$$

$\mu_{ref} = 1.716 \cdot 10^{-5}$,S = 110.4 K , T_{ref} = 273 K

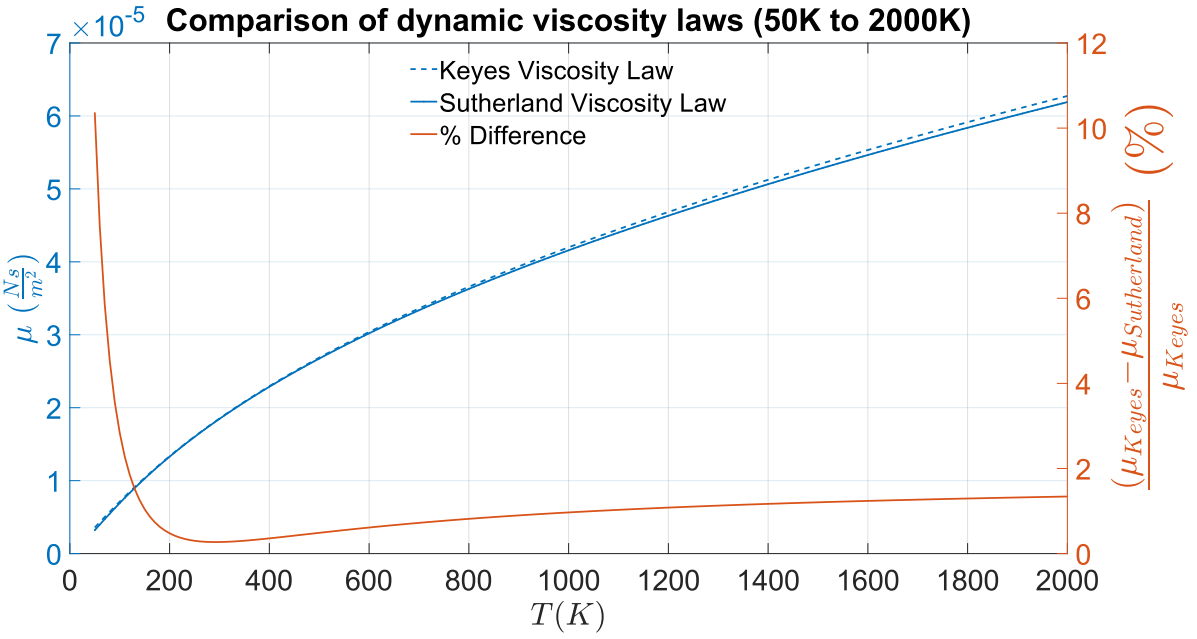


Figure 4-1: Comparison between viscosity laws. Most significant difference at low temperatures (50K – 100K).

4.1.3. Compressibility Transformation

As mentioned previously, a compressible turbulent boundary layer deviates significantly from an incompressible one. Hence, corrections are needed to account for the significant variation in properties vertically across the layers.

The compressibility transformation used in this work is the Van Driest transformation. Van Driest assumed that the viscous sublayer does not play a significant role in the shear stress above the buffer layer, and it is thus ignored, with the shear stress being entirely due to turbulent stresses. This takes the form:

$$\tau_w = -\rho\overline{u'v'} \tag{4.17}$$

Which is noted as being identical to the incompressible form of the turbulent shear stress. Assuming that the turbulent fluctuations can be described by the Prandtl mixing length method, results in a shear stress as a function of the velocity gradient:

$$\tau_w = \rho l^2 \left(\frac{du}{dy}\right)^2 \tag{4.18}$$

Van Driest assumed that the mixing length takes the form l = κy, which is the Prandtl mixing length, with κ being the von Karman constant. Substituting back to equation 4.18:

$$\tau_w = \rho\kappa^2 y^2 \left(\frac{du}{dy}\right)^2 \tag{4.19}$$

Rearranging to isolate variables du and dy results in:

$$\int_0^u \sqrt{\frac{\rho}{\rho_w}}\, d\left(\frac{u}{U_\infty}\right) = \sqrt{\frac{\tau_w}{\rho_w}} \frac{1}{\kappa U_\infty} \int \frac{1}{y}\, dy \tag{4.20}$$

A relation is thus required for the variation of density with velocity ratio. Van Driest assumed the Crocco-Busemann relation described by equation 4.11 in his original work but updated it with the Walz relation in subsequent works [116]. The expressions share the same quadratic structure and thus produce the same generic equation, but with different coefficients. Assuming that no pressure variation exists vertically in the boundary layer and that air behaves as an ideal gas described by equation 4.3:

$$\int_0^{\frac{u}{U_\infty}} \frac{1}{\sqrt{1 + \frac{(T_{aw} - T_w)}{T_w}\frac{u}{U_\infty} + \frac{T_\infty - T_{aw}}{T_w}\left(\frac{u}{U_\infty}\right)^2}}\, d\left(\frac{u}{U_\infty}\right) = \frac{u_\tau}{\kappa U_\infty}(\ln(y) + C_1) \tag{4.21}$$

Performing the integration on the left-hand side and changing the right-hand side to wall units (y+):

$$\frac{1}{a_T}\left(\sin^{-1}\left(\frac{2a_T^2 \frac{u}{U_\infty} - b_T}{q_T}\right) + \sin^{-1}\left(\frac{b_T}{q_T}\right)\right) = \frac{u_\tau}{U_\infty}\left(\frac{1}{k}\ln(y^+) + C_2\right) \tag{4.22}$$

This strongly resembles the incompressible law of the wall, but with correcting terms that account for the variation in density. Thus, the van Driest compressibility correction can be written in more generic terms:

$$u_{VD}^+ = \int_0^{U_\infty^+} \sqrt{\frac{\rho}{\rho_w}}\, du^+ \tag{4.23}$$

With the above definition, the universal incompressible velocity profile of Equation 4.10 is converted into a compressible velocity profile.

4.1.4. Final model

The models presented in the preceding subsections are combined to form the first sub-model developed in this work, providing the basis for predictions on the leading plate and subsequent compression ramps. While the approach follows established practice by applying a

compressibility correction to the velocity profile, to the author's knowledge, it is the first to employ a physically consistent universal turbulent velocity profile with a modified compressibility correction for compressible turbulent boundary layers on a flat plate.

The turbulent boundary layer equation used throughout this research combines the incompressible universal turbulent boundary layer profile with the compressibility correction of Van Driest using the modified thermal coefficients of Duan and Martin instead of the original ones of Walz, to obtain a profile for compressible turbulent boundary layers. This takes the form:

$$\frac{U_\infty}{u_\tau a_T}\left(\sin^{-1}\left(\frac{2a_T^2\frac{u}{U_\infty}-\ b_T}{q_T}\right)+\ \sin^{-1}\left(\frac{b_T}{q_T}\right)\right)=\ U_{incomp}^{+} \tag{4.24}$$

Inversion of the transformation to isolate the compressible velocity profile results in:

$$\frac{u}{U_\infty}=\ \frac{b_T}{2a_T}+\ \frac{q_T}{2a_T}\sin\left(-\sin^{-1}\left(\frac{b_T}{q_T}\right)+\ \frac{u_\tau a_T}{U_\infty}U_{incomp}^{+}\right) \tag{4.25}$$

An expression to estimate the boundary layer thickness is required to fully characterise the boundary layer. For compressible turbulent boundary layers there does not exist a universally accepted analytical method for the estimation of the thickness. Thus, a corrected version of the expression presented by Popinski and Ehrlich [117] is used. The original expression is essentially a compressibility correction to the incompressible expression for the boundary layer thickness. The incompressible expression for the boundary layer thickness is:

$$\frac{\delta_i}{x}=\ \frac{0.154}{Re_{x,i}^{\frac{1}{7}}} \tag{4.26}$$

The correction applied by Popinski and Ehrlich takes into account the density and viscosity variation within the boundary layer, using Eckert's reference temperature [118] and a power law for the temperature-viscosity relation (ω = 0.67):

$$\delta=\ \frac{0.154(x-\ x_{virt})}{\left(Re_{x-x_{virt}}\frac{T_\infty}{T_*}\frac{\mu_\infty}{\mu_*}\right)^{\frac{1}{7}}} \tag{4.27}$$

With no pressure gradient across the boundary layer (Equation 4.3), the thickness of a compressible boundary layer, as proposed by Popinski and Ehrlich is:

$$\delta = \frac{0.154(x - x_{virt})}{\left(Re_{x-x_{virt}} \left(\frac{T_\infty}{T_*}\right)^{1.67}\right)^{\frac{1}{7}}} \quad 4.28$$

This work applies further corrections to Equation 4.28 to update the constant to the more accepted value of 0.162 for the incompressible turbulent boundary layer, and the viscosity ratio is determined using Keyes' viscosity law instead of the power law. This results in the final expression for the boundary layer thickness:

$$\delta = \frac{0.162(x - x_{virt})}{\left(Re_{x-x_{virt}} \frac{T_\infty}{T_*} \frac{\mu_\infty}{\mu_*}\right)^{\frac{1}{7}}} \quad 4.29$$

where the reference temperature, T_*, is defined as:

$$T_* = 0.5T_w + 0.22T_{aw} + 0.28T_\infty \quad 4.30$$

The above equations require determination of the location of the virtual origin. The virtual origin refers to a fictitious location along the plate where a fully turbulent boundary layer would seem to start from. Determination of the virtual origin is challenging and thus for this research, it is set at the beginning of the transition region, as depicted in Figure 4-2.

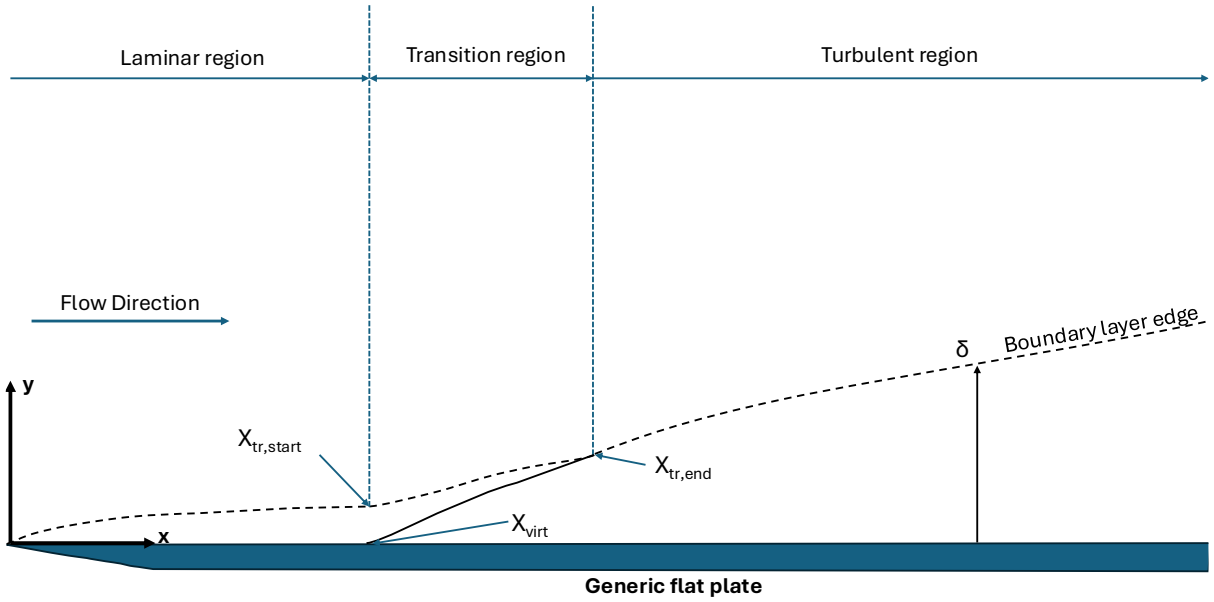


Figure 4-2: Generic flat plate showing the locations of transition start, end and virtual origin

The transition region remains one of the most challenging aspects of hypersonic boundary-layer modelling. Various studies have been conducted in an attempt to provide analytical

expressions for the prediction of the transition region [119], [120], [121], [122] . This section explores some correlations and models developed by researchers to predict supersonic/hypersonic flat plate transition end location.

The first expression considered was proposed by Simeonides [120] for low bluntness flat plates. It was determined by data regressing of various experimental studies at nearly adiabatic conditions, with some experiments being at a cooling ratio of 0.5.

The expression is a simple relation, and relates the transition onset Reynolds number to the freestream Reynolds and Mach number:

$$Re_{x,tr,start} = 0.9\frac{Re_{unit}}{Ma} \tag{4.31}$$

Kanda[122] used conservation laws for a control volume encompassing the start and end of transition zone around the boundary layer to get a prediction for the end of transition location. Assuming that the boundary layer thickness at the end of transition is larger than the thickness at the beginning by a factor, a, the location of transition onset is predicted by the equivalence:

$$\frac{\delta_t}{x_{tr,start}} = (1+a)\frac{\delta_l}{x_{tr,start}} \tag{4.32}$$

The value of factor a can be determined through the conservation of mass for the boundary layer between the bounding box of the boundary layer, resulting in an equation which uses the ratio of displacement thicknesses to the boundary layer thicknesses:

$$a = \frac{\frac{\delta_l^*}{\delta_l} - \frac{\delta_t^*}{\delta_t}}{\frac{\delta_t^*}{\delta_t}} \tag{4.33}$$

The laminar ratio is calculated using the compressible Blasius self-similarity solution, while the turbulent boundary layer is solved using a 1/9th power law velocity profile.

A third analytical expression evaluated for this research is the one proposed by Deem and Murphy[119], which accounts for the effects of freestream Mach number and Reynolds number, assuming a sharp plate (zero bluntness):

$$x_{tr,end} = 0.0254\left(\frac{6.47 * 10^3 + 2.33 * 10^3(Ma-3)^{1.5}}{(0.0254 * Re_{unit})^{0.6}}\right) \tag{4.34}$$

The expression of Deem and Murphy returns a value for the location of the end of transition. The coefficient of 0.0254 is used to convert from inches to meters, as the original formulation was done for inches.

The beginning of the transition is assumed to be a constant proportion of the end of transition, as proposed by Hopkins[123].

$$x_{tr,start} = 0.624 x_{tr,end} \tag{4.35}$$

This model allows for the prediction of the friction velocity, u_τ, boundary layer thickness, δ and the integral quantities. The value of the friction velocity is obtained using a root-finding method (Broyden's method) and the solution of equations 4.25 and 4.29. An initial estimation is required for such methods, and it is obtained by using analytical methods developed for the prediction of skin friction.

4.1.5. Flat Plate Skin Friction Coefficient correlations

The primary state of a boundary layer developed on a hypersonic vehicle will be turbulent. A problem that has been investigated for decades is that of the determination of the skin friction coefficient on a flat plate. The problem becomes of even greater importance in a mixed compression intake due to the presence of multiple flat plates. Many theories have arisen to attempt to predict the skin friction in compressible boundary layers with varying levels of success.

The most successful of these correlations are the derivations of Van Driest, known as Van Driest I and II. The models have a common starting point, that being that the entirety of the shear stress is entirely due to wall shear stress, with the viscous sublayer being ignored. Both models use the Prandtl mixing length equation, with Van Driest I [112] (VD I) making use of the Prandtl mixing length, while the Van Driest II[116] (VD II) model makes uses of the less accepted von Karman similarity mixing length.

As the Van Driest II model provides better agreement with experimental observations, derivation of Van Driest I will not be shown in this work, only the final expression.

The derivation of the Van Driest II begins with the same assumptions as the Van Driest I, with the shear stress being expressed as equation 4.17 and then using a mixing length approximation, resulting in equation 4.18.

Then, taking the mixing length as being the von Karman similarity mixing length gives:

$$\tau_w = \overline{\rho} k^2 \frac{\left(\frac{d\overline{u}}{dy}\right)^4}{\left(\frac{d^2\overline{u}}{dy^2}\right)^2} \tag{4.36}$$

The local density, $\overline{\rho}$, appears as a variable and it would be beneficial if it could be eliminated in favour of the velocity profile. This can be achieved by assuming that the lateral pressure gradient i.e dp/dy = 0. Then, the variation of the density is inversely proportional to the variation of temperature within the boundary layer. Van Driest used the Walz relation (equation 4.12) to provide the correlation between temperature and velocity. Substituting the Walz temperature relation gives:

$$\tau_w = \overline{\rho}_w (1 + b_T \bar{\bar{u}} - a_T^2 \bar{\bar{u}}^2)^{-1} \kappa^2 \frac{\left(\frac{d\overline{u}}{dy}\right)^4}{\left(\frac{d^2\overline{u}}{dy^2}\right)^2} \tag{4.37}$$

Where b_T and a_T are collected terms from the coefficients of the velocity ratio in the quadratic temperature relations, $\overline{u}$ is the local velocity, $\bar{\bar{u}}$ is the non-dimensionalised local velocity using the freestream velocity. Changing the dependent variable in the derivatives from $\bar{u}$ to $\bar{\bar{u}}$ by dividing by the freestream velocity and rearranging results in:

$$\sqrt{\frac{\tau_w}{\rho_w}} \int \frac{dy}{d\bar{\bar{u}}} \frac{d^2\bar{\bar{u}}}{dy^2} dy = \kappa U_\infty \int_0^{\bar{\bar{u}}} \frac{d\bar{\bar{u}}}{\sqrt{(1 + b_T \bar{\bar{u}} - a_T^2 \bar{\bar{u}}^2)}} \tag{4.38}$$

Integration of both sides and isolation of $\frac{dy}{d\bar{\bar{u}}}$ gives:

$$\frac{dy}{d\bar{\bar{u}}} = \exp\left(C - \frac{\kappa U_\infty}{a_T U_t} \left(\sin^{-1}\left(\frac{2a_T^2 \bar{\bar{u}} - b_T}{\sqrt{4a_T^2 + b_T^2}} \right) + \sin^{-1}\left(\frac{b_T}{\sqrt{4a_T^2 + b_T^2}} \right) \right) \right) \tag{4.39}$$

Where C is the constant of integration and is determined at a later stage. Then, Van Driest used the von Karman momentum equation for a zero pressure gradient boundary layer in conjunction with the definition of the momentum thickness, resulting in the following equation in terms of the vertical distance dy:

$$\frac{c_f}{2} = \frac{d}{dx}\left(\int_0^\delta \frac{\rho}{\rho_\infty} \frac{\bar{u}}{U_\infty} \left(1 - \frac{\bar{u}}{U_\infty}\right) dy \right) = \frac{d}{dx}\left(\int_0^\delta \frac{\rho}{\rho_\infty} \bar{\bar{u}}(1 - \bar{\bar{u}}) dy \right) \tag{4.40}$$

Substitution of Equation 4.39 into the above and successive integration by parts results in the well-known analytical solution for the skin friction coefficient in terms of the local Reynolds number:

$$\frac{\sin^{-1}\left(\frac{2a_T^2 - b_T}{q_T}\right) + \sin^{-1}\left(\frac{b_T}{q_T}\right)}{\sqrt{c_f\left(\frac{T_{aw}}{T_\infty} - 1\right)}} = 4.15\log_{10}\left(Re_x c_f \frac{\mu_\infty}{\mu_w}\right) + 1.7 \tag{4.41}$$

The above is rather challenging to solve analytically. However, Spalding and Chi noted that the above is similar to the Karman-Schoenherr incompressible equation:

$$\frac{1}{\sqrt{c_{f,inc}}} = 4.15\log_{10}\left(c_{f,inc}Re_{x,inc}\right) + 1.7 \tag{4.42}$$

And proposed that the Van Driest skin friction correlation can be expressed in terms of the incompressible skin friction coefficient:

$$c_{f,comp} = \frac{1}{F_c} c_{f,inc}\left[F_{Re_x} Re_x\right] \tag{4.43}$$

$$F_c = \frac{\left(\frac{T_{aw}}{T_\infty} - 1\right)}{\left(\sin^{-1}\left(\frac{2a_T^2 - b_T}{q_T}\right) + \sin^{-1}\left(\frac{b_T}{q_T}\right)\right)^2} \tag{4.44}$$

$$F_{Re_x} = \frac{1}{F_c}\frac{\mu_\infty}{\mu_w} \tag{4.45}$$

Prediction of the incompressible skin friction is done using equation 4.42, which, when solved for the skin friction yields the analytical equation:

$$c_{f,inc} = \frac{1}{Re_{x,inc}}\left[\frac{\ln(10)\sqrt{Re_{x,inc}}}{8.3W_0\left(\frac{\sqrt{Re_{x,inc}}\ln(10)}{8.3}e^{\frac{1.7\ln(10)}{8.3}}\right)}\right]^2 \tag{4.46}$$

The local Reynolds number, Re_x, must be transformed into an equivalent incompressible one for use in equation 4.46. This is achieved by transforming it through F_{Re_x}. The letter W in the above equation denotes the use of the Lambert ω (or W) function, with the subscript 0 denoting the principal root. Normally the function has limited analytical solutions, however an approximation to the principal root can be found by a series approximation [124], thus leading to a full analytical solution.

This correlation has been successful in predicting both adiabatic and non-adiabatic flat plate flows, but gets progressively less accurate as the cooling increases, with deviations from experimental data reaching 15% [125].

Despite the error, it is used in this work as a first approximation to the gradient method by Broyden, which is used to solve the compressible velocity profile of equation 4.25 at a given x location.

4.2. Validation of zero pressure gradient model

Validation of the model developed in this research was done in two stages. Firstly, the transition modelling was tested with the model of Deem and Murphy ultimately selected as it showed superior performance to the models of Kanda and Simeonides, as shown in Figure 4-3. Secondly, the prediction of boundary layer thickness, displacement and momentum thicknesses and the friction velocity/skin friction coefficient were calculated.

The experiments used for each stage are different due to data availability. Table 4-1 shows all experiments used, with the tag "TR" denoting use for transition validation, "SF" the use of the experiment for skin friction prediction and "VP" for the velocity profile. The freestream properties used in each experiment are also shown.

Table 4-1: Experiments used for validation of individual sub-models

Case	Ref	Case Use	M_∞	T_∞ (K)	ρ_∞ (kg/m^3)	T_{wall} (K)	Re_{unit} (1/m)
Elfstrom	[15],[126]	TR/VP	9.22	64.5	0.172	295	5.51E7
Schülein	[18]	TR/SF/VP	5	68.3	0.204	300	3.45E7
Kussoy	[17]	TR/VP	8.28	80	0.0187	300	5.3E6
Mee	[127]	TR	6.2	690	0.027	1600*	2.6E6
Fu	[128]	TR	7.3	58.3	0.034	615.5	9.1E6
Wallace	[129]	TR/SF	7.4	116.7	0.152	333.3	2.95E7
Sahoo	[130]	VP	7.2	64.9	0.0704	352	1.66E7

The value of the von Karman constant, κ, was set to 0.385, which was determined by Kagab and Chauhan to be more appropriate for incompressible boundary layers [131]. The choice was made to depart from the more commonly accepted value of 0.41 because the incompressible

universal profile is used to determine the quantities and originally, the Monkewitz profile was developed using the altered value of k.

Firstly, the prediction capabilities of the individual transition models were tested. Figure 4-3 presents the comparison of the predicted transition end lengths obtained from the models and actual transition length of the various experimental studies.

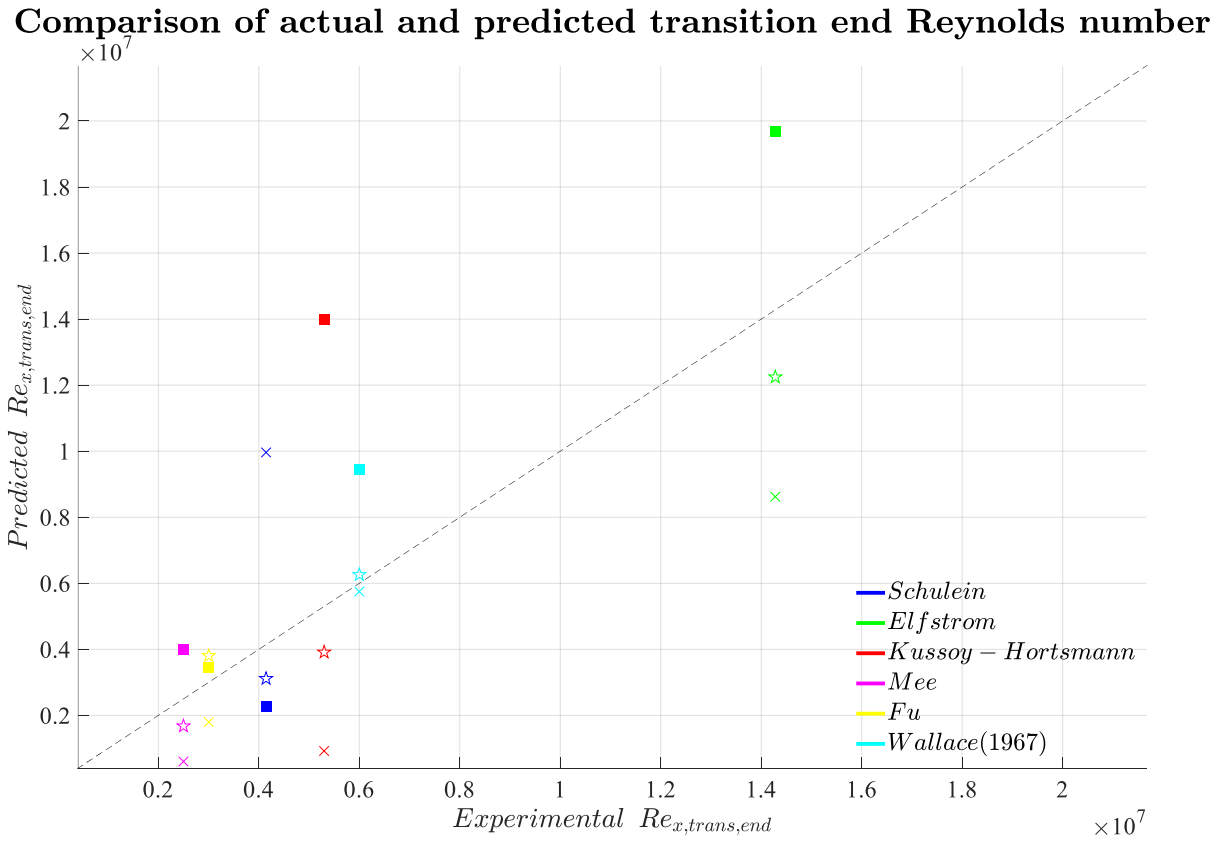


Figure 4-3: Comparison of actual and predicted transition end Reynolds number. ★- Deem & Murphy model,■ - Kanda model, ✕ - Simeonides model

The results show that the correlation of Deem and Murphy predicts the transition end location with the greatest accuracy, with both the models of Kanda and Simeonides showing various levels of accuracy. The model of Kanda appears to work better at lower Mach numbers, showing significant overpredictions for the high Mach number experiments. The correlation proposed by Simeonides generally underpredicts the transition end Reynolds number significantly. While the correlation of Deem and Murphy shows some deviation, it maintains accuracy al high Mach numbers, and it is therefore selected for this work.

4.2.1. Model structure and evaluation

The transition prediction provides the final equation required to close the system of equations and allow for prediction of any quantity for a turbulent boundary layer. For any location along

the plate, calculation of the friction velocity, boundary layer thickness and integral quantities, Algorithm 2 is followed:

ALGORITHM 2: FLAT PLATE TURBULENT BOUNDARY LAYER ALGORITHM

Input: *Freestream Flow Quantities, plate location (x)*

Output: *Boundary layer thickness, friction velocity, integral quantities*

Boundary Layer Thickness Calculation:

- Evaluate virtual origin, x_{virt} (Equations 4.33 & 4.34)
- Evaluate equivalent distance, x_{equiv}
- Evaluate reference temperature/viscosity, T^*/ μ^* (Equations 4.29 & 4.14)
- Evaluate boundary layer thickness, δ

Friction Velocity Calculation:

- Evaluate F_{Re_x} (Equation 4.44)
- Evaluate incompressible skin friction coefficient, $c_{f,inc}$ (Equation 4.45)
- Evaluate incompressible momentum thickness Reynolds number, $Re_{\theta,inc}$ (Equation 4.8)
- Evaluate wake parameter, Π (Equation 4.7)
- Solve compressible Monkewitz velocity profile for friction velocity, u_τ (Equation 4.25)

Integral Quantities Calculation:

- Evaluate integral thicknesses**,** δ^*/ θ (Equations 4.1 & 4.2)

Return *[δ, u_τ, δ^*, θ]*

The efficacy of the model in predicting high-speed turbulent velocity profiles is tested against various experimental studies. It shows very good agreement with the experimental data of Schulein and Kussoy and Hortsmann, but a poorer agreement with the results of Elfstrom. This could perhaps be attributed to the incorrect measurement of the heat flux, which was then subsequently used to calculate the skin friction coefficient by applying the Reynolds analogy $\frac{2St}{c_{f,\infty}} = 1.16$. In general, though, the method of applying a compressibility correction to an incompressible universal turbulent boundary layer profile is proven to be accurate in capturing the trends of the inner layers and the wake region.

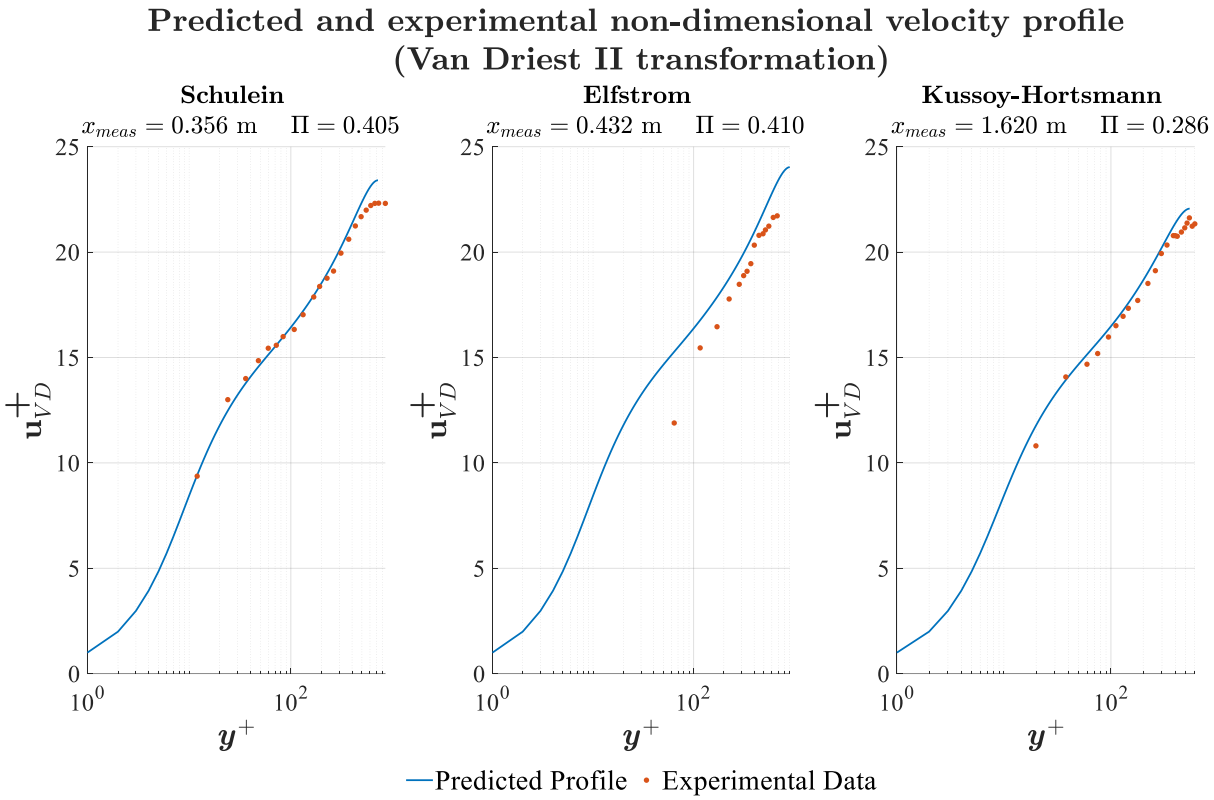


Figure 4-4: Predicted and experimental non-dimensional velocity profiles. Experiments: Schulein[18], Elfstrom[126], Kussoy & Hortsman[17]

Further validation of the universal velocity profile method employed in this work is done using the experimental velocity profile obtained by Sahoo et al.[130]. The experiment was performed at a nominal Mach number of 7.2 on an isothermal flat plate, with a wall temperature of 352K, giving a cooling ratio of 0.52. The turbulent boundary layer was established by tripping the boundary layer at 60 mm from the leading edge and the PIV was employed from 380mm to 402mm downstream of the leading edge.

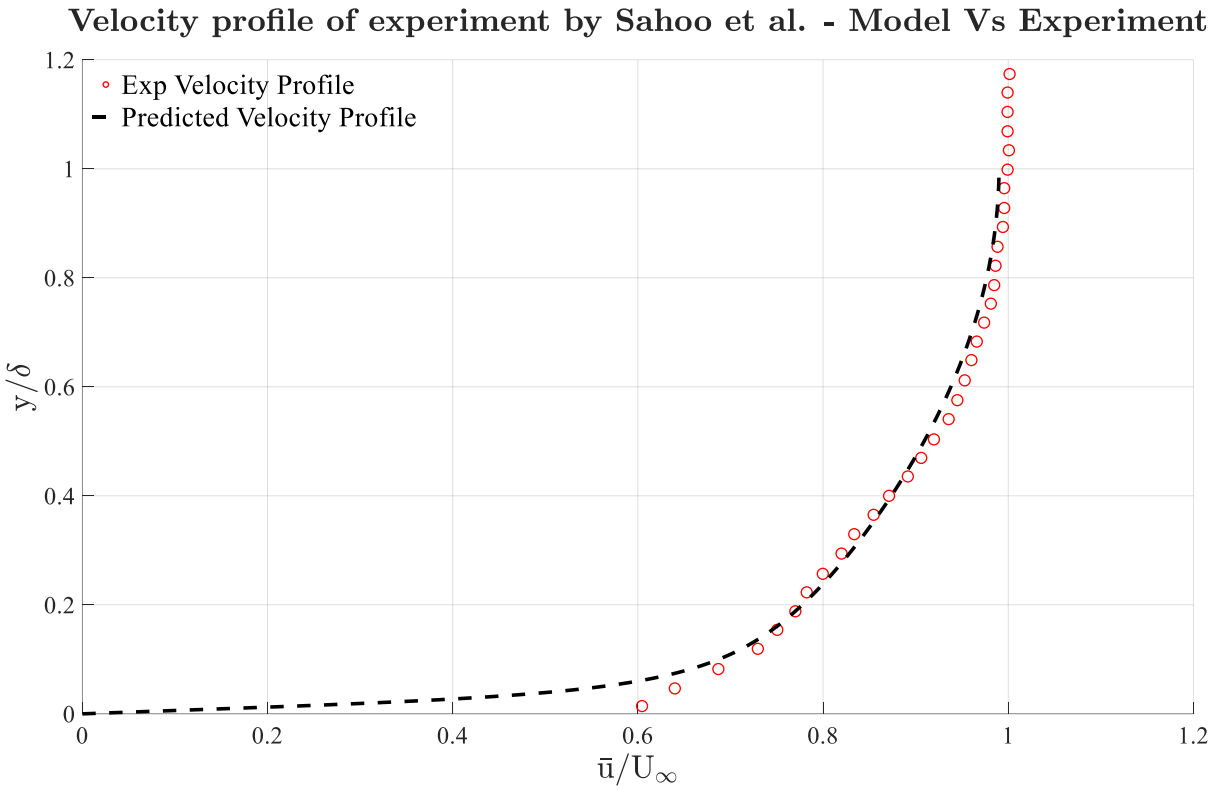


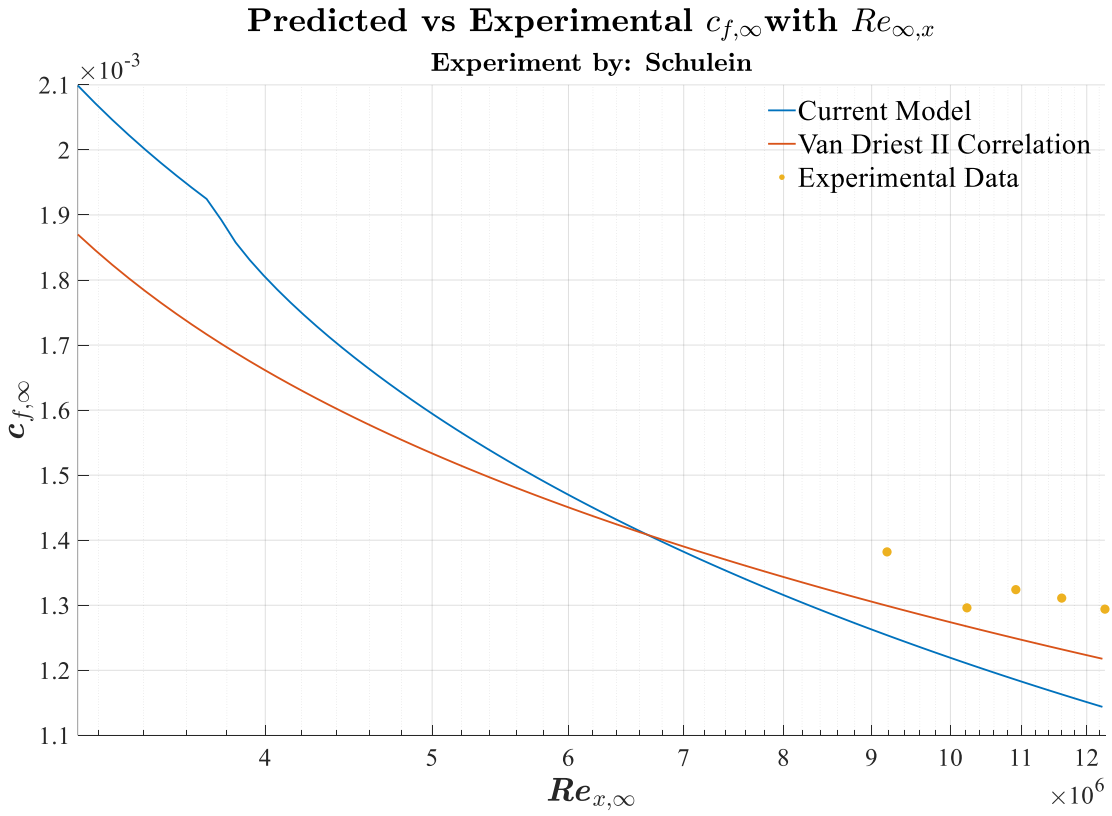
Figure 4-5: Comparison of predicted velocity profile vs experimental data of Sahoo et al.[130]

A difference in profiles is observed due to artificial tripping of the boundary layer in the experiment, which significantly alters the boundary layer structure, as observed from the work of Williams and Smits[132]. They demonstrated that the turbulent boundary layer resulting from artificial tripping has significant differences to a naturally transitioned boundary layer, manifesting in all parameters of the boundary layer, with the most significant being the influence on the wake strength. In the work by Williams and Smits[132], the boundary layer momentum thickness also shows significant differences depending on the trip height, which implies that the boundary layer in the inner region is influenced by the tripping as well.

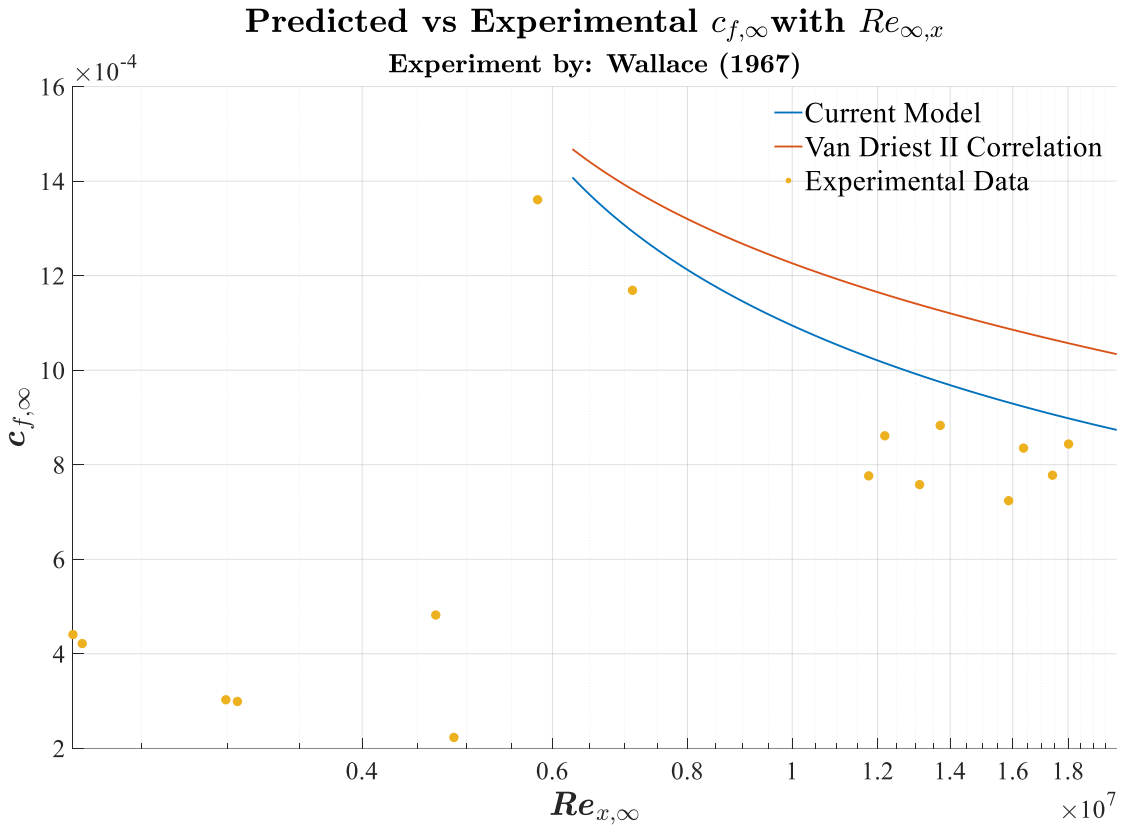
The wake parameter is increased to compensate for the non-natural transition, and the boundary layer profile of Figure 4-5 above is obtained. The wake factor is altered based on the experimental momentum thickness, which is then turned into an incompressible one with the Van Driest transformation. Equation 4.7 is subsequently used to find the updated wake parameter. The predicted velocity profile shows excellent agreement with the pitot readings from the experiment.

4.2.2. Skin friction coefficient prediction

To further evaluate the model capabilities, the variation in skin friction coefficient is evaluated and compared against experiments with available skin friction data. The variance of the skin friction coefficient is plotted against the streamwise distance from the leading edge and presented in Figure 4-6.



a)



b)

Figure 4-6: Predicted and experimental skin friction coefficient. Experiments: Schulein[18], Wallace[129]

The proposed model shows very good agreement with the experimental results of Wallace, while showing satisfactory agreement with the experiment of Schulein. The difference can be attributed to the prediction of the transition region and length, which directly affects the solution obtained for the skin friction coefficient. As discussed in Chapter 3.2, another factor that affects the skin friction coefficient value is the values reported by the authors regarding the friction velocity. This is supported by the fact that the model shows superior performance for Wallace's experiment, with which a better agreement is obtained on the transition location (see Figure 4-3), while also outperforming the Van Driest II correlation in predicting the skin friction coefficient.

An important variable present in the current model is the wake parameter, Π. Its significance is worth investigating in further detail, as it directly affects the quality of the results.

4.2.3. Influence of wake factor

Of interest is the influence of the wake factor, Π, to the overall accuracy of the model. Figure 4-7 compares the model with varying wake parameters compared to the experimental values of Schulein. There is a significant variation observed, especially in the defect region, as

expected. The reason for the heavy influence of the wake parameter is that, since the value of the boundary layer thickness is determined using equation 4.29, the wake influence is added directly to a predetermined δ^+.

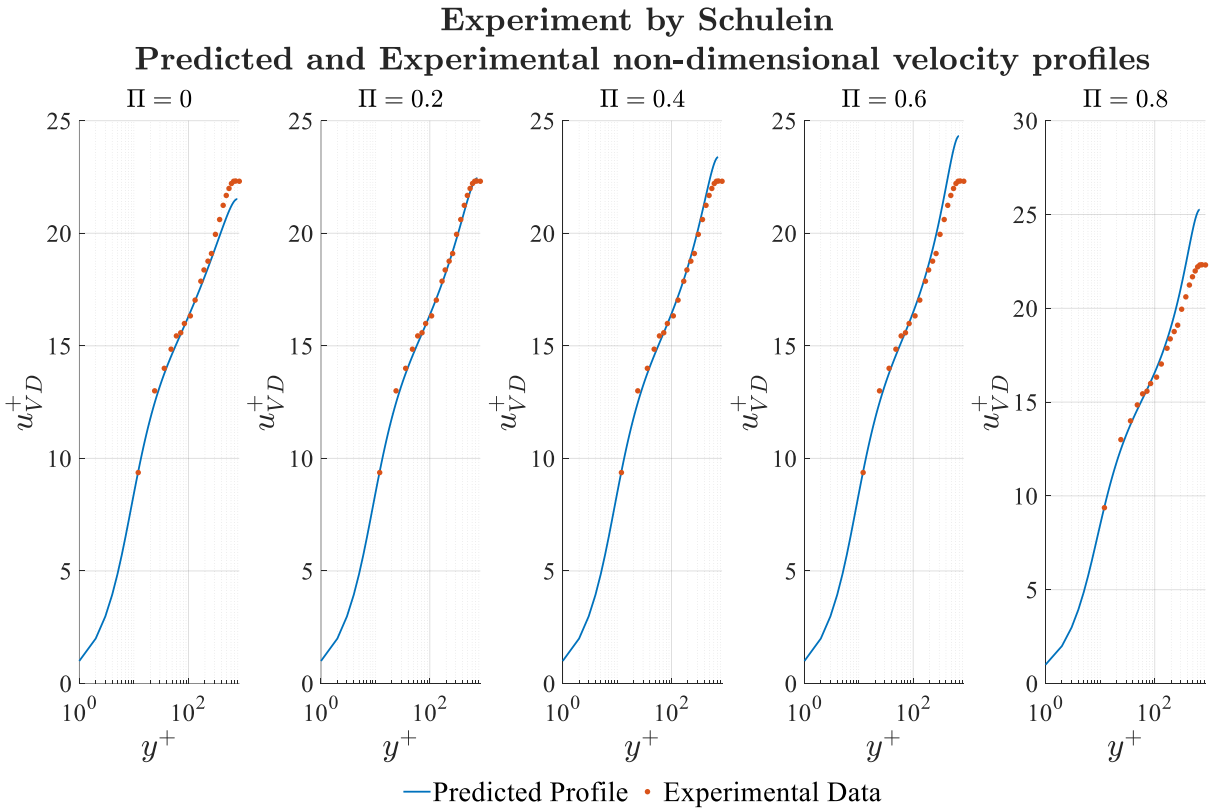


Figure 4-7: Influence of the wake factor Π on the predicted velocity profile

The wake factor influence on the predicted profile is to reduce the predicted friction velocity. This results in a higher non-dimensional velocity and lower non-dimensional distance. This influences the integral solution obtained for the momentum thickness, which, for non-dimensional units and the quadratic temperature relation is obtained using:

$$\theta = \frac{\nu_w}{u_\tau}\frac{T_\infty}{T_w}\int_0^{\delta^+}\frac{\bar{\bar{u}}^+(1-\bar{\bar{u}}^+)}{1+b_T\bar{\bar{u}}^+-a_T^2\bar{\bar{u}}^+}dy^+ \qquad 4.47$$

Table 4-2 summarises the variance of friction velocity, U_τ, non-dimensional boundary layer thickness, δ^+, and momentum thickness for the same measurement location calculated using the current model.

Table 4-2: Effect of wake parameter Π on the model prediction of δ+ and θ

Π	**U_τ (m/s)**	**δ^+**	**θ (mm)**
Exp	43.4	560	0.189

0	45.8	701.62	0.226
0.18	44.0	675.08	0.245
0.36	42.4	650.39	0.259
0.54	40.9	627.35	0.271
0.72	39.5	605.82	0.281

The values predicted by the model are very high, showing a heavy discrepancy both for δ^+ and θ. The primary reason is the underprediction of the transition point by equation 4.34, see Figure 4-3. This leads to the additional growth of the boundary layer, reflected both in the increase of δ^+ and θ but also the reduction in friction velocity. Despite this, the values provided by the equation proposed by Hasan et al. (equation 4.7) for the wake factor provide satisfactory results and allow for predictions to be made. Figure 4-8 below supports this, by showing the results from the current method and the VD II correlation on the data of Wallace.

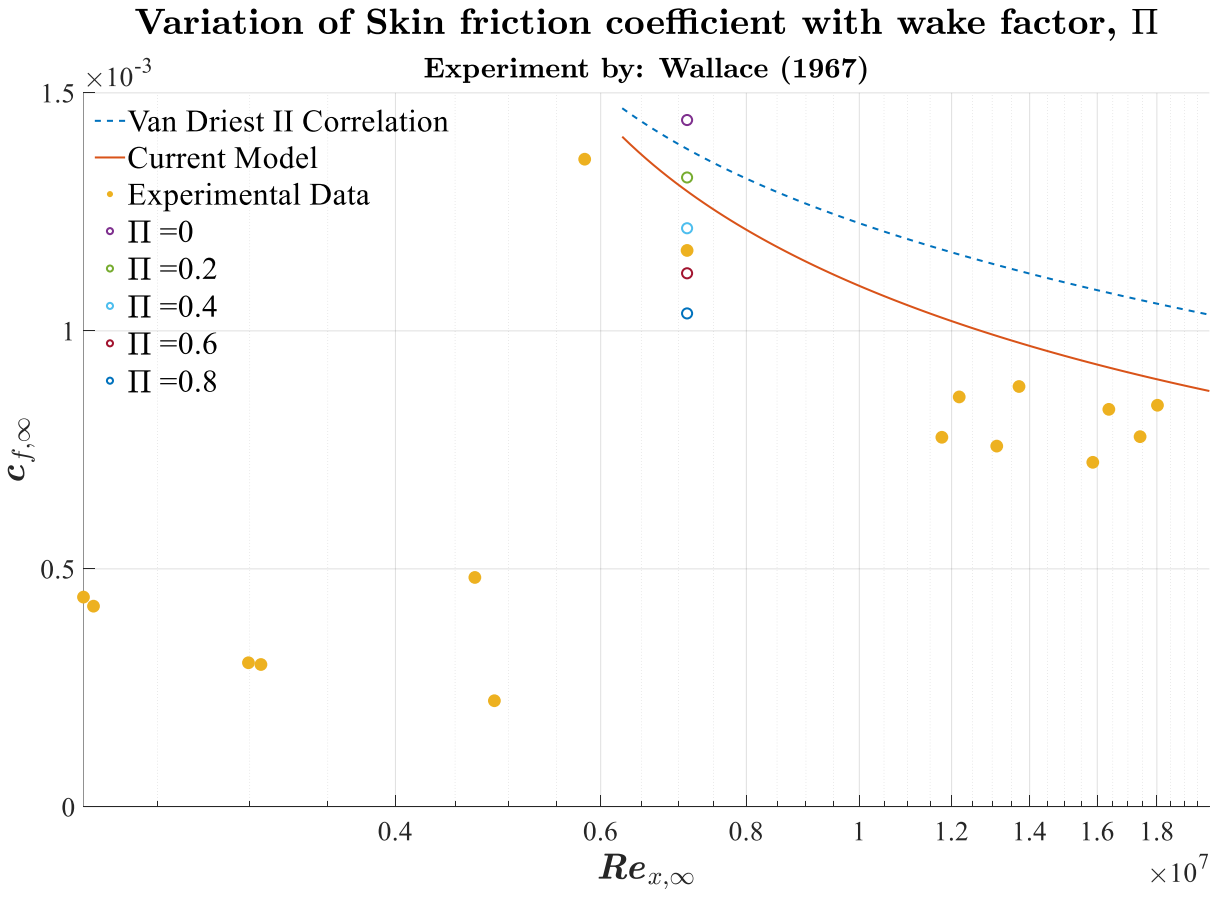


Figure 4-8: Influence of the wake factor Π on the skin friction coefficient

4.3. Chapter summary

This chapter has presented the formulation of the flat plate model used throughout this thesis. An incompressible universal turbulent velocity profile is transformed into a compressible one

through the Van Driest compressibility correction. The Monkewitz UVP is selected due to the inner and outer layer matching. The selection of the universal velocity profile is done to calculate the friction velocity and thus the integral quantities with a physics-based method.

To predict the boundary layer transition, the correlation developed by Deem and Murphy was used in its original form, for a zero-thickness plate. The final equation required to close the system of equations is the prediction of the boundary layer thickness. The general method used is the equation of Popinski and Ehrlich, but it has been modified in this work to use a different coefficient, adopting a more commonly accepted value for the coefficient of the thickness, as well as modifying the viscosity ratio to use a viscosity law instead of a power law. Solution of these equations provides a full characterisation of the boundary layer at any location past transition along the plate.

The validation of the transition and skin friction prediction models has also been presented, showing the model having superior performance to the VD II fully analytical correlation for the skin friction, and able to predict boundary layer thickness accurately provided that the transition onset location prediction is accurate.

The advantage offered by this modelling approach for a compressible turbulent boundary layer lies in its ability to predict all quantities bar the thickness at any given point from a single source, the velocity profile. As was examined in Chapter 2, most low order methods are inviscid, which, while providing the broadest design capabilities, fail significantly when CFD with viscosity is used to verify them. Other low order methods that include limited viscous considerations which typically begin in the internal section between the isolator and combustor. However, it was demonstrated that the external compression system up to and including the isolator entry shocks from the cowl are vital for the safety of the intake, as severe separation on the shoulder results in unstart. This model shows capability in predicting critical metrics such as the boundary layer thickness, wall friction velocity and momentum thickness. This is critical when coupled with the next model, that of prediction of STBLI, and the evolution of the boundary layer across the plates and cowl.

In summary, the physical and numerical consistency of the compressible boundary layer model is rigorously maintained by mapping a physically consistent incompressible turbulent velocity profile through the Van Driest II transformation, which physically accounts for the severe density variations intrinsic to high-speed flow. The quadratic relation for the temperature is altered to a more accurate variation, to be in line with higher enthalpy DNS conditions, such

as the ones that would be encountered in real flight. This only changes the coefficients, maintaining the original form of the transformation. Further, to stay in line with the original formulation of the Monkewitz velocity profile, the von Kármán constant is changed from 0.41 to 0.385 and carried throughout the solution for the boundary layer properties.

From a practical design perspective, this framework provides the evolution of critical integral quantities for intake/isolator sizing. More specifically, the displacement thickness is used to offset the capture height of the engine, while the momentum thickness that is calculated along the external system is used to size the isolator's length. The two thicknesses are also used to determine the height of the isolator. By rapidly predicting the boundary layer growth along the compression surfaces under Zero and Mild Adverse Pressure Gradient conditions, the model prevents designers from neglecting the influence of the viscous elements on the overall design of the engine.

While the compressible universal turbulent boundary layer model presented in this chapter provides a robust analytical baseline, its application is bounded by specific empirical and mathematical limitations. The framework achieves closure through heavy reliance on empirical correlations. Specifically, the equation governing the boundary layer thickness relies on a modified $1/7^{th}$ power-law formulation. Similarly, the transition onset and end locations, alongside the wake parameter, Π, used for the wake strength, are derived from empirical data. Consequently, the predictive accuracy of the profile is fundamentally tied to the prediction capabilities of these correlations.

Furthermore, physical limitations exist within the structural assumptions of the flow. The first has to do with the full bypass of the laminar and transition regions. The boundary layer is assumed to begin at the virtual origin, x_{virt}, removing the complicated transition behaviours and the entire laminar region. This might introduce errors in lower Mach numbers, where the two zones have significant development distance. The modification of the von Kármán constant (κ) to 0.385 ensures mathematical consistency with the original formulation by Monkewitz but locks the model into that specific turbulent structural assumption. Finally, because this universal velocity profile formulation is fundamentally predicated on Zero Pressure Gradient (ZPG) flat plate conditions, its accuracy is tied to the local pressure environment. While the profile's inner structure and wake formulation remain robust enough to be applied to relatively mild Adverse Pressure Gradients (APGs) without heavy profile distortion, the model cannot

physically account for more severe APGs. The inner region distorts heavily, moving the boundary layer significantly away from its equilibrium state, influencing the integral quantities.

With the flat plate model established, the next step is the establishment of a shock-turbulent boundary layer interaction model. This is required to link the states of pre- and post- shock flow properties for the plates of a mixed compression intake.

Chapter 5 - Shock-Turbulent Boundary Layer Interactions

A critical component of scramjet operation is the presence of shocks. The shocks are generated by the external compression system and the cowl. In the presence of a boundary layer, the path of the shock is altered as it penetrates deep into the boundary layer. The effect of this is a smearing of the pressure rise in the streamwise direction, reaching the inviscid value at some finite distance downstream of the interaction. A generic STBLI generated from a shock impingement and a representative pressure rise are presented in Figure 5-1.

It is evident that the presence of the boundary layer has a significant influence in the near pre- and post- shock regions. Not only are the physical properties of the boundary layer undergoing rapid changes, but the trajectory of the shock deviates from the inviscid trajectory. Estimation of the physical quantities post-shock and the viscous trajectory of the shock must hence be modelled to ensure that the resulting scramjet configuration accounts for these important interactions. This chapter presents the methodology employed to achieve this.

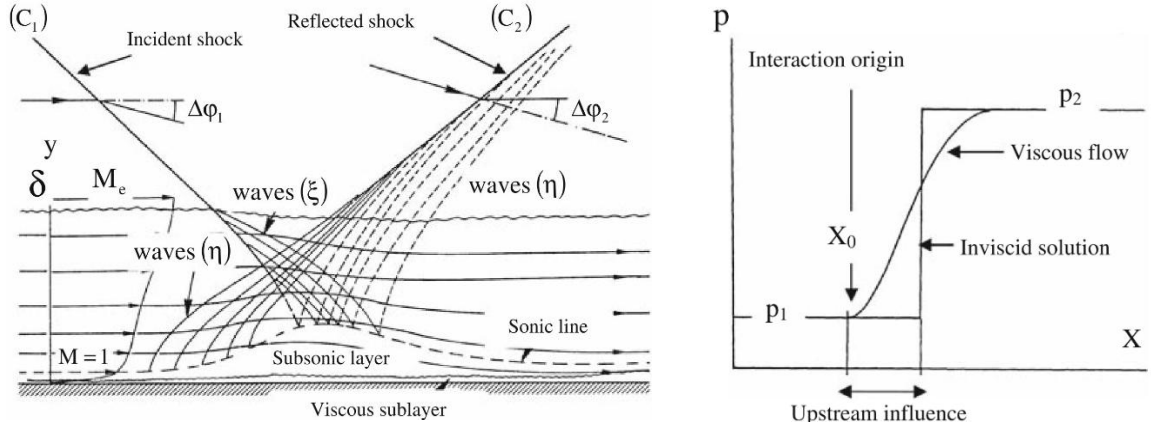


Figure 5-1: Generic shock-turbulent boundary layer interaction (left) and associated streamwise pressure rise (right). Reproduced from Delery [133]

Prediction of the behaviour of the flow in the vicinity of the interaction is a challenging problem. The interaction involves strong coupling between inviscid shocks and rapidly evolving viscous effects over very short streamwise distances. The approach adopted in this work, therefore, seeks to capture the dominant physical mechanisms governing shock penetration into a turbulent boundary layer. The primary effects that this method attempts to capture are compressibility effects, the variation of local Mach number across the boundary layer, and the associated deviation of the shock trajectory using a reduced-order, physics-based formulation.

By combining a compressible universal turbulent velocity profile with local application of inviscid shock relations across a stratified boundary layer, the method provides a physically consistent estimate of both post-shock properties and the viscosity-affected shock path. This methodology builds on the approach of Elfstrom et al. [11], which has been shown to capture key features of STBLI behaviour, and is particularly suited to the present design-oriented framework where robustness, computational efficiency, and physical transparency are required.

At the corner, the velocity profile is evaluated by application of the compressible universal turbulent velocity profile, described in Chapter 4 -. Then, the boundary layer is stratified into n points, starting from a point within the boundary layer up to first instance where the streamwise velocity reaches freestream. At each point, the Mach number is evaluated, and application of the inviscid shock relations (Equations 5.13-5.15) provides the local shock angle between successive strata. The stratification approach further allows the influence of the boundary layer on shock structure to be incorporated in a continuous manner, reflecting the progressive smearing of the pressure rise observed in experimental STBLI studies.

Before application of the method, however, the question of whether the boundary layer will separate is of importance. Separation will heavily influence the incoming boundary layer and would render the proposed method invalid. Thus, a method to predict the state of the boundary layer is needed to ensure boundary layer attachment.

5.1. STBLI Model Formulation

5.1.1. Separation state prediction

At the compression corner, it is possible, given the incoming boundary layer and the intensity of the adverse pressure gradient, that the boundary layer separates, generating a separation bubble. While very small separation bubble is acceptable, any bubble large enough to influence the flow field must be avoided, especially near the isolator entry. To avoid situations where significant flow separation occurs, a modified version of the well-known Souverein criterion is utilised.

The original Sourevein criterion[86] was developed on the principle that there is an equivalency between the mass deficit between the boundary layer entering and the boundary layer exiting the shock-turbulent boundary layer interaction. Considering mass equivalency between the two, the authors arrived at an expression for the interaction length for the interaction in terms of the displacement thicknesses, shock and deflection angles as well as the mass flow deficit:

$$L_{interaction} = \delta_{in}^{*} \frac{\sin(\beta - \theta)}{\sin(\beta)\sin(\theta)} \left(\frac{\dot{m}_{out}}{\dot{m}_{in}} - 1 \right) \quad 5.1$$

Where the mass flow deficit is defined by:

$$\dot{m}_i = \rho_i U_i \delta_i^{*} \quad 5.2$$

Non-dimensionalising the interaction length:

$$L^{*} = \frac{L}{\delta_{in}^{*}} \frac{\sin(\beta)\sin(\theta)}{\sin(\beta - \theta)} \quad 5.3$$

to define a criterion for whether separation occurs and its scale, the pressure gradient that can be supported by the boundary layer is equated to the dynamic pressure, resulting in the separation criterion, S*:

$$S^{*} = \frac{2k \left(\frac{P_{post}}{P_{pre}} - 1 \right)}{\gamma M a_{\infty,pre}^{2}} \quad 5.4$$

The value of k was found by the authors to be dependent on the momentum thickness Reynolds number:

$$k = \begin{cases} 3 \ (Re_\theta < 10000) \\ 2.5 \ (Re_\theta \geq 10000) \end{cases} \quad 5.5$$

An analytic function to relate the non-dimensional interaction length to the separation criterion was determined from data fitting of various experiments, arriving at the power-law correlation:

$$L^{*} = a S^{*b} \quad 5.6$$

The original values of a and b were set at 1.3 and 3 respectively. The value of L* indicates the state of separation. According to Souverein, a value of L* < 1 indicates an attached interaction, values between 1 and 2 indicate incipient separation, and L* > 2 indicates separation.

The coefficient, ‘a’, appears to also be dependent on the momentum thickness Reynolds number, as determined by analysis of a multitude of STBLI by Hong et al. [85] expressed by:

$$a = \begin{cases} 1.45(Re_\theta < 10000) \\ 2.33(Re_\theta \geq 10000) \end{cases} \quad 5.7$$

The criterion proved accurate for many adiabatic experiments; however, the influence of wall temperature was not explicitly factored. Jaunet et al. [84] suggested a correction to the factor ‘k’ based on the Free Interaction Theory, which results in:

$$k_{corrected} = k\sqrt{\frac{c_f^2}{c_{f,AD}^2}} \tag{5.8}$$

With the updated Souverein criterion, a determination of the separation state of the STBLI is made. If the boundary layer is predicted to be attached, the pressure distribution can be predicted.

5.1.2. Pressure distribution prediction

If separation does not occur or is small enough, the universal velocity profile can still describe the incoming boundary layer without significant distortions. The method described in this subsection describes the pressure rise along the interaction how the location where the pressure rise ends is determined.

At the compression corner, the velocity profile is constructed based on the universal profile and the Van Driest compressibility correction. With the velocity profile, a Mach number profile is also required, which will be used with the inviscid shock equations to solve for the shock angle and pressure rise.

The Mach number profile along the boundary layer is described by:

$$\frac{Ma}{Ma_\infty} = \frac{u}{U_\infty}\sqrt{\frac{T_\infty}{T}} \tag{5.9}$$

Introducing a quadratic temperature relation with the updated coefficients of Duan and Martin:

$$\frac{Ma}{Ma_\infty} = \frac{u}{U_\infty}\sqrt{\frac{T_\infty}{T_w}}\sqrt{\frac{1}{1 + b_T\left(\frac{u}{U_\infty}\right) - a_T^2\left(\frac{u}{U_\infty}\right)^2}} \tag{5.10}$$

Rearranging and solving for the velocity ratio results in a quadratic equation, which when solved for the positive root results in an expression in terms of the Mach number ratio:

$$\frac{u}{U_\infty} = \frac{\bar{M}^2\bar{T}_w b_T}{2(\bar{M}^2\bar{T}_w a_T^2 + 1)} + \frac{1}{2}\sqrt{\left(\frac{\bar{M}^2\bar{T}_w b_T}{(\bar{M}^2\bar{T}_w a_T^2 + 1)}\right)^2 - 4\left(\frac{\bar{M}^2\bar{T}_w}{(\bar{M}^2\bar{T}_w a_T^2 + 1)}\right)} \tag{5.11}$$

$$\bar{M} = \frac{Ma}{Ma_\infty}, \bar{T}_w = \frac{T_w}{T_\infty}$$

Equation 5.11 is then substituted into the velocity profile determined using Equation 4.25, which links the vertical distance to the Mach number within the boundary layer.

The next step is the simultaneous solution of Equations 4.25 and 5.11 for the local Mach number, *Ma*, vertically along the boundary layer, until the free stream is reached. The solution of the two equations provides the Mach number profile across the boundary layer. To ensure a solution exists at every point of the solution, the initial point within the boundary layer is chosen such that the imposed deflection of the ramp would result in a post-shock Mach number of unity. This ensures that the only the attached angle solutions are accepted, leading to fully physical descriptions of the shock trajectory and pressure distribution.

The equation which links the upstream Mach number and upstream deflection to the downstream Mach number is given by:

$$Ma_2^2 = \frac{(\gamma - 1)Ma_1^2 \sin^2(\beta) + 2}{\left(2\gamma Ma_1^2 \sin^2(\beta) - (\gamma - 1)\right)\sin^2(\beta - \varphi)} \tag{5.12}$$

Where β and φ are the shock angle and deflection angle in degrees respectively. The subscripts "1" and "2" are used to refer to pre- and post-shock properties respectively. The minimum incoming Mach number that will result in a post-shock Mach number of unity is then determined by solving Equation 5.12 with M_2 being 1.

Other important inviscid oblique shock relations used to determine post-shock freestream conditions are:

$$\frac{\rho_2}{\rho_1} = \frac{(\gamma + 1)Ma_1 \sin^2\beta}{(\gamma - 1)Ma_1 \sin^2\beta + 2} \tag{5.13}$$

$$\frac{P_2}{P_1} = \frac{2\gamma Ma_1 \sin^2\beta - (\gamma - 1)}{(\gamma + 1)} \tag{5.14}$$

$$\frac{T_2}{T_1} = \frac{{}^{P_2}/_{P_1}}{{}^{\rho_2}/_{\rho_1}} \tag{5.15}$$

All post-shock properties rely on knowledge of the shock angle, β. The famous β-φ-Ma relation of Equation 5.16 links the deflection imposed by the ramps and the incoming free stream Mach number to the shock angle.

$$\cot(\varphi) = \tan(\beta)\left(\frac{(\gamma + 1)Ma_1^2}{2(Ma_1^2 \sin^2(\beta) - 1)} - 1\right) \tag{5.16}$$

Solution for the shock angle, β, can be obtained by rearranging Equation 5.16 for powers of tan(β) and solving the resulting cubic formula for the positive and real root. This provides a fully analytical solution for the shock angle.

A final modification is required to fully capture the full pressure increase profile. Using the boundary layer edge values results in an incomplete profile, as the boundary layer edge Mach number may be substantially lower than the freestream Mach number. Thus, to produce a complete Mach number profile, Equation 4.25 is solved for a velocity ratio of unity, with the value of skin friction velocity determined through the normal boundary layer edge values. Then the wake profile component is modified with the vertical distance to the velocity ratio of unity instead of boundary layer edge (0.99U). The modified wake then takes the form:

$$u^+_{wake,mod} = \frac{1}{\kappa}\left((1+6\Pi)\left(\frac{y^+}{\delta^+_{\bar{u}=1}}\right)^2 - (1+4\Pi)\left(\frac{y^+}{\delta^+_{\bar{u}=1}}\right)^3\right) \qquad 5.17$$

Where $\delta^+_{\bar{u}=1}$represents the non-dimensional vertical distance where the velocity reaches the free stream value ($\bar{u} = 1$).

The difference of the two velocity profiles is shown in Figure 5-2. The extension of the velocity profile to the free stream allows for the full influence of the boundary layer on the shock to be captured. The cyan line in Figure 5-2 below was solved only up to the boundary layer and it is clear that if the full velocity profile is not considered, the pressure rise falls short of the inviscid value by a significant margin. Therefore, this modification from the original formulation is required to capture the full extent of the pressure rise.

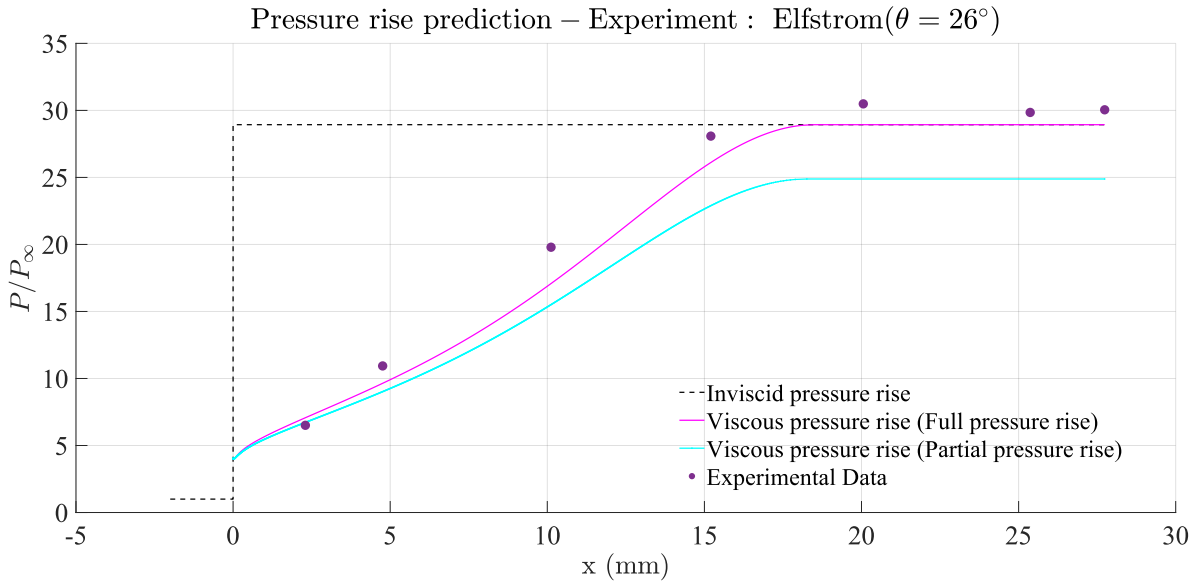


Figure 5-2: Comparison of partial (cyan - up to $\delta^+_{\bar{u}=0.99}$) and full (magenta – up to $\delta^+_{\bar{u}=1}$) velocity profiles considered at ramp foot. Considering the velocity profile up to boundary layer thickness underpredicts the shock interaction.

With the above equations, the pressure distribution across the shock can be predicted. Firstly, the value of y^+ at a given Mach number is found by simultaneous solution of equations 4.25 (compressible universal profile) and 5.11 (Mach number profile). Since the values of friction velocity and wall kinematic viscosity are known, the vertical distance within the boundary layer can be determined.

For each value of y up to the vertical distance to the freestream, the shock angle is calculated using the analytical solution obtained from equation 5.16. The streamwise location of the shock at the exit point out of the boundary layer, x_{exit} is found by the solution of a recurring geometric relation of a straight line between point $[x_i, y_i]$ and $[x_i, y_i]$ up to the last point $[x_{exit}, \delta_{\overline{\overline{u}}_{pre}=1}]$. The final equation for the shock exit location is:

$$x_{exit} = -\frac{y_1}{\tan(\beta_1)} + \frac{\delta_{\overline{\overline{u}}_{pre}=1}}{\tan(\beta_{n-1})} + \sum_{i=2}^{n-1} y_i \left(\frac{1}{\tan(\beta_{i-1})} - \frac{1}{\tan\beta_i}\right) \qquad 5.18$$

With n being the number of layers that the boundary layer is stratified in, β_i being the shock angle in the i^{th} layer, calculated using the local Mach number and the analytical solution of equation 5.16, and $\delta_{\overline{\overline{u}}_{pre}=1}$ is the distance where the velocity ratio reaches unity upstream of the shock.

An example of separating the boundary layer profile into layers, called strata, is shown below in Figure 5-3, based on the DNS of Priebe and Martin. An assumption that goes into the above method is that the number of points allows for the shock line between them to be assumed as straight (inviscid shock line), which is a fair assumption considering that outside the viscous sublayer, the effects of viscosity diminish and thus can be considered inviscid.

The second part of the pressure rise prediction is the transmission of the pressure disturbance at a given vertical distance to the surface. This is achieved through Mach waves performing the pressure transmission from the shock to the surface without reflection. The assumption is that the flow turns fully due to the shock and thus parallel to the ramp surface.

The Mach angle, μ_n, at the local post-shock Mach number is found by:

$$\mu_n = \sin^{-1}\left(\frac{1}{Ma_{post}}\right) \qquad 5.19$$

To solve for the end of pressure rise, $x_{P,end}$, the starting point is set at the previously calculated $[x_{exit}, \delta_{\overline{\overline{u}}_{pre}=1}]$, and at each stratum, indicated by n-j, Equation 5.20 below is evaluated until

the first point within the boundary layer is reached. The subscript j indicates the index of the point along the Mach line, with j = 1 indicating the point where the streamline considered meets the shock.

$$x_{P,j+1} = \frac{\left(y_j + x_{n-j}\tan(\varphi) - x_j \tan\left(\varphi - \mu_{n-j}\right) - y_{n-j}\right)}{\left(\tan(\varphi) - \tan\left(\varphi - \mu_{n-j}\right)\right)} \qquad 5.20$$

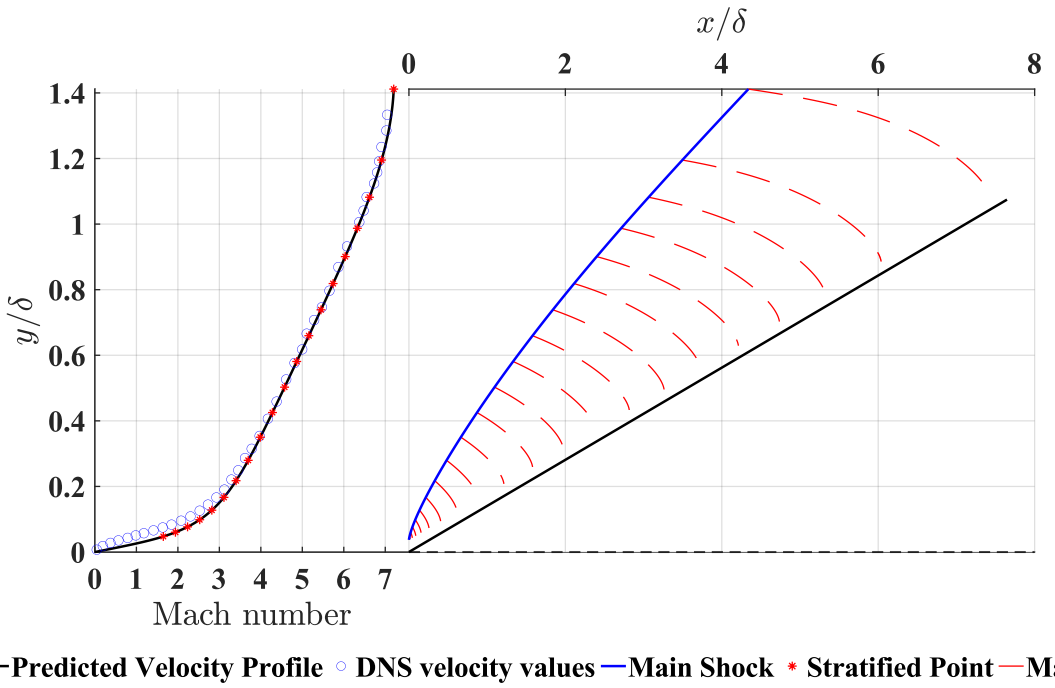


Figure 5-3: Stratification of predicted velocity profile, shock shape and Mach waves for the DNS of Priebe and Martin[125]

At $x_{P,end}$, the boundary layer is treated as a ZPG boundary layer, and therefore the ZPG compressible universal velocity profile may be used to obtain local properties.

A necessity for the boundary layer thickness at the end of pressure rise point is then encountered. It is required to determine the local skin friction coefficient (see Chapter 4 -) but also to provide the starting point for analysis of subsequent ramps in the compression system.

To model the exiting boundary layer, the x-coordinate where the incoming streamline of velocity ratio of unity meets the shock is used as the starting point, x_{exit}. As with the boundary layer on a flat plate, the vertical distance at which the outgoing streamline reaches a unity velocity ratio is needed. The longitudinal distance along the plate where this distance is required is the point where pressure reaches the inviscid value, $x_{P,end}$. The vertical distance in

the incoming plate frame of reference is then calculated by assuming that the streamline post-shock always remains parallel to the plate:

$$y_{\bar{\bar{u}}_{post}=1} = \frac{x_{P,end} + y_{P,end} - x_{exit} + {\delta_{\bar{\bar{u}}_{pre}=1}}/{\tan\varphi}}{\left(\tan\varphi + {1}/{\tan\varphi}\right)} \tag{5.21}$$

To obtain the boundary layer thickness, a rotation of axes is required. The axes are rotated by ramp angle φ. The value of $y_{\bar{\bar{u}}_{post}=1}$ in the rotated frame of reference represents the vertical distance from the surface where the velocity reaches the freestream value. Solving the compressible universal velocity profile, described by Equation 4.25 and the wake profile of Equation 5.17, provides the friction velocity and subsequently the local boundary layer thickness. With the value of the boundary layer thickness, Equation 4.29 can be solved for an equivalent length, which is used as the starting point for subsequent analysis of the next compression corner. Figure 5-4 provides a schematic representation of the system under consideration, highlighting the critical points calculated by Equations 5.18, 5.20 and 5.21.

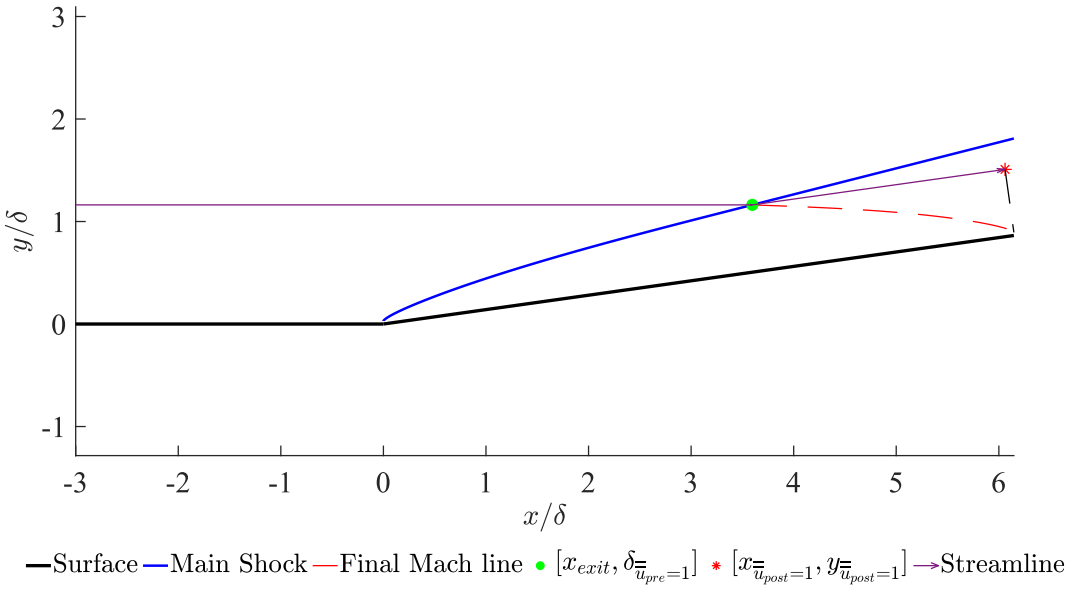


Figure 5-4: STBLI schematic for geometric points used in post-shock boundary layer thickness determination

5.2. Validation of STBLI Model

Similar to the flat plate model, validation of the STBLI model is done on experimental and numerical simulation data. The experiments of Elfstrom and Coleman as well as the DNS of

Priebe/Martin and RANS of Zuo have been used to validate the pressure rise prediction across an attached boundary layer. Freestream properties are tabulated in Table 5-1.

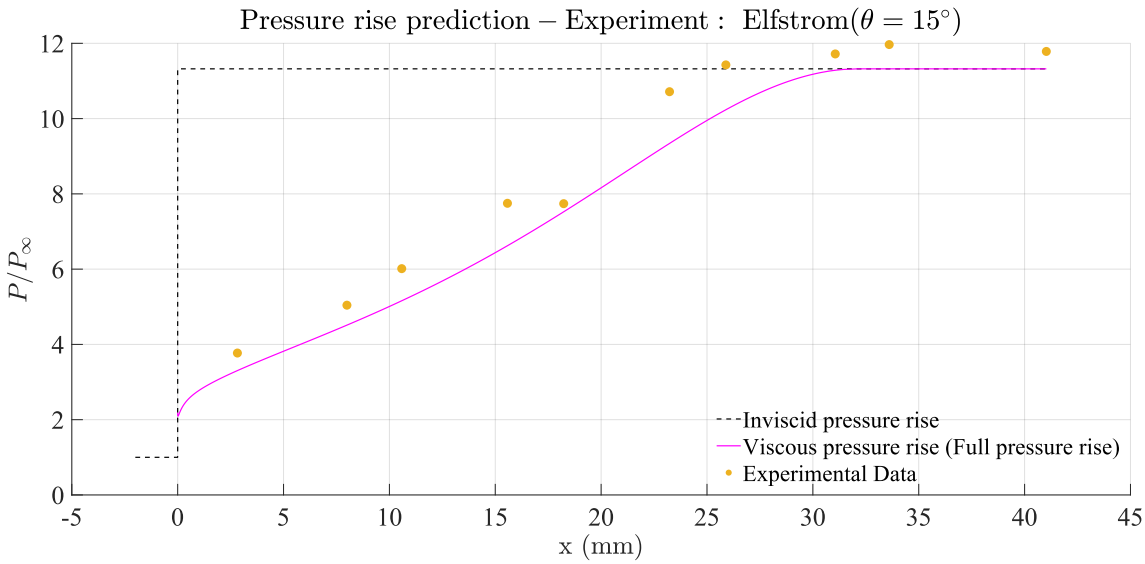
Table 5-1: Properties of validation studies

Case	Ref	M_∞	T_∞ (K)	ρ_∞ (kg/m^3)	T_{wall} (K)	Re_{unit} (1/m)	θ (deg)
Elfstrom	[15], [126]	9.22	64.5	0.172	295	5.51E7	15/26/30
Priebe	[125]	5	68.3	0.204	300	3.45E7	8
Zuo	[134]	6	71.65	0.4660	133.5	9.78E7	30

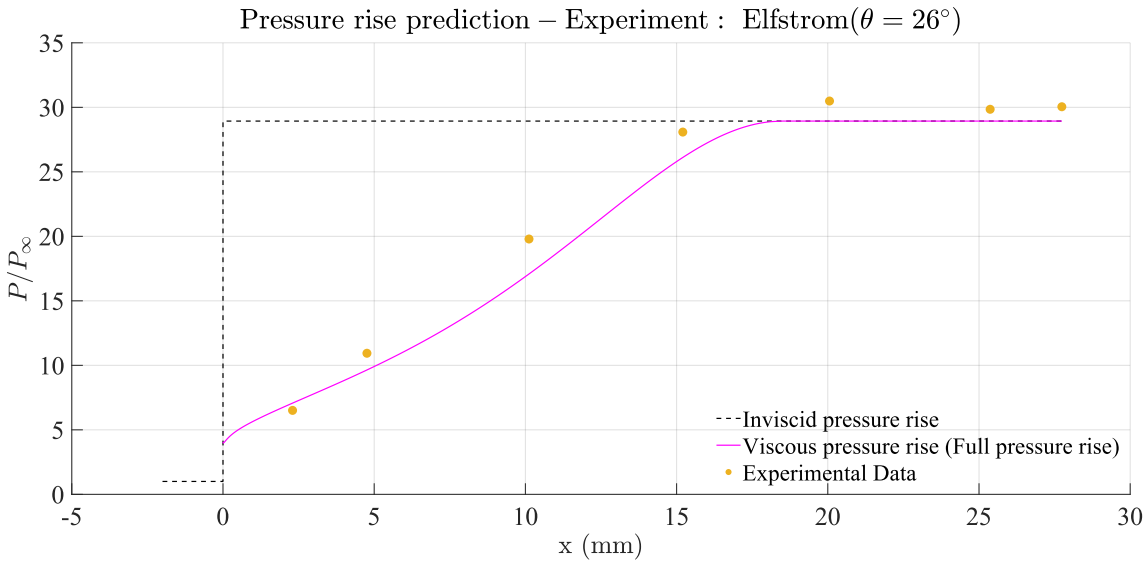
The results of the pressure prediction for the studies are shown in Figure 5-5. The model prediction shows fair to very good agreement with all studies, accurately capturing the pressure smearing trend. The experiment of Elfstrom [15], [126] shows excellent agreement for all angles, although at the highest deflection of 30^o, the pressure rise exhibits a slower increase compared to the experimental data. This could perhaps be attributed to the presence of a separation bubble at the compression corner foot, altering the flow field in the very near post-shock region.

This appears to be further supported by the pressure rise predicted for the RANS of Zuo[134]. The initial pressure rise shows a significantly stronger interaction than observed in the numerical simulations but reaches the inviscid value at the same distance as the simulation results. Worth mentioning is that the incoming boundary layer is very thin and would exhibit very low turbulence, as the length of the domain used (45 mm) would not be sufficient for a fully equilibrium turbulent boundary layer to develop. Thus, the wake parameter would be very low or zero, resulting in a fuller velocity profile. This in turn affects the pressure rise profile, making it much sharper, as observed in Figure 5-5e).

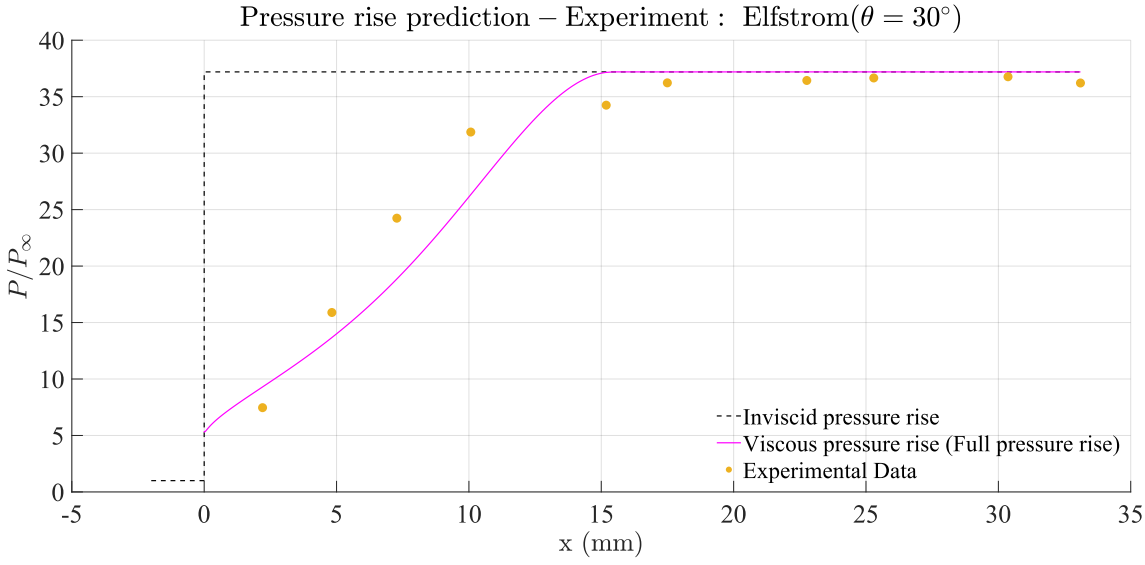
Similarly, the pressure rise prediction for the DNS of Priebe and Martin [125] rises in a sharper manner than the DNS, with the wake parameter influencing the sharpness of the pressure rise, thus reaching the inviscid value in a shorter distance than the prediction of the DNS. However, it still provides a good qualitative agreement with the data.


Pressure rise prediction – Experiment : Elfstrom($\theta = 15°$)
P/P_∞
x (mm)
Inviscid pressure rise
Viscous pressure rise (Full pressure rise)
Experimental Data

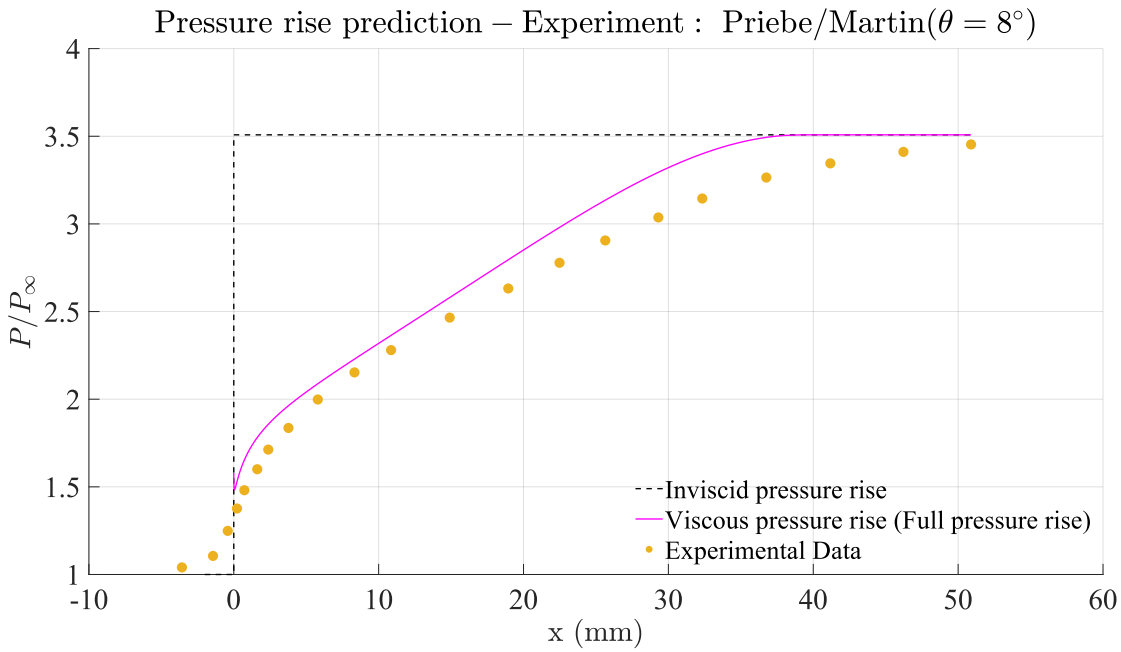
(a)


Pressure rise prediction – Experiment : Elfstrom($\theta = 26°$)
P/P_∞
x (mm)
Inviscid pressure rise
Viscous pressure rise (Full pressure rise)
Experimental Data

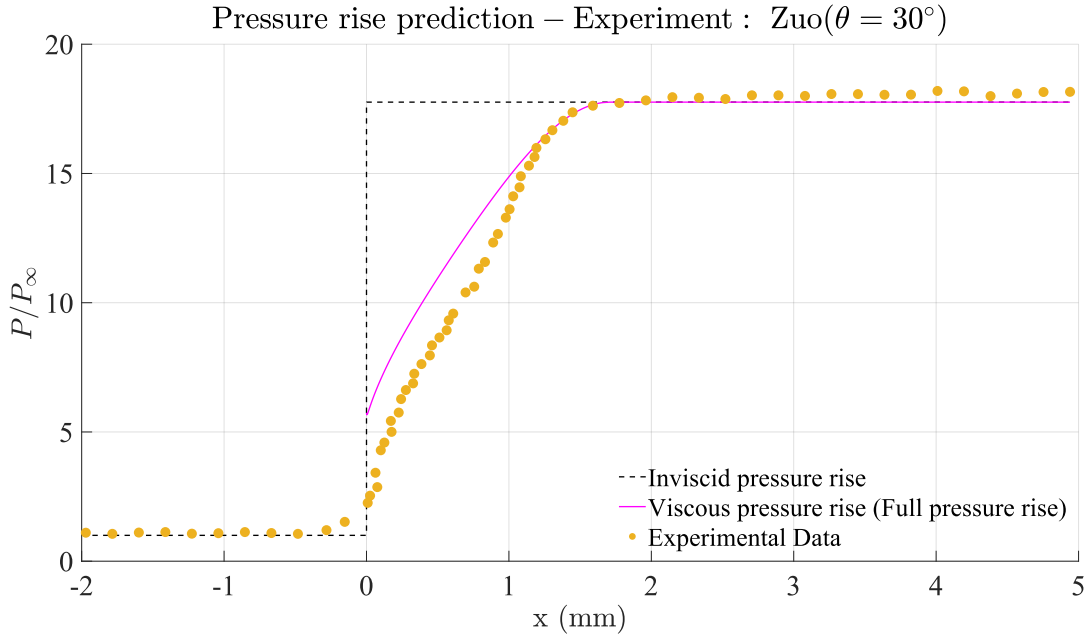
(b)


Pressure rise prediction – Experiment : Elfstrom($\theta = 30°$)
P/P_∞
x (mm)
Inviscid pressure rise
Viscous pressure rise (Full pressure rise)
Experimental Data

(c)



(d)



(e)

Figure 5-5: Comparison of pressure rise predicted by proposed model and experiment/numerical studies a-c) Elfstrom [15], [126] (EXP), d) Priebe and Martin [125] (DNS), e) Zuo [134] (RANS)

Validation of the post-shock boundary layer properties is significantly more challenging, as no experiments or numerical studies provide explicit values for the boundary layer post-shock.

The boundary layer thickness post-shock was compared to the approximate value of the boundary layer thickness after the shock in the DNS of Priebe and Martin, at matching conditions to the ones used by the authors. In the absence of velocity profiles at the far post-shock region, the approximate boundary layer thickness was determined from the numerical

Schlieren, at the location downstream of the shock where the measurements of the authors end ($x/\delta_{ref} = 22$), with $\delta_{ref} = 5$ mm. This point was selected as it is the closest to the inviscid pressure rise, meaning the pressure gradient would be at its minimum, providing the closest match to the underlying model assumption that boundary layer thickness is measured only in regions of zero pressure gradient. To obtain the boundary layer edge from the numerical Schlieren, a visual criterion is used, where the boundary layer edge is determined as the dark outline surrounding the turbulent region, as seen below in Figure 5-6.

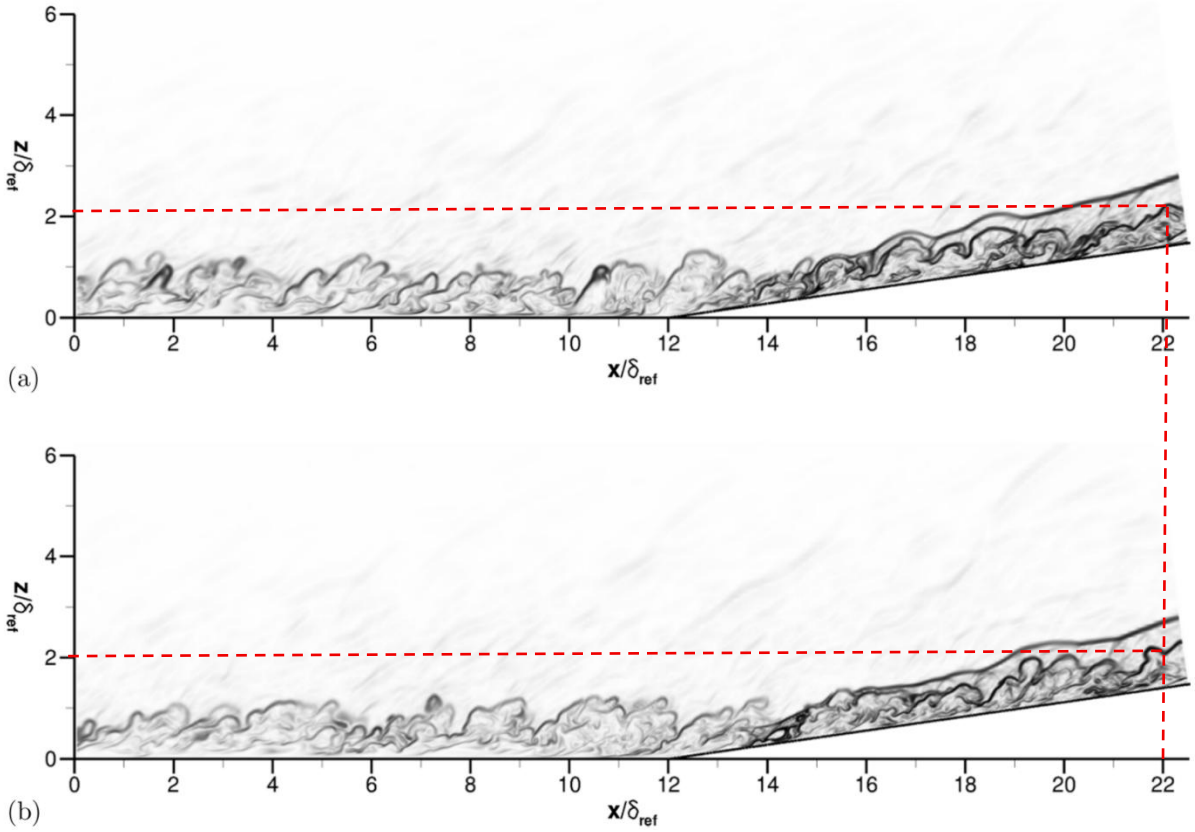


Figure 5-6: Numerical Schlieren of Priebe & Martin, recreated from[125]. Red lines indicate the location of boundary layer estimation for comparison to model prediction.

The values obtained from the proposed method show very good agreement with the DNS values. The boundary layer thickness from the DNS was determined to be between 3.46 mm in the lower Schlieren image and 3.86 mm in the upper Schlieren image, while the model value is 3.5 mm. This corresponds to a relative absolute error between the DNS and modelling approach of 1% and 9% respectively. Given the inherent uncertainty in the visual method used to estimate the boundary layer thickness, this level of agreement indicates that the proposed method captures the post-shock boundary layer growth with good accuracy, lending credence to its efficacy.

5.3. Chapter Summary

An analytical model allowing for the rapid and accurate pressure distribution across an attached turbulent boundary layer interacting with a shock wave has been proposed in this chapter.

The primary method follows closely the method of Elfstrom[15], [126], which uses a velocity profile at the foot of the compression corner or shock interaction along with the inviscid shock relations to predict the shock trajectory. The velocity profile used is changed from the original formulation, using the Van Driest I profile, to the compressible universal turbulent profile presented in Chapter 4.

New additions to the original method include a separation criterion, which is the criterion of Souverein[86], along with the temperature correction by Jaunet et al.[84], and the modification to the coefficient of Hong et al.[85]. The inclusion of the separation criterion is crucial to this work, as the optimisation of any hypersonic intake/isolator necessitates that major separation does not occur at any point, due to performance losses associated with mass flow rate loss and the potential of unstart.

Novel to this work though is the capability of the model to predict post-shock boundary layer properties. This is achieved by tracing the terminal streamline of the boundary layer along the interaction and solving the system of equations presented in Chapter 4 in reverse. It achieves good accuracy in predicting both the pressure rise profile and distance required, the skin friction rise along the interaction and the boundary layer properties.

The importance in accurately capturing the influence of the shock and boundary layer on each other is vital for the correct and optimum operation of a scramjet. Incorrect impingement of shocks on the boundary layer results in multiple adverse effects, ranging from mass spillage and thrust reduction to full unstart due to insufficient mass flow rate being fed to the combustor. The requirement of adherence to the shock-on-tip and shock-on-shoulder conditions in the presence of a boundary layer is vital to eliminate these adverse effects and minimise (or ideally eliminate) reflections of shock or expansion waves in the isolator/combustor. The model was tested against experimental and numerical studies at various Mach numbers and Reynolds numbers, showing close agreement to the results obtained by the studies. The boundary layer thickness across a shock was compared to the DNS results of Priebe and Martin and again showed close agreement with values determined by analysis of the numerical Schlieren provided by the authors.

The physical and numerical consistency of the external Shock-Turbulent Boundary Layer Interaction (STBLI) model is anchored in its discrete stratification methodology. By converting the incoming velocity profile into a Mach number profile via a modified Walz quadratic temperature relation, inviscid oblique shock turning is strictly and consistently applied only to supersonic strata where the local Mach number would result to a downstream Mach number above unity. This ensures that the deviation of the shock trajectory from the inviscid case is captured accurately

The physical extent of the interaction is bounded upstream by the shock foot location, and downstream by the location of pressure rise end. The pressure is transmitted to the wall through a single Mach wave per stratum, which partially capture the real flow features of the full expansion/compression Mach waves that exist in a full SBTLI. The solution of the downstream boundary layer allows for a hand-over between the upstream and downstream, ensuring the continuity of the solution towards the internal engine components.

Practically, this methodology directly informs the geometric design of the compression system and isolator design. By efficiently predicting the variations in boundary layer properties and shock trajectory and evaluating separation criteria for each STBLI, the model allows for the compression and cowl angles to be varied, narrowing the viable geometric design space without the computational overhead of full Navier-Stokes simulations.

While this reduced-order approach achieves significant computational efficiency, it introduces explicit physical limitations. Crucially, the model assumes that the boundary layer does not experience significant spatial growth over the short distance of the interaction zone. Depending on the interaction strength, this may lead to inaccuracies and total breakdown in significant recirculation. Furthermore, assuming pressure transmission through a singular Mach wave neglects the complex network of compression and expansion wave reflections between the surface and the sonic line. This alters the physical footprint of the adverse pressure gradient and under-predicts upstream influence, limiting the model strictly to attached or moderately separated flows. The methodology mathematically breaks down in the presence of massive recirculation, as the inviscid strata relations cannot process reversed flow.

Solution of the flat plate model in conjunction with the presented SBLI model allows solution of the entire flow field up to and including the isolator entry. From Figure 3-2, the final two shocks from the external compression system, originating from the cowl, optimally impinge on the ramp shoulder. Downstream of the final cowl shock, the flow enters the isolator (in the case

of a dual-mode scramjet), or the combustor (in the case of a pure scramjet). The final sub-model presented in the following chapter has been developed to determine the necessity for an isolator and its properties, coupled with a combustor-nozzle model to predict the specific thrust of the powerplant.

Chapter 6 - Isolator Modelling

Past the final cowl-generated shock, the model shifts to consideration of the internal flow field. Two distinct operation modes are considered for the internal flow, as was outlined in Chapter 3. The first is the dual mode scramjet, that requires an isolator to house the shock train generated because of the combustion process. The second is the pure scramjet, which removes the need for an isolator, since the incoming flow has sufficient momentum to overcome the energy release of combustion. Distinction between the modes is required for robust design, in a computationally efficient manner that is physically meaningful. This work addresses this by imposing maximum fuelling on the intake exit flow properties and checking whether the flow reaches thermal choke. Thermal choke implies a backpressure imposed on the upstream flow through the subsonic channel of the boundary layer, which leads to the formation of the shock train, and therefore dual-mode operation.

The post-combustion gases are subsequently expanded through a nozzle to produce thrust. While not strictly necessary for the analysis in this work, modelling the nozzle provides values for the specific thrust of the intake, and can thus be used as an optimisation metric.

In dual-mode operation, a rapid method of isolator length estimation is required. The method has to be consistent with experiments in the Mach number and Reynolds number range considered in this work. Prediction of the isolator length during dual-mode operation is challenging, as the backpressure imposed on the boundary layer depends on combustion. For this work, the backpressure is imposed, which enables the isolator length to be predicted. The backpressure imposed is at least 150 kPa (1.5 atmospheres), which will enable robust combustion of hydrogen fuel [11]. The combustion of the fuel depends on both temperature and pressure of the incoming flow, as seen from a representative Mach 8 example by Smart in Figure 6-1, based on the ignition and reaction time correlations by Pergament [135].

The value of the backpressure is selected on the basis of two points. The first is that, as seen from the figure below, for a given temperature, as the pressure is increased, the length required for fuel ignition and reaction is reduced. This is highly advantageous, as it reduces the required combustor length and hence engine weight. The second is that, at higher backpressures, the combustor entry temperature is higher due to longer shock trains. This aids in the robustness of combustion.

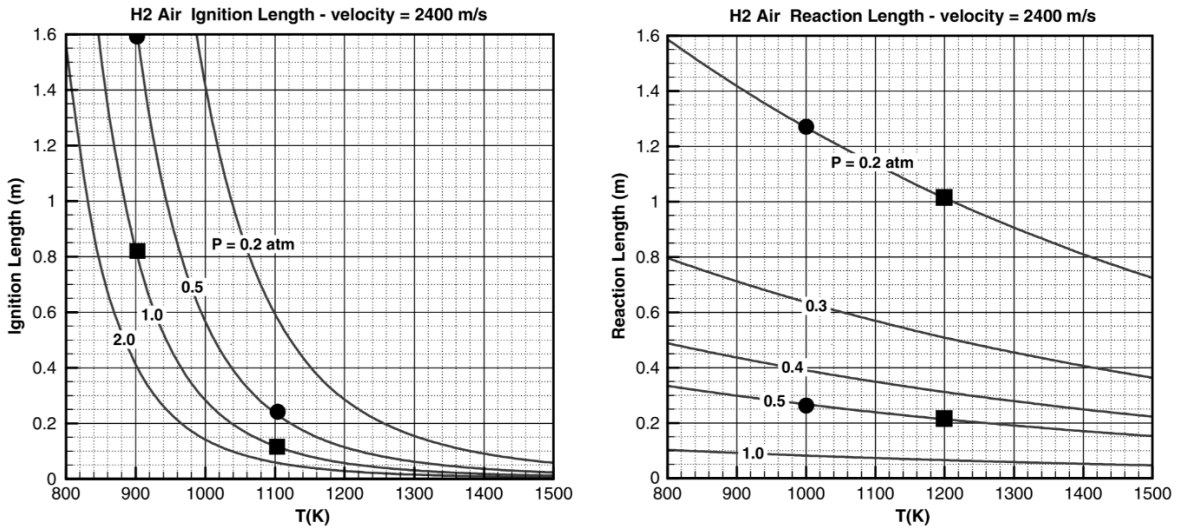


Figure 6-1: Influence of pressure and temperature on ignition (left) and reaction (right) times in a supersonic combustor. Symbols represent evaluations performed by Smart on different temperatures and pressures to investigate effect of the parameters on combustor reaction and ignition delay times. Lines represent correlations by Pergament [135] at different pressures. Reproduced from Smart [11]

A shock train develops when the boundary layer separates and moves upstream due to the backpressure. The shock system that develops is highly complicated, with multiple shock-boundary layer interactions, asymmetric boundary layer growth and other unsteady effects, that makes solving the flow field in detail rather challenging. Therefore, the internal structure of the shock train will be treated as a black box, with only the shock train start and end quantities being determined. This allows for the isolator length to be estimated based on both upstream and downstream quantities and hence optimise for the overall length of the intake-isolator configuration.

This chapter also presents the modelling approach for combustion and nozzle expansion, with considerations for unstart and operating mode.

6.1. Determination of operation mode

The primary difference between the two operating modes is the Mach number at combustor exit. In dual-mode operation, combustion reduces the incoming flow speed to unity, while in pure scramjet operation, the flow exits supersonically. To separate the two modes, a heat addition method is required which can influence the incoming flow field, and the combustor exit Mach number can be calculated.

The method of heat addition employed in this work is based on the total enthalpy of the flow, h_t and equivalence ratio, φ. The equivalence ratio is defined as the ratio between the fuel/air ratio present in the combustion chamber to the stoichiometric fuel/air ratio. As heat is added to

the incoming flow, in the form of fuel, the total enthalpy of the flow increases, and the Mach number decreases. This process can be done up to a critical value, $h_{t,choke}$, where the exit Mach number reaches unity. Any further heat addition must be accommodated by the incoming flow, which manifests as an adverse pressure gradient pushing on the boundary layer and core flow. If the pressure jump is high enough, a shock train forms to facilitate this pressure rise. The selection of the operating mode is based on the capability of the incoming flow to resist the maximum imposed fuelling, $\varphi_{max} = 0.75$. If the flow has enough momentum to exit supersonically from the combustor at this fuelling, the engine is classified as a pure scramjet, removing the need for an isolator and thus making the overall configuration shorter, with higher specific thrust. If it cannot, the maximum equivalence ratio that can be sustained is calculated as being the one needed to bring the shock train exit flow state to thermal choke. This is achieved by finding the equivalence ratio at which the total enthalpy of the incoming flow is equal to the maximum total enthalpy for the incoming flow.

The total enthalpy of the flow is calculated using:

$$h_t = h + \frac{U^2}{2} \tag{6.1}$$

Where h is the static enthalpy and U is the local velocity. To determine whether the combustor entry flow can sustain a given equivalence ratio, the maximum enthalpy that can be achieved is calculated. This is done by application of the conservation of mass and energy on the initial mass and momentum fluxes, *G* and *I*. Mathematically:

$$\begin{aligned} G_1 &= G_2 \\ G &= \rho U \end{aligned} \tag{6.2}$$

And

$$\begin{aligned} I_1 &= I_2 \\ I &= P + \rho U^2 \end{aligned} \tag{6.3}$$

The fluxes at the exit are then solved, accounting for the changes in thermal properties using the equivalence ratio.

The upper limit is obtained by setting the exit Mach number to unity, which is the Rayleigh limit for a frictionless, straight duct. Solving the choked fluxes can be done by setting the Mach number to unity, which reduces the fluxes into two equations for T* and P*, the choked pressure and temperature:

$$P^* = \frac{I_1}{\gamma + 1}$$
$$T^* = \frac{\gamma}{R}\left(\frac{I_1}{G_1(1+\gamma)}\right)^2 \quad 6.4$$

While this is a straightforward calculation in low temperatures, the combustion process and the high temperatures severely alter the ratio of specific heats, γ and gas constant, R. Hence, a bisector solver is used to make a guess for the critical temperature, solving for the critical pressure and solving a chemistry model to obtain the thermodynamic variables. The loop is terminated where the input and output fluxes match. Using these variables, the maximum total enthalpy that can be sustained by the incoming flow can be calculated. If the enthalpy of the incoming flow is higher than the maximum enthalpy, the solution is rejected and the equivalence ratio is reduced, until the two values are equivalent.

6.1.1. Combustion chemistry

To accurately capture the change in operating mode, the combustor exit conditions must be determined with high accuracy. The thermodynamic properties of air will inevitably change due to heating and the production of water and other radicals as part of the combustion and subsequent dissociation process, with specific heat capacity at constant pressure increasing, while the ratio of specific heats decreases.

To capture these changes, the values of c_p and γ are varied from the inlet/freestream values of 1005 J/kgK and 1.4, respectively. At combustor entry, station 3, the entry thermodynamic properties are determined based on the exit temperature and pressure of dry air. At combustor exit, the thermodynamics are further complicated by the extreme temperatures present. At temperatures in excess of 2200K, the molecular gases dissociate, creating radicals which initiate their own reactions. These reactions use additional energy to form and thus not all of the energy released from the initial combustion is used to raise the mixture's temperature, leading to a lower exit temperature, T_4. Two models were considered to capture the change in chemistry at combustor exit, equilibrium chemistry and frozen chemistry.

As alluded to previously, at very high temperatures, the atoms in the molecules of the primary species, N_2, O_2 and H_2 undergo dissociation. Radicals form and recombine to form other species continuously, until an equilibrium is reached where dissociation and recombination happen at the same rate. This is referred to as the equilibrium chemistry model. This is in stark opposition to the frozen chemistry model, which treats the absolute concentration of the post-

combustion products as "frozen" and therefore does not consider any dissociation. The post-combustion products are only considered though the ideal combustion reaction.

6.1.1.1. Frozen Chemistry model (FC)

The frozen chemistry model was implemented using the primary combustion equation and the concentration of each specie post-combustion per Table 6-1. The primary combustion reaction is done for gaseous hydrogen fuel reacting at an equivalence ratio φ with dry air with a composition of 78% Nitrogen, 21% Oxygen and 1% Argon:

$$H_2 + \frac{0.5}{\varphi_{fuel}}(O_2 + 3.76N_2 + 0.0476Ar) \rightarrow H_2O + 0.5(1-\varphi)O_2 + \frac{1.857}{\varphi_{fuel}}N_2 + \frac{0.0238}{\varphi_{fuel}}Ar \quad 6.5$$

Determination of the post-combustion mass fractions, Y_i, are calculated based on the number of moles, n, of each substance, the mass of each substance, M_i, and the total mass of the mixture, found by the summation of the product of number of moles and molar mass per mol:

$$Y_i = \frac{n_i M_i}{\sum_{i=1}^{N} n_i M_i} \quad 6.6$$

The values of these parameters for each specie are provided in **Error! Reference source not found.** below.

Table 6-1: Frozen chemistry specie. Number of moles, **n**, molecular mass, $\mathbf{M_i}$, and mass fraction, $\mathbf{Y_i}$, of each substance present in complete combustion of H_2 with air, based on equivalence ratio, φ

Specie	**Parameter**		
	n (mol)	$\mathbf{M_i}$ (g/mol)	$\mathbf{Y_i}$
N_2	$1.8572/\varphi_{fuel}$	28.014	$\frac{52.0276}{2.016\varphi_{fuel} + 68.775}$
O_2	$0.5\left(1/\varphi_{fuel} - 1\right)$	31.998	$\frac{15.999(1-\varphi_{fuel})}{2.016\varphi + 68.775}$
Ar	$0.0213/\varphi_{fuel}$	39.948	$\frac{0.8509}{2.016\varphi_{fuel} + 68.775}$
H_2O	1	18.015	$\frac{18.015\varphi_{fuel}}{2.016\varphi_{fuel} + 68.775}$

The specific heat capacity of each specie is also required to determine the mixture's value. The specific heat capacity is strongly dependent on local temperature. It is thus evaluated using the

NASA 5-coefficient model, which is a 4th order polynomial based on temperature. This takes the generic form:

$$c_{p,specie} = a_1 + a_2T + a_3T^2 + a_4T^3 + a_4T^4 \quad 6.7$$

Where the coefficients $a_1$to a_5 are unique to each specie [136]. The specific heat capacity of a mixture with *N* constituent species can be found by a mass fraction-weighted summation of the specific heat capacities of the constituent species:

$$c_{p,mix} = \sum_{i=1}^{N} Y_i c_{p,i} \quad 6.8$$

The value of the ratio of specific heats of the mixture, γ_{mix}, is also required. For an ideal gas, which this mixture is still assumed to be, γ_{mix} is related to $c_{p,mix}$ by:

$$\gamma_{mix} = \frac{c_{p,mix}}{c_{p,mix} - R_{mix}} \quad 6.9$$

The value of the specific gas constant, R_{mix}, is also a function of the equivalence ratio and it is found using equation 6.10 below. The quantity R_{un} is the universal gas constant and has a value of 8.3145 J/molK.

$$R_{mix} = \frac{R_{un}}{M_{mix}} = 8.3145\frac{0.5\varphi_{fuel} + 2.3785}{2.016\varphi_{fuel} + 68.8775} \quad 6.10$$

This model provides a computationally efficient and simple method of considering the change in thermodynamic properties of the exhaust gases with change in temperature and equivalence ratio and maintains the mixture as an ideal gas.

6.1.1.2. Equilibrium Chemistry model (EC)

For the equilibrium chemistry model, a custom chemical equilibrium code has been developed, which uses a 9-specie model and 6 primary reactions to capture the change in flow and thermodynamic properties. To establish equilibrium, an iterative solver is run with the selected species and reactions until conservation of the constituents of the reactions (H, O and N) are conserved and that the law of mass action is satisfied. At the equilibrium point, where both are satisfied, the chemically frozen properties are calculated.

For the chemical equilibrium model, the primary composition of the air-fuel mixture, based on the equivalence ratio is:

$$2\varphi H_2 + O_2 + 3.76N_2 \rightarrow Products \quad 6.11$$

This is similar to the frozen chemistry reaction, but the products here are defined by the chemical reactions of the primary species, instead of the explicit reaction of Equation 6.5.

The species considered are:

$$\{H_2, O_2, N_2, H_2O, OH, H, O, N, NO\}$$

The reactions considered are:

- H_2O dissociation: $H_2O \rightleftharpoons H_2 + \frac{1}{2}O_2$
- H_2 dissociation: $H_2 \rightleftharpoons 2H$
- O_2 dissociation: $O_2 \rightleftharpoons 2O$
- Hydroxyl formation: $H_2O \rightleftharpoons OH + \frac{1}{2}H_2$
- Nitrogen dissociation: $N_2 \rightleftharpoons 2N$
- Nitric Oxide Formation: $\frac{1}{2}N_2 + \frac{1}{2}O_2 \rightleftharpoons NO$

Instead of directly evaluating the ideal post-combustion products like frozen chemistry, chemical equilibrium calculates the conservation of the three primary species, H_2, O_2 and N_2, as well as the conservation of the total number of moles. This results in a system of 4 residual non-linear equations, which take the form:

H_2 conservation: $2n_{H_2} + 2n_{H_2O} + n_{OH} + n_H - 4\phi = 0$

O_2 conservation: $2n_{O_2} + n_{H_2O} + n_{OH} + n_O + n_{NO} - 2 = 0$

N_2 conservation: $2n_{N_2} + n_N + n_{NO} - 7.52 = 0$

Total mole conservation: $\sum_{i=1}^{9} n_i - n_{tot} = 0$

Where n_x represents the molar quantity of specie *x*.

These are solved until the residual vector **R(u) = 0,** where **u** is the state vector comprising of the species moles of the primary species, H_2, O_2 and N_2, and the total moles present, $\boldsymbol{u} = \left[n_{H_2}, n_{O_2}, n_{N_2}, n_{tot}\right]^{\boldsymbol{T}}$. This formulation avoids solving the full coupled equilibrium equations of all 9 species and instead reduces it to conservation of the three primary species, which is more computationally efficient for use in an optimisation algorithm.

The dependent species moles are updated based on the state vector and application of the law of Mass action and Dalton's Law of partial pressures, resulting in the moles of the dependent

species as shown below. They become functions of only the moles of the primary species, and the equilibrium constant, K_p. This constant determines the extent of the reaction, with larger values favouring the forward path for the reaction (i.e. moves to completion, for instance H_2 and O_2 to water). It is related to the non-dimensional Gibbs Free Energy, $g°$ and the reaction temperature by:

$$K_{p,i} = \exp\left(\frac{-\Delta G^{\circ}}{R_U T}\right) \tag{6.12}$$

The bracket term, is equivalent to the non-dimensional Gibbs Free Energy and thus:

$$K_{p,i} = \exp(-\Delta g_i°) \tag{6.13}$$

The change in non-dimensional Gibbs Free Energy is the difference between the non-dimensional Gibbs Free Energy between the products and the reactants. These are calculated using the NASA 9-coefficient polynomials. For each reaction, the equilibrium constant is used to determine the moles of the dependent species, as tabulated below in Table 6-2.

Table 6-2: Equilibrium model dependent specie and calculation of moles present in each computation step

Specie	Specie Mole Equation
H_2O	$n_{H_2O} = K_{p,1} n_{H_2} \left(\frac{n_{O_2}}{n_{tot}}\right)^{0.5} P_{atm}$
OH	$n_{OH} = K_{p,2}\left(n_{H_2} n_{O_2}\right)^{0.5}$
H	$n_H = K_{p,3}\left(n_{H_2} \frac{n_{tot}}{P_{atm}}\right)^{0.5}$
O	$n_O = K_{p,4}\left(n_{O_2} \frac{n_{tot}}{P_{atm}}\right)^{0.5}$
N	$n_N = K_{p,5}\left(n_{N_2} \frac{n_{tot}}{P_{atm}}\right)^{0.5}$
NO	$n_{NO} = K_{p,6}\left(n_{N_2} n_{O_2}\right)^{0.5}$

At equilibrium, equations 6.8, 6.9 and 6.10are used to determine the mixture's thermodynamic properties.

More reactions occur, such as the formation of hydrogen peroxide, H_2O_2, but they occur in such minor quantities that they would have minimal impact on the computation's accuracy. These six primary reactions account for most of the energy absorption due to chemical bond

breakage. Evidence for the use of fewer reactions and less species can be found in the work of Engblom[137], who simulated the same experiment of Burrows-Kurkov with an 8 reaction – 7 specie model in their CFD code. The code showed excellent agreement with the experimental readings.

6.1.1.3. Comparison of FC and EC models

To compare the two models, two experiments were selected, the benchmark case of Burrows and Kurkov[138], and the experiments of Paull, Frost and Alesi[139]. The experiment of Burrows was conducted on a diverging combustor with cold, pure hydrogen at Mach 2.44. Of importance is that the incoming flow is vitiated, meaning the composition of the air is altered from the normal composition. This changes the mass fraction of oxygen from about 21% to 25.6%. To account for that, the thermodynamic properties of this flow are re-calculated at the incoming static temperature, resulting in the ratio of specific heats, $\gamma = 1.28$ and specific gas constant, $R = 308$. Based on this, and since the equivalence ratio is not explicitly provided, it was calculated to be around 0.38.

The experiments of Paull, Frost and Alesi were conducted on a replica of the HyShot 2 program scramjet, at a freestream Mach number of 6.5, with normal air. The case used for comparison and validation of the combustor models is case 6782, since the pressure history in the combustor chamber's exit can be determined from the paper's figure 9. The combustor entry properties are determined using the freestream properties and oblique shock relations. Additionally, since no fuel temperature is provided, it is assumed to be at room temperature, around 300K. The combustor entry conditions and equivalence ratio used in the experiments are presented in Table 6-3 below.

Table 6-3: Experimental properties for experiments of Burrows & Kurkov and Paull, Frost & Alesi

	Experiment	
Comb. Entry Property	**Burrows-Kurkov**	**Paull/Frost/Alesi**
Mach Number	2.44	2.75
Static Temperature (K)	1260	1175
Static Pressure (kPa)	101	90
Fuel Temperature (K)	222	300*
Equivalence Ratio	0.38	0.426

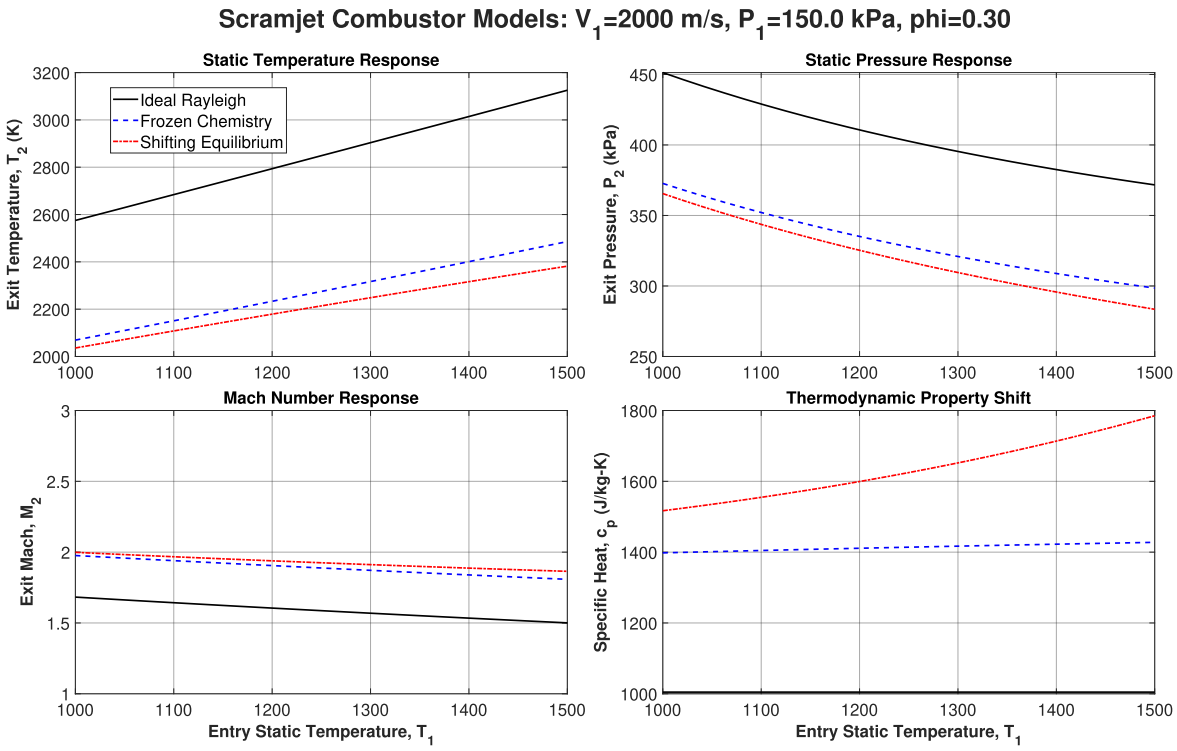
Using the two models, the calculated exit properties were compared with available combustor exit properties from the experiments. For the experiment of Burrows and Kurkov, the exit Mach number and total temperature take values of 2.38 and 2400K respectively. The frozen chemistry model predicts an exit Mach number of 2.1204 and total temperature of 2461.1K, while the equilibrium chemistry model predicts 2.1225 and 2459.4K, respectively. It is evident that at these incoming flow properties, the two models have practically identical performance, but due to the simplicity of the frozen chemistry model, it is superior for this use case.

Regarding the experiment of Paull, Frost and Alesi, only the static pressure near the exit of the combustor is known, so this is the only comparison metric used. The average value of the wall pressure response of the transducer at this location is about 250kPa. Frozen chemistry predicts a static pressure of 269kPa, while the equilibrium model predicts 249kPa. While these two values are relatively close, the specific heat capacity shows significant differences. The frozen chemistry model predicts a value of 1490 J/kgK, while the equilibrium model predicts a value of 1980 J/kgK. This difference propagates to the exit Mach number, with the frozen model's Mach number prediction being closer to choking than the equilibrium model's Mach number, 1.50 vs 1.58.

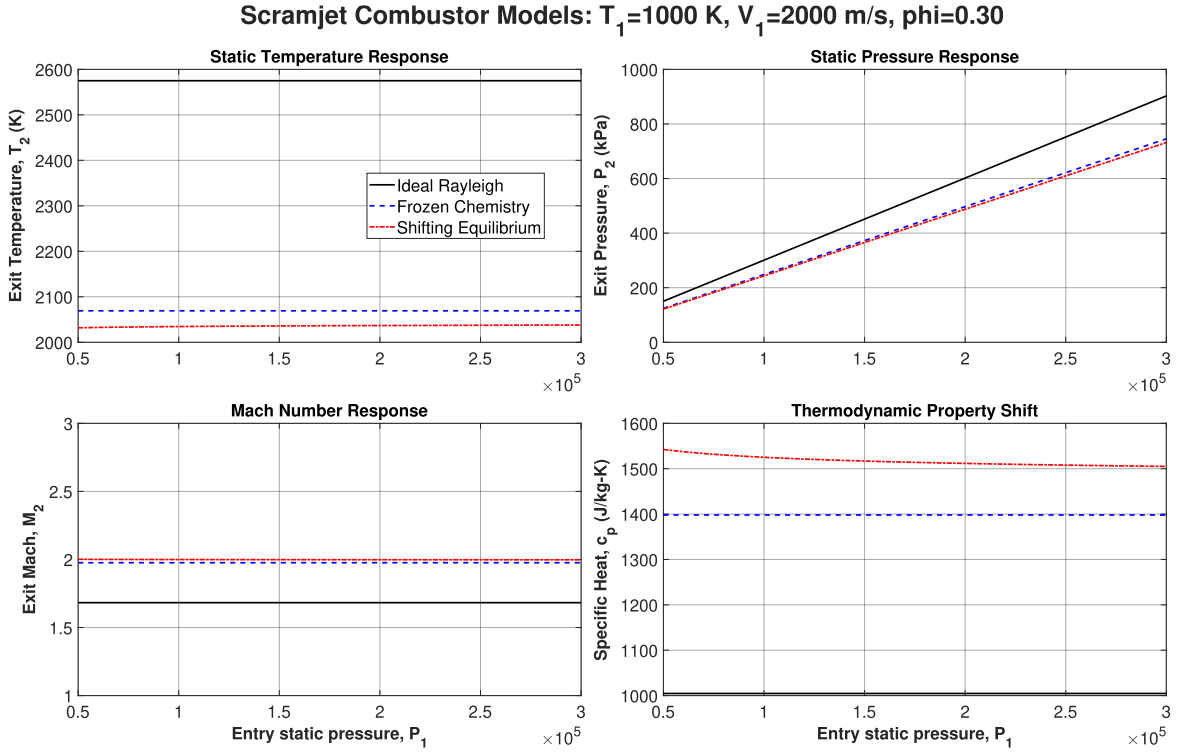
The experiments have comparable inlet conditions to what would be expected in a scramjet and thus can be considered indicative of each model's performance. As demonstrated, both models have identical performance in low equivalence ratios, where the heat addition does not increase the temperature near dissociation. To examine the effect of combustor inlet properties and equivalence ratio on the combustor exit properties, a parametric study was conducted. The combustor inlet temperature, Mach number, pressure and equivalence ratio were varied and their effects on exit temperature, Mach number, pressure and specific heat capacity were investigated. The range of each parameter varied is presented in Table 6-4, with the results being presented in Figure 6-2a – Figure 6-2d below. Along with the FC and EC models, the standard Rayleigh heat addition is investigated as a comparison.

Table 6-4: Variables and their range used in parametric study of frozen vs equilibrium chemistry models

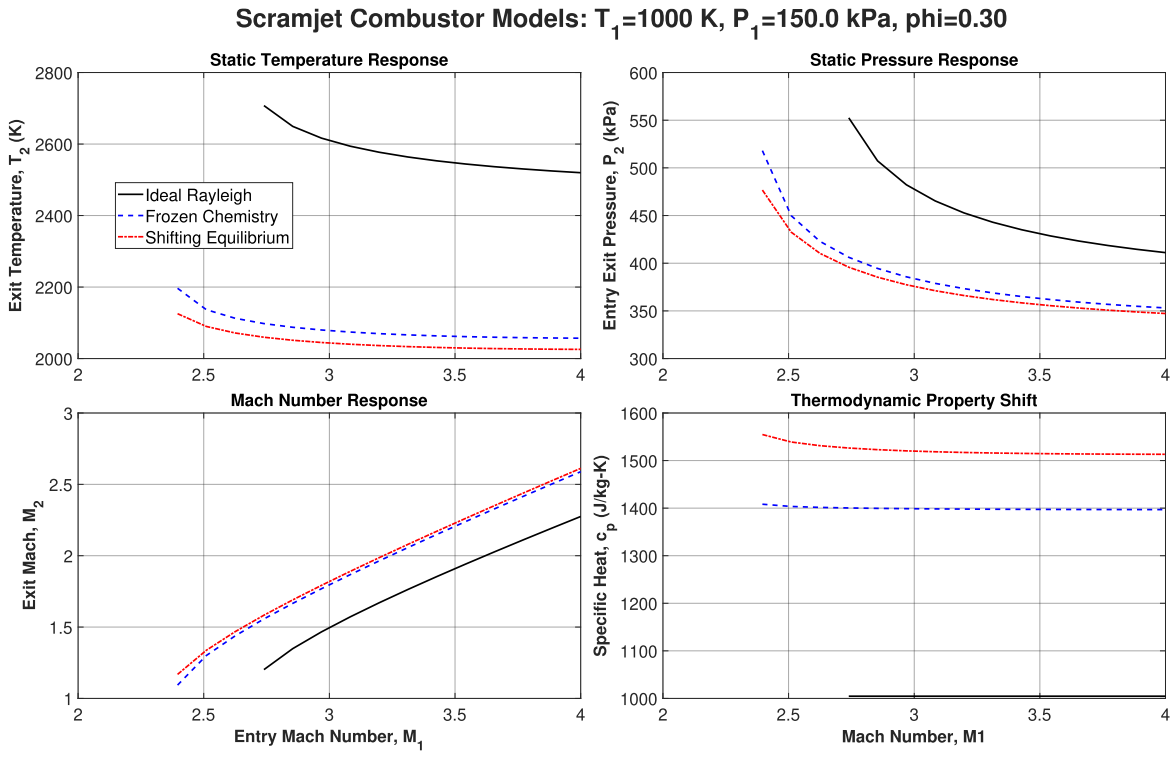
Input Variable	Lower Bound	Upper Bound
Static Temperature (K)	1000	1500
Static Pressure (kPa)	50	300
Mach Number	2	4
Equivalence Ratio	0.1	1


Scramjet Combustor Models: V1=2000 m/s, P1=150.0 kPa, phi=0.30
Static Temperature Response
Exit Temperature, T2 (K)
Ideal Rayleigh
Frozen Chemistry
Shifting Equilibrium
Static Pressure Response
Exit Pressure, P2 (kPa)
Mach Number Response
Exit Mach, M2
Thermodynamic Property Shift
Specific Heat, cp (J/kg-K)
Entry Static Temperature, T1
Entry Static Temperature, T1

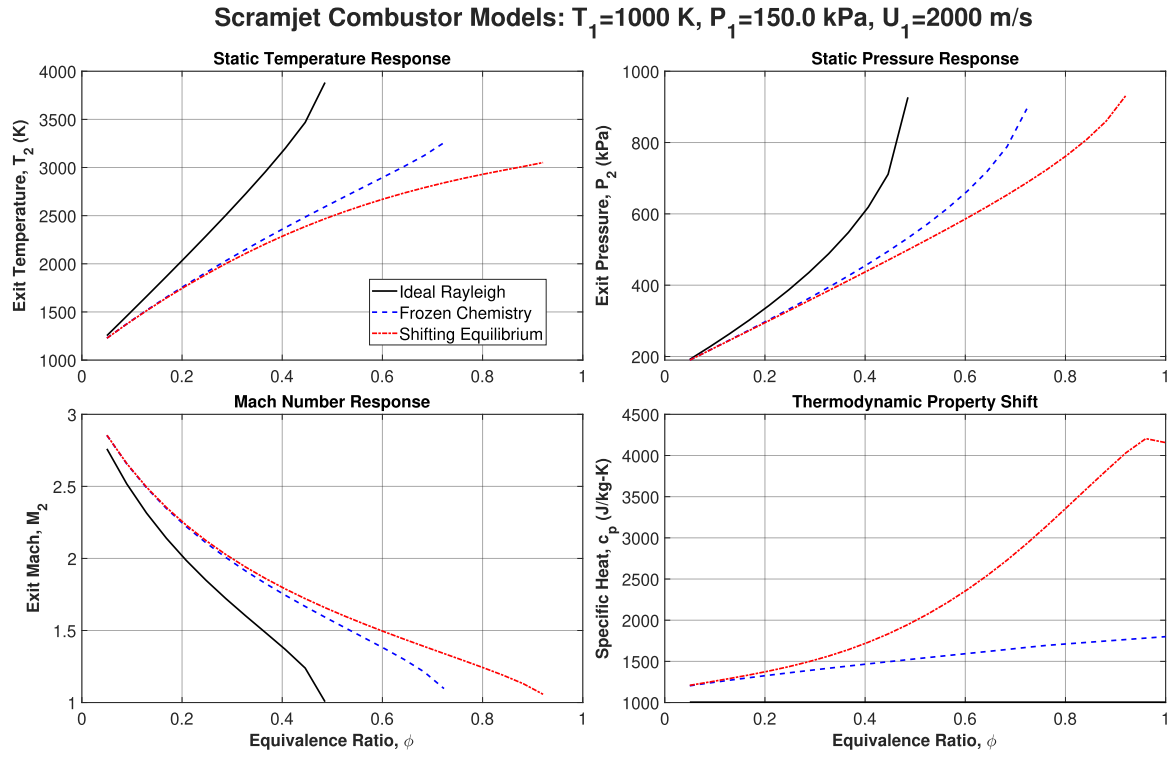
(a)


Scramjet Combustor Models: T1=1000 K, V1=2000 m/s, phi=0.30
Static Temperature Response
Exit Temperature, T2 (K)
Ideal Rayleigh
Frozen Chemistry
Shifting Equilibrium
Static Pressure Response
Exit Pressure, P2 (kPa)
Mach Number Response
Exit Mach, M2
Thermodynamic Property Shift
Specific Heat, cp (J/kg-K)
Entry static pressure, P1
Entry static pressure, P1
×10^5

(b)



(c)



(d)

Figure 6-2: Parametric study results. Variation of combustor entry (a) static temperature (K), (b) static pressure (Pa), (c) Mach number and (d) equivalence ratio

From the above figures, it is seen that the primary influence to the combustor exit properties is the equivalence ratio, and to a lesser extent, the inlet temperature. The incoming pressure and

Mach number have effectively no influence on the combustor exit properties. From Figure 6-2, the thermodynamic variables (here represented by the specific heat capacity at constant pressure, c_p), have small differences up to $\varphi = 0.4$. For the given inlet properties, this corresponds to a combustor exit temperature of 2300K. Given this, the frozen chemistry model is sufficient for equivalent ratios up to 0.4 and a corresponding temperature of 2300K. The sharp increase in the thermodynamic demonstrate the difference in energy availability after the dissociation events occur. Thus, for computational efficiency, the frozen chemistry model is used when the predicted temperature is below 2200K, while the equilibrium model is used for higher combustor exit temperatures. This corresponds to the combustor entry properties and during lower fuelling cases.

The presented components allow the proposed model to separate the two operating modes based on the incoming flow and the combustor state. While for a pure scramjet this would lead directly to the nozzle, a dual mode scramjet requires significantly more design choices, which are presented in the next subchapter.

6.2. Dual mode design

It is clear that the dual-mode engine is, both geometrically and in terms of the flow field, significantly more complex than a pure scramjet. It is, therefore, important to correctly design the isolator component, which is the primary difference between the two, and prevents dual mode engines from flaming out at best and catastrophically failing at worst. The isolator works to prevent the incoming flow from being influenced by downstream pressure disturbances originating from the combustor. However, the incoming flow properties, and more importantly, the boundary layer state, play an important role in the length of duct needed. The equations for the isolator-combustor model follow a station notation, with 2 indicating isolator entry properties, 3 represents isolator exit temperature and 4 represents combustor exit properties. For a scramjet, stations 2 and 3 are the same, as an isolating duct is not considered.

6.2.1. Shock train region

The length of the isolator is estimated using the Billig empirical formula [78] for rectangular ducts, with a prescribed pressure ratio, P_3/P_2. Solved for the isolator length, L_{ST}, the formula reads:

$$L_{ST} = \left[50\left(\frac{P_3}{P_2} - 1\right) + 170\left(\frac{P_3}{P_2} - 1\right)^2\right] \frac{\sqrt{\theta_2 H_{iso}}}{(Ma_2^2 - 1)Re_{\theta,2}^{\frac{1}{5}}} \qquad 6.14$$

With θ_2, P_2, Ma_2, $Re_{\theta,2}$ being the momentum thickness, pressure, Mach number and momentum thickness Reynolds number at the isolator entry. P_3 is the pressure at isolator exit and H_{iso} is the height of the isolator duct. It can be clearly seen that the shock train is influenced by the incoming flow properties but also the height of the duct. Both properties are heavily controlled by the intake structure, as the boundary layer compresses and relaxes through shocks, altering its structure and the Mach number decreases.

To ensure mass conservation is met and that the height of the isolator accommodates the presence of the boundary layers from the ramp and cowl, the following equation is used to determine the height of the isolator:

$$H_{iso} = \frac{\dot{m}_{req}}{\rho_2 U_2 W} + \delta^*_{2,ramp} + \delta^*_{2,cowl} \tag{6.15}$$

The height of the isolator must also satisfy geometric constraints. Equation 6.16 below provides the relation between the geometric height as the distance between the cowl and body surfaces. It is calculated in the frame of reference of the final ramp, where the origin is set to be parallel to the stream along the final ramp surface. The selection of rotating the frame of reference is done so the boundary layer can be calculated from the local properties, as well as the subsequent shock convergence to the body shoulder. A schematic is shown in Figure 6-3.

$$\begin{aligned} H_{\text{iso}} = \big[y_{\text{cowl}} - \left(x_{\text{spike}} - x_{\text{cowl}}\right) \tan\left(\theta_{\text{lastramp}} - \theta_{cowl}\right) \\ - \left(L_{\text{lastplate}} - x_{\text{spike}}\right) \tan\left(\theta_{\text{lastramp}}\right) \big] \cos\left(\theta_{\text{lastramp}}\right) \end{aligned} \tag{6.16}$$

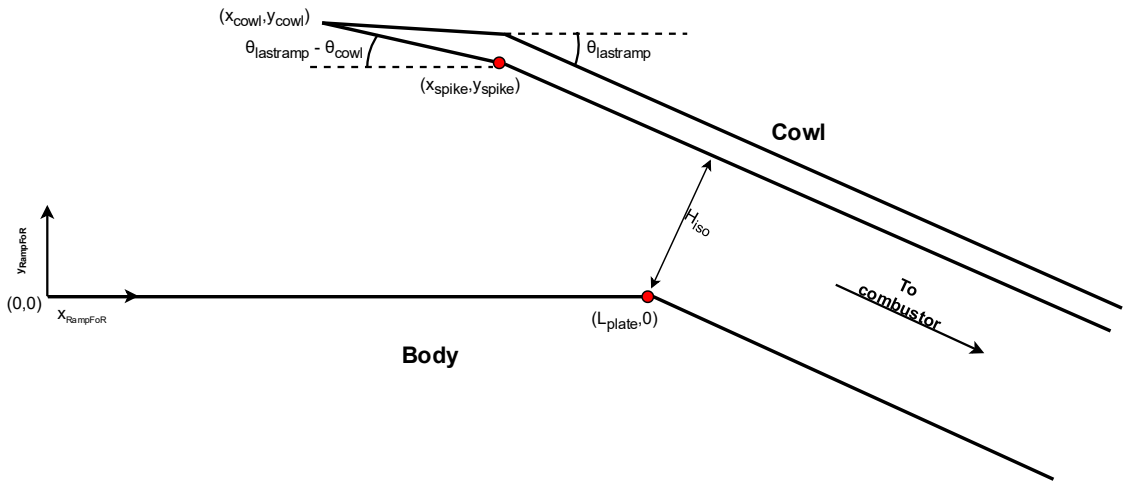


Figure 6-3: Schematic of geometric properties used to determine the isolator height based on geometric constraints. The reference frame is such that the x-axis is parallel to the final compression ramp

Both geometric parameters are seen to be dependent on the incoming boundary layer, requiring the displacement and momentum thicknesses of the boundary layers entering the isolator. To capture the highly non-equilibrium boundary layer entry properties of the body-side boundary layer, the general idea of the Rapid Distortion Theory (RDT) is used. In the frame of this theory, the turbulence has no time to adjust to the distortion, therefore having no influence on the flowfield within the interaction [140]. This is used as the boundary layer undergoes a rapid double compression, entering a highly non-equilibrium state, having no time to relax between the two disturbances. This means that the velocity profile's change is caused only by the two shocks impinging on the boundary layer, and none by the relaxation of the boundary layer. For the present case of a double shock impingement, this means that the velocity profile's distortion can be found by applying the method presented in Chapter 5 in succession. The first shock interaction follows the process described in Chapter 5, with the outputs of the first interaction being directly used to repeat the process for the second impinging shock. This yields velocity, Mach, temperature and density profiles after the second shock. The boundary layer is then reconstructed from the stratified layers. To ensure the vertical strata maintain consistent spacing, conservation of mass is enforced after each interaction. With this method, the "memory" of the boundary layer is retained across the interaction, and the momentum thickness reflects the deficit after the two shocks.

Determining the value of the momentum thickness to use in the shock train length equation is challenging. The boundary layers on the top and bottom surfaces have significantly different properties, including the momentum thickness. This asymmetry leads to separation at different distances, as the resistance of the boundary layers to the backpressure is vastly different. For all cases though, the boundary layer on the body-side will always separate first due to the significantly higher momentum thickness. Hence, the momentum thickness used in Equation 6.14 is that of the body-side boundary layer only.

Validation of the model was done by comparing the predicted leading shock train length to the experiment of Geerts and Yu [65]. The experiment of Geerts and Yu was conducted in two rectangular ducts of differing heights and fixed widths, which resulted in two configurations with different aspect ratios. The Mach number is 2.45, which results in an "X" shaped STLS, pertinent to this work.

To obtain meaningful results between the experiment and the model, the boundary layer properties are matched at $x = 0$ from the experiment. This location is post-expansion, as the

flow enters the rectangular duct. The method of matching is through the boundary layer thickness and hence determining the virtual origin of the turbulent boundary layer, as described by equations 4.34 and 4.35 in Chapter 4. Table 6-5 below presents the boundary layer properties determined through this method and the application of the UTVP of Chapter 4 to determine the displacement and momentum thicknesses.

Table 6-5: Comparison of isolator entry boundary layer properties as calculated using the UTVP developed in this work vs experimental data by Geerts & Yu

Property	**Case**			
	Experiment[65] AR = 3	**Model AR = 3**	**Experiment[65] AR = 6**	**Model AR = 6**
Mach Number	2.45	2.45	2.38	2.38
Boundary Layer Thickness, $\boldsymbol{\delta}$ (mm)	4.17	4.2	3.89	3.9
Boundary Layer Displacement Thickness, $\boldsymbol{\delta^*}$ (mm)	1.01	1.1	0.55	1.0
Boundary Layer Momentum Thickness, $\boldsymbol{\theta}$ (mm)	0.28	0.3	0.46	0.28
Shape Factor, H	3.607	3.80	1.96	3.70

The boundary layer properties show a good matching for the AR 3 case, where the turbulent boundary layer appears to be fully developed, with the shape factors closely matching that of a turbulent boundary layer. In contrast, the AR 6 case appears to not have transitioned fully to a turbulent boundary layer, with the shape factor more closely resembling that of a laminar boundary layer. Therefore, only the AR 3 case is considered, since the flow entering an isolator will be predominantly turbulent.

The predicted shock train lengths are plotted against the experimental data of Geerts and Yu for increasing backpressure ratio in Figure 6-4. As the figure shows, the model can predict the isolator length required to accommodate the pressure rise for the incoming boundary layer to an accuracy of 10%. The discrepancy, especially at higher pressure ratios, can be attributed the sidewall boundary layer. The equation used in this work and as a comparison metric by Geerts and Yu, ignores the contribution of the sidewall boundary layers. In sufficiently low aspect ratio

isolators, the blockage to the flow from the sidewall boundary layers is significant, which alters the momentum thickness in the equation.

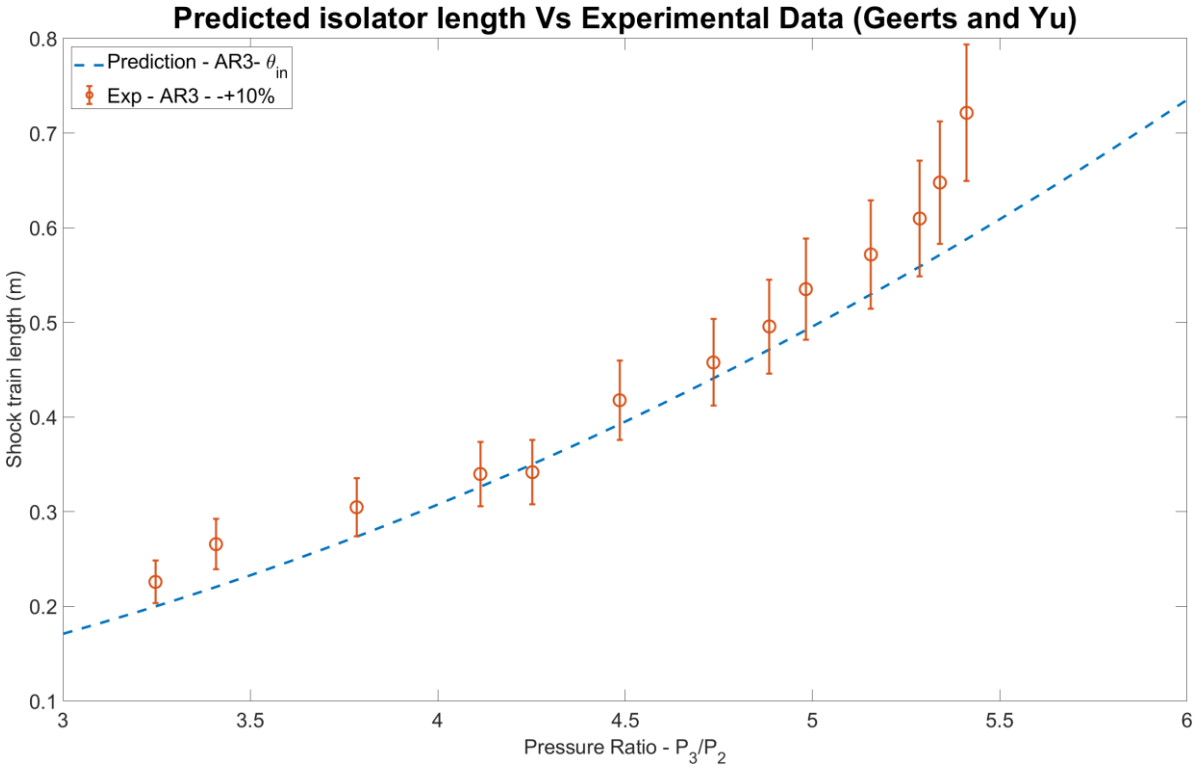


Figure 6-4: Prediction of shock train length with increasing pressure ratio (Data from experiment of Geerts and Yu[65] with the error bars being +-10%)

The discrepancy is deemed to be adequate for use in this low-order, preliminary modelling code, while being computationally inexpensive. The typical compression ratios that are expected are between 3 and 5, which fall within the region where the relation accurately captures the shock train length.

The isolator exit flow properties are also required, which are used to solve the chemistry solvers and subsequent nozzle.

Initially, the flow parameters entering the isolator are known, through analysis of the intake and cowl shocks. In a shock train, the supersonic core is assumed to be surrounded by regions of separated flow caused by the adverse pressure gradient, as shown in Figure 6-5. The isolator model is only applied to dual-mode scramjets based on the fuelling required to choke the combustor, which maximises the thrust generated for such engines. A shock train will be generated to allow for the isolator entry pressure to rise to the combustor entry pressure. A shock train might be generated before choking is reached, if the backpressure resistance of the boundary layer is insufficient to remain attached as the shock train propagates towards the

combustor. At choked conditions, the maximum possible fuelling can be achieved, and thus the maximum exit pressure and temperature, maximising thrust. Additionally, at the choking condition, the boundary layer will experience the maximum backpressure, and thus the design allows for the maximum length of isolator required, but also the maximum thrust that can be generated based on the incoming flow conditions.

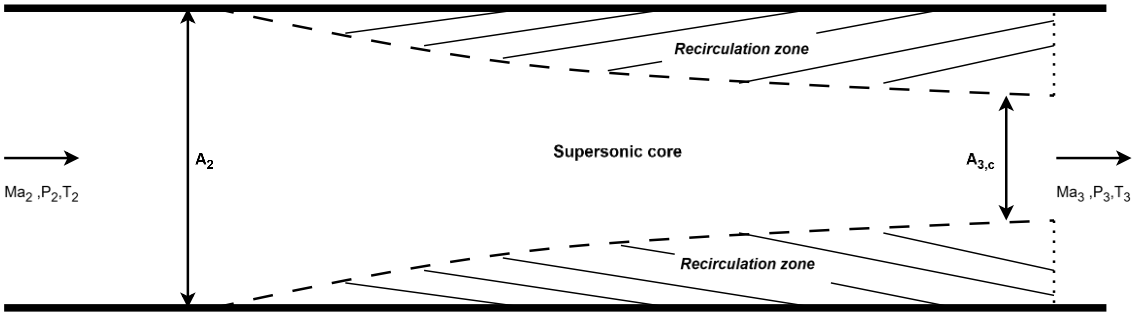


Figure 6-5: Assumed isolator flow field of a supersonic core surrounded by regions of separated flow to combustor entry

The ratio of the supersonic core area to the full duct area is found by solving the impulse functions, J_2 and J_3 at the inlet and exit of the isolator, assuming no friction forces:

$$J_2 = \dot{m}V_2 + p_2A_{2,c}$$
$$J_3 = \dot{m}V_3 + p_3A_{3,c} \qquad 6.17$$

The two impulse functions must be equal, and substituting the equation for mass flow rate and Mach number, the ratio of areas is obtained as:

$$\frac{A_{3,c}}{A_{2,c}} = \frac{1}{\gamma_3 Ma_3^2}\left(\frac{P_2}{P_3}(1 + \gamma Ma_2^2) - 1\right) \qquad 6.18$$

The above equation can be solved in conjunction with the conservation of energy equation in its steady state form (SFEE), with no heat or mass exchange. It takes the form:

$$\dot{m}_2\left(c_pT_2 + \frac{U_2^2}{2}\right) = \dot{m}_3\left(c_{p,3}T_3 + \frac{U_3^2}{2}\right) \qquad 6.19$$

Substituting the expressions for the mass flow rate at the entry and exit of the isolator, the expression of Mach number and substituting the specific heat capacity as $c_p = \frac{\gamma R}{\gamma - 1}$:

$$\frac{P_2 A_{2,c} Ma_2 R\gamma}{(\gamma-1)}\sqrt{\frac{\gamma T_2}{R}}+\frac{Ma_2^3 P_2 A_{2,c}\gamma}{2}\sqrt{\gamma R T_2} = \frac{P_3 A_{3,c} Ma_3 R\gamma_3}{(\gamma_3-1)}\sqrt{\frac{\gamma_3 T_3}{R}}+\frac{Ma_3^3 P_3 A_{3,c}\gamma_3}{2}\sqrt{\gamma_3 R T_3} \quad 6.20$$

Simplifying and rearranging to have ratio $A_{3,c}/A_{2,c}$ and pressure ratio P_3/P_2 on RHS:

$$\frac{M_2}{M_3}\sqrt{\frac{1+\frac{\gamma-1}{2}Ma_2^2}{1+\frac{\gamma_3-1}{2}Ma_3^2}} = \frac{A_{3,c}}{A_{2,c}}\frac{P_3}{P_2} \quad 6.21$$

Substitution of the area ratio equation and isolation of pressure ratio leads to:

$$\frac{P_3}{P_2} = 1+\gamma Ma_2^2 - \gamma_3 Ma_2 Ma_3\sqrt{\frac{1+\frac{\gamma-1}{2}Ma_2^2}{1+\frac{\gamma_3-1}{2}Ma_3^2}} \quad 6.22$$

As the exit pressure, P_3, is prescribed to 1.5 atmospheres, solution of the isolator exit Mach number is obtained by rearranging the above equation, obtaining:

$$Ma_3 = \frac{1+\gamma Ma_2^2-\frac{P_3}{P_2}}{\gamma_3 Ma_2}\left[1+\frac{\gamma-1}{2}Ma_2^2-\left(\frac{1+\gamma Ma_2^2-\frac{P_3}{P_2}}{\gamma_3 Ma_2}\right)^2\right]^{-0.5} \quad 6.23$$

The static temperature is solved using the conservation of energy across an adiabatic isolator. The total temperature is conserved across a shock train without heat exchange, so the static temperature can be solved using the shock train exit Mach number, Ma_3.

6.3 Combustor Length and Nozzle

The final property of the combustor required to be determined is the length. The length of the combustor is taken to be the time required for the air/fuel mixture to ignite after being mixed and the time required for the primary combustion reaction to be complete. The ignition delay time, τ_{ID}, and reaction time, τ_R , take the form proposed by Pergament[135], which itself follows the generic Arrhenius exponent form:

$$\tau_{ID} = \frac{8*10^{-3}}{P}e^{\frac{9600}{T}} \quad 6.24$$

$$\tau_R = \frac{105}{P^{1.7}}e^{\frac{-1.12*T}{1000}} \quad 6.25$$

Where the times, τ_{ID} and τ_R are the ignition delay and reaction times in microseconds (μs), p is the incoming flow pressure in atmospheres, and T is the incoming flow temperature in Kelvin. The velocity used for the calculation is the combustor entry velocity. Subsequently, the length of the combustor, L_{comb}, is calculated as:

$$L_{comb} = U_3(\tau_{ID} + \tau_R) \tag{6.26}$$

To obtain meaningful comparisons between configurations, specific impulse and specific thrust are established as additional metrics to the total pressure recovery and total engine length.

Therefore, a nozzle model is required to expand the combustion products. In this work, in the absence of an explicit nozzle exit area or thrust requirement, the nozzle model is based on the adiabatic expansion efficiency, $\eta_{n,AD}$. The definition of the adiabatic expansion efficiency assumes no heat transfer at the nozzle, and perfect expansion to freestream pressure.

$$\eta_{n,AD} = \frac{h_4 - h_{10}}{h_4 - h_{10,s}} \tag{6.27}$$

Substituting the enthalpy-temperature relation:

$$\eta_{n,AD} = \frac{c_{p,4}(T_4 - T_{10})}{c_{p,4}(T_4 - T_{10,s})} \tag{6.28}$$

The isentropic temperature ratio can be expressed in terms of pressure ratio in its isentropic form and recalling that perfect expansion is assumed ($p_{10,s} = p_0$) yielding:

$$\eta_{n,AD} = \frac{1 - \frac{T_{10}}{T_4}}{1 - \left(\frac{p_0}{p_4}\right)^{1-\frac{1}{\gamma_4}}} \tag{6.29}$$

Assuming a value for the efficiency for the nozzle, allows for direct solution for the real exit temperature, T_{10}. The adiabatic expansion efficiency is set to 0.9, which represents a value of a well-designed nozzle.

$$T_{10} = T_4\left[1 - \eta_{n,AD}\left(1 - \left(\frac{p_0}{p_4}\right)^{1-\frac{1}{\gamma_4}}\right)\right] \tag{6.30}$$

The value of the real temperature permits the evaluation of the true exit Mach number by solving the total temperature equation:

$$Ma_{10} = \sqrt{\frac{2}{\gamma_4 - 1}\left[\frac{T_4}{T_{10}}\left(1 + \frac{\gamma_4 - 1}{2}Ma_4^2\right) - 1\right]} \tag{6.31}$$

The nozzle exit area obtained through this nozzle design method thus reads:

$$A_{10} = \frac{\dot{m}}{V_{10}\frac{p_0}{R_{mix}T_{10}}} \tag{6.32}$$

This area is used during CFD simulations to properly expand the flow to ambient.

The specific thrust and specific impulse of a given configuration are then evaluated using:

$$F_{specific} = (1 + \varphi f_{stoichio})U_{10} - U_0 \tag{6.33}$$

$$I_{sp} = \frac{F_{specific}}{g(1 + \varphi f_{stoichio})} \tag{6.34}$$

While the nozzle model does not directly feed back to the intake-isolator-combustor flowfield, it serves to expand the flow and obtain the specific thrust metric. Since it is an adiabatic nozzle, it causes the flow to expand identically to ambient pressure, thus removing any contribution that might arise from under- or over-expansion.

6.3. Chapter Summary

This chapter presents the development of an isolator-combustor-nozzle model that completes the global model proposed in this work, along with a chemical equilibrium model. The novelty of the proposed approach is split into two points. The first, is the use of the rapid distortion theory to evaluate the non-equilibrium boundary layer entering the isolator. The incoming boundary layer's momentum thickness is vital to the prediction of the shock train, which is done using the Waltrup-Billig relation for rectangular ducts.

The second is the separation of operating modes based on the maximum acceptable equivalence ratio. A chemical equilibrium model is used to calculate the maximum fuelling that the incoming flow can be subjected to and separates the operating mode based on this criterion. The maximum equivalence ratio is limited to 0.75, to maintain fuel-lean conditions. In the case that it cannot be subjected to the maximum equivalence ratio, the engine operates in dual mode, with a shock train forming.

An adiabatic nozzle model is included past the combustor exit, which allows for the comparison of configurations based on specific thrust and specific impulse. The nozzle is modelled as

adiabatic and perfect expansion to remove any thrust contributed by the nozzle. Thus, the entire thrust produced is a product of the combustor exit products, providing a fair metric to compare each other against.

Within the framework, physical and numerical consistency is strictly enforced through the underlying conservation equations. The combustor receives flow that is consistent with mass conservation, for both dual-mode and pure scramjet configurations. In the case of dual-mode, the isolator exit properties are determined through conservation of impulse, mass and energy. The addition of chemistry models enables consistency with high temperature chemistry, enabling dominant reactions to absorb energy, and modify the combustor exit properties accordingly.

From a practical engineering standpoint, this internal flowpath model acts as a highly efficient preliminary screening tool for scramjet operability. It allows designers to rapidly determine the required isolator length via the Waltrup-Billig correlation to contain the internal shock train, whilst mapping the maximum fuel equivalence ratio limits. This capability is critical for rapidly identifying thermal choking boundaries and preventing internal geometries that could potentially lead to unstart from advancing to computationally expensive, high fidelity design phases

The framework presented in this chapter is limited by its reliance on one-dimensional formulations and idealised thermodynamic processes. The length of the isolator is predicted using a correlation and relies heavily on its empiricism, which may degrade in accuracy if pushed beyond its calibration range. Additionally, the use of this correlation limits the isolator to being adiabatic, in line with the assumptions of the original correlation. The chemistry models employed in this work provide the upper limit of heat addition and therefore constitute an ideal state. In real combustor flows, the thickening of the boundary layer and friction contribute to the heating of the flow, thus reducing the equivalence ratio. Lastly, the reliance on an adiabatic nozzle reduces the effective thrust that can be achieved and does not consider the method of flow expansion or detailed chemistry to nozzle exit.

The current model integrates known methods into a novel sub-model that differentiates between operation modes and considers effects of combustion, through both flow choking prediction, and a chemical equilibrium model.

Chapter 7 - Results and Discussion of Combined Modelling

This chapter presents the principal outcomes of this research and demonstrates the capability of the proposed low-order, coupled intake–isolator modelling framework to support preliminary scramjet design and optimisation. Building on the individual sub-models developed in the preceding chapters, the framework combines them into a single model and is applied within a multi-objective optimisation environment to identify scramjet configurations that satisfy operability constraints while maximising performance metrics. The results presented here directly address the central aim of the thesis by assessing whether the coupled, computationally inexpensive approach can capture the dominant intake–isolator interactions that govern dual-mode and pure scramjet operation. In doing so, this chapter evaluates the extent to which the proposed approach fulfils the thesis aim of enabling rapid, physics-informed optimisation of coupled hypersonic intake–isolator systems.

The optimisation framework combines the intake, isolator, and downstream component models with the CMOPSO algorithm to generate optimum configurations. From these, a representative configuration for a dual-mode scramjet is selected for verification using OpenFOAM, providing an independent assessment of the predictive capability of the proposed method. The chapter presents results for both dual-mode and pure scramjet operating regimes. Particular attention is given to the dual-mode configuration, where the presence of a shock train results in complex intake–isolator coupling, allowing the influence of key design variables—including the number of external compression ramps, inlet mass flow rate, and wall temperature—to be systematically examined.

The trajectory selected is that of a constant 50 kPa dynamic pressure. With the value fixed and a given Mach number, the local freestream parameters can be determined based on the atmospheric variation of pressure and temperature. Pressure is described by the barometric formula, an exponential decay based on height in conjunction with the ideal gas law:

$$P_{\infty} = P_{0,SL} e^{-\frac{Mgh}{R_{specific} T}} \tag{7.1}$$

where $P_{0,\,SL}$ is the pressure at sea level (101325 Pa), M is the molar mass of air (28.96 g/mol), g is the gravitational acceleration (9.81 m/s^2), h is the geopotential height in meters (m), $R_{specific}$ is the specific gas constant (8.314 J/molK) and T is the local ambient temperature in Kelvin (K).

Temperature is estimated based on the International Standard Atmosphere (ISA) model, in which the atmosphere has region of linear variance and regions of constant temperature with altitude. For the heights between sea level and 47 km above sea level, the temperature is determined by:

$$T = \begin{cases} T_{b,1} + m_{T,1}h & 0\ km \leq h \leq 11\ km \\ T_{b,2} & 11\ km < h \leq 20\ km \\ T_{b,2} + m_{T,3}(h - h_{T,3}) & 20\ km < h \leq 32\ km \\ T_{b,4} + m_{T,4}(h - h_{T,4}) & 32\ km < h \leq 47\ km \end{cases} \quad 7.2$$

where $m_{T,i}$ represents the local gradient of the variance between the two altitudes, $T_{b,i}$ is the starting temperature at each layer and $h_{T,i}$ the starting altitude of the current layer. Solving the two equations with the ideal gas law and the requirement for a constant dynamic pressure, defined as:

$$q_\infty = 0.5\rho_\infty U_\infty^2 = 0.5\frac{P_\infty}{RT_\infty}\left(Ma\sqrt{\gamma RT_\infty}\right)^2 \quad 7.3$$

returns the local atmospheric conditions and the altitude at which this occurs based on flight Mach number.

With the local freestream conditions and the imposed mass flow rate, the capture height, H_{capt}, can be estimated. Due to the presence of the boundary layer on the plate, solving for the height of the intake requires the solution of Equation 7.4.

$$\dot{m}_{capt} = W\left(\dot{m}_{2D,FS} + \dot{m}_{2D,BL}\right) \quad 7.4$$

where W is the width of the engine, set as a multiple n_{depth} of the capture area, H_{capt}, $\dot{m}_{2D,FS}$ is the two-dimensional mass flow rate of the freestream region and $\dot{m}_{2D,BL}$ is the two-dimensional mass flow rate contained within the boundary layer. Substituting the freestream quantities and boundary layer two-dimensional mass flow rates results in equation 7.5 below:

$$\dot{m}_{capt} = n_{depth}H_{capt}\left(\rho_\infty U_\infty\left(H_{capt} - \delta\right) + \int_0^\delta \rho(y)U(y)\,dy\right) \quad 7.5$$

Equation 7.4 is solved at the foot of the first compression corner, where the boundary layer would be the thickest before compression.

7.1. Verification of optimised solutions through CFD

For optimisation, the CMOPSO optimiser described in Chapter 3.1 is used, along with a combination of all sub-models of Chapters 4-6. The input variables to the optimiser are the number of angles required to define the designer-chosen number of ramps, the cowl closure angle and the width to depth ratio. For this work, the maximum and minimum bounds of these input variables are presented in Table 7-1 below.

Table 7-1: Range of input parameters to CMOPSO

Input Variable	Lower Bound	Upper Bound
$\theta_1, \theta_2, \ldots, \theta_n$	1	15
n_{depth}	0.1	10

To verify the modelling approach and investigate the overall how closely the predicted flowfield matches the one produced by CFD, a dual-mode scramjet configuration is tested. It is designed to operate at a flight Mach number of 6 with a required captured mass flow rate of 30 kg/s and a wall temperature for the external ramps of 600K. The resulting Pareto front is shown in Figure 7-1. The configuration presented is selected to be the one at the minimum Euclidean distance from the origin of the objective functions, determined using Equations 3.6-3.7. The resulting configuration's geometric parameters are shown in Table 7-2 below, with a schematic shown in Figure 7-2.

The optimisation routine returns the ramp and cowl angles and the width/height ratio. For a complete description of the configuration, the lengths of the external compression system are vital. The lengths are calculated by solution of the compressible flat plate model and STBLI models simultaneously. The length required for a plate depends on the boundary layer's thickness, as the shock deviates away from the inviscid solution more for thicker boundary layers. The constraints imposed upon the solution of the plate length dictate that outside the boundary layer, the inviscid shock must impinge on the cowl or shoulder, depending on the source of the shock. For the 1st to "n-1"th ramp, equations 4.25 (compressible velocity profile), 4.29 (boundary layer thickness) and the method of Chapter 5 is employed, with the Equation 7.6 below used as a constraint to be satisfied pertaining to the shock-on-tip requirement:

$$\tan\left(\beta_{ramp,\infty}\right) = \frac{y_{cowl} - \delta_{\bar{\bar{u}}_{pre}=1}}{x_{cowl} - \left(L_{plate} + x_{exit}\right)} \tag{7.6}$$

The line is a description of the shock line as a line segment connecting the exit of the boundary layer to the cowl tip. The final ramp must be calculated in a different manner, as the shocks impinging at the end of the ramp must satisfy the shock-on-shoulder condition. Thus, the final ramp length is obtained by solving the shock impingement of the cowl tip shock on the ramp boundary layer with the length of the ramp being a sum of the shock impingement length and the length required for the shock to fully penetrate into the boundary layer. The length where the cowl shock impinges on the boundary layer, L', is calculated in a similar way to equation 7.6 above:

$$\tan\left(-\beta_{cowl\ tip,\infty}\right) = \frac{y_{cowl} - \delta_{\bar{\bar{u}}_{pre}=1}}{x_{cowl} - L'} \tag{7.7}$$

And the overall length of the plate is calculated using:

$$L_{plate} = L' + abs(x_{exit}) \tag{7.8}$$

Table 7-2 Resulting geometry from optimisation used as verification

Parameter	Ramp 1	Ramp 2	Ramp 3	Cowl
Deflection (deg)	3.4549	7.3920	12.1006	6.6510
Length (m)	0.4018	0.2579	0.7198	0.1151

Although all points on the Pareto front are mathematically optimal, a representative configuration must be selected to enable detailed analysis and verification. The design highlighted by the red circle in the Pareto front figures is selected based on its minimum Euclidean distance (Equations 3.6 & 3.7) to the origin of the normalised objective space, representing a balanced trade-off between specific thrust, pressure recovery, and system length while satisfying all operability constraints.

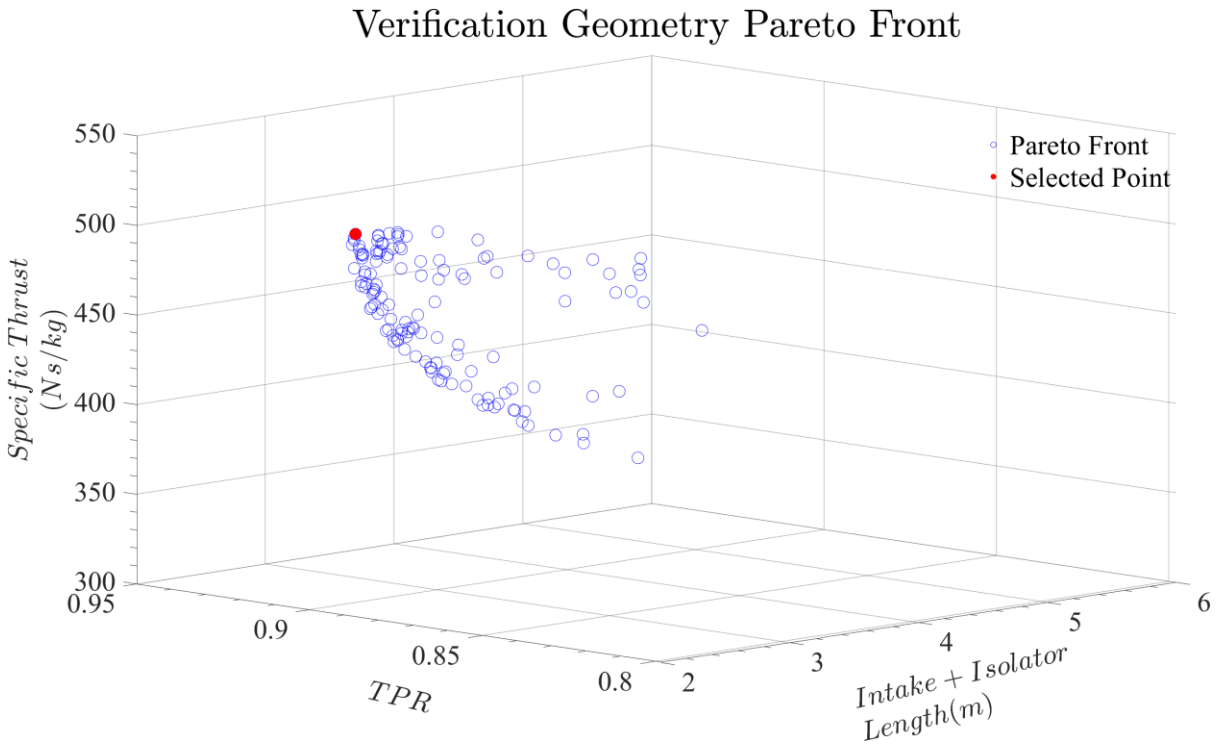


Figure 7-1: Resulting Pareto front for the parameters selected in the verification study. Red point indicates the minimum Euclidean distance point

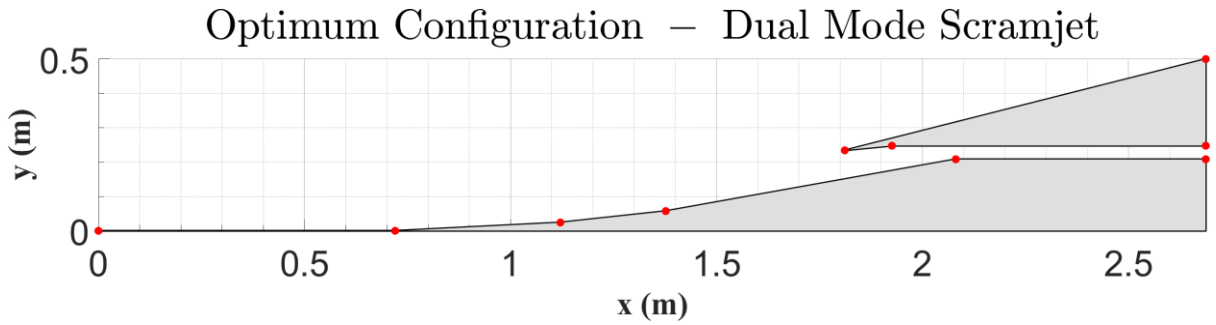


Figure 7-2: Schematic of resulting geometry used for verification. Red dots indicate points determined by model p to combustor entry

To test the predicted optimum engine's operating capabilities and ensuring that the intake remains started, the CFD method described in Chapter 3 is used, with the turbulence intensity set to 0.025%, which allows the boundary layer to transition along the plate. In OpenFOAM, the combustor is modelled as a straight duct and simulated as a heat source. Due to the complicated interactions within the combustor, assigning a precise value to the heat release due to combustion would be challenging. To simulate the heat release due to combustion, OpenFOAM requires a volumetric heat addition, $\dot{q}$, in W/m^3. The added heat is calculated using the difference in absolute specific enthalpies between the entry and exit flows at a reference temperature $(T_{ref} = 298.15K)$:

$$q_{chem} = h_f^{\circ}(T_{ref})_{reactants} - h_f^{\circ}(T_{ref})_{products} \quad 7.9$$

The absolute enthalpy of the flow at a given temperature is given by:

$$h(T) = h_f^{\circ}(T_{ref}) + \int_{T_{ref}}^{T} c_p\,(T)dT \quad 7.10$$

By solving $h(T)$ at the reference temperature, the integral vanishes, leaving only the enthalpy of formation, h_f°. This is calculated by summation of the contribution of each constituent specie in the entry and exit flow. Applying the summation to equation 7.10, yields the added heat as:

$$q_{chem} = \sum_{i=1}^{n_{react}} \left(Y_i h_{f,i}^{\circ}\right)_{T_{ref}} - \sum_{j=1}^{n_{prod}} \left(Y_j h_{f,j}^{\circ}\right)_{T_{ref}} \quad 7.11$$

To obtain the volumetric heat addition, the released heat is multiplied by the exit mass flux, G ($G_{exit} = \rho_{exit} U_{exit}$) and divided by the combustor length to obtain the volumetric heat addition:

$$\dot{q}_{EC} = \frac{G_{exit} q_{chem}}{L_{comb}} \quad 7.12$$

An additional adaptation for OpenFOAM is that the volumetric heat added is calculated using chemical equilibrium properties. Directly applying the calculated volumetric heat from the equilibrium chemistry model to OpenFOAM overpredicts the aerodynamic thermal blockage and induces premature thermal choking. This discrepancy occurs because real scramjet combustion involves both endothermic dissociation and the formation of the dependent species (such as H_2O and CO_2), which act as chemical energy sinks and significantly reduce the bulk specific heat ratio (γ) of the gas mixture. Because CFD assumes non-reacting dry air, it is significantly more sensitive to heat addition and requires substantially less specific energy to produce the same velocity reduction. The reason for the elevated sensitivity is that dry air retains a higher γ and lower c_p Therefore, to accurately replicate the backpressure necessary for isolator shock train development, the equivalent CFD heat addition (q_{eff}) was decoupled from the absolute chemical enthalpy. Instead, it was calibrated to match the exact core Mach number drop ($M_1 \rightarrow M_2$) predicted by the equilibrium solver, enforced mathematically through Rayleigh stream thrust conservation.

To inject the proper amount of heat, the calculated volumetric heat is obtained by solving the Rayleigh heat addition momentum conservation, by enforcing an exit Mach number of unity.

$$\frac{T_{2,\text{air}}}{T_1} = \left(\frac{1+\gamma_{\text{air}}(T_1)M_1^2}{1+\gamma_{\text{air}}(T_{2,\text{air}})M_2^2}\right)^2 \left(\frac{M_2}{M_1}\right)^2 \frac{\gamma_{\text{air}}(T_1)}{\gamma_{\text{air}}(T_{2,\text{air}})} \quad 7.13$$

Using this method, a different exit static temperature will be obtained, and hence a different heat addition, labelled as q_{eff}, which is calculated through integration of the specific heat capacity from combustor entry to combustor exit:

$$q_{\text{eff}} = \int_{T_{0,1}}^{T_{0,2,\text{air}}} C_{p,\text{air}}(T)dT \quad 7.14$$

The volumetric heat addition is then calculated using:

$$\dot{q}_{eff} = \frac{\dot{m}q_{\text{eff}}}{(L_{comb}H_{comb}W_{comb})} \quad 7.15$$

The equilibrium/frozen chemistry solver returns an effective volumetric heat addition of 9.5 GW/m^3. The Rayleigh heat addition returns a lower value of 2.65 GW/m^3. Both use a length of 180mm for the constant-area combustor. The combustor length is calculated by multiplying the incoming flow velocity by the sum of ignition delay and reaction times.

7.1.1. Optimum configuration results

Figure 7-3 shows the variation of boundary layer thickness, δ, along the compression ramps as predicted by the model and CFD. The first observation is that the prediction of the model from the leading plate does not start at the plate edge, but rather from a point downstream. The starting point is the virtual origin, calculated using equations 4.34-4.35, assuming that it is located at the start of the transition region. It is immediately evident that the boundary layer undergoes a thickening/thinning cycle when it crosses the shocks, caused by the compression of the streamlines due to the presence of the ramp. The model accurately predicts the trend of boundary layer growth away from STBLI regions, but the magnitude shows differing levels of accuracy. The boundary layer magnitude shows good agreement on the leading plate and past the first two shocks, but significant variation after the final ramp shock. The reason is not fully understood but could perhaps be attributed to the fact that the boundary layer has not fully recovered from the previous STBLI, thus the boundary layer encountering the final shock cannot be accurately described through the compressible universal velocity profile.

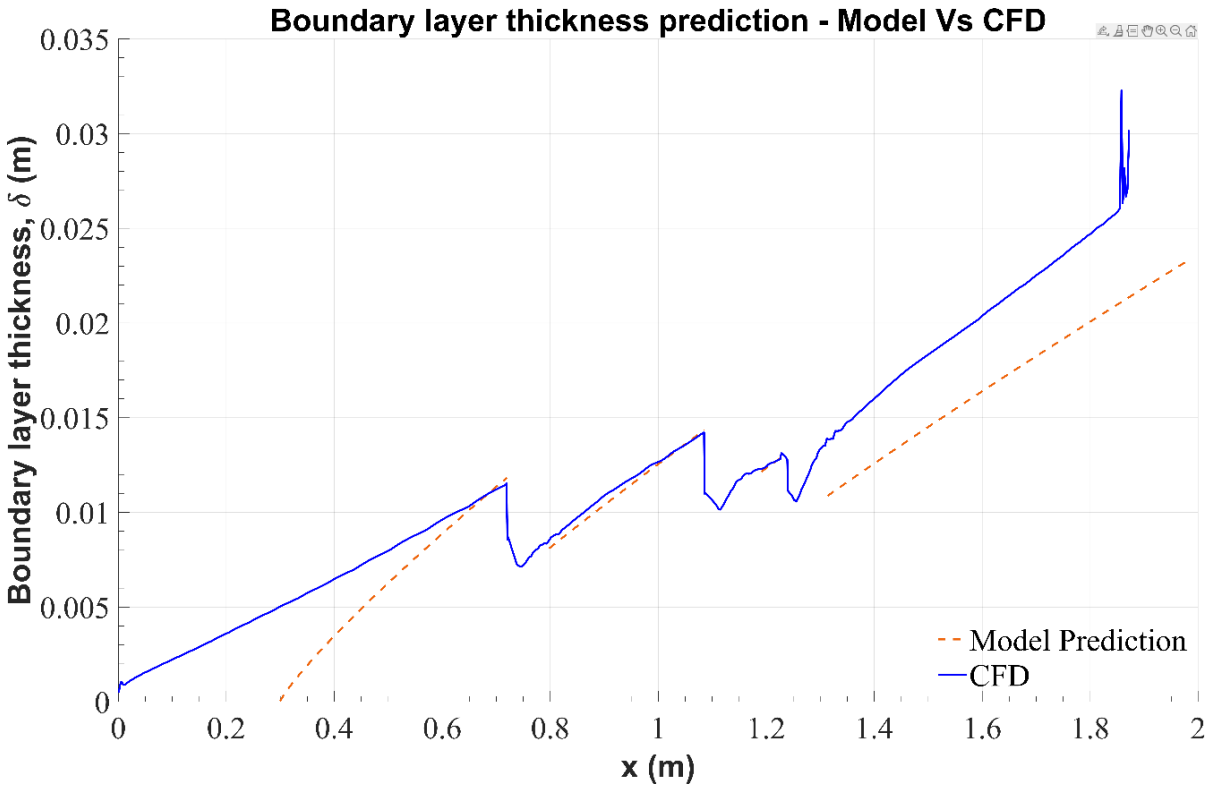


Figure 7-3: Comparison of boundary layer growth as predicted by model and CFD.

Supporting this are the wall pressure increase profile and velocity profiles at the STBLI regions, presented below in Figure 7-4 and Figure 7-5, as predicted by the model and CFD. Inspection of the pressure rise profile near the shock regions shows excellent to very good agreement with the numerical data. Specifically, along the first STBLI, the pressure rise is predicted to an excellent degree, only falling short in predicting the full distance required to achieve the pressure rise imposed by the shock. The predicted velocity profile shows a fair agreement with the CFD velocity profile, showing a very accurate capturing of the external region. Only the inner region is inaccurately captured, which also explains the higher skin friction coefficient predicted, seen in Figure 7-6.

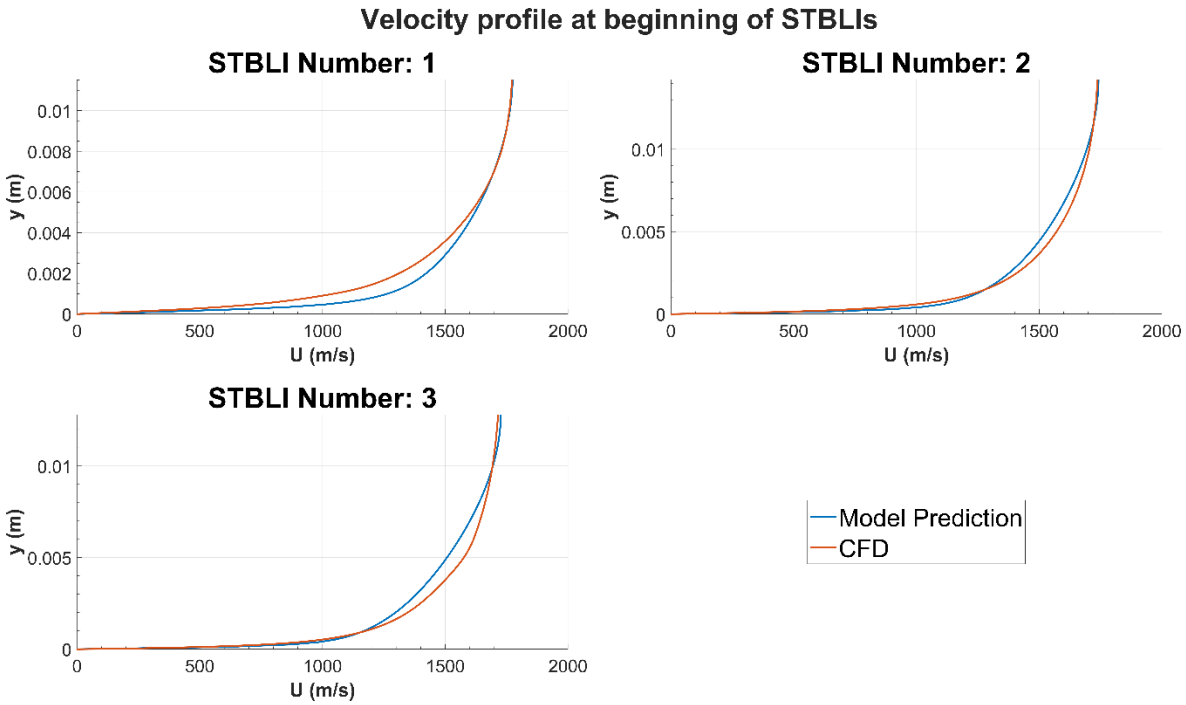


Figure 7-4: Comparison of velocity profiles before each SBTLI predicted by model and CFD.

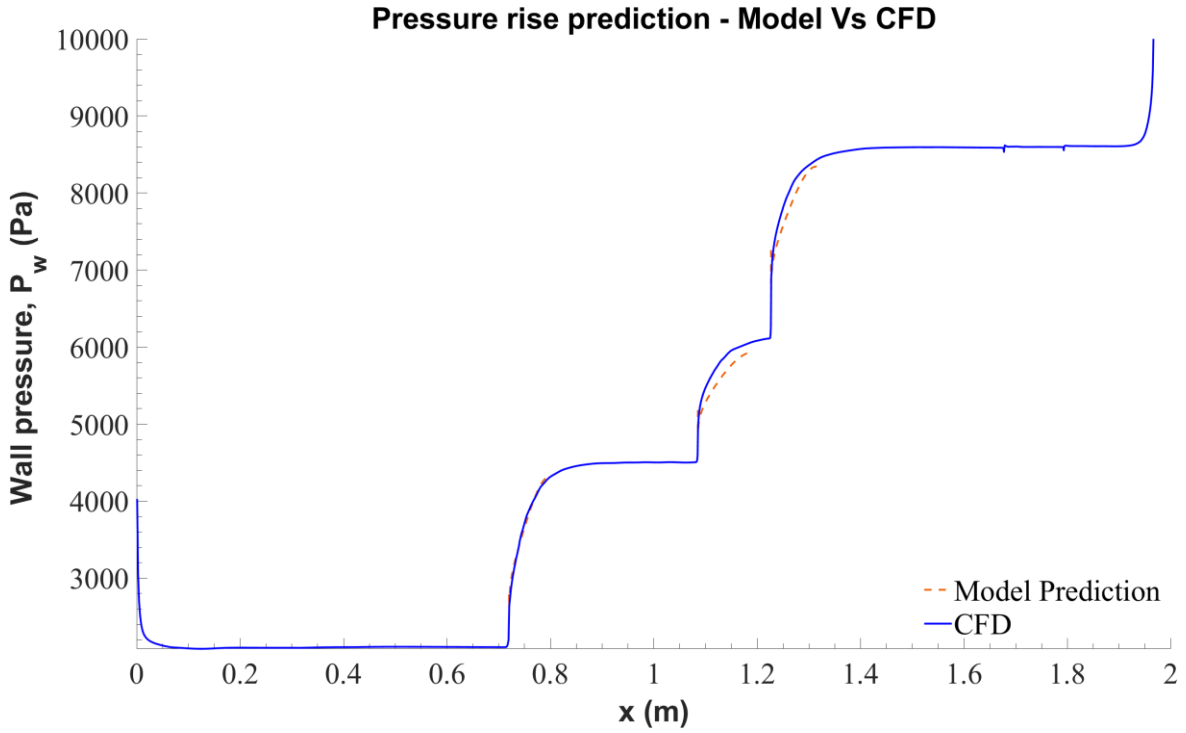


Figure 7-5: Comparison of wall pressure rise along the external compression ramps predicted by model and CFD

Past the first shock interaction, the predicted skin friction closely matches the CFD skin friction coefficient, and the boundary layer thickness nearly matches the evolution of the boundary layer observed in CFD as well. At the second STBLI, the model shows a weaker, although still accurate, predictive capability. The pressure rise prediction only shows fair agreement with

CFD, with both the amplitude and distance required to reach the pressure plateau being underestimated by the model. This can be partially attributed to the velocity profile prediction. Observations made from Figure 7-4 at the second SBTLI, which corresponds to the velocity profile at the joint between ramps 1 and 2, shows a reduction in the momentum of the predicted profile in the outer layer. This reduction, imposed on the solution of the STBLI method, results in a shallower pressure rise gradient, as in the outer profile, the Mach number is higher, which in turn results in shallower shock angles. The major departure in prediction occurs with the skin friction coefficient, which is underpredicted compared to CFD. Investigating further downstream, the third and final STBLI shows a further discrepancy/underestimation in the skin friction coefficient along the last plate. Coupled with the velocity profile at the third intersection, it is evident that the two STBLIs are linked. The last velocity profile is seen to be not fully recovered in the outer region, as the profile is not smooth, suggesting that the boundary layer has not fully recovered to an equilibrium boundary layer before undergoing further disturbance from the final shock. One of the key assumptions underpinning this model is that the location where the boundary layer has recovered sufficiently for the compressible universal turbulent velocity profile is equal to the location of pressure rise end. Combining the observations made of the velocity profiles, skin friction coefficient evolution and pressure rise, suggest that this assumption is falsified between the second and third STBLI. This, subsequently, affects the evolution of the boundary layer past the third STBLI, with the boundary layer developing significantly faster than predicted. Additional errors will be inevitably introduced using the Van Driest compressibility correction, as seen from Chapter 4. Despite the greater accuracy of this method against the analytical solution of the Van Driest II method, errors still arise compared to experiments.

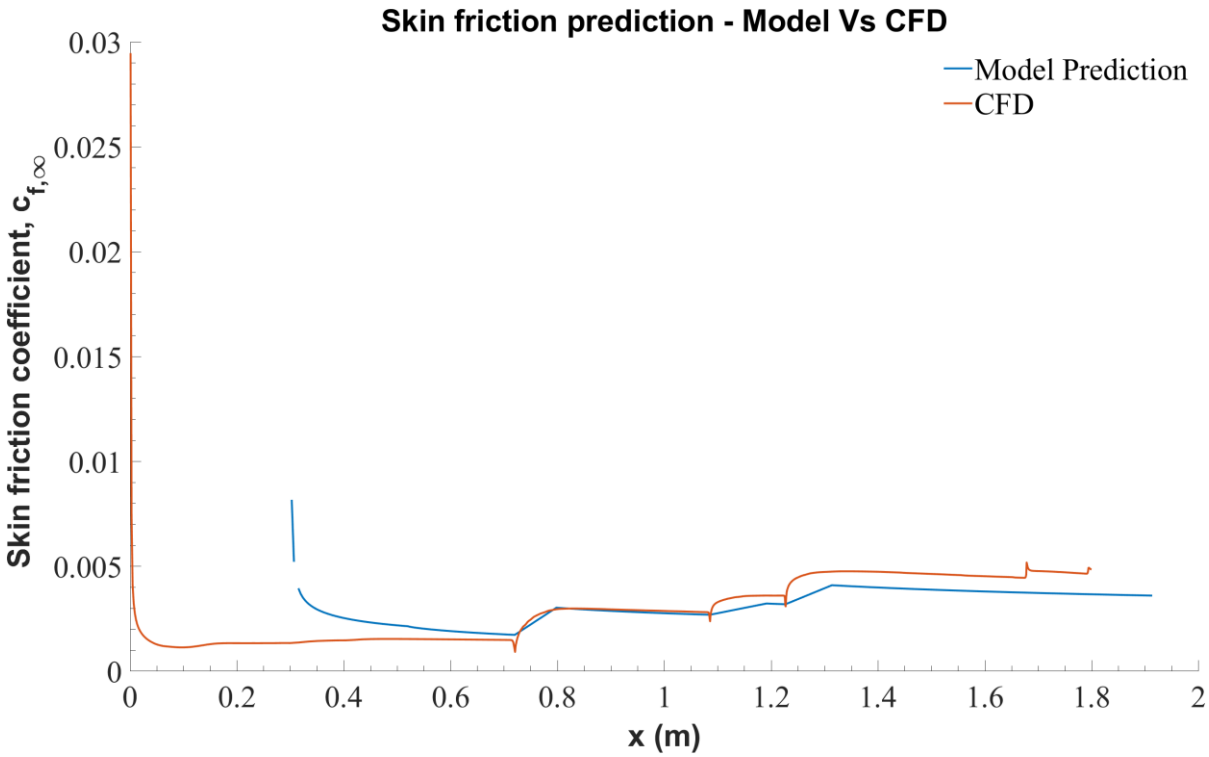


Figure 7-6: Comparison of skin friction coefficient evolution along the external compression ramps predicted by model and CFD.

Despite the discrepancies described above, the model has shown sufficient capability in predicting all aspects of a hypersonic external compression system. This also extends to the convergence of the external shocks. Although the model is designed to have shocks impinge on the cowl tip, the numerical schlieren obtained through CFD and presented in Figure 7-7, shows the shocks converging slightly ahead of the cowl tip. The red dot denotes the triple point of the external shock system, the point where all three shocks intersect.

The loss in mass flow rate is determined to be 0.053 kg/s, which is a negligible percentage of the overall design capture mass flow rate of 30 kg/s and would not have any appreciable effect on the engine's safe operation. This deviation is caused by the combination of the velocity profiles not fully matching the CFD-predicted profiles, and the simplified method of analysis of using the inviscid shock relations above the near wall region. However, as this model is developed as part of a preliminary development for scramjet engines, this is deemed as an acceptable trade-off for the overall accuracy obtained and computation speed.

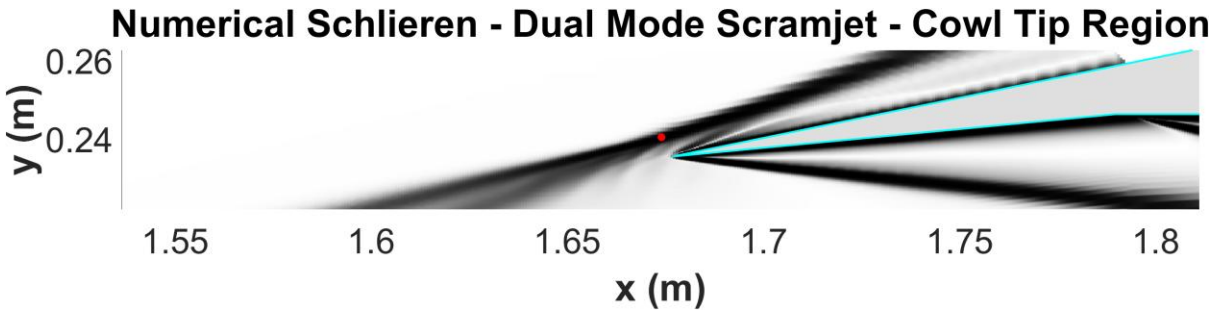
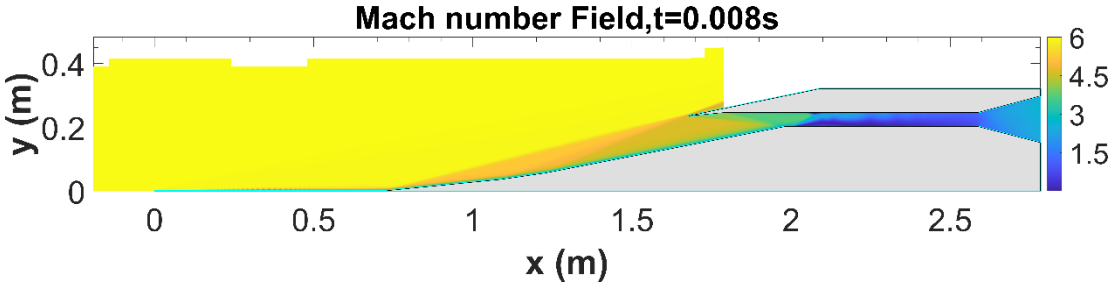


Figure 7-7: Numerical Schlieren near the cowl tip showing the location of shock convergence as a red dot. The shocks converge slightly further away from cowl tip, resulting in a loss of mass flow rate. Blue line denotes the surface of the cowl

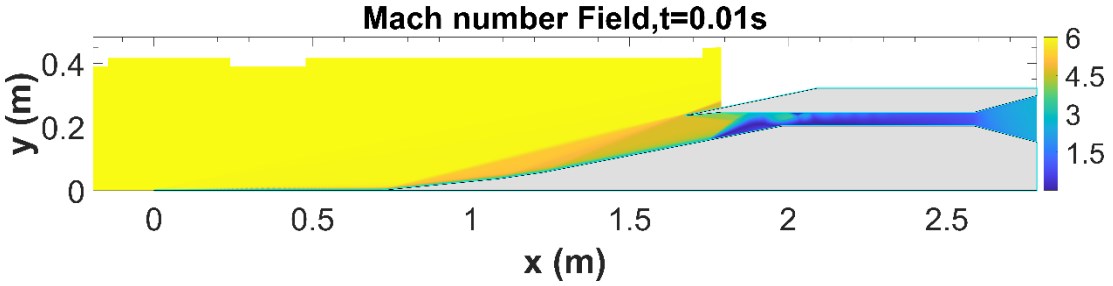
Investigation of the isolator flow shows mixed performance from the model. The primary difference arises from the maximum added heat that can be supported by the isolator and the incoming boundary layer. As discussed previously in Chapter 6.1, for a dual mode scramjet, an isolator is required to prevent combustion from unstarting the engine, and its length in this work is predicted to allow for a pressure rise of 150 kPa. Additionally, the enable maximum thrust, the engine is designed to operate at thermally choked conditions, meaning the exit Mach number will be unity. The simulation results are presented in Figure 7-8a-g). It is clear that the engine has unstarted, as the shock system has been ejected from the internal region of the engine and the flow has become fully subsonic. However, the flow does not remain in a stable configuration during unstart.

At t = 0.008s (Figure 7-8a)), the flow is still internal, showing the development of the shock train along with the separation zones on the top and bottom wall. In the next time snapshots, the boundary layer has moved upstream of the shoulder and subsequently fully ejected from the intake and the engine is unstarted. The boundary layer is seen to be at its maximum separation stage in Figure 7-8d), with severe subsonic spillage occurring. Past this point, the boundary layer is slowly being re-ingested into the intake, with Figure 7-8e) showing the boundary layer retracting downstream and subsonic spillage being supplanted by supersonic spillage. At Figure 7-8f), the boundary layer appears to move back towards the isolator, showing potential for the engine to restart automatically, but clearly from Figure 7-8g), it is re-ejected, and supersonic spillage is seen. This cyclical movement of the boundary layer and shock formation can be potentially more dangerous than a permanent unstart, as regions of the engine will experience loading cyclically at millisecond scales, which can cause the structure of the engine to fail.

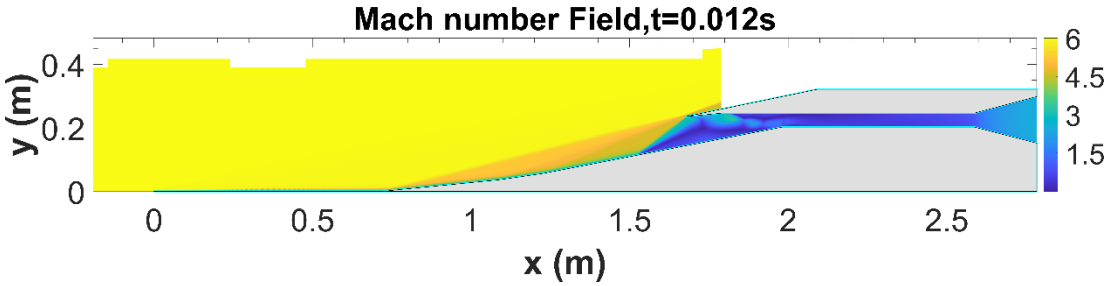
a)


Mach number Field,t=0.008s
y (m)
0.4
0.2
0
0
0.5
1
1.5
2
2.5
x (m)
6
4.5
3
1.5

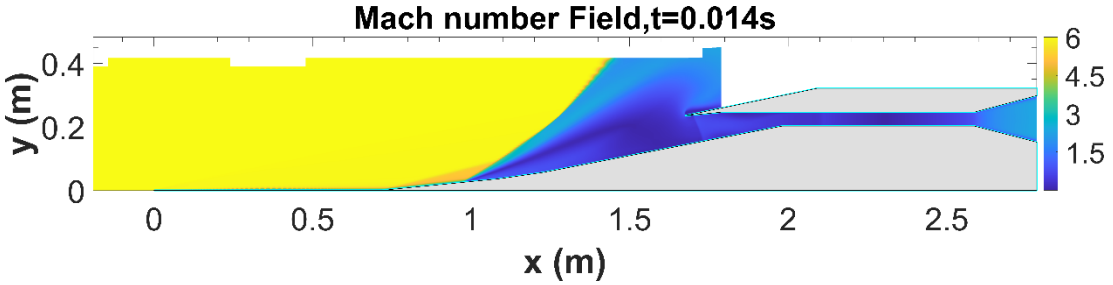
b)


Mach number Field,t=0.01s
y (m)
0.4
0.2
0
0
0.5
1
1.5
2
2.5
x (m)
6
4.5
3
1.5

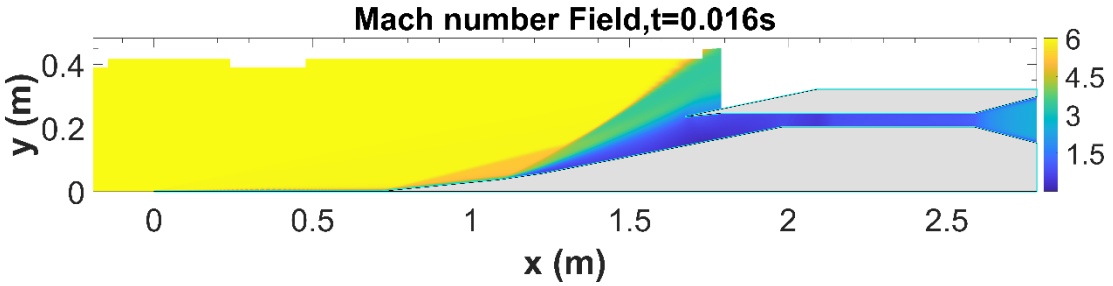
c)


Mach number Field,t=0.012s
y (m)
0.4
0.2
0
0
0.5
1
1.5
2
2.5
x (m)
6
4.5
3
1.5

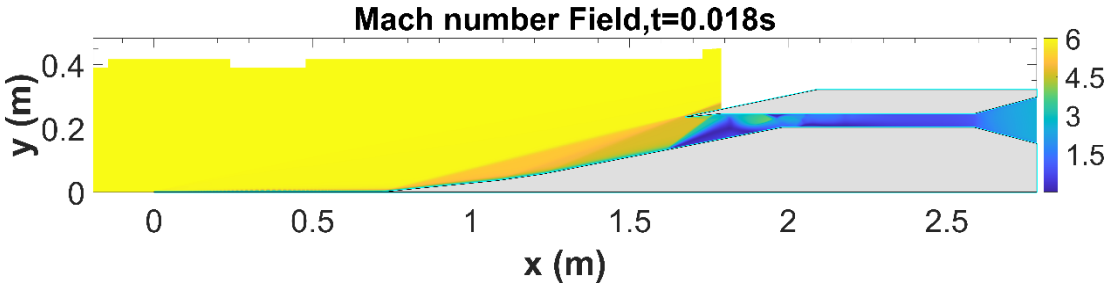
d)


Mach number Field,t=0.014s
y (m)
0.4
0.2
0
0
0.5
1
1.5
2
2.5
x (m)
6
4.5
3
1.5

e)


Mach number Field,t=0.016s
y (m)
0.4
0.2
0
0
0.5
1
1.5
2
2.5
x (m)
6
4.5
3
1.5

f)


Mach number Field,t=0.018s
y (m)
0.4
0.2
0
0
0.5
1
1.5
2
2.5
x (m)
6
4.5
3
1.5

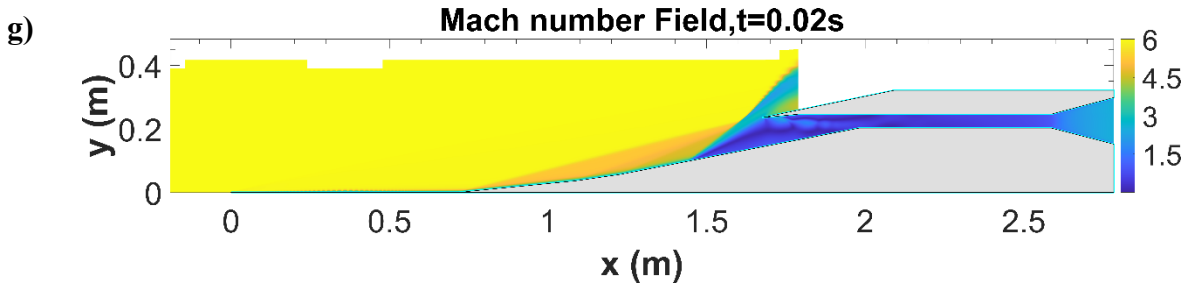


Figure 7-8: Evolution of flowfield for case of high heat addition

This serious deviation from the criteria of safe operation can be partially attributed to the CFD heat addition being modelled exclusively as a heat addition to the region instead of a combustion. The most significant influence of this is the variation in thermodynamic variables, which in the CFD, does not take into account the presence of water due to combustion.

To establish a started flow in the isolator, the heat added is reduced from 2.65 GW/m^3, calculated using equation 7.15, to 2.15 GW/m^3. The reduction is to be expected, as the heat addition predicted is an idealised condition. It assumes that the fuel combustion alone drives the temperature and pressure increase. But in real flows, the boundary layer thickening and friction contribute to the increase, meaning that the engine will achieve thermal choke at combustor exit at a lower heat addition.

At the lower heat addition, the shock system remains internal, with the shock train developing. This is evident from the numerical schlieren in Figure 7-9 below, showing the clear penta-shock system comprising of the three ramp shocks and the two cowl shocks and the shock train system in the isolator/combustor. The rest of the analysis on the convergence of the shocks on the shoulder as well as the isolator are done at the lower heat addition setting to obtain meaningful comparisons to the model predictions.

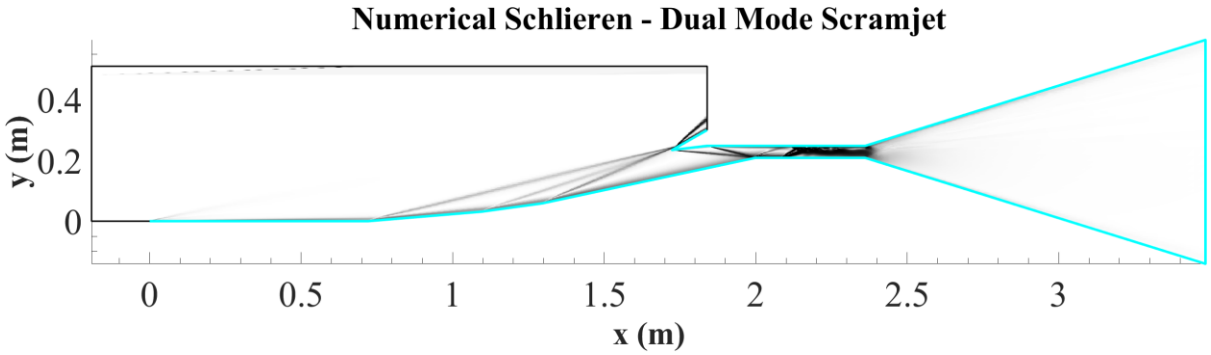


Figure 7-9: Numerical schlieren for started configuration using lower heat value of 2.15 GW/m^3

The overall flowfield shows very good agreement with the model, as was discussed in the previous segment, but only up to the isolator entry region. Figure 7-10 presents the velocity field overlayed on top of the numerical Schlieren, with the red dotted line denoting the boundary layer edge along the external compression system, calculated up to the point of shock impingement. The selection of this point is made as, after this point, the boundary layer undergoes significant distortions due to the presence of two shocks in a confined region, which are not evaluated using a velocity profile in the model.

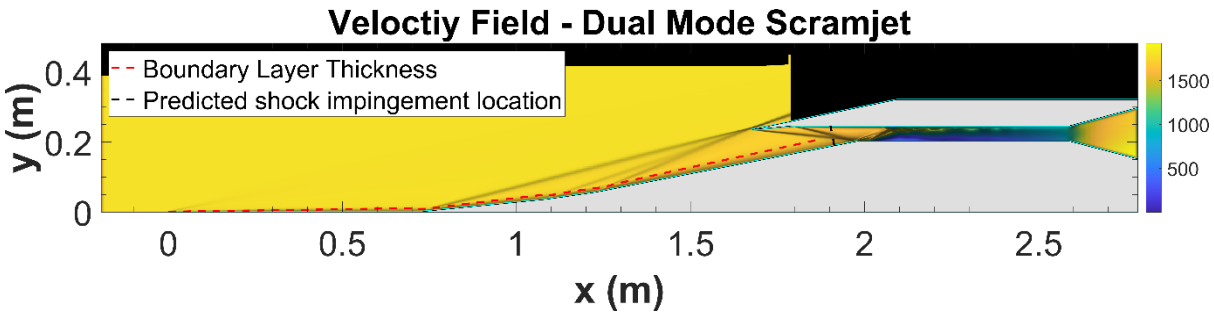


Figure 7-10: Velocity + schlieren fields along with evolution of boundary layer from CFD.

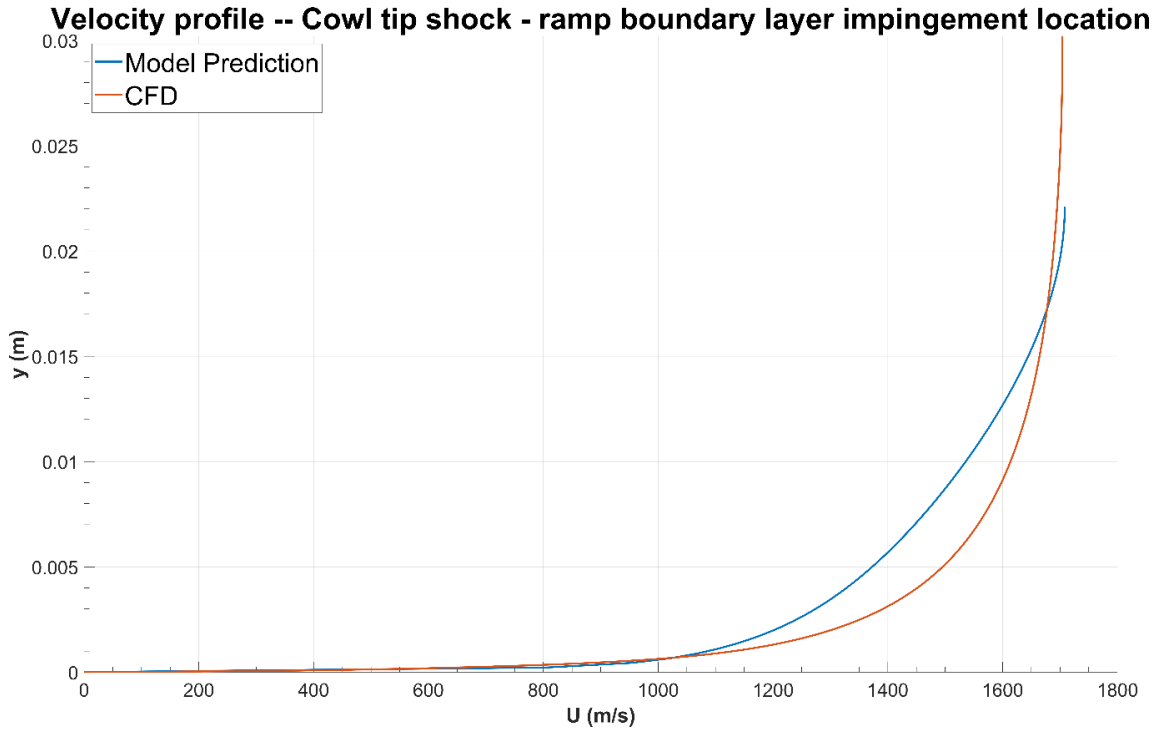


Figure 7-11: Velocity profile at location where cowl tip shock impinges on bodyside boundary layer (end of red dotted line on Figure 7-10).

The black dotted line denotes the model-predicted point of shock impingement from the cowl shock on the ramp boundary layer. It is seen that the two lines do not intersect, denoting a discrepancy between the two locations, owed to the significantly thicker boundary layer seen

in the CFD numerical results. This is evidenced even further from the velocity profile of Figure 7-11, which shows a significant mismatch between the two velocity profiles. The overall flowfield on the final ramp suggests that the final STBLI has minimal influence of the boundary layer, as it does not appear to contribute to severe loss of momentum or thinning of the boundary layer as observed in the previous STBLI.

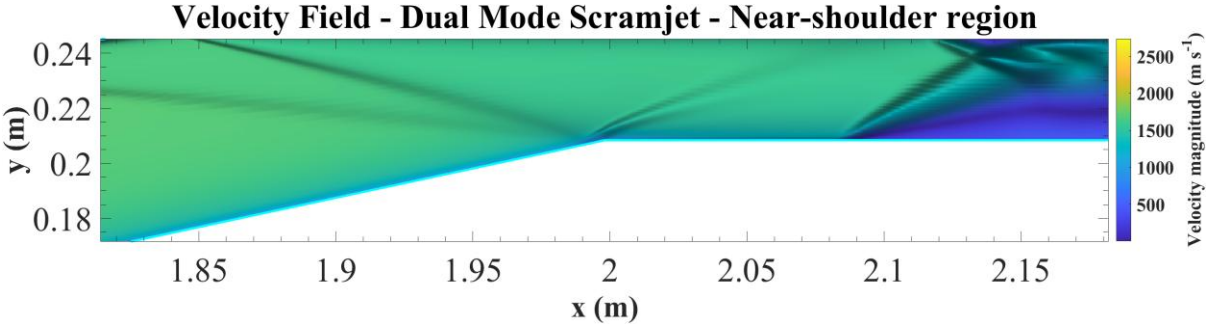


Figure 7-12: Velocity + schlieren fields at body shoulder near isolator entrance

The shock convergence and flow state on the ramp shoulder is another critical point, as the shock-on-shoulder condition must be met to eliminate propagation of shocks and expansion waves. However, this must be achieved without inducing severe flow separation, as this would narrow the effective flow area near the throat. Examining the numerical schlieren and velocity field of Figure 7-12 in the region near the shoulder, the shocks are seen to intersect near the shoulder. A small separation bubble has developed due to the pressure gradient imposed on the boundary layer, but it is not substantial enough to have significant consequences on the flow entering the isolator. The presence of the bubble produces an added system of detachment and reattachment shocks, seen from the lighter regions in Figure 7-12. However, the intensity is low, as the bubble itself is not significant enough to generate strong shocks. But both cowl shocks impinge in the same upstream location, which gives merit to the current methodology used to calculate the location of the shoulder.

Further downstream, the isolator flowfield is shown in Figure 7-13. The main features that can be seen are the significant asymmetry in separation on the upper and lower surfaces due to the difference in incoming boundary layers. The distinct “X” shaped shock pattern is seen at the leading shock, supporting the pressure rise at the supersonic core seen in Figure 7-14 below, which follows a rippling pattern, indicating the development of an X-shaped shock train. In the combustion chamber, the flow is seen to begin to mix into a significantly more uniform flow than the incoming flow.

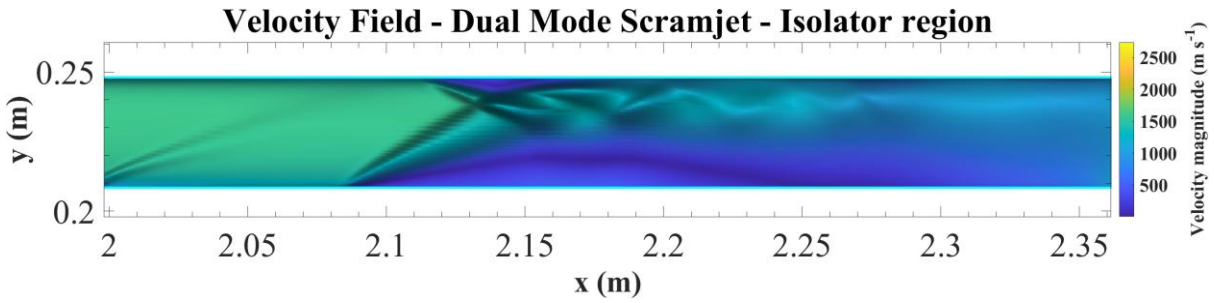


Figure 7-13: Velocity + schlieren in isolator/combustor region

Due to the geometry selected and the method of heat addition, the shock train extends past the isolator into the combustion chamber and would be difficult to determine the length of the shock train only contained in the isolator. It is evident that the isolator length predicted by the Waltrup/Billig relation is insufficient to contain the backpressure released, but accurately predicts the length required the pressure rise seen by the pressure rise trend in the supersonic core in Figure 7-14. This shows that the model can predict the pressure rise length and the associated Mach number reduction accurately. The predicted Mach number and temperature at combustor entry are 2.10 and 1065K respectively, while CFD predicts a Mach number of 2 and a core entry temperature of 1050K.

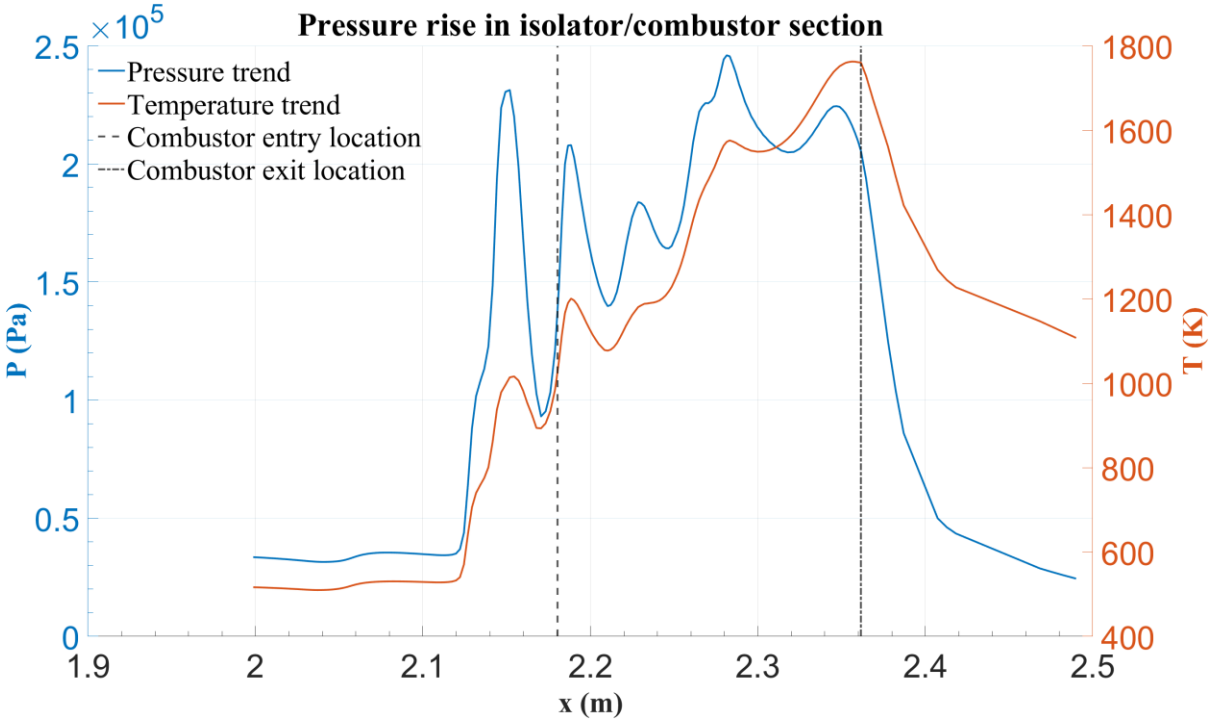


Figure 7-14: Pressure and temperature rise in supersonic core in isolator/combustor

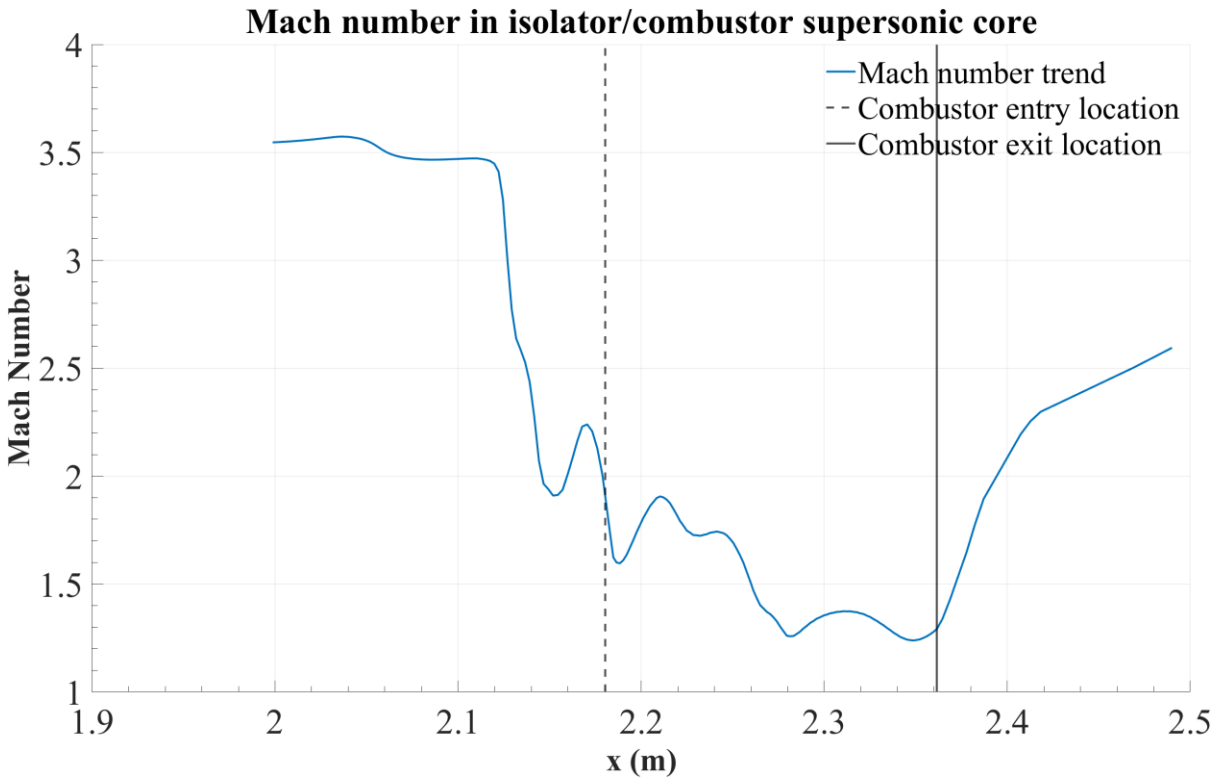


Figure 7-15: Mach number in supersonic core in isolator/combustor

The combustor exit conditions in CFD show the Mach number being higher than unity from Figure 7-15 showing that the core region is exiting at supersonic flow. However, investigating the mass-averaged Mach number, it is found that the Mach number is much closer to unity, having a value of 1.1, showing that the engine is operating effectively at thermal choke. While this is encouraging and aligns with the model requirement for thermal choke operation, it is not entirely accurate to the model or real operation. The combustor exit pressure and temperature are found from Figure 7-14 to be 210 kPa and 1800K respectively. The values predicted by the chemistry models are 578 kPa for the combustor exit pressure and 2160K for the combustor static temperature. There is a significant difference between the two values, which can be attributed to both the equilibrium chemistry and viscous effects in CFD. As alluded to previously, the presence of water and dissociation due to high temperatures will alter the heat absorption capability of the exit air composition. Additionally, one of the key assumptions made by the model is the lack of viscous elements in the combustion chamber. During simulations, the separated boundary layer continues into combustion chamber, absorbing heat in the low velocity regions. The increased heat destabilises the boundary layer, promoting further separation and propagating upstream, which would require a longer isolator, while the core does not experience the full pressure rise. The turbulence in the boundary layer dissipates energy, further reducing the pressure rise in the freestream.

Worth noting is the importance of the turbulent intensity, *I*. In this work, the URANS equations are solved with the $\gamma - Re_\theta$ turbulence closure model. The transition location, which is vital to the boundary layer growth along the ramp system, has direct reliance on the selected turbulent intensity, from Equation 3.22. Low values of turbulence intensity result in high values of transition onset momentum Reynolds number, meaning the flow would remain laminar. Conversely, high values of turbulent intensity promote early transition. The boundary layer state has two major influences on the flow, shock trajectory and resistance to separation.

No transition to turbulent boundary layer results in a much thinner boundary layer being encountering by all compression ramps, which means the generated shocks converge downstream of the cowl tip. This results in the engine operating in "supercritical" mode. While not inherently disadvantageous, the convergence of the shocks downstream of the cowl tip may cause the cowl-side boundary layer to separate depending on location and total compression. Additionally, it causes a reflected shock which impinges on the ramp and may cause separation on the ramp-side boundary layer. The effect of one, or at worst two, separation bubbles near the cowl tip would be the reduction in the flow Mach number entering the engine. At the limiting case, the flow becomes sonic, and a terminal normal shock is created, signalling the onset of unstart. In the event where the flow remains attached, the lower initial flow momentum, characteristic of laminar boundary layers, leads to lower flow momentum entering the isolator/combustor. This is captured loosely in the Waltrup/Billig relation (Equation 6.14) through the momentum thickness. The lower momentum is directly responsible for the reduction in backpressure resistance. Therefore, for the same compression and combustion characteristics, a low turbulence intensity set for simulations causes incorrect shock convergence and a "weaker" flow state entering the isolator/combustor.

Very early transition to turbulent flow also leads to inaccuracies in predicting the intake's behaviour. Early transition leads to excessive boundary layer growth along the entirety of the compression system. In contrast to the laminar case, the thickening of the boundary layer results in the shock convergence point being upstream of the cowl. Because of this, the engine operates is said to operate "sub-critical" mode. The movement of the convergence point from the downstream of the cowl to upstream alleviates the flow separation issue that may occur. However, the divergence from the shock-on-tip condition leads to leakage of air captured. The more pronounced the deviation, the greater the loss of mass flow rate. The loss of mass flow rate has a cascade of adverse effects on the engine. The most apparent one is the loss of thrust. Thrust is calculated by multiplication of specific thrust, $F_{specific}$, described by equation 6.33 by

the captured mass flow rate. Beyond the obvious reduction, the exit velocity, U_{10}, may also contribute to the reduction in thrust, depending on whether combustion is adjusted. If the fuel mass flow rate is not reduced from the optimum case, the effective equivalence ratio increases, as there is reduced air flow. This leads to more intense combustion, causing an increase in backpressure, lengthening the shock train. In turn, this destabilises the internal system, which may lead to unstart if the isolator is not long enough. In the case where fuel flow is adjusted to maintain constant equivalence ratio, one of two possible states occurs. The first and most catastrophic is that combustion ceases, as combustion can no longer maintained with the reduction in fuel added. The second is the reduction in combustion pressure increase and thus exit velocity, U_{10}, further contributing to loss of thrust as alluded to earlier. Hence, an artificially high turbulence intensity leads to a less stable engine and will inevitably distort the overall verification of the model.

While the model has shown good agreement in capturing the external shock locations and internal shock train, the CFD shows the limitations of the modelling approach. It is evident from the boundary layer thickness that at the last ramp, the boundary layer grows faster than the model can predict. This was attributed to the boundary layer undergoing successive SBLI without reaching equilibrium first, heavily distorting the profile in succession, which is a case the model cannot account for. Because the analytical model fundamentally assumes the boundary layer returns to a ZPG equilibrium state between interactions, it cannot account for this compounding profile distortion, leading to deviations in both boundary layer thickness and the skin friction coefficient on the final ramp.

Internally, the shock train is captured accurately but the combustor exit properties are significantly lower than the ones predicted by the equilibrium model. As stated previously, the difference arises due to two reasons. First, the CFD models combustion as a simple heat addition, neglecting the formation of new species, whereas the analytical model explicitly calculates multi-species chemical equilibrium. The second is that in the chemistry modelling, it is implicitly assumed that all the work to raise the pressure and temperature is done by the heat released by combustion. In CFD, the boundary layer thickening also contributes to the combustor compression in a constant area duct. This viscous displacement reduces the effective flow area, inducing an aerodynamic choking effect that further reduces the core Mach number and raises the static pressure and temperature, which cannot be captured by the current formulation of combustion.

Of interest is the influence of the designer-selected values, namely required mass flow rate, wall temperature of external ramps and flight Mach number. The next sections investigate these influences and present their effect on the objective functions.

7.2. Influence of design parameters on objective functions

The design space for a scramjet is rather wide, encompassing a Mach number range between 6 and 10, below which ramjet operation occurs, and above which the air is too rarified to be efficiently compressed. Additionally, the designer is able to select number of compression ramps, their wall temperature and the required mass flow rate to be captured by the intake.

The tool must be able to provide meaningful viable designs and do so with all the constraints outlined in Chapter 3. To investigate the influence of these design inputs, a parametric study is performed on each of the main designer-decided parameters. The default values selected are:

- Mach number, Ma = 6 (dual-mode) / Ma = 9 (pure scramjet)
- Wall temperature, $T_w = 600K$
- External ramp number, $n_{ramps} = 3$
- Required mass flow rate, $\dot{m}_{capt} = 30\ kg/s$

Initial optimisations for pure scramjets provided no results when required to meet ICR limits imposed as per constraint 5, which is $\frac{H_{iso}}{H_{cowl}} < ICR_{F\&G}(Ma_{closure})$. Thus, to obtain results for the pure scramjet configurations, the ICR criterion is not considered.

From these default values, one is altered per study. The range of variance of the parameters are presented in Table 7-3 below:

Table 7-3: Range and increment of designer-selected inputs used in parametric study

Parameter	Minimum Value	Increment	Maximum Value
Mach number	6	1	10
Wall temperature, K	300	100	1200
Ramp number	2	1	5
Mass flow rate, kg/s	10	10	100

7.2.1. Variation of Mach number

The first primary designer selection is the flight Mach number. The flight Mach number at cruise dictates the operating mode that the engine operates in. The flow momentum imposes limitations on the fuel that can be safely combusted without reaching unstart. A direct

consequence of this is the operation mode selection between dual-mode scramjet and pure scramjet. This is a critical choice, as incorrect selection might lead to a full unstart occurring due to over-combustion of fuel or insufficient thrust being generated. It is also of interest to predict where transition between modes would occur for optimum configurations. It is, however, understood that for each optimum configuration, the transition will vary due to sub-optimal performance during off-design performance. Despite this, it is a helpful initial reference point for the required mass flow rate and number of ramps.

Figure 7-16 shows the variation of the objective functions with increasing Mach number. All functions show sensitivity to the Mach number, as expected. A shift in the trend of all functions, except the specific thrust, is observed between Mach 8 and Mach 9. This indicates a change in the optimum operation mode, from dual-mode to pure scramjet. The specific thrust maintains an increasing trend, reflecting the increase in combustor exit temperature and velocity, leading to a higher thrust generated.

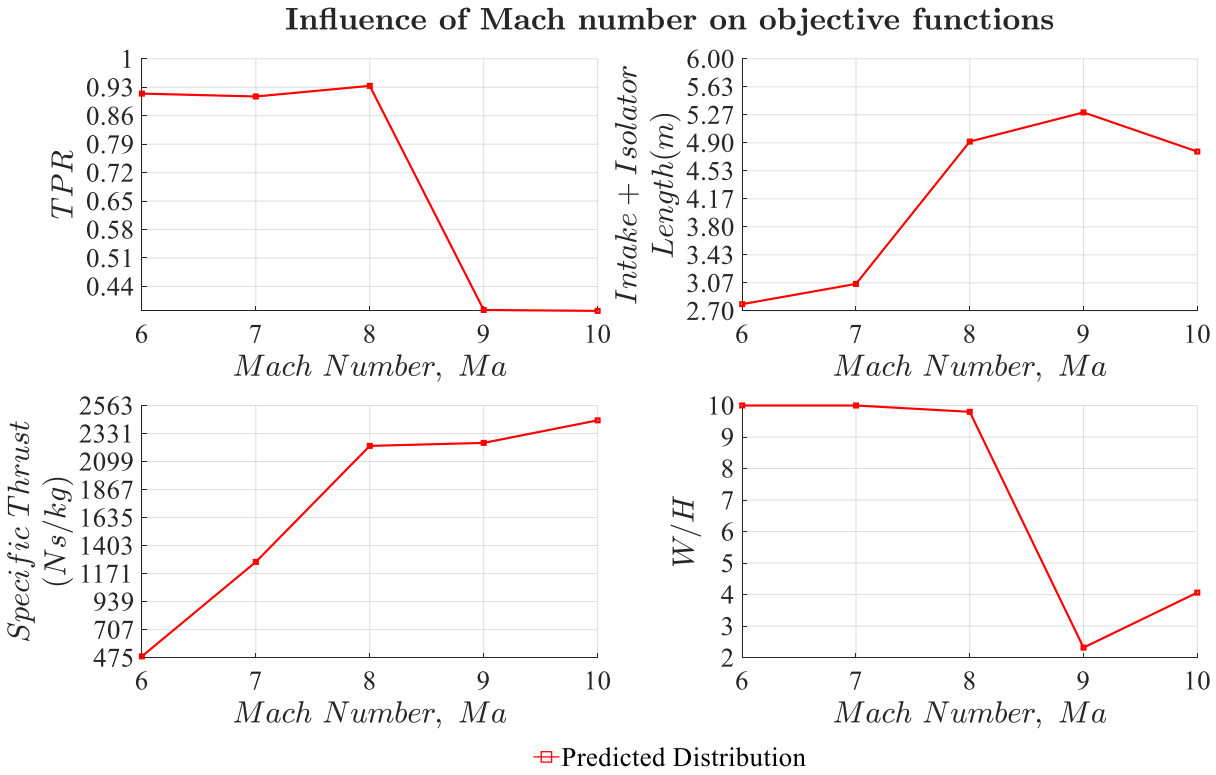


Figure 7-16: Influence of Mach number on objective functions

Before the transition, the dual mode operation shows very high total pressure recovery for the intake compared to pure scramjets. This is due to the shallower ramp angles, which while producing lower static pressure and temperature rise, result in more efficient compression. The low pressure and temperature are compensated for by the shock train generation in the isolator.

As the Mach number is increased, the ramp angles become shallower, as the Mach number increase compensates for the deflection, as seen by Table 7-4.

Table 7-4 Angles and width/height ratio representing the optimum configurations at the Mach numbers considered

Mach Number	θ_1	θ_2	θ_3	θ_{cowl}	n_{depth}
6	3.3839	3.5666	4.9249	5.8197	10.0000
7	2.8689	4.0937	3.5290	5.2219	10.0000
8	2.8282	1.0000	3.3656	2.9200	9.7991
9	5.7540	6.5967	10.8027	5.9031	2.3172

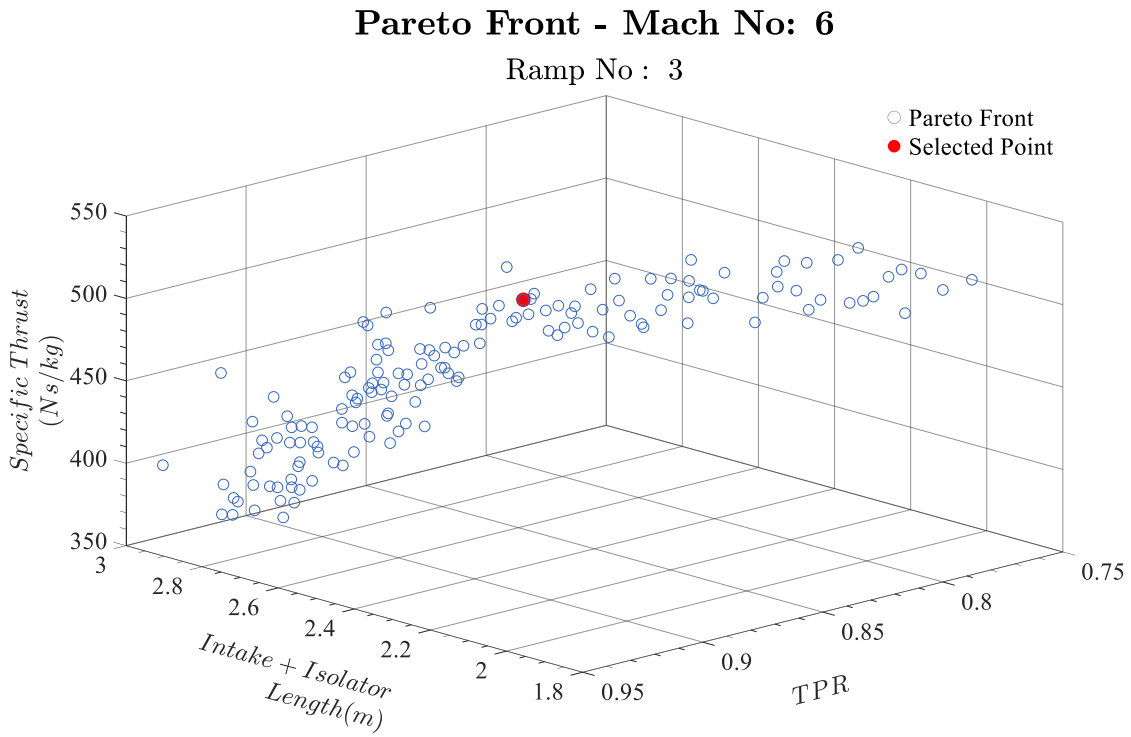
In contrast, pure scramjets must perform the entire compression through the external ramps. Flying at higher altitudes, the ambient pressure is lower and thus the static pressure ratio required is higher as well. The combination of these two manifests in very low total pressure recoveries, seen by the drop between Mach 8 and Mach 9. This also signifies the mode change from dual-mode to pure scramjet.

Figure 7-17 shows the Pareto fronts for Mach numbers 6 to 9. For dual mode configurations (Mach numbers 6 and 7), the overall Pareto fronts look similar. The fronts can be separated into two sections. The first are configurations that show a linear decrease in length and increase in specific thrust, while maintaining almost constant total pressure ratio. These configurations are comprised by shallow ramp and cowl angles, which result in the increased length, low compression and low specific thrust. The second section is comprised by the high external compression configurations. The higher compression angles result in shorter ramps and higher thrust generation at the penalty of lower total pressure recovery. The increase in thrust and reduction in length saturate near the optimum point, but the reduction in total pressure recovery is still present. This is due to the different permutations in arranging the external compression system, which results in similar static properties at the exit, but different total pressure losses.

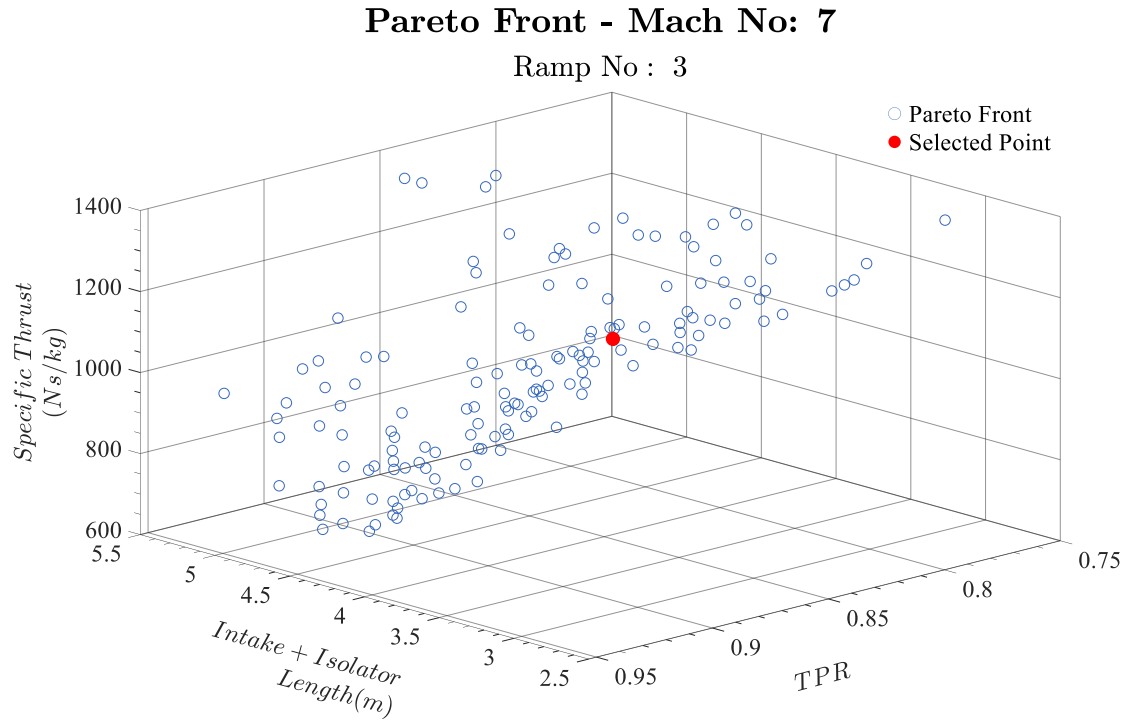
The Pareto front for Mach 8 shows a hybrid Pareto front. The front is separated into two clusters, with the left cluster representing the dual-mode configurations and the right representing pure scramjets. The right cluster shows an increase in thrust generated at the cost of a severe penalty to the TPR, which points towards a pure scramjet configuration. This indicates that even at Mach 8, a significant proportion of the configurations produce sufficient compression to remove the need for internal compression. Despite the availability of pure scramjet configurations, at Mach 8, the dual-mode configuration is still selected as the optimum configuration. The selection of the dual mode is due to the high specific thrust of the optimum configuration but still performs efficient compression at a relatively low engine length.

Mach 9's Pareto front shows the change to pure scramjet. The Pareto front of pure scramjets spreads into a surface. Due to the requirement for the entire compression to be performed by the external section, the geometric variation is significant. This is reflected by both the variation in length, but also the total pressure recovery. The optimum point is found to lie in the centre of the surface.

a)



b)



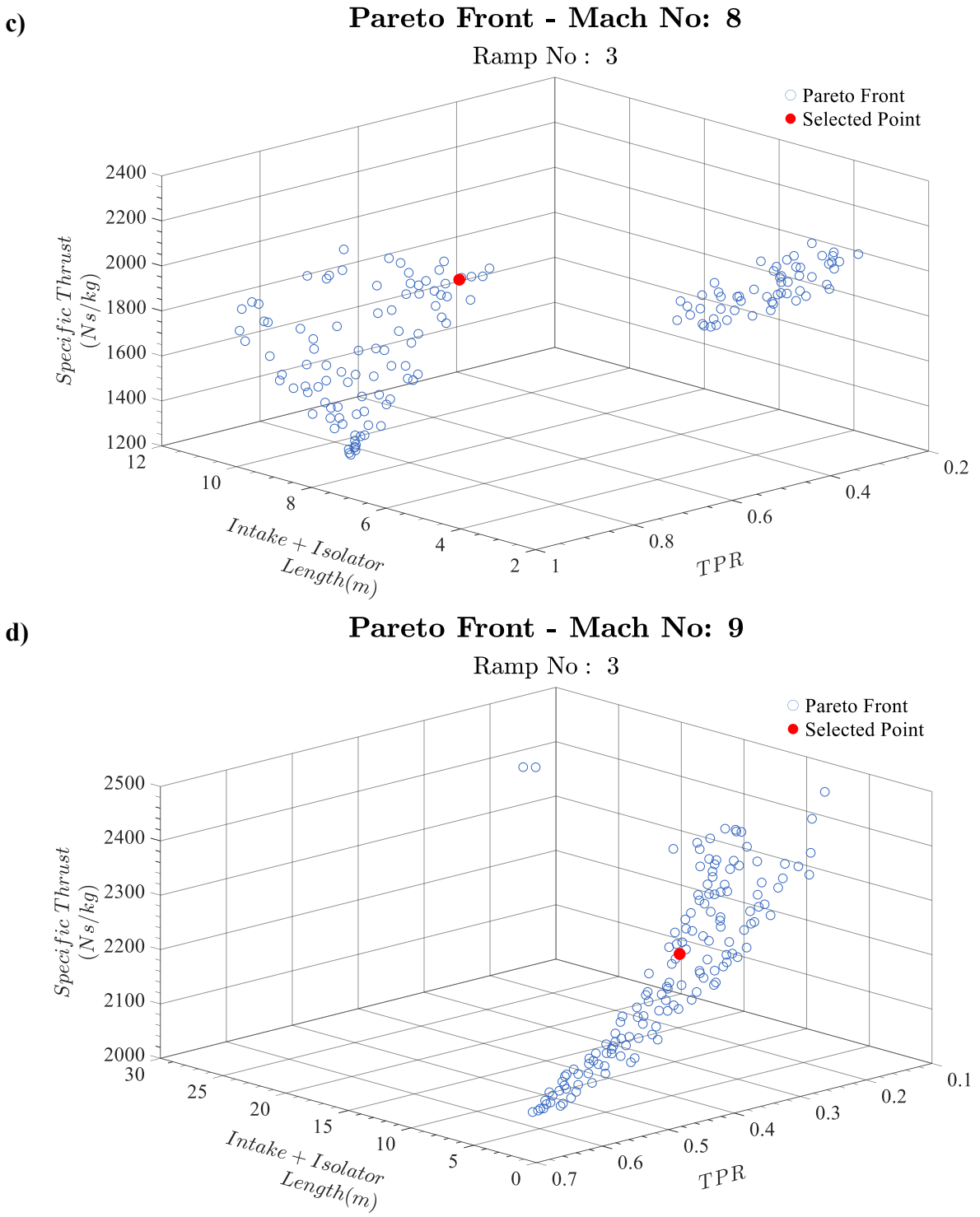


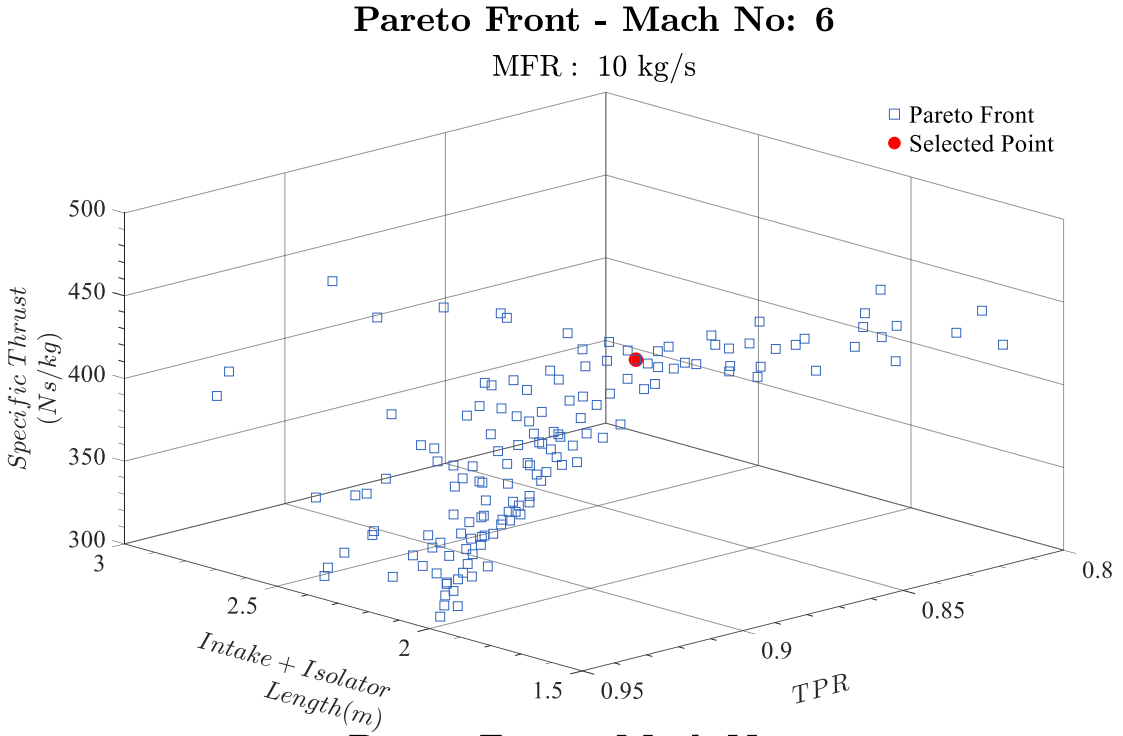
Figure 7-17: Pareto front variation with Mach number. a) Mach 6, b) Mach 7, c) Mach 8, d) Mach 9

7.2.2. Variation of mass flow rate

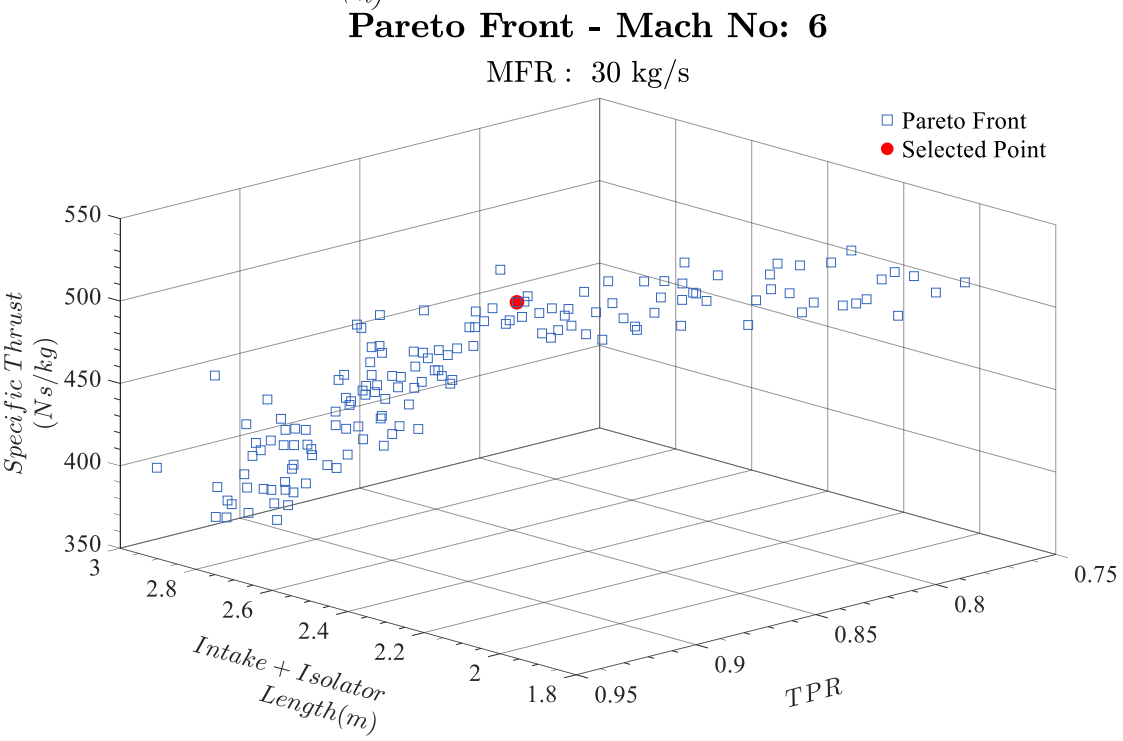
Following the Mach number study, the variation in mass flow rate is investigated. The evolution of the Pareto front with increasing mass flow rate captured at dual-mode and pure scramjets is presented in Figure 7-18 for the dual mode configuration and Figure 7-19 for the pure scramjet.

The optimum point for each configuration is selected based on equations 3.6 & 3.7 and highlighted on the respective Pareto front.

a)



b)



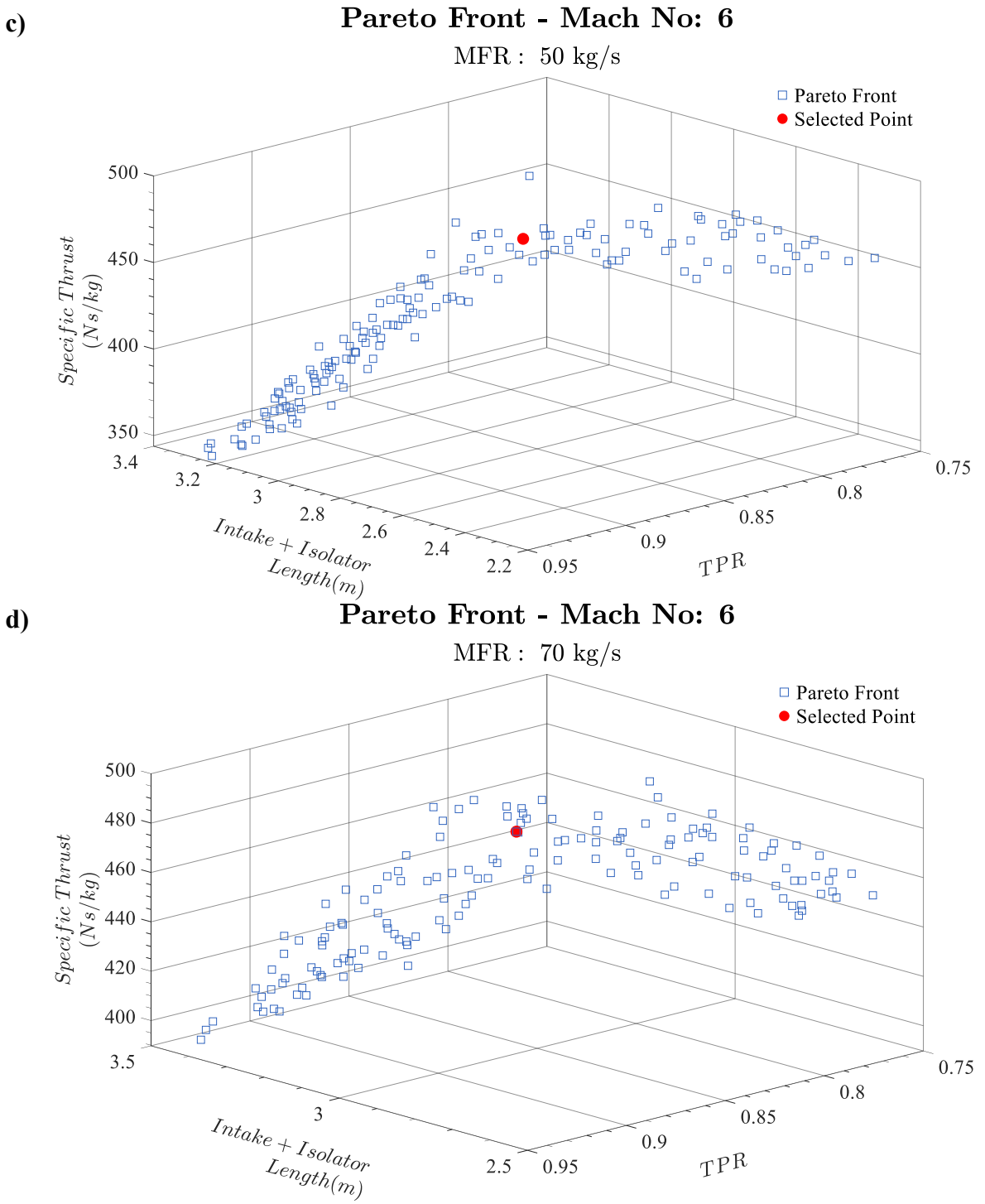


Figure 7-18: Pareto front variation of dual-mode scramjet with mass flow rate, MFR. a) MFR = 10 kg/s, b) MFR = 30 kg/s, c) MFR = 50 kg/s, d) MFR = 70 kg/s

The results show distinct differences in behaviour between the dual-mode and pure scramjet configurations. In the case of the dual-mode, the generic behaviour follows the one seen in the previous sub-section, with variance in Mach number. The two segments exist for all mass flow rates but exhibit slightly different behaviours. As the mass flow rate required is increased, the high compression segment becomes more populated.

Segment A, denoted in Figure 7-18 as the members of the Pareto front to the left of the selected point, contains the configurations with a higher TPR, which remains constant, with the length becoming shorter along the cluster and the thrust generated increasing. This is as a direct result of two components. Firstly, the total compression produced by the external ramps remains almost constant, around 12 degrees. This results in shallower shocks and, by extension, longer compression ramps. The specific thrust increases as the generated is a direct result of the increasing static pressure ratio contributed by the external compression system. The TPR remains essentially constant as well, as the compression remains constant, and the cowl closure angle remains similar. Being a dual-mode configuration, the rest of the compression is required to be made up by internal shock train, resulting in longer configurations, although as external compression increases, the length decreases accordingly. The other component is the width-to-height ratio, n_{depth}. An increase in this quantity results in shorter configurations. This is due to the geometric restrictions imposed by Equation 7.5. An increase in n_{depth} results in lower vertical capture area, which, to compensate the shallower shocks, the compression ramps must shorten to allow the shock impingement on the cowl tip, satisfying the cowl-on-tip condition. A separate cause of an increased length compared to Segment B is the increased length of the isolator section. From the relation of Waltrup and Billig (Equation 6.14), an increase in the required pressure ratio increase, results in an increase in a rapid increase in length, due to the quadratic relation between the two.

Segment B, denoted on Figure 7-18 as the members of the Pareto front to the right of the selected point, shows a more complicated relationship between the three objective functions. Near the minimum Euclidean point, there is a rapid change in the Pareto front. The rate of change of the intake length and available compression, represented by the specific thrust, severely slow down, and the total pressure recovery shows a steep decline along Segment B. The configurations characterising this cluster show a higher compression than those of Segment A. The increased compression is the result of higher compression angles, resulting in shorter external compression ramps, and due to the higher entry pressure, a shorter isolator section. This is compensated by a rapid decrease in TPR, representing higher entropic losses as a result of uneven and stronger compression from the ramps. The optimum configuration selected produces high compression with almost equal pressure ratio. This maintains a high specific thrust output, with high efficiency (TPR) and low configuration length.

At low mass flow rates, the low compression configurations of Segment A dominate the Pareto front. This reflects the lower availability of viable configurations that would satisfy all criteria.

As the mass flow rate required is low, the height of the intake calculated through equation 7.5 is low as a result. At low mass flow rates, the inclination of the shocks is restricted by the height of the intake. The compression angles and width to height ratio representing the optimum configuration of each mass flow rate condition are presented in Table 7-5.

Table 7-5: Angles and width/height ratio representing the optimum configuration at the mass flow rates considered for dual-mode scramjet

Mass Flow Rate (kg/s)	θ_1	θ_2	θ_3	θ_{cowl}	n_{depth}
10	4.1359	7.7502	11.5476	6.1244	10
30	4.4646	7.2866	11.9468	6.1799	9.9470
50	4.9479	8.4703	12.1059	4.8067	10
70	4.9392	8.7079	12.1675	4.1758	9.9846

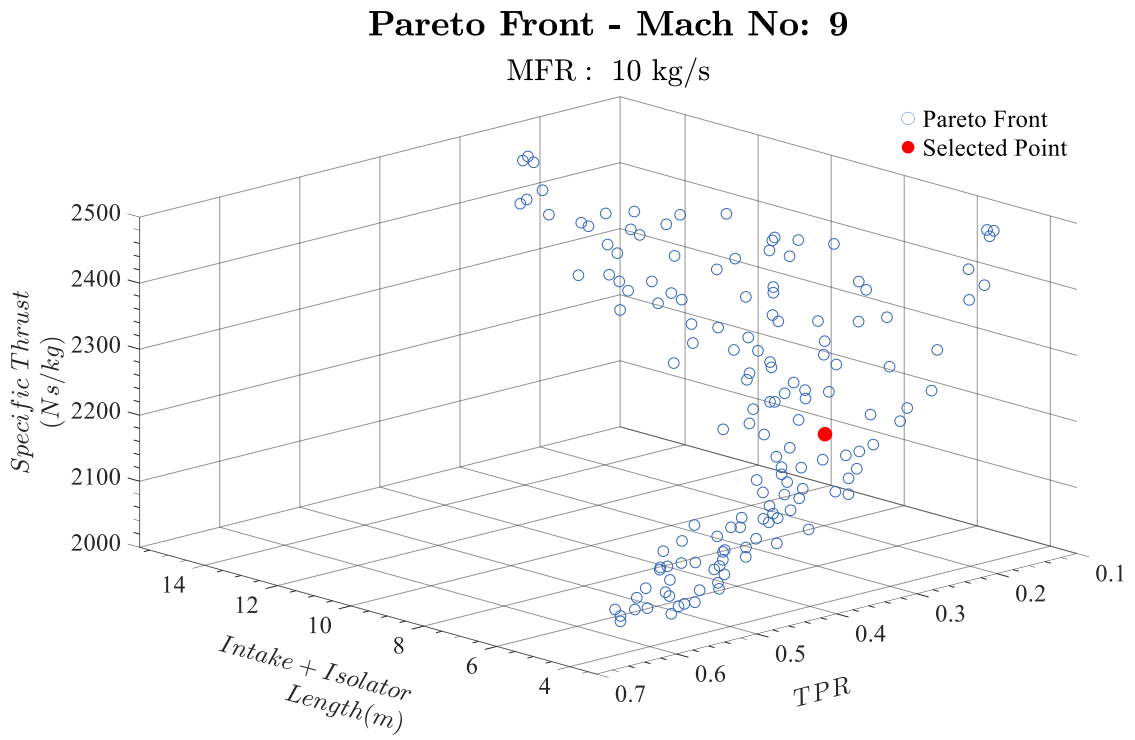
It can be seen that the optimum configurations share similar compression angles, producing a total compression of about 12 degrees. The cowl angle, θ_4, is also roughly half the overall compression produced by the ramps. This splits the compression between the cowl tip and spike shocks, increasing efficiency of compression. The cowl angle shows a decreasing trend as the mass flow rate required is increased. This is due to the increase in capture height.

It is also worth noting that the width to height ratio, N, is kept at the maximum limit. This seems counterintuitive at first, since a lower value would result in a taller intake (Equation 7.5), which would in turn result in sharper shocks being generated to satisfy the shock-on-tip condition. As elucidated previously, configurations that are heavily rectangular (i.e. n_{depth} is larger), exhibit lower lengths due to shorter ramps. Another point of interest is the fact that no optimum configurations operate with the cowl fully open. The cowl is kept partially closed, inducing an internal spike shock, splitting the overall compression between the two shocks. This may impact the overall performance of the engine negatively, however, as profile drag will be increased. This was not considered in this work, however, and thus configurations with partially closed cowls appear to be optimum for dual-mode scramjet operation with increasing mass flow rate.

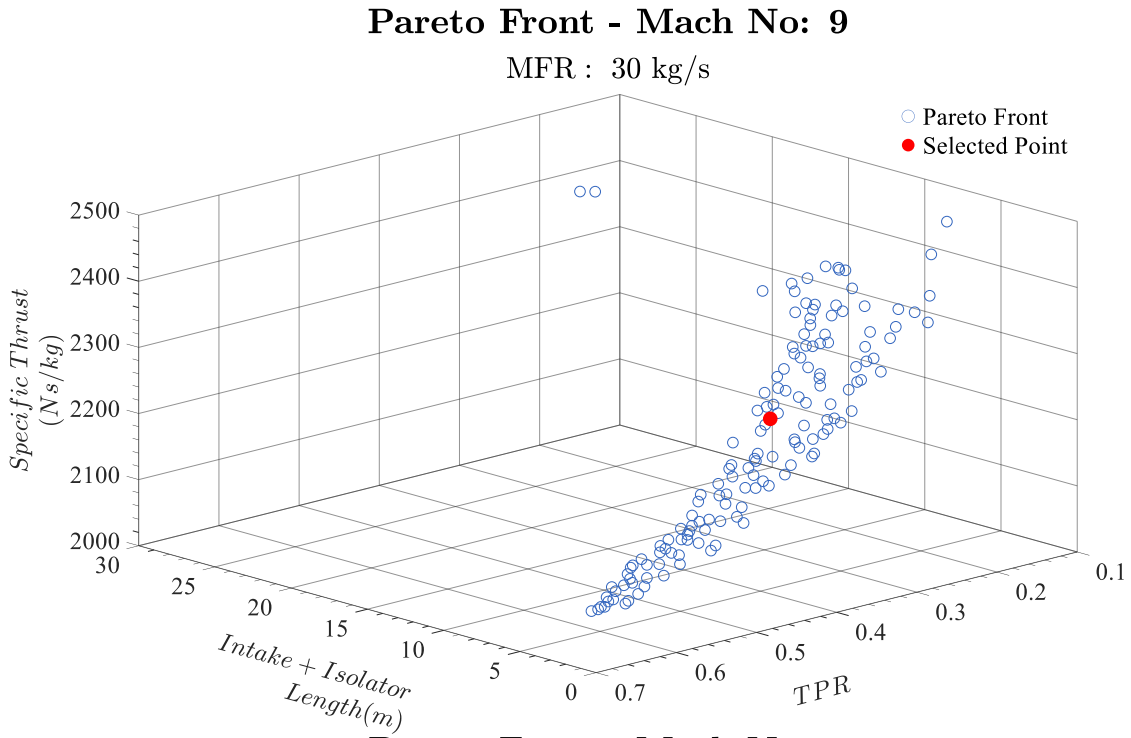
The pure scramjet optimisation has a significantly more complicated Pareto front than the dual mode optimisation. Looking at Figure 7-19, the Pareto front is seen to smear into a surface. At the lower specific thrusts, the engine length is maintained constant, while the TPR is linearly decreased. Near the optimum point, a shift is seen to occur, with a rapid shift in all objective functions. The intakes in this region show a rapid lengthening, with a dramatic loss of compression efficiency and gain in thrust. This is characteristic of very high compression by

one of the ramps. It is noted that at the inefficient compression region, the first or last ramp deflections near the maximum bounds imposed by the optimisation algorithm. The very high deflections at high Mach numbers has two significant effects. The first is that the static pressure rises dramatically, at the expense of total pressure recovery. This links to the second effect, which is the much higher specific thrust, since the scramjet entry pressure and temperature have risen significantly due to the high singular compression. The optimum point for all mass flow rates is selected to be in the middle of the surface, similarly to the Mach number parametric study. At this point, the compression is split more evenly across the intake, increasing the efficiency dramatically.

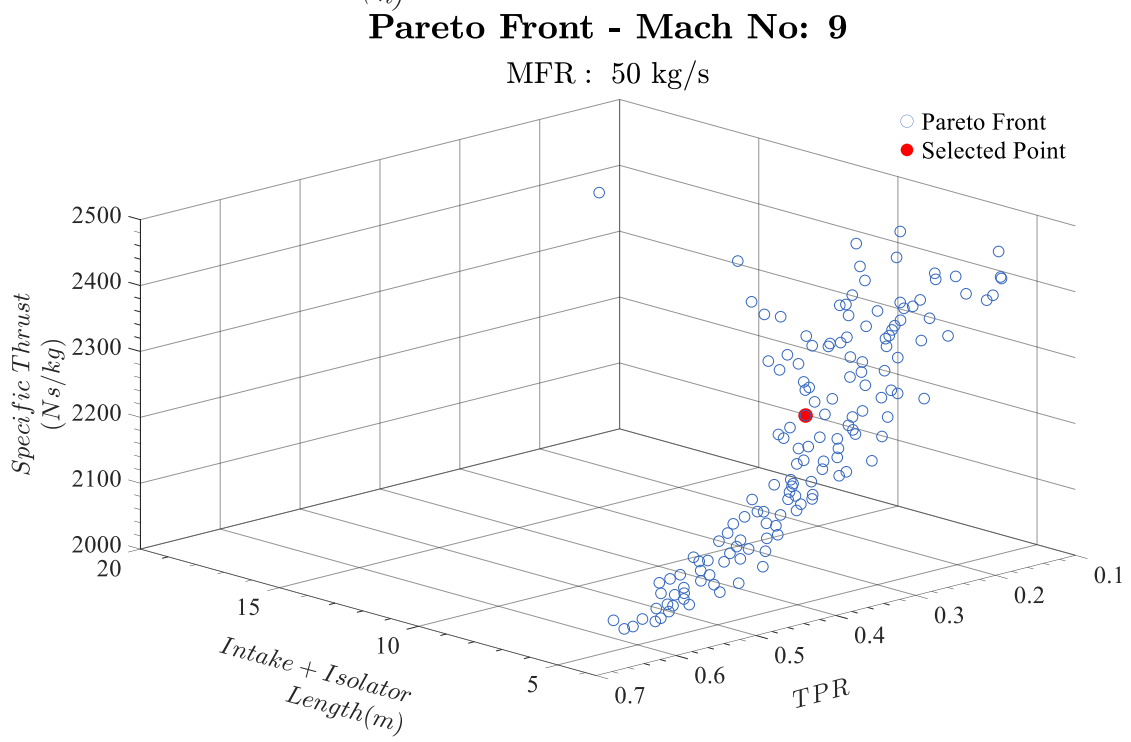
a)



b)


Pareto Front - Mach No: 9
MFR : 30 kg/s
Pareto Front
Selected Point
Specific Thrust (Ns/kg)
2500
2400
2300
2200
2100
2000
30
25
20
15
10
5
0
Intake + Isolator Length(m)
0.7
0.6
0.5
0.4
0.3
0.2
0.1
TPR

c)


Pareto Front - Mach No: 9
MFR : 50 kg/s
Pareto Front
Selected Point
Specific Thrust (Ns/kg)
2500
2400
2300
2200
2100
2000
20
15
10
5
Intake + Isolator Length(m)
0.7
0.6
0.5
0.4
0.3
0.2
0.1
TPR

d)

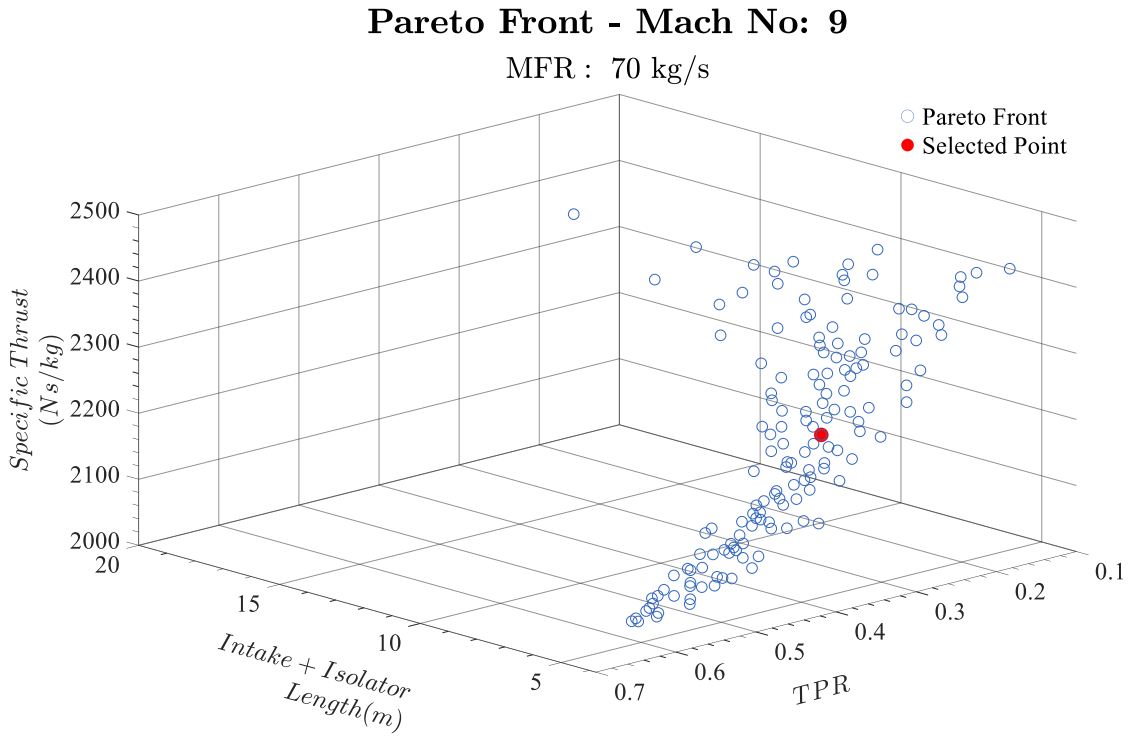


Figure 7-19: Pareto front variation of pure scramjet with mass flow rate, MFR. a) MFR = 10 kg/s, b) MFR = 30 kg/s, c) MFR = 50 kg/s, d) MFR = 70 kg/s

Table 7-6: Angles and width/height ratio representing the optimum configuration at the mass flow rates considered for pure scramjet

Mass Flow Rate (kg/s)	θ_1	θ_2	θ_3	θ_{cowl}	n_{depth}
10	8.2293	13.5264	23.1345	6.4654	1.2874
30	5.7540	12.3507	23.1534	5.9031	2.3172
50	6.4188	13.2469	23.3607	5.3289	2.9190
70	6.5402	13.2856	22.8874	5.2530	6.5221

Table 7-6 reflects the observations observed in the full Pareto front. Interestingly, while some parallels can be observed, the behaviour of the optimum points with increasing mass flow rate deviates from what would be expected. In common with the dual-mode, the overall compression produced by the ramps remains constant, about 23 degrees. Also, in common is the constant value of the cowl closure angle, although the compression by the cowl is predominantly performed by the cowl tip shock. The difference is observed in width/height ratio, with increasing rectangular ducts being the optimal configuration as the required mass flow increases. For low mass flow rate requirements, the value of width/height ratio drops near unity, meaning the intake is almost square. It then monotonically increases as the mass flow rate required increases. The length shows different trend, with an increase in length noted up to MFR = 50 kg/s, which then decreases until the maximum mass flow rate in this study. This

is in spite of the width/height ratio increase. The reason is that, while the width/height ratio shows an upward trend, it is not sufficient to offset the increase in length near the low mass flow rate demands. At higher mass flow rate demands, the width/height ratio increases rapidly and is able to contribute to the reduction of the engine length.

The reason is a combination of the solution of Equation 7.5 and the need for the scramjet to perform compression without internal shocks (no isolator). To accommodate the increase in mass flow rate capture and subtend the shocks on the cowl and shoulder, while performing enough compression, the intake becomes wider. This is in contrast to the dual-mode, which remains almost exclusively at the maximum ratio, which minimises the length.

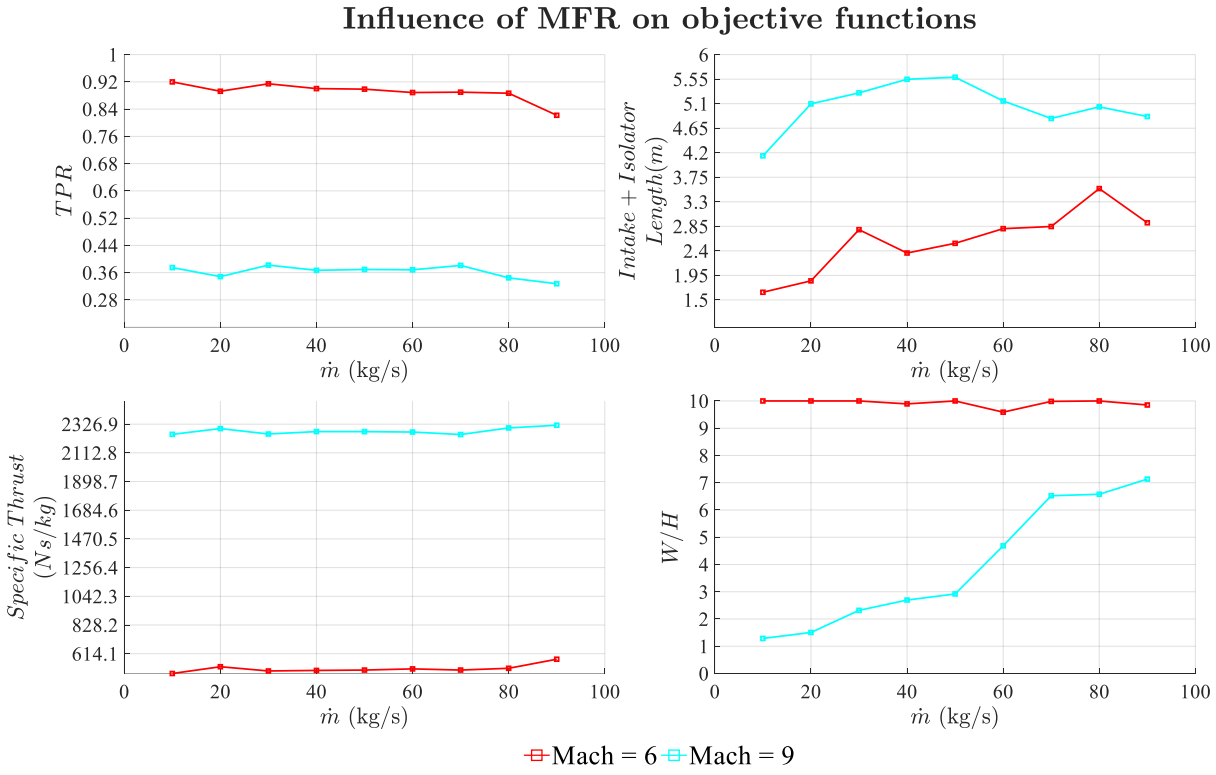


Figure 7-20: Influence of MFR on objective functions for dual-mode (red) and pure scramjet (blue) configurations

The overall influence of the mass flow rate on the objective functions is shown in Figure 7-20. The compression efficiency is, as expected, significantly higher for the dual mode configurations, due to lower entropic losses from the external shocks. As a result, the overall compression produced by the ramps is significantly lower, which is reflected by the lower specific thrust generated. Pure scramjet configurations result in longer intakes, but as mass flow rate requirements increase for the dual-mode, the trend appears to show that it would overtake pure scramjet lengths. There is a significant variance in width/length configuration

for pure scramjets, while dual-modes benefit from the maximum imposed ratio. Pure scramjets show a linear increase in width/length ratio, but almost constant length for above-unity ratios.

The influence of the mass flow rate on the design of scramjets takes different forms for dual mode and pure scramjets. For dual-mode, the intake-isolator combination becomes longer for increasing mass flow rate. For pure scramjets, both the intake length and width significantly vary. The reason lies in the lack of isolator to compensate for the reduction in external compression. Without the internal compression provided by the shock train, pure scramjets must perform the compression entirely through the ramp/cowl shock system.

7.2.3. Variation of wall temperature

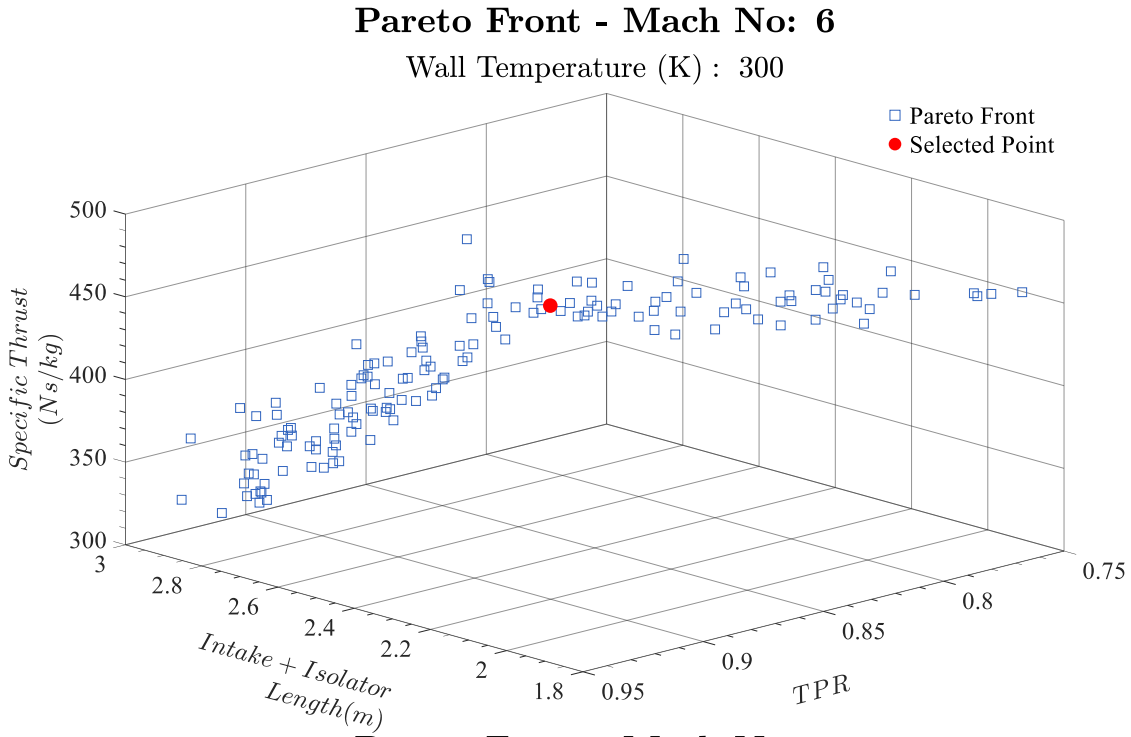
As part of the design requirements, the wall temperature for the ramps is required. Due to the high ambient temperature and high Mach numbers, the wall temperature under adiabatic conditions would reach temperatures that would compromise any known material. For instance, a scramjet operating at Mach 9 would experience a wall temperature of 3785K. Thus, wall cooling is required to mitigate thermal damage caused to the structure.

A secondary effect of wall cooling is its effect on the boundary layer. Severe wall cooling influences the growth of the boundary layer, seen by its influence on the thermal coefficients used in the Van Driest transformation (Equations 4.22-4.25) as well as directly on the boundary layer thickness through equation 4.29.

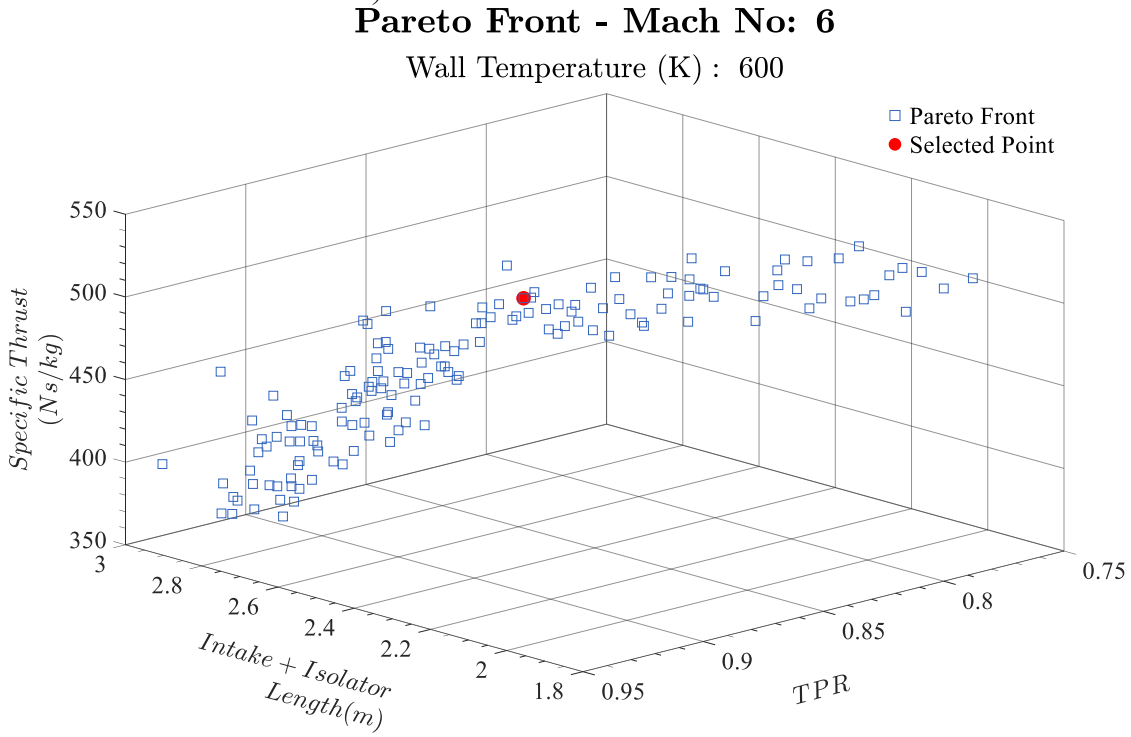
As the viscous elements have a significant effect on the intake, it is of importance to investigate the effect of the wall temperature on the boundary layer and the subsequent overall impact on the objective functions. The wall temperature is varied from 300K to 1200K. The mass flow rate required is kept constant at 30 kg/s, and the number of external compression ramps is maintained at 3.

An analysis of the Pareto front evolution with increasing wall heating (or reduced wall cooling) is done in a similar fashion to the mass flow rate requirement. Figure 7-21 shows the change of the Pareto front for the dual-mode configuration. As with the mass flow rate pareto fronts for the dual-mode configuration, all four Pareto fronts for the variation in wall temperature split into two segments. The overall shape of the Pareto front remains very similar between the increasing temperature figures but becomes sparser in Segment A as temperature is increased. The sparseness is attributed to the increase in thickness of the boundary layer along the length of the intake, resulting in more varied configurations.

a)


Pareto Front - Mach No: 6
Wall Temperature (K) : 300
Pareto Front
Selected Point
Specific Thrust (Ns/kg)
500
450
400
350
300
3
2.8
2.6
2.4
2.2
2
1.8
Intake + Isolator Length(m)
0.95
0.9
0.85
0.8
0.75
TPR

b)


Pareto Front - Mach No: 6
Wall Temperature (K) : 600
Pareto Front
Selected Point
Specific Thrust (Ns/kg)
550
500
450
400
350
3
2.8
2.6
2.4
2.2
2
1.8
Intake + Isolator Length(m)
0.95
0.9
0.85
0.8
0.75
TPR

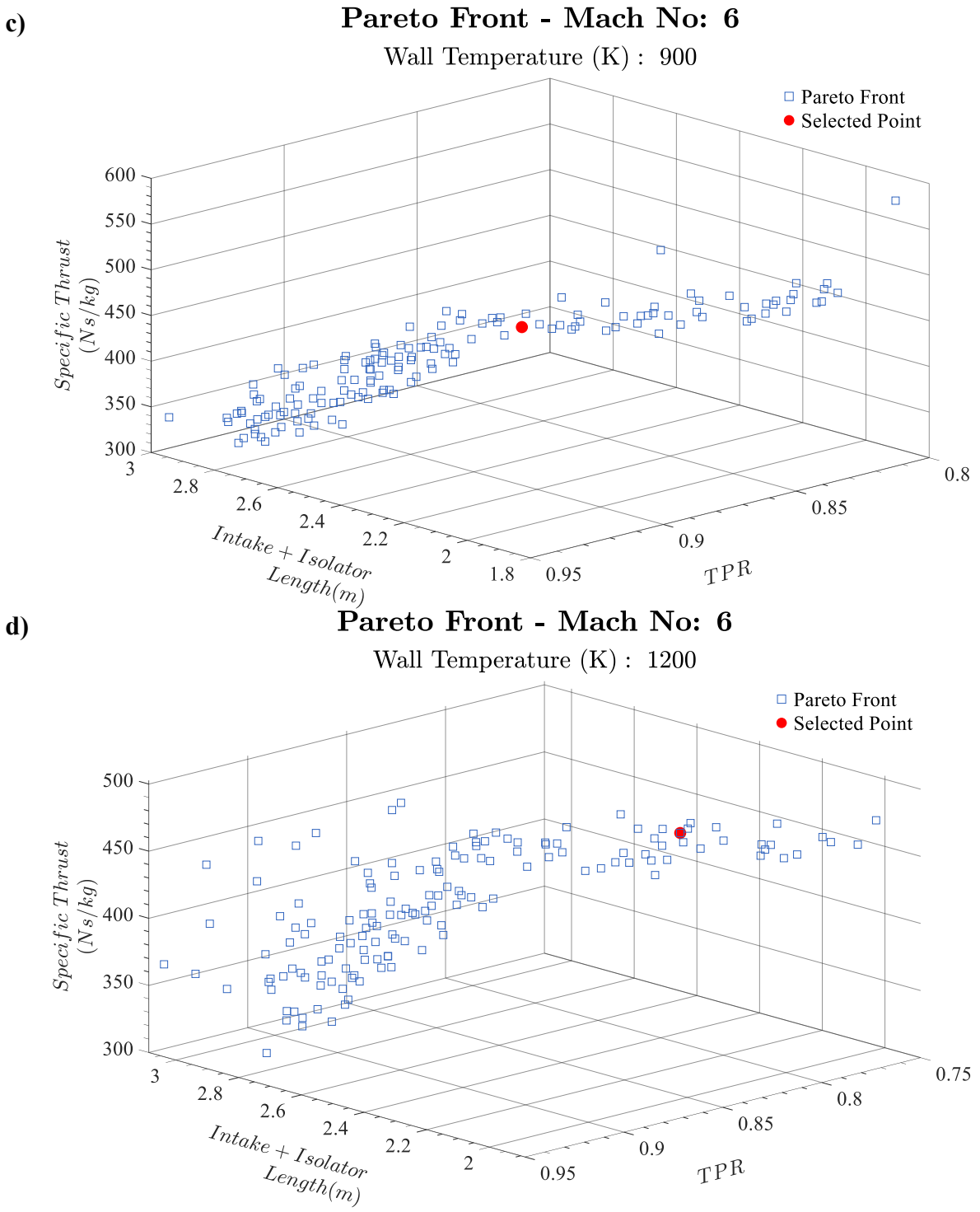


Figure 7-21: Pareto front variation of dual-mode scramjet with wall temperature. a) 300K, b) 600K, c) 900K, d) 1200K

Table 7-7: Angles and width/height ratio representing the optimum configuration at the wall temperatures considered for dual mode scramjet

Wall Temperature (K)	T_w/T_r	θ_1	θ_2	θ_3	θ_{cowl}	n_{depth}
300	0.182	5.0867	8.6949	11.8937	5.5004	10
600	0.364	4.4646	7.2866	11.9468	6.1799	9.9470
900	0.547	4.9193	7.7864	11.9321	6.3112	10

1200	0.729	5.5109	11.2870	12.4911	3.1182	9.8447

Table 7-7 reinforces this, showing an almost constant total compression angle, width/height ratio. The cowl angle shows a reduction of about 3 degrees at the lowest wall cooling, which occurs due to the increased thickness of the boundary layer on both ramps and cowl. Only small variations exist in the arrangement of the ramp angles, which leads to the slight fluctuation in overall compression efficiency observed. Despite this, it can be concluded that cooling the plate to prevent thermal damage will have little impact on the optimum configurations. A summary of these observations is presented in Figure 7-22 below. The minimal reduction in compression efficiency is seen from Figure 7-22a), which is accompanied by a minimal decrease in length in Figure 7-22b). All metrics remain effectively constant, showing that for a dual mode scramjet that the wall temperature has minimal influence on the overall performance and geometry.

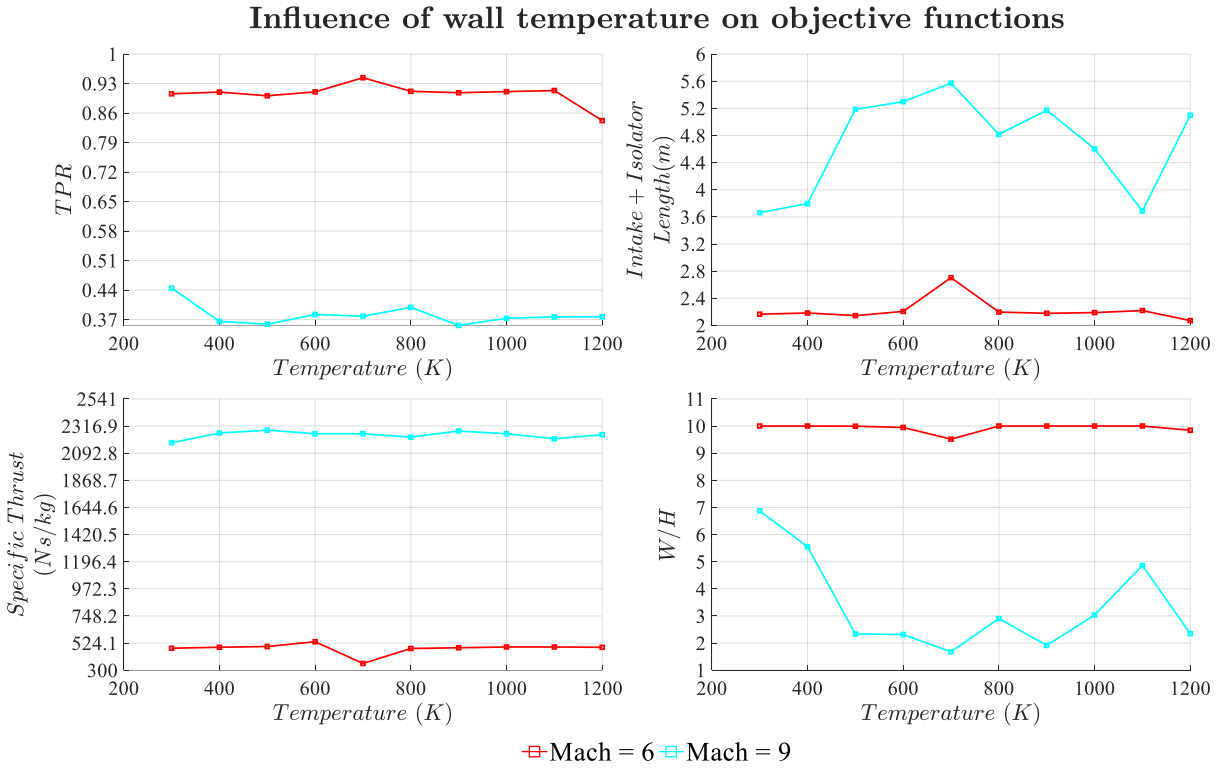
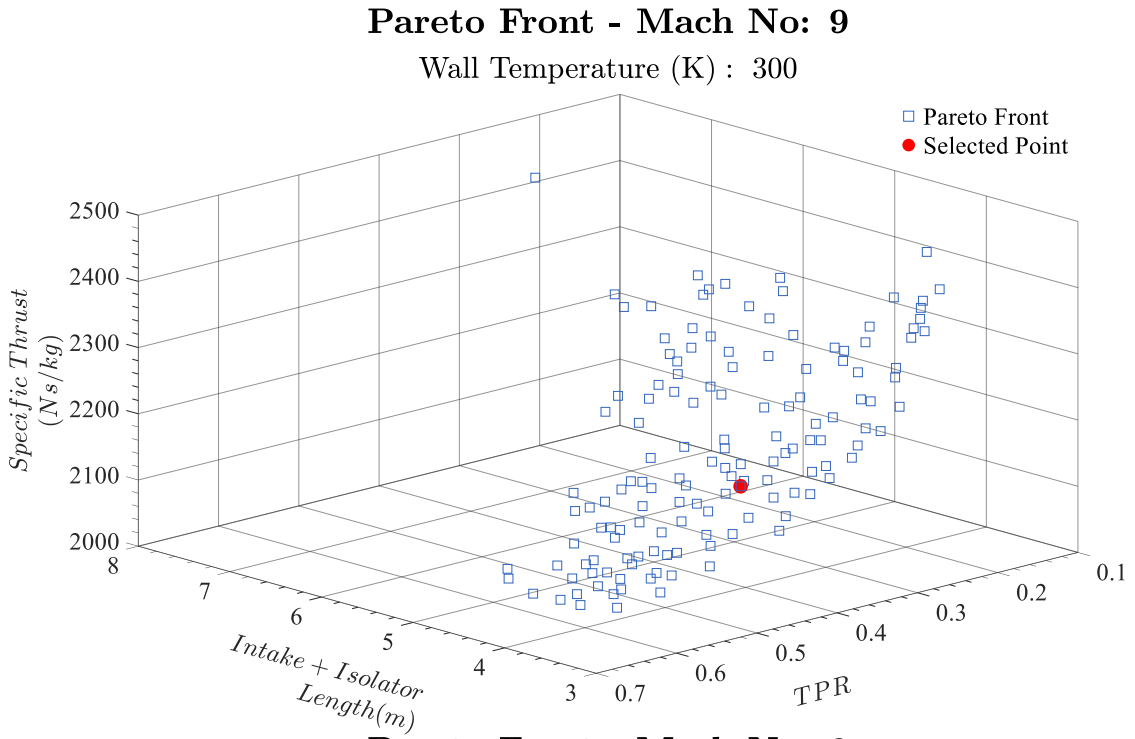


Figure 7-22: Influence of wall temperature of external ramps on objective functions for dual-mode (red) and pure scramjet (blue) configurations

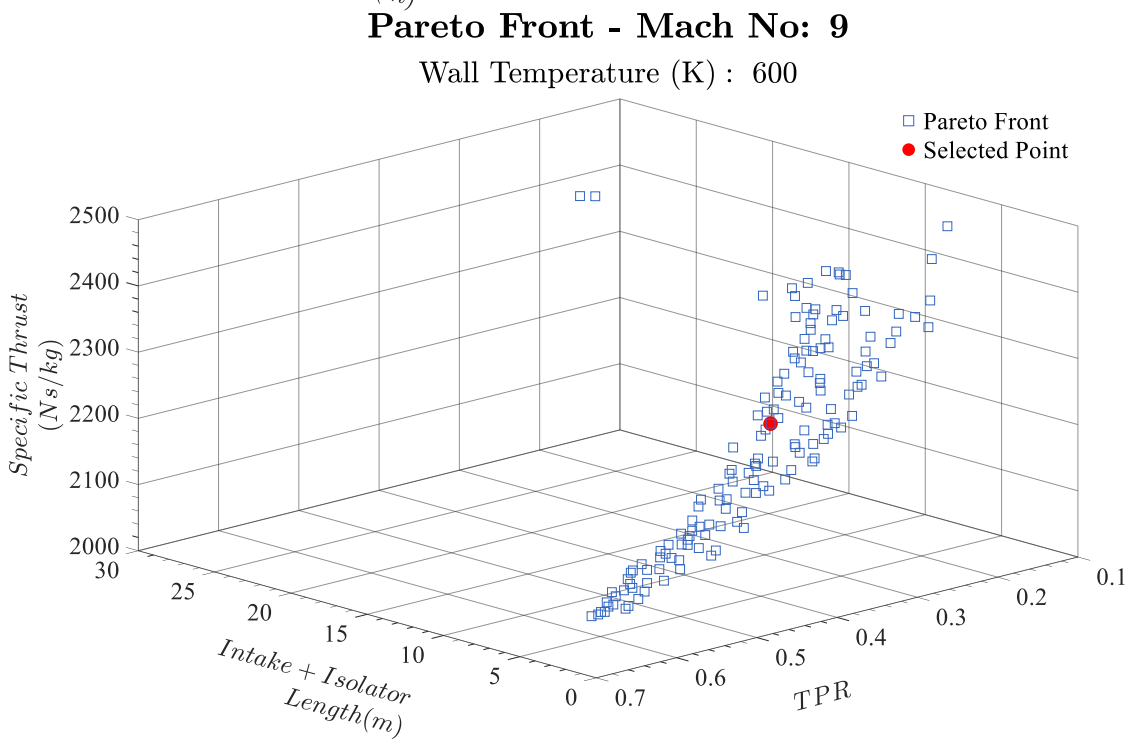
The Pareto fronts for the pure scramjet are almost identical, as seen from Figure 7-23, showing that, like the dual-mode fronts, the wall temperature does not change the overall structure of the Pareto front. The only significant change that can be noted is the perceived sparseness of the front at the highest cooling (lowest wall temperature). This is an artifact produced by the lower predicted maximum length that the higher wall temperatures. It results in a more zoomed

in view, causing this perceived sparseness. Unlike the dual-mode. however, the wall temperature has a profound effect on the geometry of the engine.

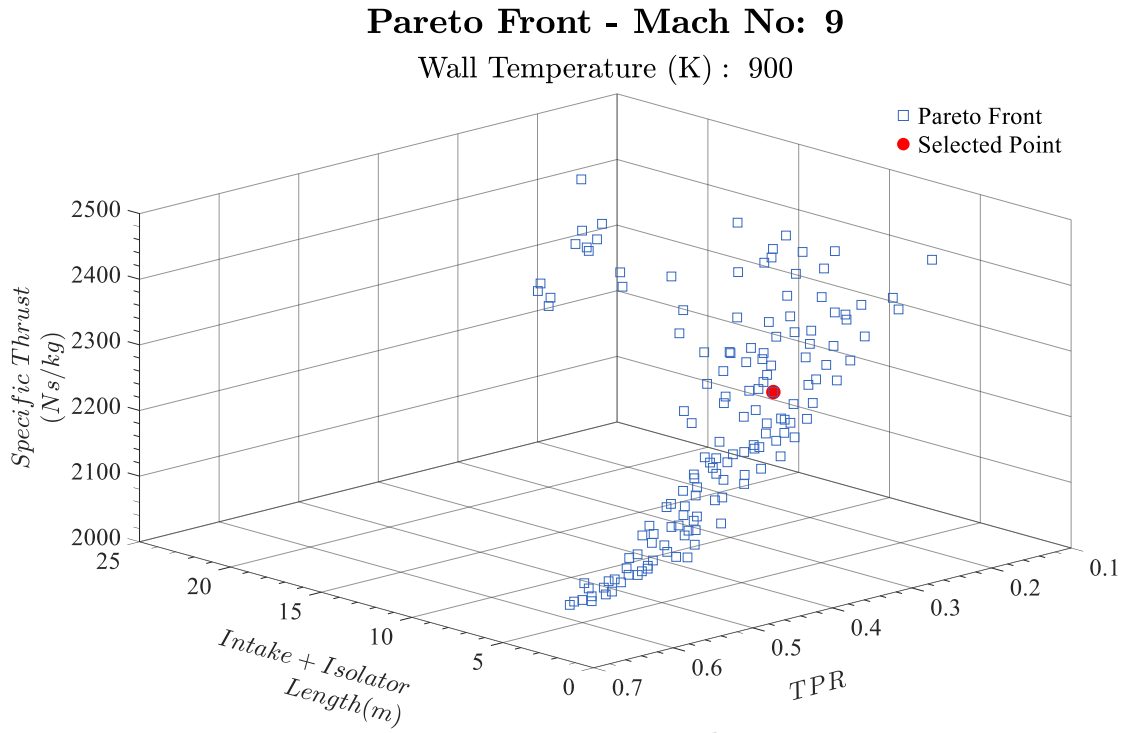
a)



b)



c)



d)

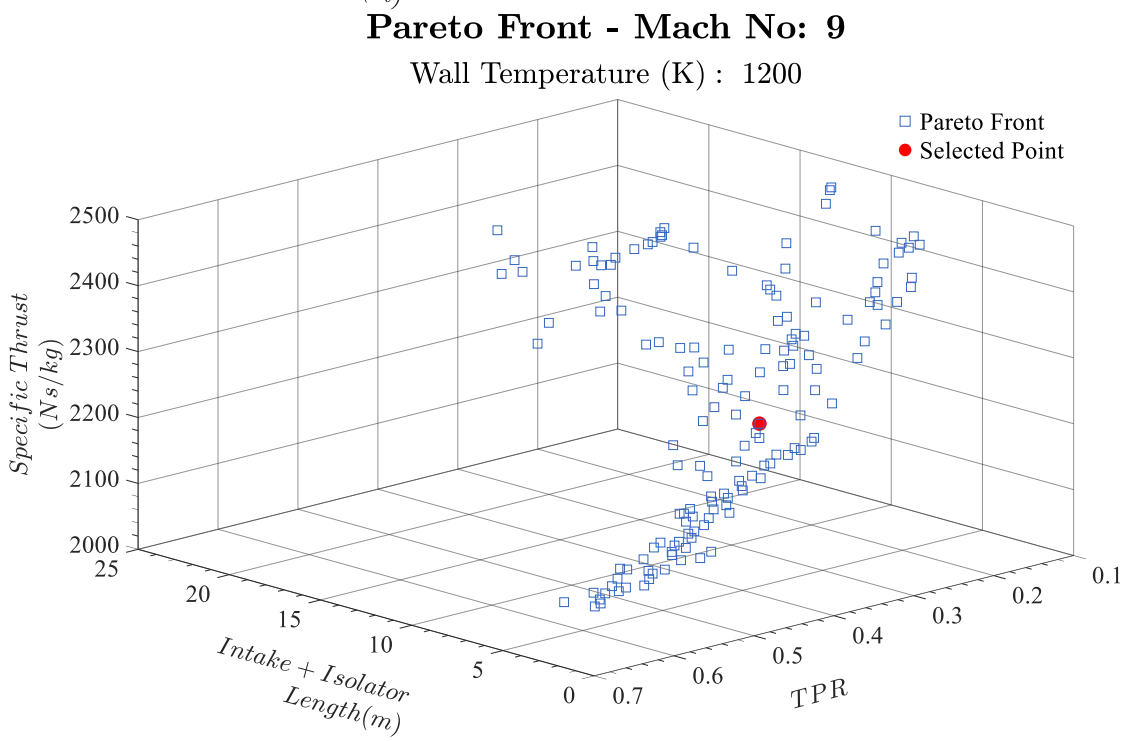


Figure 7-23: Pareto front variation of pure scramjet with wall temperature. a) 300K, b) 600K, c) 900K, d) 1200K

From Figure 7-22, the length and width show significant sensitivity with increased wall temperature. The length of the engine shows an increase between 300K and 700K, increasing from 3.6m to 5.6m between the two wall temperatures. This is despite the compression remaining at nearly the same total compression performed by the ramps, as seen from Table 7-7. However, as the wall temperature is further increased, the length is generally decreased,

with a spike observed at 1100K. This spike corresponds to the spike in width/height ratio. It can thus be concluded that, like the MFR study, the width/height ratio sudden increase results in the drop in length observed.

This can be ascribed to the influence of the thicker boundary layer. With increasing temperature, the boundary layer increases in thickness, having a heavier influence on the shock trajectory. Another influence of the thicker boundary layer is the increased displacement thickness, which means that more mass flow rate is trapped within the boundary layer. These cause the cowl to increase in height instead of width to accommodate the mass flow rate requirement. Thus, reducing wall cooling would generally lead to longer and taller configurations to achieve the same effect as higher wall cooling configurations, for the same mass flow rate required at a given Mach number and number of ramps. This is clear from the trend seen in Figure 7-22 above. The length of the intake follows the trend of the width/height ratio, showing an inverse relationship, as previously found in the MFR study.

Despite the sharp change in geometric parameters, the compression efficiency and specific thrust remain constant. This displays the capability of the algorithm to maintain the optimum configuration at a fixed thrust, despite the disturbances imposed by changing the wall temperature of the compression ramps, as seen from Table 7-8.

Table 7-8: Angles and width/height ratio representing the optimum configuration at the wall temperatures considered for pure scramjet

Wall Temperature (K)	T_w/T_r	θ_1	θ_2	θ_3	θ_{cowl}	n_{depth}
300	0.085	7.9854	16.3287	22.1441	9.6099	6.8748
600	0.170	5.7540	12.3507	23.1534	5.9031	2.3172
900	0.256	7.4933	14.4324	22.9951	4.4141	1.9155
1200	0.341	6.5274	15.2527	22.5611	4.9161	2.3482

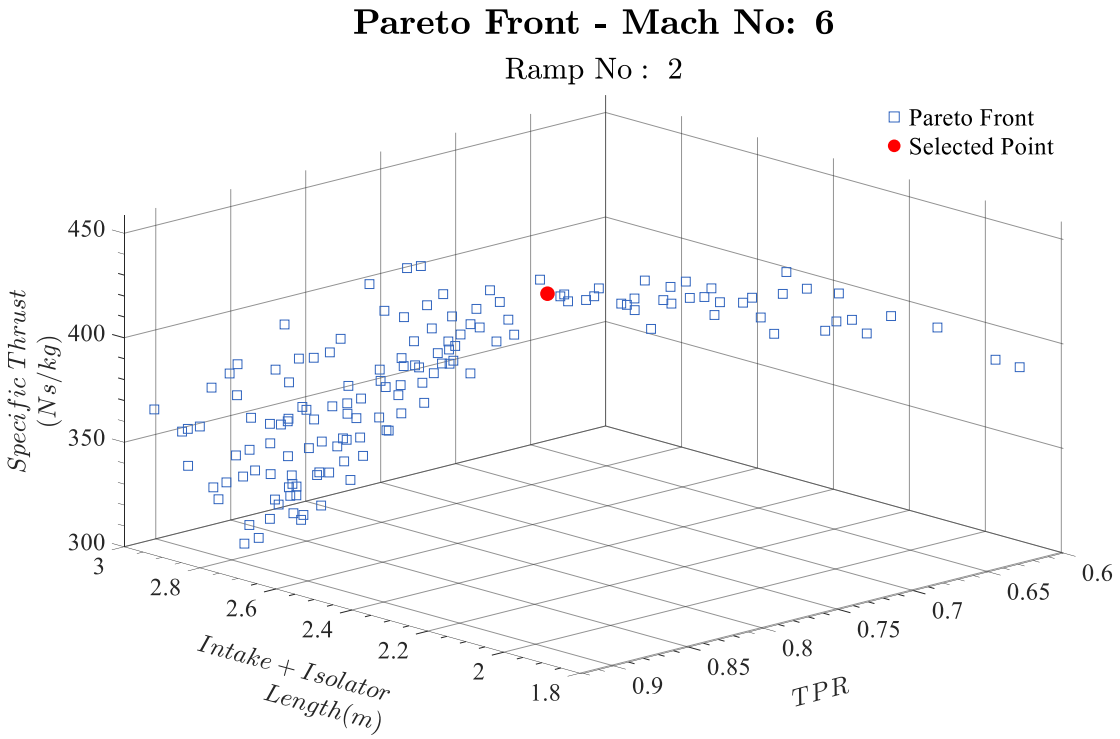
In summary, dual-mode scramjet configurations have lower sensitivity to wall cooling, with performance and geometry not being heavily affected by cooling. On the contrary, pure scramjets exhibit significant fluctuations in geometry with reduction in wall cooling. While performance remains stable, geometry displays substantial variations, with the length increasing by a factor of 1.55 and the width reducing by a factor of 3.5. Overall, this shows that wall cooling is essential for pure scramjets and must be carefully considered during the design process.

7.2.4. Variation of number of ramps

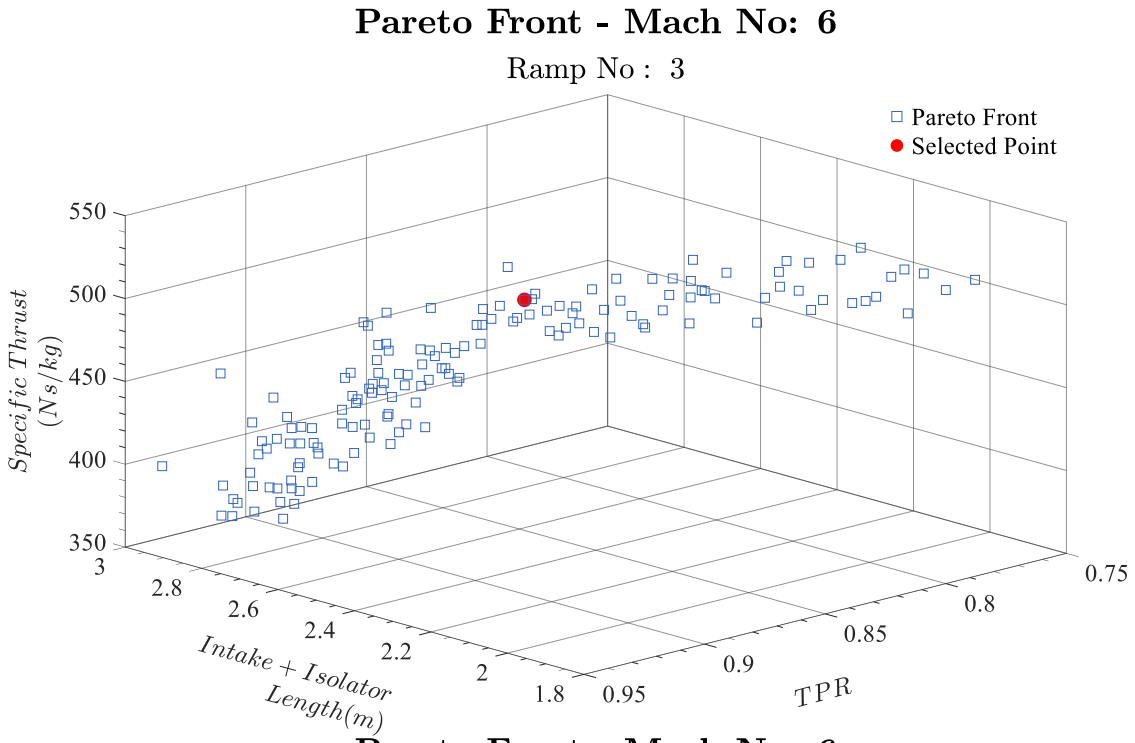
Finally, one of the most important choices a designer makes for a mixed compression intake, is the number of ramps for the external compression system. In general, it is expected that with an increase in number of ramps, compression becomes more efficient, due to the distribution of the pressure rise across more shocks. This would result in a higher TPR with increasing number of ramps. This should be compensated by an increase in length for the overall configuration.

The change in the trend of the Pareto front is investigated along the same lines as the previous analyses on MFR capturing and wall temperature. A look at the Pareto fronts in Figure 7-24 shows that, while the overall shape of the Pareto fronts is similar, there are some distinct differences arising from the number of shocks present in the intake. For the 2-ramp configuration, the range of configurations obtained from optimisation shows a very high variance in TPR, going between 0.6 and 0.95. This is due to the higher number of configurations that can fulfil all geometric conditions. Despite the variety in configurations, the highest specific thrust reached does not go above 460 Ns/kg. This is in contrast to an increased number of ramps, which reach about 500 Ns/kg. Higher number of ramps also limits the available configurations, thus contracting the Pareto fronts in a narrower TPR range.

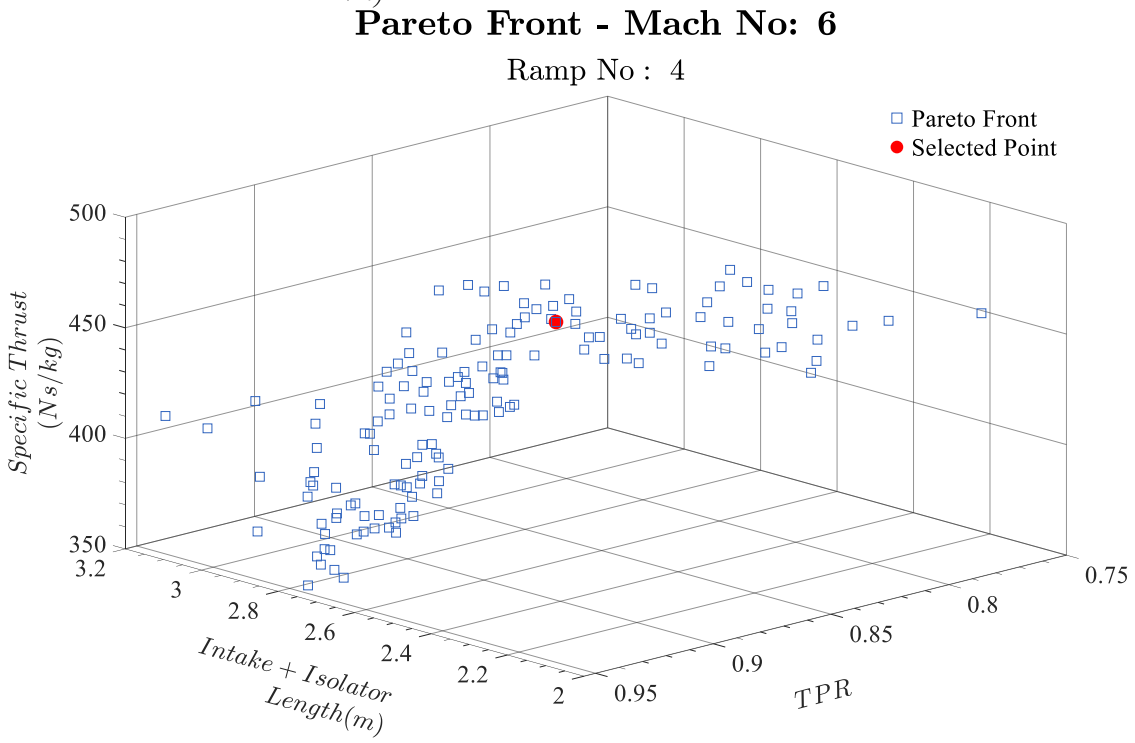
a)



b)


Pareto Front - Mach No: 6
Ramp No : 3
Pareto Front
Selected Point
Specific Thrust (Ns/kg)
550
500
450
400
350
3
2.8
2.6
2.4
2.2
2
1.8
Intake + Isolator Length(m)
0.95
0.9
0.85
0.8
0.75
TPR

c)


Pareto Front - Mach No: 6
Ramp No : 4
Pareto Front
Selected Point
Specific Thrust (Ns/kg)
500
450
400
350
3.2
3
2.8
2.6
2.4
2.2
2
Intake + Isolator Length(m)
0.95
0.9
0.85
0.8
0.75
TPR

d)

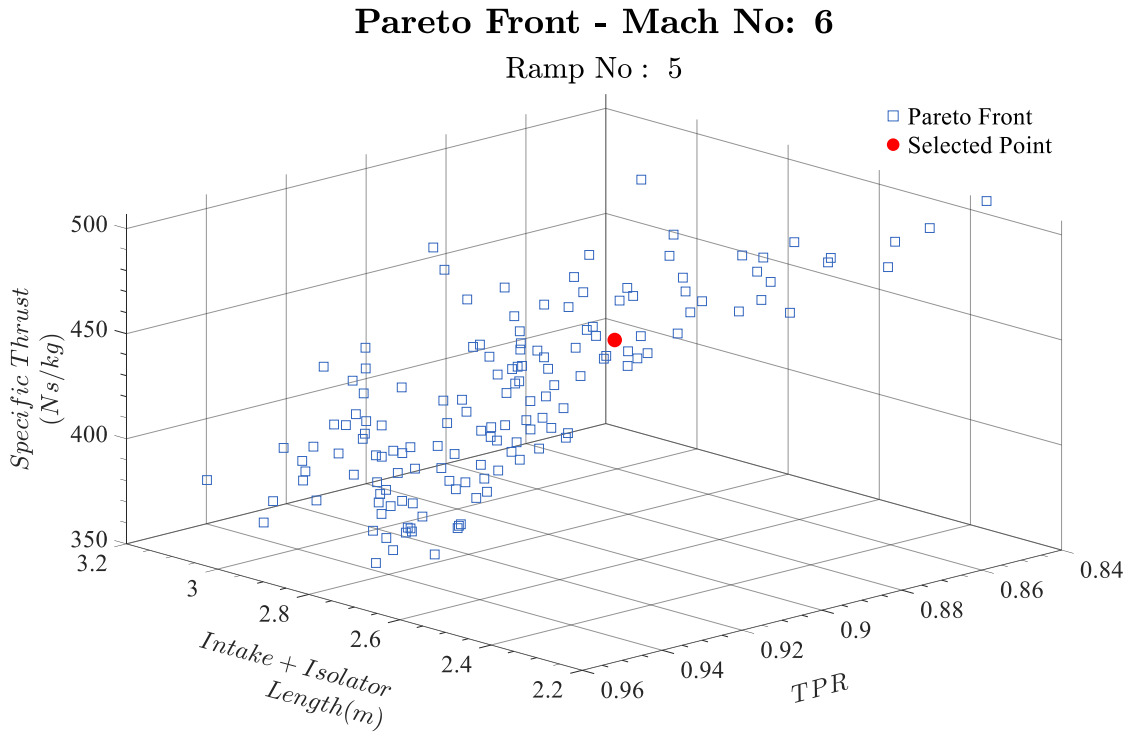


Figure 7-24: Pareto front variation of dual-mode scramjet with number of external ramps. a) 2, b) 3, c) 4, d) 5

Table 7-9 presents the optimum configurations for the dual mode scramjet. As with the previous sub-sections, the overall compression produced by the ramps remains constant, with the only difference being that the ramps adjust so it is spread over shallower angles as the number of ramps increases. The cowl is partially closed, with the cowl closure angle being roughly half the total ramp compression angle, maximising efficiency of compression. Identically to the previous analyses, the width/height ratio takes its maximum value.

Table 7-9: Angles and width/height ratio representing the optimum configuration at the number of external ramps considered for dual mode scramjet

Ramp Number	θ_1	θ_2	θ_3	θ_4	θ_5	θ_{cowl}	n_{depth}
2	6.6412	11.7990	N/A	N/A	N/A	5.3838	10
3	4.4646	7.2866	11.9468	N/A	N/A	6.1799	9.9470
4	3.8691	6.0535	8.7625	11.8799	N/A	5.9608	10
5	2.8981	3.8981	6.2347	9.0898	11.7697	6.4211	10

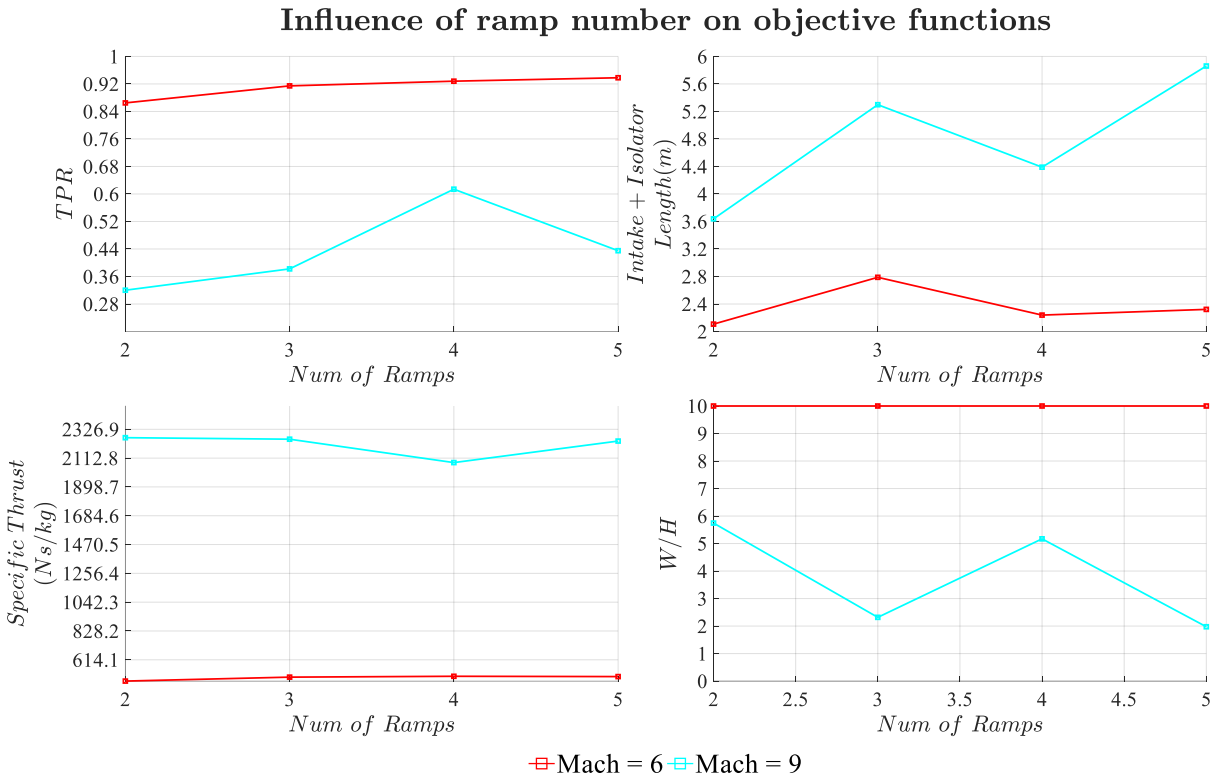


Figure 7-25: Influence of number of external ramps on objective functions for dual-mode (red) and pure scramjet (blue) configurations

From Figure 7-25 above, increasing the number of external compression ramps results in results in a significant increase in compression efficiency. The TPR increases from 86% with 2 external compression ramps to 92% at 5 compression ramps. This is compensated by a small increase in overall length, although not as severe as would be expected with the addition of three ramps. This can be explained by the high required mass flow rate (30 kg/s), which allows for a high intake height. The increased height allows for a longer overall configuration, allowing for multiple ramps to fit within the same length. The increase is also mitigated due to the presence of the isolator, since the system need not produce the entirety of the compression using the ramp-cowl shock system.

A more pronounced change is observed for the pure scramjet configuration. The length increases dramatically between the 2-ramp and 5-ramp configurations, with a fluctuation observed in the intermediary configurations.

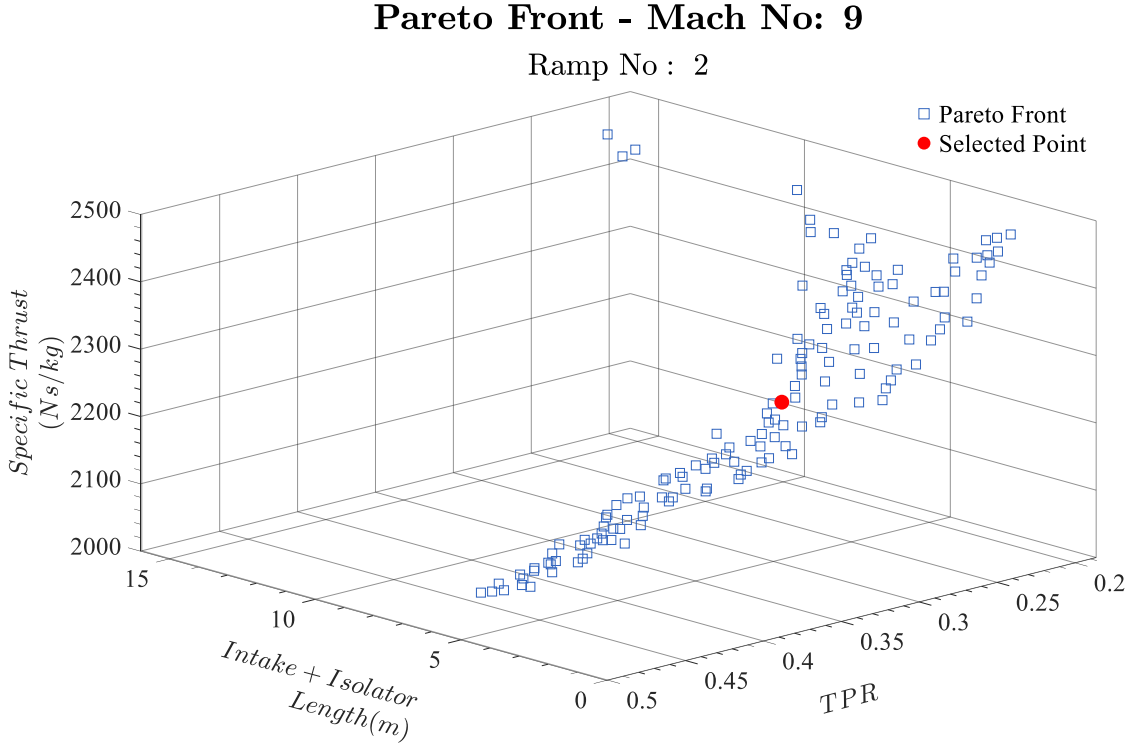
These are accompanied by an increase in TPR, and a change in the width/height ratio. The TPR increase is expected, as spreading the same compression over multiple shocks reduces the overall entropy increase. Similar to the previous studies. This is as a direct consequence of the requirement for the pure scramjet to produce the necessary pressure/temperature rise to feed to the combustor without isolators. This drives the scramjet to lower rectangularity as the number

of ramps increases, since it is of greater benefit to have the cowl at a higher vertical location. It allows the shock system to converge on cowl tip despite the influence of the boundary layer. Despite this, the 4-ramp configuration has a higher width/height ratio, which drives the length down. This might be because the mass flow rate examined favours a 4-ramp, with the shock system being the optimum for this mass flow rate.

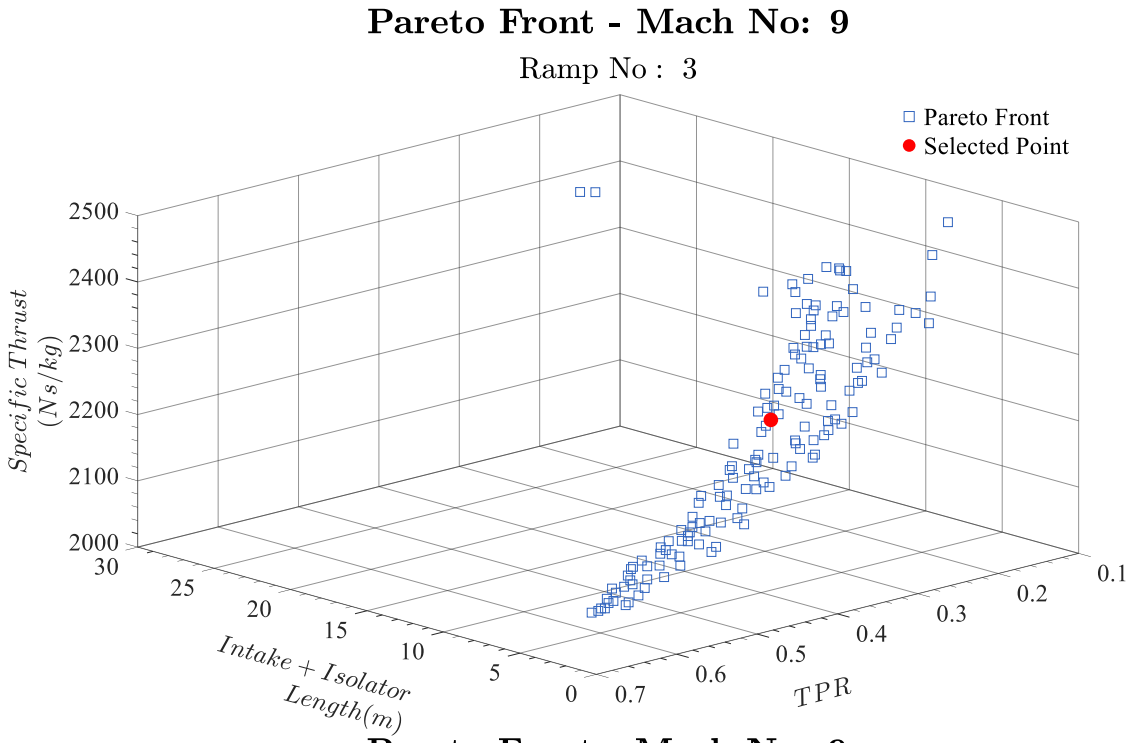
This can be explained by the fact that for an increasing number of ramps, there are only limited ways to arrange the number of ramps within the space available. Additionally, the increased number of shocks that the boundary layer has to undergo STBLI with, causes significant thickening. Thus, as the boundary layer thickness increases towards the isolator, the shock deviation caused is significant. This might suggest that based on the mass flow rate required, a different number of ramps is optimum.

Similar to the previous parametric studies, the Pareto fronts presented in Figure 7-26 have small differences between them but overall maintain the same structure. Contrary to the Mach 6 Pareto fronts, the maximum bounds for the TPR are the lowest for the 2-ramp configuration but has also the lowest spread in engine lengths. This indicates that a lower number of viable candidates at 2 ramp angles is available.

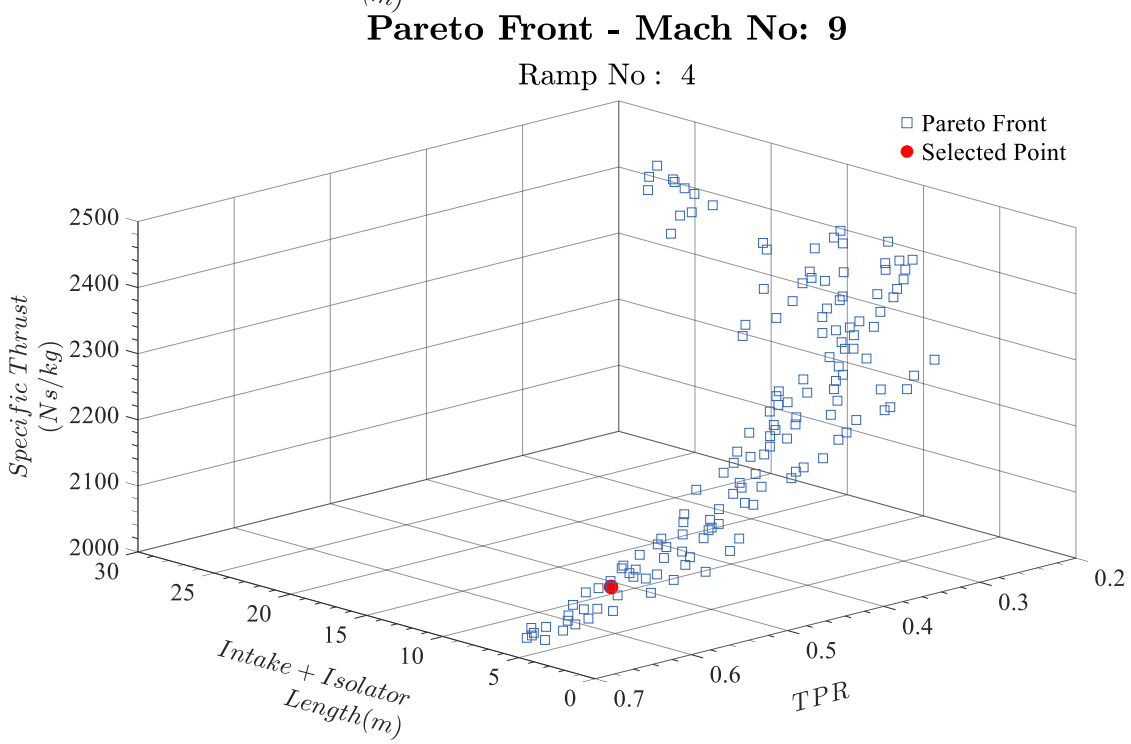
a)



b)


Pareto Front - Mach No: 9
Ramp No : 3
Pareto Front
Selected Point
Specific Thrust (Ns/kg)
2500
2400
2300
2200
2100
2000
Intake + Isolator Length(m)
30
25
20
15
10
5
0
TPR
0.7
0.6
0.5
0.4
0.3
0.2
0.1

c)


Pareto Front - Mach No: 9
Ramp No : 4
Pareto Front
Selected Point
Specific Thrust (Ns/kg)
2500
2400
2300
2200
2100
2000
Intake + Isolator Length(m)
30
25
20
15
10
5
0
TPR
0.7
0.6
0.5
0.4
0.3
0.2

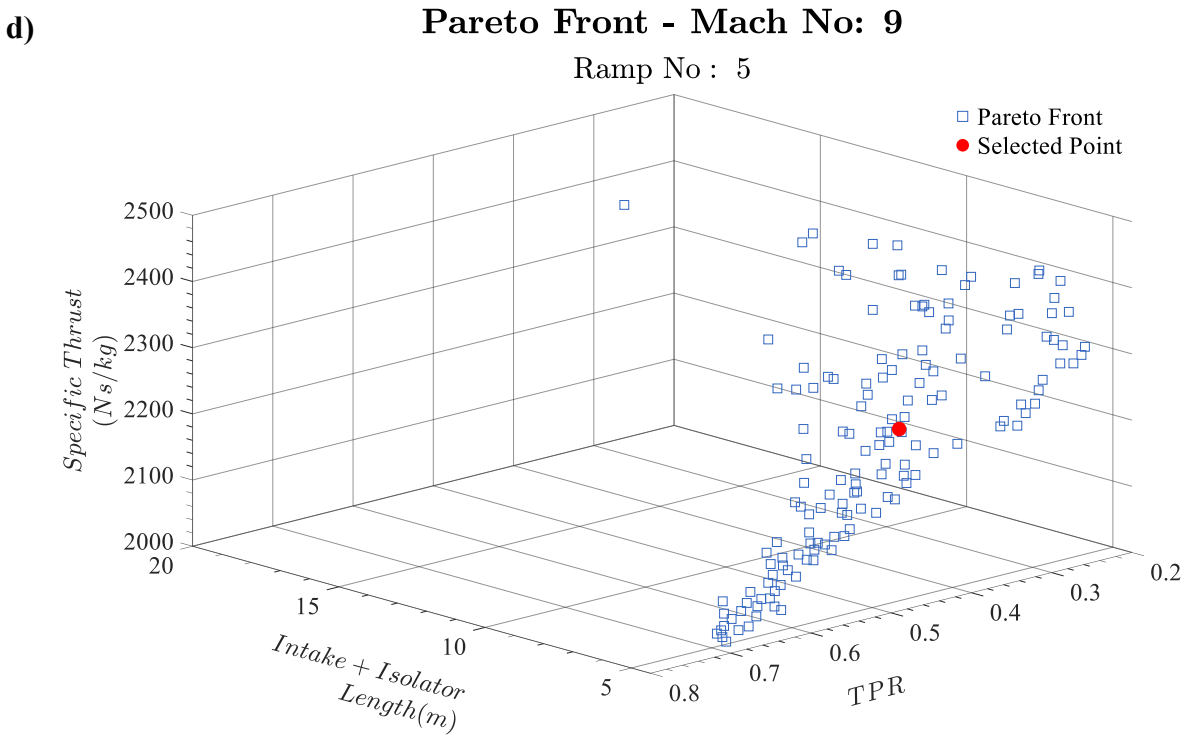


Figure 7-26: Pareto front variation of pure scramjet with number of external ramps. a) 2, b) 3, c) 4, d) 5

To investigate the change in compression angles and total angle compression produced, Table 7-10 presents the optimum configurations for the pure scramjet at each investigated ramp number. The overall compression is seen to be generally equal, but for the 4-ramp configuration, it is significantly lower, with 20.5 degrees against 23 degrees for the rest. As with the dual mode configurations, the ramps adjust into shallower angles with increasing ramp number. The cowl is partially closed, as expected from all configurations, but interestingly, the cowl angle fluctuates with increasing ramp number. For configurations with 2 and 4 ramps, the cowl angle is roughly half of the total external compression angle, meaning the compression is divided almost evenly between cowl tip and cowl spike shocks. On the other hand, for odd number of ramps, the cowl angle is very shallow, with the vast majority of the compression being done by the cowl tip shock. This is one of the contributing factors to the lower TPR observed between 4 and 5 ramps, along with the reduced overall compression. This demonstrates the importance of the cowl and the angle at which it is closed.

This reflects the trend that the TPR exhibits in Figure 7-25. As discussed previously, spreading the compression over more ramps should result in higher TPR, however, the higher compression produced by the tip shock leads to higher entropic losses, and thus TPR peaks at 4 ramps instead of continuing to increase in a manner exhibited by the dual-mode. Identically to the previous analyses, the width/height ratio directly influences the length of the engine. As

the width/height ratio reduces, the engine increases in length, seen by the increase in length of the configuration with 5 ramps as compared to the 2-ramp configuration. Along similar lines with other variables, the width/height ratio does not take the maximum value. Even at the lowest ramp number of 2, the selected configuration only has a value slightly higher than half the maximum value. As the number of ramps increases, the intakes become less rectangular, with the exception of the 4-ramp configuration, which exhibits a higher width/height ratio. This might be due to the lower overall compression performed.

Table 7-10: Angles and width/height ratio representing the optimum configuration at the number of external ramps considered for pure scramjet

Ramp Number	θ_1	θ_2	θ_3	θ_4	θ_5	θ_{cowl}	N
2	9.8407	22.2961	N/A	N/A	N/A	12.5313	5.7436
3	5.7540	12.3507	23.1534	N/A	N/A	5.9031	2.3172
4	5.1394	9.2441	14.0995	20.5467	N/A	10.1995	5.1704
5	4.7032	9.2347	13.7576	18.5325	23.5861	3.7942	1.9754

Summarising the influence of the number of ramps on the objective functions, it is evident that it has the most significant influence on the length of the engine, with a minor impact on compressive efficiency through TPR. The influence manifests more prominently in pure scramjet configurations. In dual-modes, only the compression efficiency is impacted, with the length increasing at a minor degree between 2 and 5 ramps. In pure scramjets, the TPR peaks at 4 compression ramps, and the length increases as the width/height ratio is decreased.

7.3. Chapter Summary

This chapter has demonstrated the application of the proposed low-order, coupled intake–isolator modelling framework to the optimisation of dual-mode and pure scramjet configurations. By integrating the proposed model with a constrained multi-objective optimisation algorithm, the method has been shown to systematically identify feasible, Pareto-optimal design candidates that satisfy operability constraints while balancing competing performance objectives. In doing so, the chapter fulfils the core aim of the thesis by showing that a computationally inexpensive approach can be used to explore scramjet design trade-offs at an early design stage.

To verify the proposed model, CFD simulations were performed on a dual mode scramjet at Mach 6 using the open-source software, OpenFOAM, which demonstrated the capability of the model to capture the dominant external compression behaviour with good accuracy and provides a reasonable prediction of isolator behaviour and heat addition required to induce shock formation and thrust generation. Discrepancies are observed in the internal flow, where

the predicted heating required to bring the combustor to thermal choke while maintaining started flow, which can be attributed to differences in combustion representation and the absence of viscous effects in the combustion region of the proposed model. The continuation of the boundary layer into the combustion chamber in numerical simulations and the method of heat addition, which does not account for the actual combustion process and thus the formation of new species, are attributed as the major reasons for the difference in the supported heat injection before unstart. This suggests that higher fidelity combustion modelling would be required in CFD for combustion and more robust combustion modelling for viscous effects would be required. Nevertheless, the global trends and macroscopic flow features, most notably the formation and propagation of the shock train, are consistently captured by the proposed approach.

A parametric study is carried out for the designer-determined inputs was subsequently performed to determine the main drivers that would influence the design of scramjets. Flight Mach number is identified as a primary driver of scramjet operating mode and achievable performance, as it dictates the available flow momentum and consequently the amount of fuel that can be safely combusted without inducing unstart. The optimisation results show that all objective functions are sensitive to Mach number, with a clear shift in optimal behaviour occurring between Mach 8 and Mach 9, marking a transition from dual-mode to pure scramjet operation. At lower Mach numbers, dual-mode configurations remain optimal due to the isolator's ability to compensate for reduced external compression, whereas at higher Mach numbers, pure scramjet configurations become preferable as sufficient compression can be achieved through the ramp–cowl shock system alone. At intermediate Mach numbers, mixed Pareto fronts are observed, reflecting competing compression strategies; however, optimisation consistently favours dual-mode configurations due to their superior balance between thrust generation, pressure recovery, and operability. This behaviour demonstrates the framework's capability to capture operating-mode transitions and highlights Mach number as a critical early-stage design decision.

As expected, the mass flow rate required to be captured plays a pivotal role in the design of scramjets. For dual-mode scramjets, the isolator plays a critical role in accommodating variations in captured mass flow rate, resulting in increased intake–isolator length as mass flow demand increases. In contrast, pure scramjet configurations exhibit variation in length based on the variations in width to compensate for the absence of internal compression through a

shock train. This distinction highlights the importance of correctly identifying the intended operating mode when undertaking preliminary optimisation studies.

The influence of wall cooling is also distinctly different between the two operating modes. Dual-mode scramjets show a relatively low sensitivity to wall temperature changes in the investigated range. Pure scramjets, however, exhibit strong geometric sensitivity to wall temperature, with significant fluctuations in length and generally a reduction in width as cooling is reduced. These results indicate that wall cooling is a key design parameter for pure scramjet engines and must be explicitly incorporated into early-stage optimisation strategies.

The number of external compression ramps is found to be the dominant geometric design variable across both engine classes. Increasing ramp number primarily influences engine length and cross-sectional shape, while exerting only a secondary effect on total pressure recovery. In pure scramjet configurations, pressure recovery peaks at four ramps, while geometric penalties continue to increase, suggesting diminishing returns from additional external compression. In dual-mode configurations, ramp number primarily affects compression efficiency, with only modest changes to overall length.

Overall, the results demonstrate that the optimisation framework performs as intended, enabling rapid identification of feasible, well-balanced scramjet configurations and revealing key sensitivities that govern intake–isolator design. The method provides clear preliminary design guidance: dual-mode scramjets benefit from isolator-centric optimisation with moderate sensitivity to thermal conditions, while pure scramjets require careful control of external compression geometry and wall cooling to achieve acceptable performance. As such, the proposed low-order framework constitutes a practical and effective tool for preliminary scramjet intake–isolator optimisation, bridging the gap between empirical design methods and computationally intensive CFD-based approaches.

Chapter 8 - Conclusions / Future Work

8.1. Conclusions

Scramjet engines allow for the air-breathing envelope to be expanded significantly, promising faster and more efficient travel within the atmosphere and offer their high specific impulse for the hypersonic flight regime on combined cycle engines. Such engines rely heavily on their intake and isolator components to achieve these feats. However, practical development and robust design of these components remain a challenging endeavour. A comprehensive survey of the current experimental and modelling literature points to multiple routes taken by researchers to investigate and model these components and their operation, as presented in Chapter 2. The methods and results were discussed, along with the limitations of generally implementing viscous modelling and coupling of the two components in a low-order and rapidly evaluated model. This thesis was therefore dedicated to advancing the modelling efforts made by overcoming the limitations of previous modelling approaches. The advancements made and contributions to literature can be summarised as follows:

A viscous flat plate model was developed with its core being a physics-based incompressible velocity profile, which has been adapted for hypersonic flowfields using the ubiquitous Van Driest compressibility correction. This profile was coupled with a compressibility-corrected boundary layer thickness correlation and a transition correlation to close the system of equations. This novel approach was compared to experimental studies and high-quality numerical simulations, showing good to excellent agreement with the literature. Thus, this modelling approach is suitable for use in the prediction of zero-pressure-gradient (ZPG) hypersonic turbulent boundary layers.

Following the successful implementation of viscous elements along the ZPG regions of the intake ramps, modelling of shock-turbulent boundary layer interactions was necessary. This was achieved by a simple, yet effective modelling method. The velocity profile developed in the previous chapter was solved together with a velocity/temperature relation at the foot of the shock and solved the inviscid shock relations outside the near-wall viscous sublayer to predict the distortion of the shock trajectory away from the idealised inviscid case. The resulting modelling resulted in the determination of a prediction for the exit boundary layer thickness and location where pressure stops to rise. Once again, comparison with experimental and numerical studies has demonstrated very good agreement across a variety of flow conditions and shock intensities.

The final model was developed to introduce the isolator, combustor and nozzle to the model. A successful empirical relation was used to predict the isolator length. Combustion was modelled as a heat release process due to combustion using a combination of frozen and equilibrium chemistry, while expansion was modelled as an adiabatic expansion to ambient conditions. As part of the modelling of these components, a method of distinguishing between the two operating modes of a scramjet, dual-mode and pure scramjet is also developed, based on maximum allowable equivalence ratio and choking of the combustor exit. The frozen/equilibrium chemistry models were included based on the equivalence ratio, which captures the variation in thermodynamic variables to increase the accuracy of the overall modelling.

With the models developed and linked, a metaheuristic optimisation algorithm capable of handling multiple objectives and constraints was used to obtain optimised configurations based on performance and safety objectives and restrictions. The resulting dual-mode geometry was verified using the open-source CFD software, OpenFOAM. The resulting verification showed that the model can successfully predict flows in ZPG regions and STBLIs. However, inaccuracies were observed when two shock-boundary layer interactions were close enough to influence each other, significantly thickening the boundary layer and increasing the skin friction coefficient. Despite this, the model has shown its capability in predicting shock convergence locations, with only a negligible loss in mass flow rate from the designed case. The internal flow is captured with less accuracy, as the intake unstarts with the predicted heat addition. Reducing the heat added allows the intake to remain started and the predicted shock train length to form. Discrepancies are ascribed to differences in species modelling between model and CFD, but also the influence of the boundary layer, which causes an aerodynamic nozzle effect, compressing the flow due to the increase in displacement thickness. The additional compression by the boundary layer reduces the effective heat required for thermal choke.

Following the verification of the model and its demonstration in capturing the macroscopic flow features and in many cases the finer details, a parametric study of the design parameters selected by the designers is conducted. Results show that pure scramjets show significant fluctuations in length and performance with the design parameters, whereas dual-mode scramjets can adapt easier to changes due to the presence of the isolator.

The verification and parametric study conducted have proven the importance and efficacy of the work and modelling approach proposed for the purposes of fast and accurate development of scramjet intake/isolator configurations during the preliminary design process.

The central objective of this research was to address the following question:

'Can a reduced-order modelling approach that sequentially couples intake, isolator, and combustor models capture the dominant physics governing hypersonic intake–isolator interactions with sufficient fidelity to support preliminary scramjet design and optimisation?'

The findings presented in this thesis demonstrate that it can. The developed framework successfully resolves the dominant physical phenomena by combining a compressibility corrected, physics-based, velocity profile for ZPG regions. This is combined with a shock interaction model capable of capturing shock trajectory distortion and exit boundary layer growth under an STBLI. By sequentially coupling these viscous elements up to the internal region with an empirical isolator shock train correlation and an equivalence ratio-dependent frozen/equilibrium chemistry model, the framework accurately captures mode transition, thermal choking boundaries, and shock convergence locations without the computational expense of CFD. Although CFD verification highlighted limitations in accounting for insufficient boundary layer redevelopment length, the model successfully demonstrated its capability to capture the viscous influence on the shock trajectory, shock train length and overall flowfield associated with dual-mode scramjets. Consequently, this work confirms that the proposed sequentially coupled methodology possesses sufficient fidelity to serve as a fast, physics-grounded tool for preliminary scramjet design and multi-objective optimisation.

8.2. Future perspectives

A novel approach in the design of scramjet intake-isolator configurations with viscous elements considered has been developed and demonstrated successfully in this thesis. This approach lays the foundation for accelerating the preliminary design process for scramjets. Future progress and research efforts could be directed in the following ways:

Addition of further viscous elements

As part of the novelty of this work, viscous elements were included to predict unstart and predict the length of isolator required. However, the viscous elements were not fully implemented to reduce the complexity and cost of the calculation. Most notably, the cowl boundary layer was not included extensively in the calculations due to the ramp's boundary layer being the most prominent. Additionally, the length of the isolator was determined through

Billig's equation, which is a semi-empirical equation, only valid within the range of Reynolds numbers and heights used to fit the equation. The former could be rectified by including the development of the cowl's boundary layer and the upper wall, after the cowl shock. The latter could be potentially addressed by coupling the Free Interaction Theory with a Lag Entrainment Method and a flux conserved model to couple the backpressure to the upstream behaviour of the shock train.

Higher fidelity computational fluid dynamics

The performance of the open-sourced CFD package OpenFOAM with the shockFluid explicit solver has been validated as shown in Chapter 3. It has shown great capability in predicting hypersonic flows, in zero pressure conditions, as seen by the pre-shock prediction of the boundary layer properties. Despite this, as mentioned in the same chapter, post-shock performance severely degrades due to the assumptions inherent to the RANS approach. Higher fidelity approaches, such as DES (Detached Eddy Simulation) or LES (Large Eddy Simulation) can balance the increased computational cost with greater accuracy. Even higher fidelity simulations using DNS (Direct Numerical Simulations) would be greatly beneficial in resolving the ramp shoulder shock convergence flow as well as the isolator shock train.

More robust combustor-expansion model

To assess the performance of the intake – isolator coupling, the specific thrust of each configuration was used as one of the metrics. As part of the specific thrust calculation, the heat release from combustion and expansion to freestream were required. As such, the combustor and nozzle were modelled using low order models, listed in Chapter 6. To increase the accuracy and predictive power of the model, a finite rate kinetics combustion model may substitute the current frozen chemistry/equilibrium model. Such model could provide better mixing dynamics, including allowed mixing rate, more precise streamwise pressure release and chemical kinetics. This would lead to greater accuracy in choking prediction and thus greater accuracy in shock train formation and propagation. Lastly, a nozzle model of greater sophistication would be advantageous, allowing for the prediction of thrust and impulse to be improved. Both models would benefit from consideration of viscous effects, which is absent in this work.

Chapter 9 - References

[1] P. Klink and H. Ogawa, “Investigation on the performance and feasibility of RBCC-based access-to-space via multi-objective design optimization,” *Acta Astronaut.*, vol. 157, pp. 435–454, Apr. 2019, doi: 10.1016/j.actaastro.2018.12.034.

[2] J. Zheng, J. Chang, S. Yang, X. Hao, and D. Yu, “Trajectory optimization for a TBCC-powered supersonic vehicle with transition thrust pinch,” *Aerosp. Sci. Technol.*, vol. 84, pp. 214–222, Jan. 2019, doi: 10.1016/j.ast.2018.10.026.

[3] R. S. Fry, “A Century of Ramjet Propulsion Technology Evolution,” *J. Propuls. Power*, vol. 20, no. 1, pp. 27–58, Jan. 2004, doi: 10.2514/1.9178.

[4] N. Viola, R. Fusaro, D. Ferretto, and V. Vercella, “Research, development and production costs prediction parametric model for future civil hypersonic aircraft,” *Acta Astronaut.*, vol. 204, pp. 58–72, Mar. 2023, doi: 10.1016/j.actaastro.2022.12.036.

[5] A. FERRI, “Review of scramjet propulsion technology.,” *J. Aircr.*, vol. 5, no. 1, pp. 3–10, Jan. 1968, doi: 10.2514/3.43899.

[6] A. Roudakov, V. Semenov, V. Kopchenov, and J. Hicks, “Future flight test plans of an axisymmetric hydrogen-fueled scramjet engine on the Hypersonic Flying Laboratory,” in *Space Plane and Hypersonic Systems and Technology Conference*, in International Space Planes and Hypersonic Systems and Technologies Conferences. Reston, Virigina: American Institute of Aeronautics and Astronautics, Nov. 1996. doi: 10.2514/6.1996-4572.

[7] C. R. McClinton, V. L. Rausch, L. T. Nguyen, and J. R. Sitz, “Preliminary X-43 flight test results,” *Acta Astronaut.*, vol. 57, no. 2–8, pp. 266–276, Jul. 2005, doi: 10.1016/j.actaastro.2005.03.060.

[8] J. Hank, J. Murphy, and R. Mutzman, “The X-51A Scramjet Engine Flight Demonstration Program,” in *15th AIAA International Space Planes and Hypersonic Systems and Technologies Conference*, in International Space Planes and Hypersonic Systems and Technologies Conferences. Reston, Virigina: American Institute of Aeronautics and Astronautics, Apr. 2008. doi: 10.2514/6.2008-2540.

[9] M. K. Smart, N. E. Hass, and A. Paull, “Flight Data Analysis of the HyShot 2 Scramjet Flight Experiment,” *AIAA Journal*, vol. 44, no. 10, pp. 2366–2375, Oct. 2006, doi: 10.2514/1.20661.

[10] S. Im and H. Do, “Unstart phenomena induced by flow choking in scramjet inlet-isolators,” *Progress in Aerospace Sciences*, vol. 97, pp. 1–21, Feb. 2018, doi: 10.1016/j.paerosci.2017.12.001.

[11] M. K. Smart, “How Much Compression Should a Scramjet Inlet Do?,” *AIAA Journal*, vol. 50, no. 3, pp. 610–619, Mar. 2012, doi: 10.2514/1.J051281.

[12] G. S. Settles and L. J. Dodson, “Supersonic and hypersonic shock/boundary-layer interaction database,” *AIAA Journal*, vol. 32, no. 7, pp. 1377–1383, Jul. 1994, doi: 10.2514/3.12205.

[13] C. J. Roy and F. G. Blottner, “Review and assessment of turbulence models for hypersonic flows,” *Progress in Aerospace Sciences*, vol. 42, no. 7–8, pp. 469–530, Oct. 2006, doi: 10.1016/j.paerosci.2006.12.002.

[14] G. T. Coleman and J. L. Stollery, “Heat transfer from hypersonic turbulent flow at a wedge compression corner,” *J. Fluid Mech.*, vol. 56, no. 4, pp. 741–752, Dec. 1972, doi: 10.1017/S0022112072002630.

[15] G. M. Elfstrom, “Turbulent hypersonic flow at a wedge-compression corner,” *J. Fluid Mech.*, vol. 53, no. 1, pp. 113–127, May 1972, doi: 10.1017/S0022112072000060.

[16] M. Holden, “Database of Aerothermal Measurements in Hypersonic Flow ‘Building Block’ Experiments,” in *41st Aerospace Sciences Meeting and Exhibit*, Reston, Virigina: American Institute of Aeronautics and Astronautics, Jan. 2003. doi: 10.2514/6.2003-1137.

[17] M. I. Kussoy and K. C. Horstman, “Intersecting Shock-Wave/ Turbulent Boundary-Layer Interactions at Mach 8.3,” Feb. 1992.

[18] E. Schülein, P. Krogmann, and E. Stanewsky, “Documentation of Two-Dimensional Impinging Shock/Turbulent Boundary Layer interaction Flow,” Oct. 1996.

[19] E. Schülein, “Skin Friction and Heat Flux Measurements in Shock/Boundary Layer Interaction Flows,” *AIAA Journal*, vol. 44, no. 8, pp. 1732–1741, Aug. 2006, doi: 10.2514/1.15110.

[20] D. Knight and N. Kianvashrad, *Hypersonic Shock Wave Turbulent Boundary Layers*. IOP Publishing, 2023. doi: 10.1088/978-0-7503-5002-0.

[21] S. N. B. Murthy and E. T. Curran, “Scramjet Inlets,” in *Scramjet Propulsion*, Reston ,VA: American Institute of Aeronautics and Astronautics, 2001, pp. 447–511. doi: 10.2514/5.9781600866609.0447.0511.

[22] R. Saravanan, S. L. N. Desikan, K. J. Francise, and R. Kalimuthu, “Experimental investigation of start/unstart process during hypersonic intake at Mach 6 and its control,” *Aerosp. Sci. Technol.*, vol. 113, p. 106688, Jun. 2021, doi: 10.1016/j.ast.2021.106688.

[23] S. kyun Im and H. Do, “Unstart phenomena induced by flow choking in scramjet inlet-isolators,” *Progress in Aerospace Sciences*, vol. 97, pp. 1–21, Feb. 2018, doi: 10.1016/J.PAEROSCI.2017.12.001.

[24] D. Van Wie, F. Kwok, and R. Walsh, “Starting characteristics of supersonic inlets,” in *32nd Joint Propulsion Conference and Exhibit*, Reston, Virigina: American Institute of Aeronautics and Astronautics, Jul. 1996. doi: 10.2514/6.1996-2914.

[25] K. Oswatitch, “Pressure Recovery for Missiles with Reaction Propulsion at High Supersonic Speeds (The Efficiency of Shock Diffusers),” Jun. 1947. Accessed: Aug. 16, 2026. [Online]. Available: https://ntrs.nasa.gov/citations/19990049423

[26] A. Ferri and L. M. Nucci, “The Origin of Aerodynamic Instability of Supersonic Inlets at Subcritical Conditions,” Jan. 1951. Accessed: Aug. 16, 2026. [Online]. Available: https://ntrs.nasa.gov/citations/19930086483

[27] C. L. DAILEY, “Supersonic Diffuser Instability,” *Journal of the Aeronautical Sciences*, vol. 22, no. 11, pp. 733–749, Nov. 1955, doi: 10.2514/8.3452.

[28] J. K James, A. Suryan, and H. D. Kim, “Buzz characteristics and separation bubble dynamics in supersonic intake,” *Aerosp. Sci. Technol.*, vol. 115, p. 106795, Aug. 2021, doi: 10.1016/j.ast.2021.106795.

[29] M. Abedi, R. Askari, and M. R. Soltani, “Numerical simulation of inlet buzz,” *Aerosp. Sci. Technol.*, vol. 97, p. 105547, Feb. 2020, doi: 10.1016/j.ast.2019.105547.

[30] E. T. Curran, “Scramjet Engines: The First Forty Years,” *J. Propuls. Power*, vol. 17, no. 6, pp. 1138–1148, Nov. 2001, doi: 10.2514/2.5875.

[31] J. Chang, L. Wang, W. Bao, J. Qin, J. Niu, and W. Xue, “Novel Oscillatory Patterns of Hypersonic Inlet Buzz,” *J. Propuls. Power*, vol. 28, no. 6, pp. 1214–1221, Nov. 2012, doi: 10.2514/1.B34553.

[32] F. De Vanna, F. Picano, E. Benini, and M. K. Quinn, “Large-Eddy Simulations of the Unsteady Behavior of a Hypersonic Intake at Mach 5,” *AIAA Journal*, vol. 59, no. 10, pp. 3859–3872, Oct. 2021, doi: 10.2514/1.J060160.

[33] A. Kantrowitz and C. D. Donaldson, “Preliminary Investigation Of Supersonic Diffusers,” May 1945. Accessed: Aug. 15, 2026. [Online]. Available: https://ntrs.nasa.gov/citations/19930093667

[34] A. K. Flock and A. Gülhan, “Modified Kantrowitz Starting Criteria for Mixed Compression Supersonic Intakes,” *AIAA Journal*, vol. 57, no. 5, pp. 2011–2016, May 2019, doi: 10.2514/1.J057283.

[35] M. K. K. Devaraj, P. Jutur, S. M. V. Rao, G. Jagadeesh, and G. T. K. Anavardham, “Experimental investigation of unstart dynamics driven by subsonic spillage in a hypersonic scramjet intake at Mach 6,” *Physics of Fluids*, vol. 32, no. 2, p. 026103, Feb. 2020, doi: 10.1063/1.5135096.

[36] O. M. Hohn and A. Gülhan, “Experimental Characterization of Three-Dimensional Scramjet Inlet with Variable Internal Contraction,” *J. Propuls. Power*, vol. 38, no. 1, pp. 71–83, Jan. 2022, doi: 10.2514/1.B38315.

[37] N. C. Joseph, S. S, F. K J, S. Chandran R, and M. B, “Experimental Studies to Design a Robust and Optimal Scramjet Engine Intake Configuration,” in *25th AIAA International Space Planes and Hypersonic Systems and Technologies Conference*, Reston, Virginia: American Institute of Aeronautics and Astronautics, May 2023. doi: 10.2514/6.2023-3003.

[38] S. Emami, C. A. Trexler, A. H. Auslender, and J. P. Weidner, “Experimental Investigation of Inlet-Combustor Isolators for a Dual-Mode Scramjet at a Mach Number of 4,” May 1995. Accessed: Aug. 15, 2026. [Online]. Available: https://ntrs.nasa.gov/citations/19950021922

[39] F. Lanson and J. L. Stollery, “Some hypersonic intake studies,” *The Aeronautical Journal*, vol. 110, no. 1105, pp. 145–156, Mar. 2006, doi: 10.1017/S0001924000001123.

[40] A. Idris, M. Saad, H. Zare-Behtash, and K. Kontis, “Luminescent Measurement Systems for the Investigation of a Scramjet Inlet-Isolator,” *Sensors*, vol. 14, no. 4, pp. 6606–6632, Apr. 2014, doi: 10.3390/s140406606.

[41] J. Sandeep and A. V. S. S. K. S. Gupta, “Assessment of the hypersonic intake isolator and performance evaluation at various flight conditions,” *Aerospace Systems*, vol. 8, no. 3, pp. 619–632, Sep. 2025, doi: 10.1007/s42401-024-00316-y.

[42] L. Krishnan, N. D. Sandham, and J. Steelant, “Shock-Wave/Boundary-Layer Interactions in a Model Scramjet Intake,” *AIAA Journal*, vol. 47, no. 7, pp. 1680–1691, Jul. 2009, doi: 10.2514/1.41107.

[43] N. Khobragade, S. Unnikrishnan, and R. Kumar, “Flow instabilities and impact of ramp–isolator junction on shock–boundary-layer interactions in a supersonic intake,” *J. Fluid Mech.*, vol. 953, p. A30, Dec. 2022, doi: 10.1017/jfm.2022.933.

[44] U. Gaisbauer, H. Knauss, N. N. Fedorova, and Y. V. Kharlamova, “Experimental and Numerical Investigations of Shock/Turbulent Boundary Layer Interaction on a Double Ramp Configuration,” 2006, pp. 297–304. doi: 10.1007/978-3-540-33287-9_37.

[45] M. A. Goldfeld, Yu. V. Zakharova, and N. N. Fedorova, “Investigation of separation properties of turbulent boundary layer at its sequential interaction with shocks of different strengths,” *Thermophysics and Aeromechanics*, vol. 15, no. 3, pp. 453–461, Sep. 2008, doi: 10.1134/S0869864308030116.

[46] F. Tong, J. Duan, and X. Li, “Shock wave and turbulent boundary layer interaction in a double compression ramp,” *Comput. Fluids*, vol. 229, p. 105087, Oct. 2021, doi: 10.1016/j.compfluid.2021.105087.

[47] L. Shi *et al.*, “Research and development on inlets for rocket based combined cycle engines,” *Progress in Aerospace Sciences*, vol. 117, p. 100639, Aug. 2020, doi: 10.1016/J.PAEROSCI.2020.100639.

[48] P. P. B. Araújo, M. V. S. Pereira, G. S. Marinho, J. F. A. Martos, and P. G. P. Toro, "Optimization of scramjet inlet based on temperature and Mach number of supersonic combustion," *Aerosp. Sci. Technol.*, vol. 116, p. 106864, Sep. 2021, doi: 10.1016/j.ast.2021.106864.

[49] R. H. KORKEGI, "A Simple Correlation for Incipient-Turbulent Boundary-Layer Separation due to a Skewed Shock Wave," *AIAA Journal*, vol. 11, no. 11, pp. 1578–1579, Nov. 1973, doi: 10.2514/3.50637.

[50] P. P. B. Araújo, R. Y. Tanaka, C. A. Silva, A. Passaro, and P. G. P. Toro, "Multi-objective optimization of a hypersonic airbreathing vehicle," *Physics of Fluids*, vol. 36, no. 2, Feb. 2024, doi: 10.1063/5.0181366.

[51] N. Verma and P. Panda, "Reduced Order Model Based on Gradient Optimization for Two Dimensional Scramjet Inlets," in *AIAA SCITECH 2022 Forum*, Reston, Virginia: American Institute of Aeronautics and Astronautics, Jan. 2022. doi: 10.2514/6.2022-1411.

[52] M. L. Fotia and J. F. Driscoll, "Isolator-Combustor Interactions in a Direct-Connect Ramjet-Scramjet Experiment," *J. Propuls. Power*, vol. 28, no. 1, pp. 83–95, Jan. 2012, doi: 10.2514/1.B34367.

[53] F. S. Billig and G. L. Dugger, "The interaction of shock waves and heat addition in the design of supersonic combustors," *Symposium (International) on Combustion*, vol. 12, no. 1, pp. 1125–1139, Jan. 1969, doi: 10.1016/S0082-0784(69)80490-X.

[54] A. Chakir, E. M. Collins, A. Zope, and S. Bhushan, "Predicting the Functionality of a Scramjet Engine Using Quasi 1D Model," in *AIAA AVIATION 2023 Forum*, Reston, Virginia: American Institute of Aeronautics and Astronautics, Jun. 2023. doi: 10.2514/6.2023-4139.

[55] A. C. Ispir, B. O. Cakir, and B. H. Saracoglu, "Design space investigations of scramjet engines using reduced-order modeling," *Acta Astronaut.*, vol. 217, pp. 349–362, Apr. 2024, doi: 10.1016/j.actaastro.2024.01.036.

[56] G. S. Lee and T. Lee, "Design and analysis of an ideal scramjet flowpath," *Physics of Fluids*, vol. 36, no. 3, Mar. 2024, doi: 10.1063/5.0194396.

[57] N. J. DiGregorio, T. K. West, and S. Choi, "Robust Design Under Uncertainty of Hypersonic Inlets," in *AIAA AVIATION 2022 Forum*, Reston, Virginia: American Institute of Aeronautics and Astronautics, Jun. 2022. doi: 10.2514/6.2022-3862.

[58] S. Brahmachary, C. Fujio, and H. Ogawa, "Multi-point design optimization of a high-performance intake for scramjet-powered ascent flight," *Aerosp. Sci. Technol.*, vol. 107, p. 106362, Dec. 2020, doi: 10.1016/j.ast.2020.106362.

[59] F. De Vanna, D. Bof, and E. Benini, "Multi-Objective RANS Aerodynamic Optimization of a Hypersonic Intake Ramp at Mach 5," *Energies (Basel).*, vol. 15, no. 8, p. 2811, Apr. 2022, doi: 10.3390/en15082811.

[60] H. L. Kline, T. D. Economon, and J. J. Alonso, “Mulit-Objective Optimization of a Hypersonic Inlet Using Generalized Outflow Boundary Conditions in the Continuous Adjoint Method,” in *54th AIAA Aerospace Sciences Meeting*, Reston, Virginia: American Institute of Aeronautics and Astronautics, Jan. 2016. doi: 10.2514/6.2016-0912.

[61] L. Crocco, “B. One-Dimensional Treatment of Steady Gas Dynamics,” in *Fundamentals of Gas Dynamics*, Princeton University Press, 1958, pp. 64–349. doi: 10.1515/9781400877539-004.

[62] H. Sugiyama, R. Minato, K. Mizobata, A. Tojo, and Y. Muto, “Study on shock wave and turbulent boundary layer interactions in a square duct at Mach 2 and 4,” *Journal of Thermal Science*, vol. 15, no. 1, pp. 37–42, Mar. 2006, doi: 10.1007/s11630-006-0037-3.

[63] X. Fan, X. Bing, Y. Wang, and T. Yuan, “Experimental study on the self-excited oscillation and the forced oscillation of shock train in a rectangular isolator,” in *21st AIAA International Space Planes and Hypersonics Technologies Conference*, Reston, Virginia: American Institute of Aeronautics and Astronautics, Mar. 2017. doi: 10.2514/6.2017-2115.

[64] B. Xiong, Z.-G. Wang, X.-Q. Fan, and Y. Wang, “Experimental study on the flow separation and self-excited oscillation phenomenon in a rectangular duct,” *Acta Astronaut.*, vol. 133, pp. 158–165, Apr. 2017, doi: 10.1016/j.actaastro.2017.01.009.

[65] J. S. Geerts and K. H. Yu, “Shock Train/Boundary-Layer Interaction in Rectangular Isolators,” *AIAA Journal*, vol. 54, no. 11, pp. 3450–3464, Nov. 2016, doi: 10.2514/1.J054917.

[66] K. Matsuo, Y. Miyazato, and H.-D. Kim, “Shock train and pseudo-shock phenomena in internal gas flows,” *Progress in Aerospace Sciences*, vol. 35, no. 1, pp. 33–100, Jan. 1999, doi: 10.1016/S0376-0421(98)00011-6.

[67] C. Fischer and H. Olivier, “Experimental Investigation of Wall and Total Temperature Influence on a Shock Train,” *AIAA Journal*, vol. 52, no. 4, pp. 757–766, Apr. 2014, doi: 10.2514/1.J052599.

[68] F. Gnani, H. Zare-Behtash, and K. Kontis, “Pseudo-shock waves and their interactions in high-speed intakes,” *Progress in Aerospace Sciences*, vol. 82, pp. 36–56, Apr. 2016, doi: 10.1016/j.paerosci.2016.02.001.

[69] T. IKUI, K. MATSUO, and M. NAGAI, “The Mechanism of Pseudo-Shock Waves,” *Bulletin of JSME*, vol. 17, no. 108, pp. 731–739, 1974, doi: 10.1299/jsme1958.17.731.

[70] T. IKUI, K. MATSUO, and K. SASAGUCHI, “Modified Diffusion Model of Pseudo-Shock Waves Considering Upstream Boundary Layers,” *Bulletin of JSME*, vol. 24, no. 197, pp. 1920–1927, 1981, doi: 10.1299/jsme1958.24.1920.

[71] M. K. Smart, “Flow modeling of pseudoshocks in backpressured ducts,” *AIAA Journal*, vol. 53, no. 12, pp. 3577–3588, 2015, doi: 10.2514/1.J054021.

[72] R. Fiévet, V. Raman, and A. H. Auslender, “Data-driven one-dimensional modeling of pseudoshocks,” *J. Propuls. Power*, vol. 35, no. 2, pp. 313–327, 2019, doi: 10.2514/1.B37175.

[73] L. M. Edelman, “Physics and Modeling of Quasi-Steady and Forced Shock Trains,” PhD Thesis, University of Michigan, 2022.

[74] L. M. Edelman, M. Gamba, R. L. Hunt, and A. Auslender, “Assessment of Pseudoshock Models Against Experiment in a Low-Aspect-Ratio Isolator,” *J. Propuls. Power*, vol. 39, no. 5, pp. 653–664, Sep. 2023, doi: 10.2514/1.B38913.

[75] P. J. Ortwerth, “Scramjet Flowpath Integration,” in *Scramjet Propulsion*, Reston ,VA: American Institute of Aeronautics and Astronautics, 2001, pp. 1105–1293. doi: 10.2514/5.9781600866609.1105.1293.

[76] G. McLAFFERTY, “Theoretical Pressure Recovery Through a Normal Shock in a Duct with Initial Boundary Layer,” *Journal of the Aeronautical Sciences*, vol. 20, no. 3, pp. 169–174, Mar. 1953, doi: 10.2514/8.2582.

[77] P. J. WALTRUP and F. S. BILLIG, “Structure of Shock Waves in Cylindrical Ducts,” *AIAA Journal*, vol. 11, no. 10, pp. 1404–1408, Oct. 1973, doi: 10.2514/3.50600.

[78] F. S. Billig, “Research on supersonic combustion,” *J. Propuls. Power*, vol. 9, no. 4, pp. 499–514, Jul. 1993, doi: 10.2514/3.23652.

[79] J.-R. Byun, C. Park, O. J. Kwon, and J. Ahn, “Experimental Study of Combustor–Isolator Interactions in a Dual-Combustion Ramjet,” *J. Propuls. Power*, vol. 31, no. 2, pp. 592–603, Mar. 2015, doi: 10.2514/1.B35391.

[80] E. T. Curran and S. N. B. Murthy, “Scramjet Flowpath Integration,” in *Scramjet Propulsion*, Reston ,VA: American Institute of Aeronautics and Astronautics, 2001, pp. 1105–1293. doi: 10.2514/5.9781600866609.1105.1293.

[81] C. Segal, “Supersonic Combustion Processes,” in *The Scramjet Engine*, Cambridge University Press, 2009, pp. 127–214. doi: 10.1017/CBO9780511627019.007.

[82] K.-C. Lin, C.-J. Tam, K. Jackson, D. Eklund, and T. Jackson, “Characterization of Shock Train Structures inside Constant-Area Isolators of Model Scramjet Combustors,” in *44th AIAA Aerospace Sciences Meeting and Exhibit*, Reston, Virigina: American Institute of Aeronautics and Astronautics, Jan. 2006. doi: 10.2514/6.2006-816.

[83] W. Hartill, T. Goebel, and V. Van Camp, “Study of hypersonic propulsion/airframe integration technology,” Jan. 1978. Accessed: Aug. 19, 2026. [Online]. Available: https://ntrs.nasa.gov/citations/19780011153

[84] V. Jaunet, J. F. Debiève, and P. Dupont, “Length Scales and Time Scales of a Heated Shock-Wave/Boundary-Layer Interaction,” *AIAA Journal*, vol. 52, no. 11, pp. 2524–2532, Nov. 2014, doi: 10.2514/1.J052869.

[85] Y. HONG, Z. LI, and J. YANG, “Scaling of interaction lengths for hypersonic shock wave/turbulent boundary layer interactions,” *Chinese Journal of Aeronautics*, vol. 34, no. 5, pp. 504–509, May 2021, doi: 10.1016/j.cja.2020.12.028.

[86] L. J. Souverein, P. G. Bakker, and P. Dupont, “A scaling analysis for turbulent shock-wave/boundary-layer interactions,” *J. Fluid Mech.*, vol. 714, pp. 505–535, Jan. 2013, doi: 10.1017/jfm.2012.495.

[87] K. Srinivasan, P. K. Maurya, K. Abhishek, S. L. N. Desikan, and B. Murugan, “Supersonic combustion of a scramjet engine using hydrogen fuel in shock tunnel,” *AIAA Journal*, vol. 56, no. 9, pp. 3600–3609, 2018, doi: 10.2514/1.J056761.

[88] K. H. Lee and K. W. Kim, “Performance comparison of particle swarm optimization and genetic algorithm for inverse surface radiation problem,” *Int. J. Heat Mass Transf.*, vol. 88, pp. 330–337, Sep. 2015, doi: 10.1016/j.ijheatmasstransfer.2015.04.075.

[89] Z. Su, J. Zhao, and J. Liu, “Reentry trajectory optimization of hypersonic glide vehicle based on improved particle swarm algorithm,” *J. Phys. Conf. Ser.*, vol. 2764, no. 1, p. 012069, May 2024, doi: 10.1088/1742-6596/2764/1/012069.

[90] Y. Ma *et al.*, “Dynamic multi-objective optimization of scramjet inlet based on small-sample Kriging model,” *Physics of Fluids*, vol. 35, no. 9, Sep. 2023, doi: 10.1063/5.0170231.

[91] J. Kennedy and R. Eberhart, “Particle swarm optimization,” in *Proceedings of ICNN’95 - International Conference on Neural Networks*, IEEE, 1995, pp. 1942–1948. doi: 10.1109/ICNN.1995.488968.

[92] C. A. C. Coello, G. T. Pulido, and M. S. Lechuga, “Handling multiple objectives with particle swarm optimization,” *IEEE Transactions on Evolutionary Computation*, vol. 8, no. 3, pp. 256–279, Jun. 2004, doi: 10.1109/TEVC.2004.826067.

[93] T. M. Inc., “MATLAB version: 24.2.0.2923080 (R2024b) Update 6,” 2025, *The MathWorks Inc., Natick, Massachusetts, United States*. [Online]. Available: https://www.mathworks.com

[94] H. Kita, Y. Yabumoto, N. Mori, and Y. Nishikawa, “Multi-objective optimization by means of the thermodynamical genetic algorithm,” 1996, pp. 504–512. doi: 10.1007/3-540-61723-X_1014.

[95] T. Thanh Binh and U. Korn, “MOBES: A Multiobjective Evolution Strategy for Constrained Optimization Problems.”

[96] OpenFOAM, “OpenFOAM.” Accessed: Sep. 05, 2025. [Online]. Available: https://www.openfoam.com/

[97] C. J. Greenshields, H. G. Weller, L. Gasparini, and J. M. Reese, “Implementation of semi-discrete, non-staggered central schemes in a colocated, polyhedral, finite volume framework, for high-speed viscous flows,” *Int. J. Numer. Methods Fluids*, vol. 63, no. 1, pp. 1–21, May 2010, doi: 10.1002/fld.2069.

[98] L. F. Gutiérrez Marcantoni, J. P. Tamagno, and S. A. Elaskar, “HIGH SPEED FLOW SIMULATION USING OPENFOAM,” 2012.

[99] H. Stoldt, C. T. Johansen, A. Korobenko, and P. Ziade, “Verification and Validation of a High-Fidelity Open-Source Simulation Tool for Supersonic Aircraft Aerodynamic Analysis,” in *AIAA AVIATION 2020 FORUM*, Reston, Virginia: American Institute of Aeronautics and Astronautics, Jun. 2020, pp. 1–38. doi: 10.2514/6.2020-2758.

[100] J. Lee, S. G. Lee, S. H. Kang, and H.-J. Namkoung, “Numerical Study on the Non-Oscillatory Unstarted Flow in a Scramjet Inlet-Isolator Model,” *Aerospace*, vol. 9, no. 3, p. 162, Mar. 2022, doi: 10.3390/aerospace9030162.

[101] R. B. Langtry and F. R. Menter, “Correlation-Based Transition Modeling for Unstructured Parallelized Computational Fluid Dynamics Codes,” *AIAA Journal*, vol. 47, no. 12, pp. 2894–2906, Dec. 2009, doi: 10.2514/1.42362.

[102] F. R. Menter, “Improved Two-Equation k-Turbulence Models for Aerodynamic Flows,” Oct. 1992. Accessed: Aug. 15, 2026. [Online]. Available: https://ntrs.nasa.gov/citations/19930013620

[103] D. J. Friedlander and N. J. Georgiadis, “Exploring the Langtry-Menter Transition Model for High Speed Applications Using FUN3D,” in *AIAA AVIATION 2023 Forum*, Reston, Virginia: American Institute of Aeronautics and Astronautics, Jun. 2023. doi: 10.2514/6.2023-3270.

[104] L. Zhou, C. Yan, Z. H. Hao, and R. F. Du, “Improved k – ω – γ model for hypersonic boundary layer transition prediction,” *Int. J. Heat Mass Transf.*, vol. 94, pp. 380–389, Mar. 2016, doi: 10.1016/j.ijheatmasstransfer.2015.11.048.

[105] G. D. van Albada, B. van Leer, and W. W. Roberts, “A Comparative Study of Computational Methods in Cosmic Gas Dynamics,” in *Upwind and High-Resolution Schemes*, Berlin, Heidelberg: Springer Berlin Heidelberg, 1997, pp. 95–103. doi: 10.1007/978-3-642-60543-7_6.

[106] R. A. HUMBLE, G. E. ELSINGA, F. SCARANO, and B. W. van OUDHEUSDEN, “Three-dimensional instantaneous structure of a shock wave/turbulent boundary layer interaction,” *J. Fluid Mech.*, vol. 622, pp. 33–62, Mar. 2009, doi: 10.1017/S0022112008005090.

[107] J. Fang, A. A. Zheltovodov, Y. Yao, C. Moulinec, and D. R. Emerson, “On the turbulence amplification in shock-wave/turbulent boundary layer interaction,” *J. Fluid Mech.*, vol. 897, p. A32, Aug. 2020, doi: 10.1017/jfm.2020.350.

[108] B. Morgan, K. Duraisamy, N. Nguyen, S. Kawai, and S. K. Lele, “Flow physics and RANS modelling of oblique shock/turbulent boundary layer interaction,” *J. Fluid Mech.*, vol. 729, pp. 231–284, Aug. 2013, doi: 10.1017/jfm.2013.301.

[109] P. A. Monkewitz, K. A. Chauhan, and H. M. Nagib, “Self-consistent high-Reynolds-number asymptotics for zero-pressure-gradient turbulent boundary layers,” *Physics of Fluids*, vol. 19, no. 11, Nov. 2007, doi: 10.1063/1.2780196.

[110] A. Manzoor Hasan, J. Larsson, S. Pirozzoli, and R. Pecnik, “Estimating Mean Profiles and Fluxes in High-Speed Turbulent Boundary Layers Using Inner/Outer-Layer Scalings,” *AIAA Journal*, vol. 62, no. 2, pp. 848–853, Feb. 2024, doi: 10.2514/1.J063335.

[111] P.-å. Krogstad, R. A. Antonia, and L. W. B. Browne, “Comparison between rough- and smooth-wall turbulent boundary layers,” *J. Fluid Mech.*, vol. 245, pp. 599–617, Dec. 1992, doi: 10.1017/S0022112092000594.

[112] E. R. VAN DRIEST, “Turbulent Boundary Layer in Compressible Fluids,” *J. Spacecr. Rockets*, vol. 40, no. 6, pp. 1012–1028, Nov. 2003, doi: 10.2514/2.7048.

[113] A. Walz, *Boundary layers of flow and temperature*, no. 3. MIT Press, 1970. [Online]. Available: https://aiche.onlinelibrary.wiley.com/doi/10.1002/aic.690160302

[114] L. Duan and M. P. Martín, “Direct numerical simulation of hypersonic turbulent boundary layers. Part 4. Effect of high enthalpy,” *J. Fluid Mech.*, vol. 684, pp. 25–59, Oct. 2011, doi: 10.1017/jfm.2011.252.

[115] Y.-S. Zhang, W.-T. Bi, F. Hussain, and Z.-S. She, “A generalized Reynolds analogy for compressible wall-bounded turbulent flows,” *J. Fluid Mech.*, vol. 739, pp. 392–420, Jan. 2014, doi: 10.1017/jfm.2013.620.

[116] E. R. Van Driest, “The problem of Aerodynamic Heating,” *Aeronautical Engineering Review*, vol. 15, pp. 26–41, 1956.

[117] Z. Popinski and C. F. Ehrlich, “DEVELOPMENT DESIGN METHODS FOR PREDICTING HYPERSONIC AERODYNAMIC CONTROL CHARACTERISTICS,” Sep. 1966.

[118] E. R. G. Eckert, “Engineering Relations for Heat Transfer and Friction in High-Velocity Laminar and Turbulent Boundary-Layer Flow Over Surfaces With Constant Pressure and Temperature,” *J. Fluids Eng.*, vol. 78, no. 6, pp. 1273–1283, Aug. 1956, doi: 10.1115/1.4014011.

[119] R. DEEM and J. MURPHY, “Flat plate boundary layer transition at hypersonic speeds,” in *2nd Aerospace Sciences Meeting*, in Aerospace Sciences Meetings. Reston, Virigina: American Institute of Aeronautics and Astronautics, Jan. 1965. doi: 10.2514/6.1965-128.

[120] G. A. Simeonides, “LAMINAR-TURBULENT TRANSITION CORRELATIONS IN SUPERSONIC / HYPERSONIC FLAT PLATE FLOW,” in *24th ICAS Congress*, Yokohama, Sep. 2004.

[121] G. A. Simeonides, “Correlation of laminar-turbulent transition data over flat plates in supersonic/hypersonic flow including leading edge bluntness effects,” *Shock Waves*, vol. 12, no. 6, pp. 497–508, May 2003, doi: 10.1007/s00193-003-0184-3.

[122] T. KANDA, “Conservation-Law Approach to Prediction of Boundary Layer Transition,” *Trans. Jpn. Soc. Aeronaut. Space Sci.*, vol. 54, no. 183, pp. 7–15, 2011, doi: 10.2322/tjsass.54.7.

[123] E. J. Hopkins, “Simple Methods for Determining the Virtual Origin of Turbulent Boundary Layers in Hypersonic Flow on Sharp-Edged Flat Plates,” *J. Appl. Mech.*, vol. 41, no. 3, pp. 551–553, Sep. 1974, doi: 10.1115/1.3423346.

[124] K. Yabushita and G. Okahata, “Determination of Form Factor Using Proportional Relationship Derived From Kármán-Schoenherr Formula,” *Journal of the Japan Society of Naval Architects and Ocean Engineers*, vol. 27, no. 0, pp. 23–30, 2018, doi: 10.2534/jjasnaoe.27.23.

[125] S. Priebe and M. P. Martín, “Turbulence in a hypersonic compression ramp flow,” *Phys. Rev. Fluids*, vol. 6, no. 3, p. 034601, Mar. 2021, doi: 10.1103/PhysRevFluids.6.034601.

[126] G. Macdonald Elfstrom, “TURBULENT SEPARATION IN HYPERSONIC FLOW,” PhD Thesis, Imperial College, London, 1971.

[127] D. J. Mee, “Boundary-Layer Transition Measurements in Hypervelocity Flows in a Shock Tunnel,” *AIAA Journal*, vol. 40, no. 8, pp. 1542–1548, Aug. 2002, doi: 10.2514/2.1851.

[128] Fu Jia, Yi Shi-He, Wang Xiao-Hu, Zhang Qing-Hu, and He Lin, “Experimental study on flow visualization of hypersonic flat plate boundary layer,” *Acta Physica Sinica*, vol. 64, no. 1, p. 014704, Jan. 2015, doi: 10.7498/aps.64.014704.

[129] J. E. Wallace, “Hypersonic turbulent boundary layer studies at cold wall conditions,” Feb. 1967. Accessed: Aug. 15, 2026. [Online]. Available: https://ntrs.nasa.gov/citations/19670052225

[130] D. Sahoo, M. Schultze, and A. Smits, “Effects of Roughness on a Turbulent Bloundary Layer in Hypersonic Flow,” in *39th AIAA Fluid Dynamics Conference*, Reston, Virigina: American Institute of Aeronautics and Astronautics, Jun. 2009, pp. 2009–3678. doi: 10.2514/6.2009-3678.

[131] H. M. Nagib and K. A. Chauhan, “Variations of von Kármán coefficient in canonical flows,” *Physics of Fluids*, vol. 20, no. 10, Oct. 2008, doi: 10.1063/1.3006423.

[132] O. J. H. Williams and A. J. Smits, “Effect of tripping on hypersonic turbulent boundary-layer statistics,” *AIAA Journal*, vol. 55, no. 9, pp. 3051–3058, 2017, doi: 10.2514/1.J055471.

[133] J. Délery and J.-P. Dussauge, “Some physical aspects of shock wave/boundary layer interactions,” *Shock Waves*, vol. 19, no. 6, pp. 453–468, Dec. 2009, doi: 10.1007/s00193-009-0220-z.

[134] F.-Y. Zuo, “Hypersonic Shock Wave/Turbulent Boundary Layer Interaction over a Compression Ramp,” *AIAA Journal*, vol. 61, no. 4, pp. 1579–1595, Apr. 2023, doi: 10.2514/1.J062521.

[135] H. PERGAMENT, “A THEORETICAL ANALYSIS OF NON-EQUILIBRIUM HYDROGEN-AIR REACTIONS IN FLOW SYSTEMS,” in *Hypersonic Ramjet Conference*, Reston, Virigina: American Institute of Aeronautics and Astronautics, Apr. 1963. doi: 10.2514/6.1963-113.

[136] B. J. Mcbride, M. J. Zehe, and S. Gordon, “NASA Glenn Coefficients for Calculating Thermodynamic Properties of Individual Species,” 2002. [Online]. Available: http://www.sti.nasa.gov

[137] W. Engblom, F. Frate, and C. Nelson, “Progress in Validation of Wind-US for Ramjet/Scramjet Combustion,” in *43rd AIAA Aerospace Sciences Meeting and Exhibit*, Reston, Virigina: American Institute of Aeronautics and Astronautics, Jan. 2005, pp. 86–93. doi: 10.2514/6.2005-1000.

[138] M. C. BURROWS and A. P. KURKOV, “An Analytical and Experimental Study of Supersonic Combustion of Hydrogen in Vitiated Air Stream,” *AIAA Journal*, vol. 11, no. 9, pp. 1217–1218, Sep. 1973, doi: 10.2514/3.50564.

[139] A. Paull, M. Frost, and H. Alesi, “HyShot-T4Supersonic Combustion Experiments,” Jan. 2000.

[140] G. K. BATCHELOR and I. PROUDMAN, “THE EFFECT OF RAPID DISTORTION OF A FLUID IN TURBULENT MOTION,” *Q. J. Mech. Appl. Math.*, vol. 7, no. 1, pp. 83–103, 1954, doi: 10.1093/qjmam/7.1.83.